NANYANG
TECHNOLOGICAL
UNIVERSITY
SINGAPORE

SORBONNE
UNIVERSITÉ

LPENS
LABORATOIRE DE PHYSIQUE
DE L'ÉCOLE NORMALE SUPÉRIEURE

OPTICAL SPECTROSCOPY OF SINGLE PEROVSKITE NANOCRYSTALS FOR QUANTUM PHOTONICS

Mohamed-Raouf Amara

SCHOOL OF PHYSICAL AND MATHEMATICAL SCIENCES
NANYANG TECHNOLOGICAL UNIVERSITY

LABORATOIRE DE PHYSIQUE DE L'ÉCOLE NORMALE SUPÉRIEURE
SORBONNE UNIVERSITÉ

2023

OPTICAL SPECTROSCOPY OF SINGLE PEROVSKITE NANOCRYSTALS FOR QUANTUM PHOTONICS

Mohamed-Raouf Amara

SCHOOL OF PHYSICAL AND MATHEMATICAL SCIENCES
NANYANG TECHNOLOGICAL UNIVERSITY

LABORATOIRE DE PHYSIQUE DE L'ÉCOLE NORMALE SUPÉRIEURE
SORBONNE UNIVERSITÉ

A thesis submitted to Nanyang Technological University and Sorbonne Université in partial fulfilment of the requirement for the degree of
Doctor of Philosophy

2023

Statement of originality

I hereby certify that the work embodied in this thesis is the result of original research done by me except where otherwise stated in this thesis. The thesis work has not been submitted for a degree or professional qualification to any other university or institution. I declare that this thesis is written by myself and is free of plagiarism and of sufficient grammatical clarity to be examined. I confirm that the investigations were conducted in accord with the ethics policies and integrity standards of Nanyang Technological University and that the research data are presented honestly and without prejudice.

August 10, 2022

M-R Amara

Mohamed-Raouf Amara

Supervisor declaration statement

I have reviewed the content and presentation style of this thesis and declare it of sufficient grammatical clarity to be examined. To the best of my knowledge, the thesis is free of plagiarism and the research and writing are those of the candidate's except as acknowledged in the Author Attribution Statement. I confirm that the investigations were conducted in accord with the ethics policies and integrity standards of Nanyang Technological University and that the research data are presented honestly and without prejudice.

August 10, 2022

Weibo Gao

Weibo Gao

Authorship attribution statement

This thesis contains material from one paper in which I am listed as an author.

Ch. 5 is based on *C. Huo*, *C. F. Fong*, ***M.-R. Amara***, Y. Huang, B. Chen, H. Zhang, L. Guo, H. Li, W. Huang, C. Diederichs and Q. Xiong, “Optical spectroscopy of single colloidal $CsPbBr_3$ perovskite nanoplatelets”, Nano Letters **20**, 3673-3680 (2020)

The contributions of the co-authors are as follows:

- C.H. synthesized the nanoplatelets and C.H. and I, M.-R. A, prepared the samples
- C.H., C.F.F., Y.H. and I performed the measurements and analysed the results
- C.H. performed the TEM characterisation with C.B. under the supervision of H.Z.
- C.H. and C.F.F. wrote the manuscript
- C.D. and Q.X. supervised the project

August 10, 2022

M-R Amara

Mohamed-Raouf Amara

Abstract

Lead halide perovskites in their nanocrystal form have recently emerged as efficient quantum light emitters despite their low-temperature colloidal synthesis and structural lability. This has led to an intense debate about the band-edge exciton in these materials and the bright or dark character of the lowest energy exciton state. While symmetry arguments predict a lowest-lying dark exciton state, it was hypothesised that the combination of strong-spin orbit and structural instability should lead to a Rashba effect which places the bright exciton state below the dark exciton, in contrast with all other established materials. This work is a detailed study of single $CsPbBr_3$, in the spectral and time domain, which provides critical information about the band-edge exciton fine structure. It should help the community refine theoretical models and converge towards an accurate description of the band-edge exciton of these fledgling materials, thus helping to shed light on their outstanding properties.

Digest

Summary

Lead halide perovskites (LHPs) in their nanocrystal (NC) form have recently emerged as efficient quantum light emitters despite their low-temperature colloidal synthesis and the structural lability of the perovskite lattice. This has led to an intense debate about the nature of the excitonic states at the origin of the emission of photons. In particular, the nature of the band-edge exciton states and the bright or dark character of the lowest energy exciton state remain open questions. While symmetry arguments predict a lowest-lying dark exciton state, it was hypothesised that the combination of strong-spin orbit and structural instability should lead to a Rashba effect which places the bright exciton state below the dark exciton, in contrast with all other established materials. This work is a detailed study, both in the spectral and time domain, of single $CsPbBr_3$ NCs. To do so, experimental platforms for the synthesis and optical characterisation at the singe object level were put in place by the author both at NTU and LPENS. Thanks to detailed spectral analysis of the emission, the full spectral fingerprint of single $CsPbBr_3$ NCs, comprised of a bright triplet exciton, trion and biexciton each with its own set of optical phonon replica, is revealed across a wide range of NCs sizes from $\sim$7 nm to $\sim$20 nm. The fast emission of single $CsPbBr_3$ NCs at the lowest cryogenic temperatures is investigated in detail and put in perspective with the decay times across LHPs. In addition, in light of the debate about the exciton fine structure ordering in $CsPbBr_3$, we report on experiments to probe the dark exciton state via both magneto-optical and temperature-dependent photoluminescence decay measurements. While these measurements do not directly evidence a spectral fingerprint for the dark exciton, they enable us to gain insight into the population redistribution mechanisms at play in setting the populations of the exciton fine structure states. Thus, thanks to a combination of spectral and temporal analysis of the emission of single $CsPbBr_3$ NCs, critical information about the band-edge exciton fine structure is obtained. This work should help the community refine theoretical models and converge towards an accurate description of the band-edge exciton of these fledgling materials, thus helping to shed light onto the oustanding properties of LHPs.

Résumé

Les nanocristaux de perovskite, synthétisés pour la première fois en 2015, ont récemment émergé comme des émetteurs quantiques efficaces malgré leur synthèse colloidale à basse température et le caractère labile de la structure perovskite. Ces propriétés étonnantes ont donné lieu ces dernières années à un débat intense au sujet de la nature des états excitoniques à l'origine de l'émission de photons. En particulier, la nature de l'exciton proche de la bande interdite et le caractère brillant ou sombre de l'exciton de plus basse énergie restent des questions ouvertes. Alors que les arguments de symétrie prédisent un exciton sombre comme premier état excité, la combinaison d'un important couplage spin-orbite à l'instabilité de la structure perovskite et de potentielles brisures de symétrie d'inversion pourrait donner lieu à un effet Rashba qui rendrait le premier état excité brillant, à contrario de tous les semiconducteurs connus. Dans ce cadre, ce travail est une étude experimentale détaillée, dans le domaine spectral et temporel, de nanocristaux individuels de $CsPbBr_3$ à température cryogénique. Pour ce faire, des plateformes expérimentales dédiées à la synthèse et la caractérisation optique à l'échelle de l'objet unique ont été mises en place par l'auteur à NTU et au LPENS. Nos mesures spectrales détaillées révèlent la complexité de l'empreinte spectrale des nanocristaux de $CsPbBr_3$ composée de l'exciton brillant, du trion et du biexciton chacun accompagné par des répliques phonons, ainsi que sa dépendence en taille de nanocristaux. Le déclin de l'émission est examiné dans le cas de $CsPbBr_3$ et comparé aux déclins observés dans les pérovskites en général. De plus, compte tenu du débat sur l'ordre des états de la structure fine de l'exciton, nous avons mené des expériences de magnéto-optique ainsi que de déclin en fonction de la température visant à sonder l'exciton sombre via son

interaction avec l'exciton brillant. Bien que nos expériences n'aient pas révélé de signature spectrale de l'exciton sombre, elles permettent une compréhension approfondie des mécanismes de redistribution de population en jeu dans la structure fine de l'exciton. Ainsi, grâce à la combinaison d'études spectrales et temporelles de l'émission de nanocristaux de $CsPbBr_3$, nous apportons des informations critiques sur l'exciton proche de la bande interdite. Ce travail devrait aider la communauté à raffiner les modèles théoriques et, ce faisant, converger vers une description réaliste de l'exciton dans ces matériaux naissants qui permettra finalement d'élucider l'origine des remarquables propriétés des nanocristaux de pérovskite.

Acknowledgements

At NTU, I would like to thank my first supervisor Prof. Xiong and then Prof. Gao for taking me on after Prof. Xiong's departure. Much of the work performed at NTU was conducted in PAP01-04 and in Prof. Xiong's group chemistry room where I spent much time together with Caixia Huo and Chee Fai Fong trying to perfect our respective sample preparation methods. I hope that your academic journeys are only starting and I wish you the best of luck. Special thanks go to SPMS technical staff and in particular to the liquid nitrogen facility and mechanical workshop which were instrumental in many experimental aspects of this work.

At LPENS, my deepest thanks go to my supervisor Carole Diederichs. It was, and still is, a pleasure to work under your supervision on such a new and fast moving field. Thank you for your instrumental help with the Joint PhD procedures, a purely theoretical abstraction at the beginning, which we managed to make a reality although at the expense of much experimental work. I am also grateful to Christophe and Yannick for their genuine interest in our work and their constant availability to hear and help with any theoretical or experimental difficulty. Major thanks go to the people of the L065 and the atmosphere maintained there. It was a pleasure to partake in the political and philosophical debates that punctuated our meals, where ideas were heard and critically discussed. Special thanks go to the LPENS staff for their availability and their key help in the functioning of the lab. In particular, I'd like to thank Aurélie and Pascal for their help with the chemistry room and the sample holder.

Finally, of course, I would like to thank my parents and close friends and family for their unconditional support and for putting up with me. Thank you.

Contents

Figures and Tables

List of Figures

List of Tables

Introduction

Electromagnetism is one of the fundamental interactions of nature. In the context of the Standard Model, this interaction is mediated by a gauge boson corresponding to elementary excitations of the electromagnetic field called photons [1]. In atoms, the resulting electromagnetic force between atomic nuclei and their surrounding electron cloud, *i.e.* Coulomb interaction, is understood as a virtual exchange of photons between charges making photons essential in the description of the cohesion of atoms. Electrons in atoms further occupy discrete energy levels and can gain/lose energy via their interaction with the electromagnetic field. This naturally-occuring basic interaction, between a single electron and the electromagnetic field, proceeds through the absorption/emission of a single photon as first evidenced in sodium atoms in 1977 [2]. Electromagnetism is thus at the foundation of our understanding of all chemical bonding in molecules and solids and thus of chemistry, solid state physics, nanotechnology and in fact all modern electronic technologies.

Global communications today rely on the use of lasers coupled into optical fibers connecting all continents. In these fibers, information is encoded as bits of information with two possibles values 0 and 1 and the security of the infrastructure relies on technological assumptions. For example, the widely used RSA public key system proposed in 1977 relies on the fact that there are no known classical algorithms that can factorise large integers into prime factors within a finite time [3]. And indeed, the longest RSA-key decrypted up to now, while only 829 bits long, took the equivalent of 2700 computing core-years for a premium desktop computer to crack [4]. In contrast, 1024 and 2048 bits keys are routinely used today in applications and decryption of the latter is estimated to take 300 trillion years with current known technologies. Quantum algorithms, however, such as Shor's algorithm could reduce the exponential complexity of breaking RSA to polynomial [5]. Experimental realisations of Shor's algorithm have thus been one of the main goals of quantum information scientists which have been successful in a variety of systems from ensemble quantum systems [6] to solid-state quantum bits [7] and photonic systems [8–10]. Photonic systems are in that respect the most advanced and can readily factorise numbers up to 21 using Shor's algorithm [10]. The security of quantum cryptography protocols based on optics and quantum computation schemes however rely on the presence of a definite number of photons [11, 12], making single-photon and more generally N-photon sources an important requirement for future applications.

The second half of the twentieth century has seen tremendous achievements in the reduction of the dimensions of semiconductors. The pioneering works of Ekimov in glass matrices [13, 14] and Brus in solutions [15] revealed the size-dependent optical properties of quantum confined nanostructures and in particular, their ability to confine electrons in the three dimensions of space giving rise to discrete energy levels. Even though they are composed of several thousands of atoms, systems that replicate the single photon emission of atoms can now be designed. However, as is the case in the solid state, the spontaneous emission of these nanostructures is strongly influenced by their local environment and they cannot be considered as ideal isolated quantum systems. Since the late 1980s, researchers have thus been greatly interested in the study and control of the spontaneous emission of nanoemitters through the careful control of their morphology, size and environment.

A wide diversity of materials have been proposed as efficient single photon emitters. Among them, epitaxial quantum dots have shown exceptional properties as quantum emitters but they operate only at cryogenic temperatures [16, 17], except for some nitride-based quantum dots [18] that yield a lower optical quality which in addition to their complex production techniques renders them impractical. Nitrogen-vacancy centres in diamond, on the other hand, offer the possibility to operate at room temperature but they exhibit a broad emission spectrum due to strong emission in the phonon side bands which prevents efficient spectral filtering of the emission [19]. Several unexpected emitters have also emerged in the last years, such as carbon nanotubes [20–22], point defects in 2D materials [23–26] and in silicon [27], all of which have demonstrated single photon emission at low temperature while detailed studies are currently being carried out to assess their potential in telecom wavelengths. Nanocrystals (NCs) synthesized by relatively facile and low-cost chemical methods appear promising, as they preserve a single photon emission up to room temperature and present narrow peaks with low multi-photon emission [28, 29] thanks to fast non-radiative Auger recombination [30] and quantum confinement. While in the last decades, much attention was given to the proper passivation of NCs, the latest newcomers in the realm of bright-emitting NCs present with outstanding properties *out of the box*. These are lead halide perovskites (LHPs) [31–33], the subject of this study.

As for the established zinc blende and wurtzite colloidal nanocrystals (NCs), the emission energy of cesium lead halide ($CsPbX_3$) NCs (X = Cl, Br, I or a mixture) is tunable over the whole visible spectrum by combination of substitution of the halogen atom and quantum confinement [31]. The emission is spectrally narrow [31] and highly efficient (quantum yield from 50 % to 90 % [34]). The emission intensity is found to be more stable for LHPs NCs than for conventional core-shell colloidal NCs, which comes as striking considering the optimisation of the latter structures over the past twenty years [33]. In fact, while defects are plenty in LHPs, optoelectronic properties seem impervious to such defects. This is evidenced at the single NC level, where first studies of low temperature photoluminescence on first-generation single LHP NCs have evidenced narrow peaks grouped in doublets or triplets [33, 35] with stable and bright emission. Besides, single photon emission was evidenced both at cryogenic [33] and room [32] temperatures making LHPs promising quantum emitters which, thanks to their colloidal character, are readily and easily handled at a minimal cost in contrast with epitaxial quantum dots.

Despite much interest in the optical properties of LHP NCs in the recent years, no clear understanding of these outstanding properties has emerged. In particular, there is still an intense debate about the states at the origin of light emission as detailed in Sec. 1.2.3. Notably, it was hypothesised that the combination of a strong-spin-orbit coupling and the instability of the perovskite lattice should lead to a Rashba effect that could place the bright exciton below the dark exciton, in contrast to all other known semiconductors. The general interest in LHPs stemmed from ensemble studies which revealed a bright and narrow emission at room temperature [31, 36]. A significant body of ensemble studies have aimed at characterising LHPs NCs by variety of both time-averaged and time-resolved spectroscopic techniques thus providing with significant insight into their photophysical properties [31, 37–39]. However, structural differences between different single emitters as well as their interaction lead to inhomogeneities in the spectral and temporal properties of the emission and thus significantly complicate the interpretation of ensemble experiments based on underlying microscopic mechanisms. The study of nanoemitters at the single object level is therefore of utmost importance to probe the underlying intrinsic phenomena rather than the collective and averaged phenomena, thus paving the way for potential quantum information applications. In addition, due to homogeneous broadening the discrete emission lines characteristic of nanoemitters can not be resolved at room temperature and cryogenic temperature studies are therefore required to resolve the discrete states leading to the emission of photons. At the single object level, the spectrum of a single nano-emitter is given by: intrinsic properties such as its composition, size and shape and thus electronic structure and vibrational landscape; and extrinsic effects related to different surface passivation degree and the local dielectric environment. Influence of the surface passivation or of the local environment can thus be studied by an analysis of the variability in optical response observed between single nanoemitters. Because of this and the difference in size and shape between emitters, intrinsic properties can only be probed by a statistical analysis of the response of many emitters. As such, the study of single NCs with a sufficient sample size is critical to reveal both the underlying characteristics of single NCs and the variability between them.

Thesis objective

In this context, the objective of this thesis is to provide a detailed experimental study of the fine structure of the band-edge exciton in $CsPbBr_3$ NCs, the material for which the original prediction of a lower-lying bright exciton was formulated a few months before the start of this thesis. To do so, I synthesised perovskite NCs of sufficient quality and successfully isolated single objects. Both at NTU and LPENS, using home-made scanning confocal microscopes, I studied their optical properties and gained some insight into the structural and electronic properties of these fledgling

NCs. With an optimised spectroscopy platform, a high number of NCs was studied revealing the underlying size-dependences of the full spectrum of $CsPbBr_3$ NCs across a wide range of sizes from 7 and 20 nm. In addition to this detailed spectral study, the dark exciton state was also probed by a set of temperature-dependent time-resolved measurements.

This manuscript is an account of this work and is organised as follows:

CH. 1 The conceptual elements related to the optoelectronic properties of LHP NCs are presented. We detail the electronic band structure of our material both in bulk and in these quantum confined structures in light of their peculiar crystal structure. Emphasis is placed on the band-edge exciton and the ongoing debate related to its fine structure. Finally, the interaction of a quantum emitter with its environment is presented.

CH. 2 We detail the experimental methods used in this work. In particular, we focus on: (i) the synthesis of $CsPbBr_3$ nanocrystals and preparation of samples for single NC studies and (ii) the experimental optical platforms, home-built scanning confocal microscopes.

CH. 3 is a detailed study of the spectral properties of single $CsPbBr_3$ NCs at liquid helium temperature providing the full spectral fingerprint of single $CsPbBr_3$ NCs across a wide range of NC sizes. Thanks to automated scanning techniques put in place by the author, a large number of NCs could be studied and instrinsic effects were successfully evidenced.

CH. 4 is a study of single NCs in the time-domain. Namely, we first report on measurements of the PL decay of single NCs at liquid helium temperature and compare our measurements to the literature across the LHP family. The interaction between the bright and dark excitons was studied via two sets of experiements: (i) via magneto-optical PL and PL decay measurements and (ii) temperature-dependent PL decay measurements on single $CsPbBr_3$ NCs. For the latter, we investigate several bright-dark level orderings and phonon-assisted bright-dark population mixing mechanisms, and based on our experiment results, we discuss critically each mixing mechanism and its potential contribution to the exciton-fine structure population redistribution.

Ch. 5 is a side study on perovskite nanocrystals with a one dimensional confinement, so-called nanoplatelets. Notably, we reveal that single $CsPbBr_3$ emit single photons at cryogenic temperature.

References

[1] G. N. Lewis, "The Conservation of Photons", Nature **118**, 874–875 (1926) (p. 17).

[2] H. J. Kimble et al., "Photon Antibunching in Resonance Fluorescence", Physical Review Letters **39**, 691 (1977) (p. 17).

[3] R. L. Rivest et al., "A method for obtaining digital signatures and public-key cryptosystems", Communications of the ACM **21**, 120–126 (1978) (p. 17).

[4] F. Boudot et al., *Factorization of RSA-250*, (Feb. 28, 2020) `https://caramba.loria.fr/rsa250.txt` (visited on 05/06/2020) (p. 17).

[5] P. Shor, "Algorithms for quantum computation: discrete logarithms and factoring", in Proceedings 35th Annual Symposium on Foundations of Computer Science (Nov. 1994), pp. 124–134 (p. 18).

[6] L. M. K. Vandersypen et al., "Experimental realization of Shor's quantum factoring algorithm using nuclear magnetic resonance", Nature **414**, 883–887 (2001) (p. 18).

[7] E. Lucero et al., "Computing prime factors with a Josephson phase qubit quantum processor", Nature Physics **8**, 719–723 (2012) (p. 18).

[8] B. P. Lanyon et al., "Experimental Demonstration of a Compiled Version of Shor's Algorithm with Quantum Entanglement", Physical Review Letters **99**, 250505 (2007) (p. 18).

[9] C.-Y. Lu et al., "Demonstration of a Compiled Version of Shor's Quantum Factoring Algorithm Using Photonic Qubits", Physical Review Letters **99**, 250504 (2007) (p. 18).

[10] E. Martín-López et al., "Experimental realization of Shor's quantum factoring algorithm using qubit recycling", Nature Photonics **6**, 773–776 (2012) (p. 18).

[11] E. Knill et al., "A scheme for efficient quantum computation with linear optics", Nature **409**, 46–52 (2001) (p. 18).

[12] P. Kok et al., "Linear optical quantum computing with photonic qubits", Reviews of Modern Physics **79**, 135–174 (2007) (p. 18).

[13] A. I. Ekimov et al., "Quantum size effect in three-dimensional microscopic semiconductor crystals", Journal of Experimental and Theoretical Physics **34**, 363 (1981) (p. 18).

[14] A. I. Ekimov et al., "Quantum size effect in semiconductor microcrystals", Solid State Communications **56**, 921–924 (1985) (p. 18).

[15] L. Brus, "Electronic wave functions in semiconductor clusters: experiment and theory", The Journal of Physical Chemistry **90**, 2555–2560 (1986) (p. 18).

[16] C. Santori et al., "Triggered Single Photons from a Quantum Dot", Physical Review Letters **86**, 1502–1505 (2001) (p. 18).

[17] P. Senellart et al., "High-performance semiconductor quantum-dot single-photon sources", Nature Nanotechnology **12**, 1026–1039 (2017) (p. 18).

[18] C. Santori et al., "Photon correlation studies of single GaN quantum dots", Applied Physics Letters **87**, 051916 (2005) (p. 18).

[19] J. Wrachtrup et al., "Processing quantum information in diamond", Journal of Physics: Condensed Matter **18**, S807–S824 (2006) (p. 18).

[20] A. Högele et al., "Photon Antibunching in the Photoluminescence Spectra of a Single Carbon Nanotube", Physical Review Letters **100**, 217401 (2008) (p. 18).

[21] A. Jeantet et al., "Widely Tunable Single-Photon Source from a Carbon Nanotube in the Purcell Regime", Physical Review Letters **116**, 247402 (2016) (p. 18).

[22] X. He et al., “Carbon nanotubes as emerging quantum-light sources”, Nature Materials **17**, 663–670 (2018) (p. 18).

[23] A. Srivastava et al., “Optically active quantum dots in monolayer WSe2”, Nature Nanotechnology **10**, 491–496 (2015) (p. 18).

[24] P. Tonndorf et al., “Single-photon emission from localized excitons in an atomically thin semiconductor”, Optica **2**, 347–352 (2015) (p. 18).

[25] T. T. Tran et al., “Quantum emission from hexagonal boron nitride monolayers”, Nature Nanotechnology **11**, 37–41 (2016) (p. 18).

[26] T. T. Tran et al., “Room-Temperature Single-Photon Emission from Oxidized Tungsten Disulfide Multilayers”, Advanced Optical Materials **5**, 1600939 (2017) (p. 18).

[27] A. Durand et al., “Broad Diversity of Near-Infrared Single-Photon Emitters in Silicon”, Physical Review Letters **126**, 083602 (2021) (p. 18).

[28] B. Lounis et al., “Photon antibunching in single CdSe/ZnS quantum dot fluorescence”, Chemical Physics Letters **329**, 399–404 (2000) (p. 19).

[29] P. Michler et al., “Quantum correlation among photons from a single quantum dot at room temperature”, Nature **406**, 968–970 (2000) (p. 19).

[30] V. I. Klimov, “Spectral and Dynamical Properties of Multiexcitons in Semiconductor Nanocrystals”, Annual Review of Physical Chemistry **58**, 635–673 (2007) (p. 19).

[31] L. Protesescu et al., “Nanocrystals of Cesium Lead Halide Perovskites ($CsPbX_3$, X = Cl, Br, and I): Novel Optoelectronic Materials Showing Bright Emission with Wide Color Gamut”, Nano Letters **15**, 3692–3696 (2015) (pp. 19, 20).

[32] Y.-S. Park et al., “Room Temperature Single-Photon Emission from Individual Perovskite Quantum Dots”, ACS Nano **9**, 10386–10393 (2015) (p. 19).

[33] G. Rainò et al., “Single Cesium Lead Halide Perovskite Nanocrystals at Low Temperature: Fast Single-Photon Emission, Reduced Blinking, and Exciton Fine Structure”, ACS Nano **10**, 2485–2490 (2016) (p. 19).

[34] X. Li et al., “$CsPbX_3$ Quantum Dots for Lighting and Displays: Room-Temperature Synthesis, Photoluminescence Superiorities, Underlying Origins and White Light-Emitting Diodes”, Advanced Functional Materials **26**, 2435–2445 (2016) (p. 19).

[35] M. Fu et al., “Neutral and Charged Exciton Fine Structure in Single Lead Halide Perovskite Nanocrystals Revealed by Magneto-optical Spectroscopy”, Nano Letters **17**, 2895–2901 (2017) (p. 19).

[36] G. Nedelcu et al., “Fast Anion-Exchange in Highly Luminescent Nanocrystals of Cesium Lead Halide Perovskites ($CsPbX_3$, X = Cl, Br, I)”, Nano Letters **15**, 5635–5640 (2015) (p. 20).

[37] M. A. Becker et al., “Long Exciton Dephasing Time and Coherent Phonon Coupling in $CsPbBr_2Cl$ Perovskite Nanocrystals”, Nano Letters **18**, 7546–7551 (2018) (p. 20).

[38] M. I. Bodnarchuk et al., “Rationalizing and Controlling the Surface Structure and Electronic Passivation of Cesium Lead Halide Nanocrystals”, ACS Energy Letters **4**, 63–74 (2019) (p. 20).

[39] W. Shcherbakov-Wu et al., “Temperature-Independent Dielectric Constant in $CsPbBr_3$ Nanocrystals Revealed by Linear Absorption Spectroscopy”, The Journal of Physical Chemistry Letters **12**, 8088–8095 (2021) (p. 20).

1

Perovskite nanocrystals as quantum emitters

In this chapter we mobilize the theoretical foundations of solid state physics and light-matter interactions to rationalise the outstanding properties of LHPs in light of the most recent literature.

To understand the detail of the absorption and emission of photons by nanocrystals (NCs), we start by a presentation of the crystallographic structure of the material we study (a metal halide perovskite) and its peculiarities. With that in mind, we will see how electrons behave in these semiconductors and how, from the band-edge wavefunctions, we can infer the resulting light-matter interactions and provide a realistic picture of the outstanding properties of LHP NCs.

1.1 Perovskite structure

Used as early as in 1999 in light-emitting applications [1], halide perovskites only emerged in the early 2010s as efficient absorbers in the solar cell community with the pioneering works of Kojima, Snaith and collaborators [2, 3]. Since then, the outstanding optoelectronic properties of LHPs have only begun to be unveiled, with single-junction perovskite solar cells already over 25% efficiency [4] and tandem solar cells approaching 30% very closely [5]. This has lead to a tremendous amount of attention on these materials, which soon led to the synthesis of bright luminescent NCs [6, 7] especially needed in the green spectral range [8]. While these achievements and the surrounding buzz in the optoelectronic community are not much older than a decade, the history of perovskites started in the first part of the 19th century.

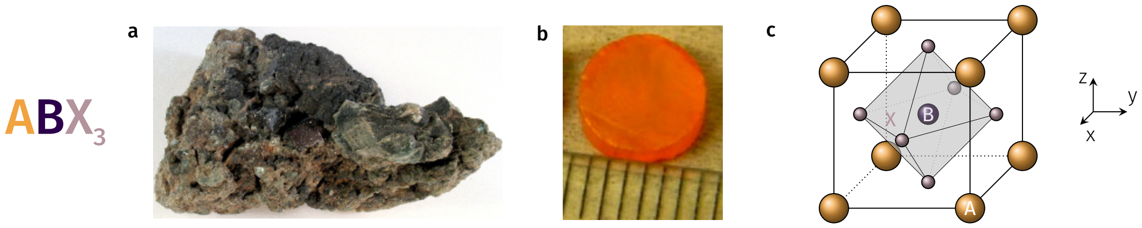

Figure 1.1 | Prototypical perovskite. **a**, Original calcium titanate crystal discovered in 1839. **b**, Single crystal of the perovskite material studied in this work: $CsPbBr_3$. **c**, 3D view of the unit cell of cubic perovskites. Panels are reprinted from: **a** [11]; **b** [12].

1.1.1 The ideal cubic perovskite

Perovskites

Perovskites are a class of materials that adopt the same crystal structure as the prototypical calcium titanate oxide $CaTiO_3$ mineral discovered in [9] and shown in FIG. 1.1a. While the term perovskite originally only referred to this particular mineral, it was later generalised by Goldschmidt in his seminal paper [10] to other oxide and fluoride perovskite compounds of the form ABX_3 where A and B are cations and X is an anion (FIG. 1.1c). In this structure, A sits at the corners of the cubic perovskite structure which contains the body centred $[PbX_6]$ octahedra characteristic of perovskites. In fact, it is this seminal paper that set the basic principles of materials synthesis, first considering the size of the involved ions, the coordination number of the cation and packing of the structure [10]. This shows the close link between perovskites and the history of crystallography.

Halide perovskites

Crystalline compounds with composition $CsPbX_3$, where X is a halogen (Br, I, Cl) as studied in this work, were also identified as early as in 1893 [13] while their actual perovskite structure and photoconductivity were investigated in the late 1950s [14, 15]. More generally, halide perovskites (ABX_3 with A = Cs, MA methylammonium, FA formamidinium) share the same perovskite structure as the oxides originally reported, however their physical properties strongly differ as illustrated by their appearance in FIG. 1.1a-b ($CsPbBr_3$). The different physical properties are explained in part by the less charged constituents (e.g. $Cs^{+}Pb^{2+}3Br^{-}$ vs. $Ca^{2+}Ti^{4+}3O^{2-}$) and the resulting bonds. Notably, and of interest to us, halide perovskites are semiconductors with direct bandgaps in the visible to near-infrared range of the electromagnetic spectrum.

Tolerance factor

For an ideal cubic perovskite ABX_3 as shown in FIG. 1.1c, the distance d_{AX} between the A and X sites on a face diagonal is $\sqrt{2}$ larger than the distance between the X and B sites. Considering a closely packed structure, we obtain the relation between the constituents radii $(r_A + r_X) = \sqrt{2}\,(r_X + r_B)$ which can only be nearly met in ideal cubic perovskites. This is the basis for the commonly-used geometric Goldschmidt tolerance factor t [10] which describes the ideality of the perovskite lattice as $t = {}^{(r_A+r_X)}\!/\!_{\sqrt{2}(r_X+r_B)}$ where $0.8 < t < 1$ is the region of stability of perovskites — although the structure may be distorted by octahedral tilting and thus has a lower symmetry as the A cation is still a bit too small. As such, the tolerance factor only assesses the ability of the A cation to fit within the spaces between the BX_6 octahedra. Other purely geometrical factors can be used to further refine the range of stability of perovskites as shown in FIG. 1.2a-d.

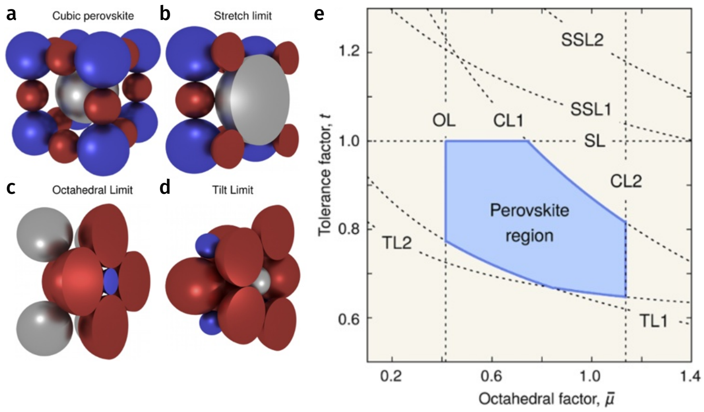

Figure 1.2 | Perovskites stability range and distortions. **a**, Hard spheres representation of the unit cell of ternary perovskites ABX_3 with cross-sectional views in the: **b**, stretch, **c**, octahedral and **d**, tilt limits. **e**, 2D-stability map of ternary perovskites based on the **b**-**d** limits and additional chemical limits. For $CsPbBr_3$ we have t = 0.92 and μ = 0.50 [16]. Reprinted from [17].

Octahedral factor

An alternative to redefining the ionic radii for each compound [18] has been to increase the dimensionality of the description [16], placing perovskites on 2D structure maps rather than on a line (FIG. 1.2e). The octahedral factor μ can be introduced [19] as $\mu = r_B/r_X$. Doing so gives significant improvements on the discrimination between perovskites and non-perovskites and further extends the geometrical constraints imposed on the perovskite lattice as started by Goldschmidt [17]. From this discussion and the fact that $t \leq 1$, it becomes clear that despite the use of the cubic perovskite structure as a model, a variety of lower-symmetry structures can form depending on the compounds but also on the actual phase (P, T) investigated.

1.1.2 Real perovskites

Distortions

Most perovskites are hettotypes, i.e. lower symmetry structures of the cubic aristotype. Indeed, distortions causing a lowering of the crystal structure symmetry are ubiquitous among perovskites. Even the original perovskite, $CaTiO_3$, does not crystallise in a cubic perovskite in ambient conditions (space group 221: Pm3m), but rather as an orthorhombic distortion of Pm3m: Pbmn [20]. This tilting usually occurs because all perovskites have $t < 1$, i.e. the A cation is too small for the voids between octahedra. In 1972, Glazer gave the description and classification of octahedral tilts in perovskites [21]. By enumerating all possible structures with no-tilt, one tilt, two tilts or three tilts along one or more of the rotation axes [100], [010] or [001], he identified 23 unique possible tilted systems. Later, group theory arguments reduced the number of tilt systems to 15 [22]. Most perovskites in fact exhibit distortions from the cubic structure because of tilting of the BX_6 octahedra and/or Jahn-Teller distortions involving BX_6 or A and B [23]. Here, we focus on lead halide perovskites $APbX_3$ with A = Cs, $HC(NH_2)_2$ (FA, formamidinium) and $(CH_3)NH_3$ (MA, methylammonium) which are reported to exhibit the most common distortion: octahedral tilting.

Table 1.1 | Crystal structures of $CsPbBr_3$. *Space groups are denoted by a numeric index and a symbol. We show here the symbol in both the International (Intl.) and the Schoenflies (Schoe.) notations. Arrows indicate phase transitions in bulk $CsPbBr_3$.

	Crystal system	No.*	Intl*	Schoe.*	Tilt system
	No tilt				
	Cubic α	221	$Pm\bar{3}m$	O_h^1	(1) $a^0a^0a^0$
↕ 130 °C	**One tilt**				
	Tetragonal ϵ	140	I4/mcm	D_{4h}^{18}	(6) $a^0a^0c^-$
	Tetragonal β	127	P4/mbm	D_{4h}^{5}	(2) $a^0a^0c^+$
↕ 88 °C	**Two tilts**				
	Orthorhombic γ	62	Pnma	D_{2h}^{16}	(13) $a^+b^-b^-$

Phase transitions

Perovskites also exhibit several crystal phases depending on the temperature and pressure [24]. Notably, perovskites are tilted structures at low temperature and only exhibit a cubic perovskite structure at high temperature. The observed crystal phases for $CsPbBr_3$ are summarised in TAB. 1.1 and depicted in FIG. 1.3a. In bulk, the orthorhombic structure Pnma γ reported up to ∼88 °C transitions to a tetragonal structure with space group P4/mbm β or I4/mcm ϵ depending on the in-phase or out-of-phase character of the tilt. Increasing the temperature above 130 °C then reveals the cubic aristotype Pm3m α [15]. For NCs, the same phase transitions are observed but at much lower temperature, as evidenced for $CsPbBr_3$ nanocrystals [25]. Other halide perovskites exhibit similar phase transitions while the actual temperatures depend on the composition.

Structural instability

In fact, as depicted in FIG. 1.3b, the high temperature cubic phase is understood as an averaged structure due to fluctuations between different lower symmetry phases related to tilting of the PbX_6 octahedra [26]. Depending on the time scale of these fluctuations, which is set by temperature and the depth of the local minima, LHPs can exhibit what is called either a static or dynamic disorder. At low temperature in particular, these fluctuations may happen slower than all relevant optoelectronic processes, such that carriers experience the local low symmetry structures leading to a static disorder. At high temperature however, these fluctuations may happen on similar time scales than electronic processes which may further impact carrier relaxation [26, 27].

Because of this highly dynamic structure and the resulting anharmonic behaviour of the lattice [28, 29], an actual assignment of the crystal structure may be difficult depending on the method. In this context, the initial incorrect assignment of the crystal structure of LHPs, and in particular $CsPbBr_3$, using convential X-ray diffraction may be understood now as a result of this high temperature instability. Indeed, the long-range order probed by the beam corresponds to the sum of all local orientations displaying the high symmetry structure [30, 31]. So in LHPs, the local crystal structure may deviate from the average measured symmetry. Even at lower temperature, the $PbBr_6$ cage rotations along the z and xy axes, shown in FIG. 1.3c, can lead to a thermally activated hopping between the two potential minima of the anharmonic potential [26, 28, 32]. The energy surface of $CsPbBr_3$ as a function of the amplitude of in-phase ($00a^+$) and out-of-phase (b^-b^-0) octahedral tilts was recently studied theoretically [33, 34]. It reveals that the cubic phase α is a potential maximum, the tetragonal phase β a saddle point and the orthorhombic phase γ is a global minimum. This is further complicated by the fact that cage rotations are also associated with displacements of the Cs and Br atoms [32] which may lead to further symmetry breaking and in particular inversion symmetry breaking.

In sum, there are thus three types of relevant perovskite structures: the cubic average showing no tilting of octahedra, the symmetrically tilted perovskite exhibiting inversion symmetry (Fig. 1.3d) and the asymmetrically tilted perovskites breaking inversion symmetry (Fig. 1.3e).

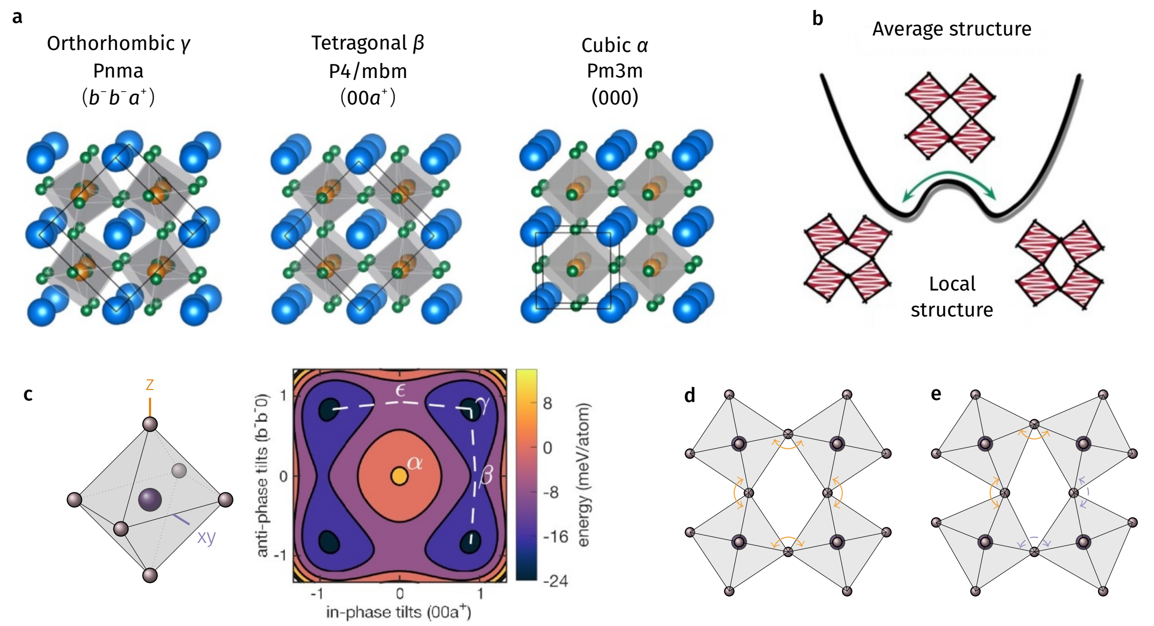

Figure 1.3 | Perovskites crystallographic phases. **a**, High temperature cubic phase and low temperature tetragonal and orthorhombic phases with the unit cell shown in dark lines. **b**, Cartoon of the average cubic and local tilted structures exhibited by the perovskite lattice. **c**, Energy surface of CsPbBr$_3$ as a function of tilt amplitudes along the (*z*) and (*xy*) axes. **d-e**, Tilting of the perovskite structure. Perovskite structure with: **d**, symmetric tilts of the PbBr$_6$ octahedra and **e**, asymmetric tilts of the PbBr$_6$ octahedra breaking inversion symmetry. Panels **a-c** are adapted from: **a** [27], **b** [26], **c** [33].

Defect tolerance

The local disorder is manifested in LHPs by the coexistence of several nm-size phases both in bulk [35] and within a single NC [36–38]. As shown in Fig. 1.4a, crystallographic domains are separated by twin planes forming nm scale domains. Besides this twinning, LHPs can in fact host a wide range of defects shown in Fig. 1.4b as a function of their formation energy. Seemingly in contrast with the conventional wisdom acquired over years of research that high-quality optoelectronic properties in semiconductors require a minimal amount of defects [40], solution-processed LHPs are readily synthesized via low temperature chemical synthesis and contain a high density of defects all the while presenting outstanding optical and electronic

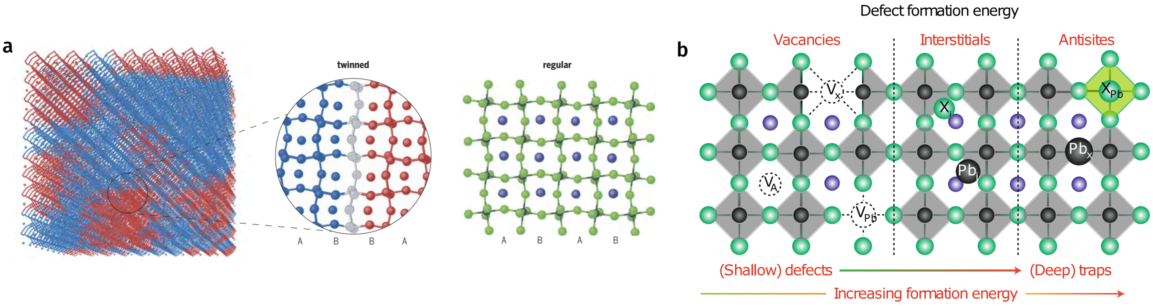

Figure 1.4 | Coexistence of crystal phases and defects. **a**, Atomistic view of a single perovskite NC showing coexistence of multiple crystalline domains separated by twin planes. The regular un-twinned structure is also shown. **b**, Schematic of the point defects hosted by the perovskite lattice shown for increasing defect formation energy. Panels are reproduced from: **a** [31]; **b** [39].

properties. As such, they have been identified as defect-tolerant very soon after first reports [41, 42], which manifests itself in three main ways. First, their crystal structure leads to low formation energy for vacancies while the presence of other point defects is minimal [42, 43]. Secondly, the peculiar electronic structure in these materials leads to the formation of defect states within or close to bands rather than midgap states as in zinc-blende and wurtzite semiconductors [44, 45] such that defects do not alter bandgap states. In NCs, surface defects are present but can be effectively passivated as discussed in SEC. 2.1.1. While this tolerance was explicitly mentioned in the literature as soon as 2017 [42], recent reports are reconsidering the electronic tolerance issue as defects in perovskites are being studied with increasing detail [46–48]. Finally, as discussed later, the soft and dynamic perovskite lattice is such that the material is referred to as a crystalline liquid, highlighting the coexistence of crystalline and liquid-like properties [49], a favorable ground for the formation of polarons that shield carriers from defects.

1.1.3 Lattice vibrations

Lead halide perovskites are heavy compounds compared to technologically-relevant established materials and thus host a low energy phonon landscape. Lattice vibrations are characterised by frequencies $\omega \propto (M)^{-1/2}$ where M is the reduced mass of the involved ions. Furthermore, a wide diversity of modes is hosted in the lattice of ternary perovskites especially when the symmetry of the lattice is lowered to tetragonal and orthorhombic and the unit cell expands (FIG. 1.3a) with up to 30 and 60 expected phonon modes respectively.

In addition to the rich phonon landscape hosted by the perovskite lattice, LHPs are relatively soft ionic compounds which together with their highly dynamic structure leads to large anharmonic motions of the perovskite lattice [50]. This softness is manifested by small bulk Young moduli, almost an order of magnitude smaller than for GaAs [51], and nearly liquid-like properties [49, 52]. Perovskites' outstanding optoelectronic properties seem closely related to their peculiar dynamic structure and rich phonon physics. In the following, we present the fundamental properties of phonons in LHPs and the unusual anharmonic effects.

Lattice vibrations can be classified as either acoustic or optical and both types exist as longitudinal and transverse modes with a wavevector parallel, resp. perpendicular, to the displacements (latter shown in FIG. 1.5a). While, depending on their polarisation, optical phonons can interact with light via the electric dipole approximation and are therefore referred to as infrared active, acoustic phonons cannot (FIG. 1.5b). As we will see however, both can interact with electronic excitations. The full phonon band structure of cubic $CsPbBr_3$ is shown in FIG. 1.5c. The harmonic phonon spectrum of LHPs exhibits negative frequency branches as the cubic phase is not stable at low temperature [53]. Taking into account anharmonicity stabilises the negative branches and gives a typical band dispersion for cubic $CsPbBr_3$ with the expected 15 modes: 3 acoustic and 12 optical modes.

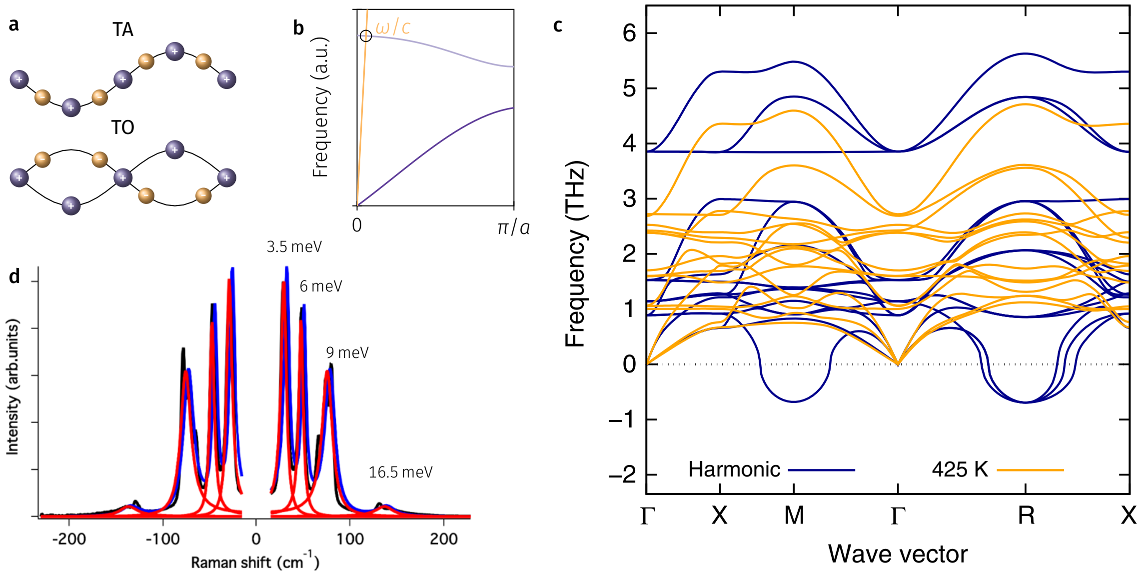

Figure 1.5 | Phonons in $CsPbBr_3$. **a**, Cartoon of transverse acoustic and optical phonon modes. **b**, Idealised phonon dispersion of a diatomic lattice showing the dispersions of acoustic phonons, optical phonons and light. **c**, Phonon dispersion of cubic $CsPbBr_3$ assuming harmonic potentials (— 0 K) and high temperature (— 425 K). **d**, Raman spectrum of a $CsPbBr_3$ crystal at 80 K. Panels **c** and **d** are reprinted from: **c** [29], **d** [50].

Acoustic phonons

At small wavevector, the acoustic branch is linear and its dispersion is given by $\omega \sim v_s k$, where v_s is the velocity of sound in the material along the relevant crystal direction. Because of their linear dispersion, they do not interact with light (FIG. 1.5b). Probing acoustic phonons therefore require neutron scattering studies. In a 3D NC, for wavelengths much larger than the lattice, acoustic phonon modes can be determined using the Christoffel equation and the material can be described by its elastic constants [54]. These constants can be calculated [55] or measured directly [56, 57] and are related to the velocity of sound in the material. For cubic $\mathrm{CsPbBr_3}$, we can calculate the velocity of sound along a symmetry axis for both transverse and longitudinal modes using $C_{11} = 42\,\mathrm{GPa}$ and $C_{44} = 4.2\,\mathrm{GPa}$ [55] and a material density of $\varrho = 4.5\,\mathrm{g\,cm^{-3}}$ as

$$v_l = \sqrt{C_{11}/\varrho} = 3060\,\mathrm{m\,s^{-1}} \quad \text{and} \quad v_t = \sqrt{C_{44}/\varrho} = 970\,\mathrm{m\,s^{-1}}$$

There further exists a maximum wavelength of acoustic waves that can be hosted in a NC due to its finite size. This leads to the discretisation of acoustic phonon modes with a energy unit given by $\hbar q_{\mathrm{min}}$. The corresponding smallest wavevector possible q_{min}, taken along a symmetry axis, is given by $q_{\mathrm{min}} = \pi/L$ such that, for typical lengths $L \sim 10\,\mathrm{nm}$ we have

$$\begin{aligned} \hbar\omega_{\mathrm{LA}} &= \hbar q_{\mathrm{min}} v_l = \frac{\hbar\pi}{L}\sqrt{C_{11}/\varrho} \sim 630\,\mathrm{\mu eV} \\ \hbar\omega_{\mathrm{TA}} &= \hbar q_{\mathrm{min}} v_t = \frac{\hbar\pi}{L}\sqrt{C_{44}/\varrho} \sim 200\,\mathrm{\mu eV} \end{aligned}$$

So in NCs with edge length L we expect a lack of available acoustic phonon modes at small $\boldsymbol{k}$ below the calculated energies due to the finite size of the crystal. However, due to the dispersion of acoustic modes, there still exists a large number of acoustic phonon modes with higher energies. More generally, in LHP, acoustic phonons are found to exhibit low energies and short lifetimes as evidenced by their linewidth broadening across the entire LHP family [56, 58, 59].

Optical phonons

Optical phonons on the other hand usually show up at higher energy than acoustic phonons and can be probed with light via Raman measurements. Low-temperature Raman measurements on single $\mathrm{CsPbBr_3}$ crystals reveal four sets of distinct peaks located at ~ 3.5, 6, 9 and 16.5 meV (FIG. 1.5d) [50, 60]. In fact, the entire optical phonon landscape of the inorganic cage in LHPs is comprised of modes confined to low energies below 20 meV [50, 61]. These modes can directly be related to motions of the Pb-Br sublattice, with modes below 12 meV related to Pb-Br bending modes while higher energy modes are related to Pb-Br stretching [52]. For hybrid LHPs, rotational modes related to the organic cation are also found at much higher energies [62]. As temperature is increased, in both hybrid and all-inorganic LHPs, a central broadened peak appears in Raman measurements at low energy, characteristic of local polar fluctuations in the presence of dynamic disorder [50, 63]. Despite the rich spectrum of phonons in LHPs, the scattering due to optical phonons is found to be dominated by the mode at 16 meV [60, 64], related to Pb-Br stretching [52]. This is much lower than the main optical mode in wurtzite and zinc-blende semiconductors, where we have $E_{LO} = 26, 36$ and 37 meV respectively for CdSe [65], GaAs [66] and CdS [65].

In NCs, surface modes are further expected to play a role. Such modes were evidenced in the outer layers of the NCs with an energy from 12 meV to 19 meV [67]. Recently (under review), the importance of surface modes was reappraised with a study that shows the overwhelming contribution of surface phonon modes to the linewidth of LHP NCs [68]. The contribution to the emission linewidth in small NCs was revealed to be due to low-energy modes from 2 to 7 meV.

Anharmonicity

In essence, normal modes of the crystal lattice are represented as a collection of independent harmonic oscillators. Within the harmonic approximation, phonons in solids are understood as quantised particles or waves displaying discrete and well-defined energies such that they live forever and propagate freely through the infinite crystal. However, interesting properties of LHPs arise from anharmonicity and cannot be described within this approximation. Even basic

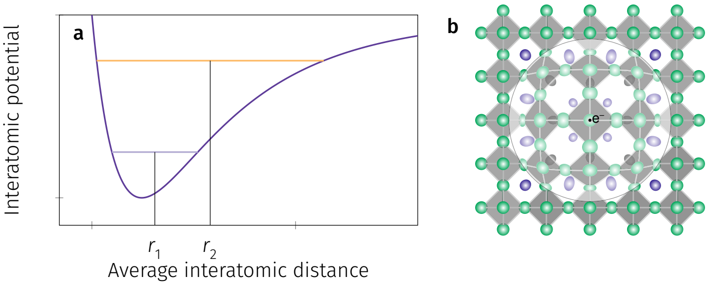

Figure 1.6 | Anharmonicity and polaron. **a**, Because of the anharmonicity of interatomic potential, an increase in temperature leads to an increase of the average interatomic distances. **b**, Cartoon of local structural distortions of the perovskite lattice which together with a charge carrier form a polaron. Panel **b** is reprinted from [39].

mechanical properties of solids such as their thermal expansion cannot be explain within the harmonic approximation. FIG. 1.6 shows an idealised interatomic potential displaying its anharmonicity. In contrast to the harmonic potential, as temperature is increased, the amplitude of atomic oscillations increases and the average position shifts towards larger values. Thus the thermal expansion of solids arises solely because of the anharmonicity of lattice potentials, essential to describe the mechanical properties of solids as evidenced in the early 1900s [69, 70]. Deviations from the perfect harmonic oscillator, induced by anharmonicity or lattice defects, introduce phonon-phonon interactions and can be described in terms of the phonon self-energy $\Sigma(\omega)$. The self-energy $\Sigma(\omega)$ is a complex function, defined as $\Sigma(\omega) = \Sigma_r(\omega) + i\Sigma_i(\omega)$, that describes the renormalisation of the phonons energy and endows them with a finite lifetime [71]. Assuming a frequency-independent $\Sigma(\omega)$, the imaginary part of the self-energy directly describes the full-width at half-maximum of the phonon mode spectrum $I(\omega, \boldsymbol{q})$. In this context, phonons decay within a characteristic time-window given by the time-energy uncertainty relation $\tau = \hbar/2\Gamma$ and a shortening of the lifetime is related to a broadening of the phonon spectrum as observed in LHPs [63]. So while anharmonic effects are critical for a realistic description of the carrier-phonon complex and in particular for non-radiative relaxation, a proper description taking into account *polaron* states, as was provided for epitaxial QDs [72–74], remains out of reach at the current stage of research in LHPs.

Polarons

Nonetheless, when considering the interaction of electrons with polar lattice vibrations, the concept of polaron naturally emerges. Put simply, an electron traveling in a polar lattice produces a local displacement of neighbouring lattice ions which travels with the electron in the lattice (FIG. 1.6b). This charge/local displacement complex is called a polaron. With a similar reasoning as for infrared active phonons, we can show that it is again longitudinal optical phonons that participate in this polaron effect. Several works have suggested the presence of Fröhlich polarons in LHPs [52, 75, 76], however the exact interplay of all the peculiar properties of the perovskite lattice is still not fully understood. Let us note that the case of polarons in LHPs is particularly interesting to consider for its seeming intrinsic contradiction. The polaron is formed by a charge carrier and a phonon. In LHPs, in the presence of anharmonicity, the picture of a phonon breaks down. The coexistence of these two aspects should lead to interesting physical phenomena.

Summary

LHPs are heavy and soft ionic compounds that exhibit a variety of crystal structures. At high temperature, they usually exhibit a cubic crystal structure. However, as temperature is lowered, the lead halide octahedra tilt first along one axis lowering the symmetry to tetragonal and then along the other axis further lowering the symmetry to orthorhombic. In fact, the structure is highly dynamic such that, even at low temperature, the crystal structure can show coexistence of several local crystalline phases corresponding to different tilts of octahedra. Lattice vibrations in LHPs in these lower-symmetry structures are therefore very rich and further exhibit striking anharmonic effects. This is manifested in the low-energy short-lifetime acoustic phonons and the apparition of a broad Raman peak centered at zero energy. Acoustic phonon energies are smaller than 5 meV across the entire Brillouin zone and the optical phonon landscape is comprised of a set of modes below $\sim$ 16 meV, with a dominant mode at 16 meV and related to Pb-Br stretching.

1.2 Optoelectronic properties of semiconductor nanocrystals

Semiconductor NCs properties are constrained by the underlying symmetry of the lattice. This in turn dictates the allowed energy levels for electrons in energy bands and therefore the optoelectronic response of NCs. In this section, we apply basic semiconductor physical principles to LHPs in general and NCs in particular. The optical properties of LHP NCs are explained in terms of allowed energy levels and optical transitions and the band-edge exciton states and wavefunctions are discussed in detail.

1.2.1 Electrons in solids

The current physical picture for electrons in a lattice is as follows. Electrons exhibit discrete energy atomic orbitals in atoms. When atoms are put close together, their atomic orbitals hybridise and in a lattice they form sets of closely-spaced energy levels referred to as bands. Electrons in the lattice are treated as free electrons in a periodic potential. They do not scatter on ions, as originally thought, but rather on the lattice impurities.

Single electron hamiltonian

Further considering that electrons move much faster than the nuclei given their respective masses (adiabatic or Born-Oppenheimer approximation [77]) and that the potential felt by a single electron can be expressed as a mean field $V(\boldsymbol{r})$ generated by all other nuclei and electrons (mean field or Hartree-Fock) we can write the hamiltonian and corresponding wavefunction for a single electron in a crystal as

$$\hat{\mathcal{H}}_0 = \frac{\boldsymbol{p}^2}{2m} + V(\boldsymbol{r}) \quad \text{with} \quad \Psi_{n,\boldsymbol{k}}(\boldsymbol{r}) = \Omega^{-1/2} e^{i\boldsymbol{k}\cdot\boldsymbol{r}} u_{n,\boldsymbol{k}}(\boldsymbol{r}) \tag{1.1}$$

where the wavefunctions, normalised over the crystal volume Ω, can be written using Bloch's theorem [78] for band n as plane waves $e^{i\boldsymbol{k}\cdot\boldsymbol{r}}$ modulated by a periodic function $u_{n,\boldsymbol{k}}(\boldsymbol{r})$ with the same periodicity as the crystal lattice. $\boldsymbol{k}$ is the wavevector inside the Brillouin zone, also referred to as crystal momentum, and $E_n(\boldsymbol{k})$, the electron energy dispersion, is known as the band structure.

Spin-orbit coupling

The electrons can also exhibit spin-orbit interaction, i.e. coupling of the electron spin to its orbital angular momentum. This coupling is a purely relativistic effect ($1/c^2$ term) which is expected to be more pronounced for heavier elements[1] [79]. LHPs are thus expected to exhibit a large spin-orbit coupling. Indeed, in the electron frame the electron spin $\boldsymbol{\sigma}$ interacts with an effective magnetic field induced by the varying lattice potential ∇V. This interaction is spin-orbit coupling and the hamiltonian of an electron needs to be modified to include a spin-orbit term [80]

$$\mathcal{H}_{\mathrm{SO}} = \frac{\hbar}{4m_0^2c^2}\boldsymbol{\sigma} \times \nabla V \cdot \boldsymbol{p} \tag{1.2}$$

where $\boldsymbol{\sigma}$ are the Pauli spin matrices. The spin-orbit hamiltonian is kept in its most general form where no assumption relating to a spherical geometry is made [81].

---

[1] In increasing order Ga, As, Se, Br, Cd, Pb

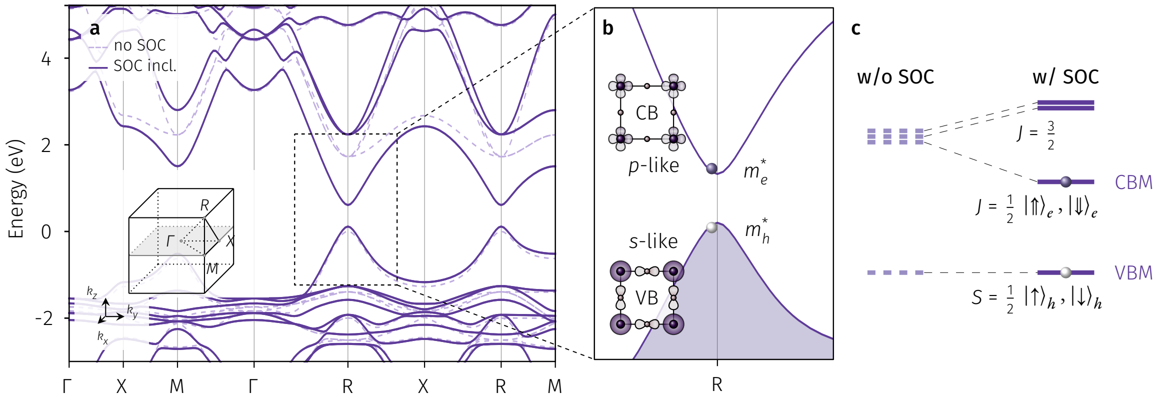

Figure 1.7 | Band structure of cubic CsPbBr$_3$. **a**, Computed band structure of cubic CsPbBr$_3$. Reciprocal space 3D view of the first Brillouin zone of the cubic lattice. **b**, Zoom-in view on the band edge when taking into account spin-orbit coupling. **c**, Schematic of the degeneracy lifting due to spin-orbit coupling.

1.2.2 Electrons in metal halide perovskites

To describe the band structure of LHPs, we will consider the prototypical cubic perovskite as a model and discuss the effect of the non-cubic perovskite lattice structure as distortions to the cubic unit cell. Indeed, lattice constants of lower symmetry structures are very close to that of the cubic lattice such that band structure modifications due to lattice distortions can be fully characterised by small atomic displacements and strain applied on the cubic lattice [82]. In this setting, we can treat the problem in a cubic lattice and later include the differences via strains induced on the lattice along the relevant cubic crystallographic axis.

Band structure of MHPs

Cesium LHPs are direct band-gap semiconductors with a band-edge located at the R point of the cubic Brillouin zone[83]. For cubic semiconductors, the R-point is isomorphic to the Γ-point [84, 85]. As the unit cell expands when lowering the crystal phase symmetry, the Brillouin zone shrinks, and the R point of the cubic Brillouin zone is folded back onto the Γ point of the orthorhombic Brillouin zone [86]. Fig. 1.7a shows the calculated band structure of cubic CsPbBr$_3$ with spin-orbit interaction switched on (—) and off (--). [2] Spin-orbit coupling lifts the degeneracy of the band-edge conduction band such that the band edge is formed by two non-degenerate (ignoring spin) levels.

---

[2] The band structures of LHPs in general, especially near the band edge, are similar for all compositions despite some peculiarities for hybrid LHPs due to cation rotation.

Band-edge spin-1/2 states

The band-edge is thus formed by a conduction band from Pb $6p$ orbitals with total angular momentum $j = 1/2$ and valence band with overall s-like symmetry with spin $s = 1/2$, mixture of Pb $6s$ and Br $4p$ atomic orbitals as depicted in FIG. 1.7b [87]. The valence wavefunctions can thus be defined as $|\uparrow\rangle_h = |\mathrm{S}\rangle \otimes |\uparrow\rangle$ and $|\downarrow\rangle_h = |\mathrm{S}\rangle \otimes |\downarrow\rangle$. For the electron, due to the strong spin-orbit coupling, the three spatial components for the electron wavefunction $|\mathrm{X}\rangle$, $|\mathrm{Y}\rangle$ and $|\mathrm{Z}\rangle$ are mixed with spin such that $|\uparrow\rangle_e, |\downarrow\rangle_e \rightarrow |\Uparrow\rangle_e, |\Downarrow\rangle_e$. In the case of cubic crystal, the electron eigenfunctions read [85, 88]:

$$|\Uparrow\rangle_e = \frac{-1}{\sqrt{3}}\Big[\big(\,|\mathrm{X}\rangle + i\,|\mathrm{Y}\rangle\,\big) \otimes |\downarrow\rangle_e + |\mathrm{Z}\rangle \otimes |\uparrow\rangle_e\Big] \tag{1.3a}$$

$$|\Downarrow\rangle_e = \frac{1}{\sqrt{3}}\Big[\,|\mathrm{Z}\rangle \otimes |\downarrow\rangle_e - \big(\,|\mathrm{X}\rangle - i\,|\mathrm{Y}\rangle\,\big) \otimes |\uparrow\rangle_e\Big] \tag{1.3b}$$

where from here onwards we omit the Hilbert spaces product signs $\otimes$. Reducing the lattice symmetry from cubic to tetragonal or orthorhombic leads to additional crystal field terms in the hamiltonian, such that the conduction band states expressions need to be adapted [88, 89]. In contrast with established zinc-blende and wurtzite semiconductors [84], spin-orbit coupling happens in the conduction band rather than in the valence band and splits the three-fold degenerate conduction band minimum such that the band-gap occurs between two non-degenerate bands [90]. When considering band edge excitations, there are no heavy-light electrons to take into account.

Global descriptions of the band structure of bulk materials can readily be obtained via pseudo-potentials (as shown in FIG. 1.7 with density functional theory) or tight-binding and yield very accurate results. However, they do not provide expressions for the effective masses and wavefunctions which we are mainly interested in here. In particular, and nearly exclusively, the optical properties probed in this work can be fully characterised by the energy dispersion and wavefunctions near the band edge at R. Indeed, light-matter interaction requires both conservation of energy and momentum. As light has a negligible momentum, optical transitions happen nearly vertically in the diagrams shown in FIG. 1.7b and FIG. 1.8a-b. Thus in the following, we provide the local description of the band structure: the $\boldsymbol{k} \cdot \boldsymbol{p}$ method.

Effective mass

We can develop the Schrödinger equation with the hamiltonians and Bloch functions in (1.1) and (1.2) to get the Schrödinger equation for the periodic part $u_{n,\boldsymbol{k}}(\boldsymbol{r})$

$$\left\{\frac{\boldsymbol{p}^2}{2m_0} + V(\boldsymbol{r}) + \frac{\hbar}{4m_0^2c^2}\boldsymbol{\sigma} \times \nabla V \cdot \boldsymbol{p} + \frac{\hbar \boldsymbol{k}^2}{2m_0} + \frac{\hbar \boldsymbol{k}}{m_0}\left[\boldsymbol{p} + \frac{\hbar}{4m_0c^2}\boldsymbol{\sigma} \times \nabla V\right]\right\} u_{n\boldsymbol{k}} = E_{n\boldsymbol{k}}\, u_{n\boldsymbol{k}}(\boldsymbol{r}) \tag{1.4}$$

in which we can identify a k-dependent part and a k-independent part and the modified expression of the electron momentum $\boldsymbol{\pi}$ which in the presence of spin-orbit coupling reads

$$\boldsymbol{\pi} = \boldsymbol{p} - \frac{e\hbar}{4m_0c^2}\boldsymbol{\sigma} \times \boldsymbol{E} \tag{1.5}$$

For clarity, we will set $\boldsymbol{k}_R = \boldsymbol{0}$, and following standard procedures [91, 92], we can express the wavefunctions $u_{n\boldsymbol{k}}$ and energies $E_{n\boldsymbol{k}}$ at $\boldsymbol{k} \sim \boldsymbol{k}_R$ as first order perturbations to the unperturbed u_{n0} with energies E_0. Up to second order in k, we can obtain the dispersion relations of the non-degenerate parabolic bands near R as

$$E_{n\boldsymbol{k}} = E_{n0} + \frac{\hbar \boldsymbol{k}^2}{2m^*} = E_{n0} + \frac{\hbar \boldsymbol{k}^2}{2}\left(\frac{1}{m_0} + \frac{2}{m_0^2\boldsymbol{k}^2}\sum_{n' \neq n}\frac{|\langle u_{n0}|\boldsymbol{k}\cdot\boldsymbol{\pi}|u_{n'0}\rangle|^2}{E_{n0} - E_{n'0}}\right) \tag{1.6}$$

where we recognize the standard $\boldsymbol{k} \cdot \boldsymbol{p}$ dispersion endowing the charge carriers with effective masses m^*, defined in (1.6), that describes the curvature of the band around the extrema. The corresponding perturbed wavefunctions $u_{n\boldsymbol{k}}$ are given by

$$u_{n\boldsymbol{k}} = u_{n0} + \frac{\hbar}{m}\sum_{n' \neq n}\frac{|\langle u_{n0}|\boldsymbol{k}\cdot\boldsymbol{\pi}|u_{n'0}\rangle|^2}{E_{n0} - E_{n'0}}u_{n'0} \tag{1.7}$$

The obtained wavefunctions within the effective mass approximation and $\boldsymbol{k} \cdot \boldsymbol{\pi}$ model describe the effect of nearby bands on the local electron dispersion and the effect of remote bands, such as the spin-orbit split bands, which can further be included [85, SI]. Calculations of effective masses in LHPs predict similar small masses for the electron and hole $m^*_{e,h} \sim 0.15\, m_e$. Reported carrier mobilities on the other hand, with $\mu_{e,h} \propto (m^*_{e,h})^{-1}$, are found to be orders of magnitude lower than established semiconductors [93]. While photoemission band mapping experiments directly probed the curvature of the valence band and revealed an effective mass $m_{\text{exp}} = 0.26\, m_e$ larger than theoretical predictions, this discrepancy remains unexplained despite increasing attention [94, 95].

Interaction hamiltonian

Considering that electronic states are quantised in the nanostructures we study, with thermal de Broglie wavelengths $\lambda_B \sim 180$ nm at 5 K vs. 20 nm at 300 K, we can consider transitions between discrete states. We can write the transition rate between electronic states $|i\rangle$ with energy E_i and $|f\rangle$ with energy E_f using Fermi's golden rule as [96, 97]

$$\Gamma_{i\to f} = \frac{2\pi}{\hbar} \left|\langle f|H_{\text{int}}|i\rangle\right|^2 \delta\left(E_f - E_i - \hbar\omega\right) \tag{1.8}$$

Transition rates therefore depend on the interaction hamiltonian matrix elements

$$\left\langle \Psi_f \middle| H_{\text{int}} \middle| \Psi_i \right\rangle = \int \Psi_f^* H_{\text{int}} \Psi_i \, d\tau \tag{1.9}$$

The light matter interaction term between a nanoemitter and an external electromagnetic field is given by the interaction Hamiltonian $-\frac{e}{m_0 c}\boldsymbol{p} \cdot \boldsymbol{A}$ where the vector potential $\boldsymbol{A} \propto \left(e^{i(\boldsymbol{k}\cdot\boldsymbol{r}-\omega t)}\boldsymbol{e} + h.c.\right)$ with E_0 the amplitude of the electric field, ω its frequency, $\boldsymbol{q}$ its wavevector and $\boldsymbol{e}$ its polarisation vector. Considering the dimensionality of the nanostructures studied with respect to the electromagnetic field wavelength ($L \ll \lambda$), we can neglect the spatial dependence of the vector potential. This is the so-called dipole approximation in which the interaction hamiltonian can be rewritten as $\mathcal{H}_{\text{int}} \propto \boldsymbol{e} \cdot \boldsymbol{p}$ and the transition rate is given by

$$\Gamma \propto \frac{2\pi}{\hbar} \left|\langle f|\boldsymbol{e}\cdot\boldsymbol{p}|i\rangle\right|^2 \delta\left(E_f - E_i - \hbar\omega\right) \tag{1.10}$$

Transition rates are thus directly given by the momentum operator taken between the initial and final states. From these matrix elements arise the so-called selection rules defining which transitions are allowed and which are not. Looking at (1.10), there are several points of interest. The Dirac delta ensures energy conservation during the transition. The matrix elements, which are equally written as $\int \psi_f^* \boldsymbol{e} \cdot \boldsymbol{p} \psi_i d\tau$, are non-zero only if the integral is non-zero. Considering that the momentum operator is odd, this means that electric dipole transitions between states i and f are allowed only if i and f are of opposite parity. Further considering the symmetry of the involved states in terms of group theory, these matrix elements are non-zero only if the representation Γ_f of the final state is contained within the product of the representations of the interacting hamiltonian and the initial state $\Gamma_H \otimes \Gamma_i$, i.e. if the transition is symmetry-allowed.

Summary

Electrons in LHPs experience a strong spin-orbit coupling in addition to the Bloch potential. The band-edge excitations in LHPs are a hole with *s*-like character and a *p*-like electron from the spin-orbit split-off band, forming a direct gap between two non-degenerate (excluding spin) bands in contrast with established wurtzite and zincblende compounds. These band-edge states are discrete owing to the finite size of our objects, well below the de Broglie wavelength, such that optical transitions are also discrete. We now consider further effects of this finite size on the band-edge electron and hole.

1.2.3 Excitons in metal halide perovskites

Besides the confinement of carriers at lengths smaller than the de Broglie wavelength, which leads to discretisation of electronic states, the proximity of the electron and hole in NCs needs to be considered. So, within the complex band structure of semiconductors, upon excitation of a single electron to the conduction band, we recover a situation reminiscent of the hydrogen atom: two particles of opposite charge in interaction, which we can treat using usual tools. This gives rise to a quasi-particle: the exciton, an electron-hole pair bound by Coulomb interaction as depicted in FIG. 1.8C. In addition to the charge of the electronic excitations, their spin must also be considered which leads to an additional electron-hole exchange interaction. Starting from the bulk exciton wavefunctions, we develop the band-edge exciton states in LHPs and discuss the band-edge exciton fine structure ordering in light of the recent debate in the field.

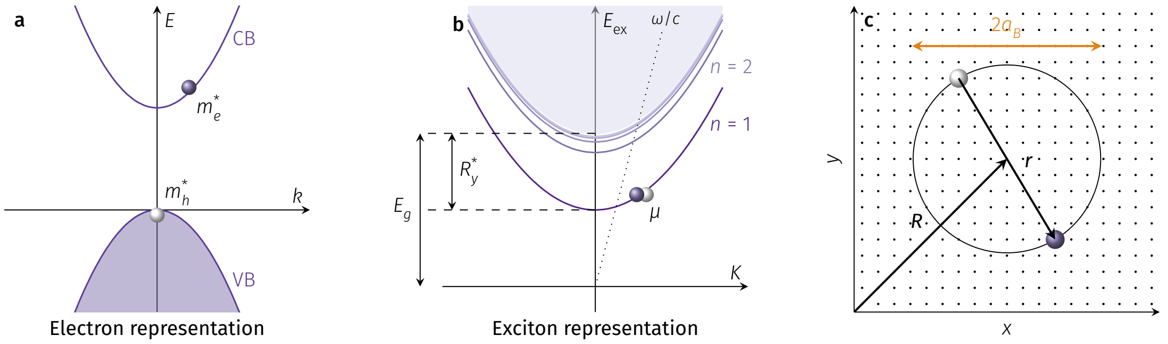

Figure 1.8 | Electron, hole and exciton. **a**, Electron-hole pair shown in the electron picture. **b**, Same electron-hole pair under Coulomb interaction in the exciton picture. The two types of solutions for the electron-hole pair hamiltonian are represented. **c**, Schematic picture of an electron-hole pair with an expected separation $2a_B$.

Band-edge exciton states

The theoretical description of the band edge excitons in zinc-blende and wurtzite NCs was given by A. Efros's group starting in the late 1980s [98–101]. Because of the unusual band-edge of LHPs, with spin-orbit coupling in the conduction band and a band-edge formed by the split-off band and the valence band, this description needed to be adapted for LHPs. The exciton states in LHPs were considered by J. Even and collaborators [82, 86, 87, 90, 102] as soon as in 2012 with further theoretical inputs by A. Efros et al [85, 103–105] and Chamarro et al [89, 106, 107] for the band-edge exciton states in NCs. These works are briefly summarised here with a focus on the debate about the exciton fine structure ordering.

The effective mass Hamiltonian describing band-edge carriers is a 4 × 4 matrix related to the upper valence band and the lowest conduction band that can be extracted from the full 8 × 8 Luttinger-Kohn matrix taking into account all 4 bands. Using standard rules for composition of angular momenta [108], the electron and hole wavefunctions in (1.3) are combined to give a four-fold degenerate exciton comprised of a *singlet* ($J = 0$) and a *triplet* ($J = 1$) state.[3] The four exciton wavefunctions Ψ_{JJ_z} can thus be written as [85]:

$$\left|\Psi_{0,0}\right\rangle = \frac{1}{\sqrt{2}}\Big[\,|\Downarrow\rangle_e\,|\uparrow\rangle_h - |\Uparrow\rangle_e\,|\downarrow\rangle_h\,\Big] \qquad \begin{aligned} \left|\Psi_{1,\ 0}\right\rangle &= \frac{1}{\sqrt{2}}\Big[\,|\Downarrow\rangle_e\,|\uparrow\rangle_h + |\Uparrow\rangle_e\,|\downarrow\rangle_h\,\Big] \\ \left|\Psi_{1,-1}\right\rangle &= |\Downarrow\rangle_e\,|\downarrow\rangle_h \\ \left|\Psi_{1,+1}\right\rangle &= |\Uparrow\rangle_e\,|\uparrow\rangle_h \end{aligned} \tag{1.11}$$

where indices i, j in $\Psi_{i,j}$ refer respectively to the total angular momentum J and its projection along the z axis J_z.

The probability of light emission resulting from the recombination of an electron-hole pair is given by Fermi's golden rule and ultimately by the projection between the exciton state and the ground state $|0\rangle$ as $\langle 0|\boldsymbol{p}|\Psi\rangle$. Calculations yield the significant result that radiative recombination of the $J = 0$ state is forbidden while that of the $J = 1$ states is allowed [85], and the states are therefore referred to as dark singlet and bright triplet. Depending on the crystal structure considered, these exciton sublevels are expected to exhibit different symmetries and polarisations [85, SI]. Group theory further supports this result as the band-edge electron and

---

[3] Note here that singlet/triplet refers not to a spin singlet/triplet but rather total angular momentum singlet/triplet.

hole states transform respectively as R_6^- and R_6^+, which under Coulomb and exchange interaction give a dark singlet R_1^- and bright triplet R_4^- states [85, 102]. This is coherent with the reported brightness of these emitters, with three quarters of bright states, but is in stark contrast with the band-edge exciton states in zinc-blende and wurtzite semiconductors which do not usually host a majority of dipole-allowed states [101]. In contrast, in LHPs three quarters of the exciton manifold is bright such that in these weakly confined NCs ($L \geq 2a_B$) the concentration of the optical transition oscillator strength in the low lying exciton states should give rise to a giant oscillator strength effect at low temperature [85, 109] as reported for CuCl microcrystals [110].

Electron-hole interaction

Electron-hole interactions in semiconductor NCs consist in a Coulomb charge interaction part, leading to binding energies, as well as the exchange term leading to splitting of the bright and dark excitons. Within the effective mass approximation, the electron and hole wavefunctions in NCs are written as products of the lattice Bloch functions and envelope functions describing the finite nature of the NC. The exciton wavefunctions can therefore be written as

$$\Psi_{J,J_z}^{\mathrm{NC}} = \Psi(\boldsymbol{r}_e, \boldsymbol{r}_h)\, \Psi_{J,Jz} = \Psi(\boldsymbol{R})\, \Phi(\boldsymbol{r})\, \Psi_{J,J_z} \tag{1.12}$$

where the second equality holds assuming we can separate the electron and hole motions with the relative position $\boldsymbol{r} = \boldsymbol{r}_h + \boldsymbol{r}_e$ and the center of mass position $\boldsymbol{R} = \left(m_h \boldsymbol{r}_h + m_e \boldsymbol{r}_e\right)/M$ (Fig. 1.8c). Doing so yields two sets of solutions for the two-particle Coulomb hamiltonian:

- $\Phi(\boldsymbol{r})$ describing the relative motion and Coulomb interaction between the pair constituents;
- $\Psi(\boldsymbol{R})$ describing the center of mass motion and the potential confinement effects.

Coulomb interaction The relative motion wavefunction $\Phi(\boldsymbol{r})$ can be expressed as a function of three quantum numbers n, l and m in spherical coordinates as

$$\Phi_{nlm}(\boldsymbol{r}) = R_{nl}(r)\, Y_{lm}(\theta, \phi) \tag{1.13}$$

where the radial part is expressed in terms of Laguerre polynomials and the angular part are the spherical harmonic functions. Assuming isotropic effective masses, we can write the energy of the set of states obtained for a 3D exciton as $E_n = -R_y^*/n^2$ where R_y^* is the Rydberg constant for the exciton given by $R_y^* = \frac{\mu}{m_0 \epsilon_r^{*2}} \frac{e^2}{2a_B}$ and a_B is the exciton Bohr radius. The energy of the electron-hole pair is therefore lowered, for the ground exciton state, by R_y^* (FIG. 1.8b).

Confinement regime For the center of mass motion, two confinement regimes can be defined, depending on the relative size of the bulk exciton Bohr radius and NC. If the exciton is much smaller than the NC, it is not confined and the envelope function approaches the Bloch functions defined above. If the NC is much smaller than the bulk exciton Bohr radius, the exciton is confined and the envelope function approaches the particle-in-a-box functions. These functions can easily be obtained as particle-in-a-box states by setting appropriate boundary conditions. For a parallelepiped with edge lengths L_x, L_y and L_z, the exciton center of mass motion is quantised and can be expressed as

$$\Psi(\boldsymbol{R}) = \sqrt{\frac{8}{L_x L_y L_z}} \cos\left(\frac{n_x \pi}{L_x} X\right) \cos\left(\frac{n_y \pi}{L_y} Y\right) \cos\left(\frac{n_z \pi}{L_z} Z\right) \tag{1.14}$$

where X, Y, Z are the coordinates of the exciton center of mass and n_x, n_y and n_z are the quantisation indices along each direction. So for each exciton state, there is a k dispersion with discrete levels.

All in all, the electron-hole pair is reduced by E_b due to Coulomb interaction and increased by E_{conf} due to confinement in the NC. Taking into account the discussed interaction terms, we can write the size-dependence of the band-edge exciton energy in $CsPbBr_3$ as a sum of a bulk value, a confinement term and a Coulomb term using an approximate expression in the intermediate confinement regime as [104]

$$E(L) \sim E_g + E_b \left(\frac{3\pi^2}{(L/a_x)^2} - \sqrt{1 + \left(2 \times 3.05 \frac{a_x}{L}\right)^2} \right) \tag{1.15}$$

where E_g is the bulk band gap, E_b is the exciton binding energy, L is the edge length of the NC and a_x is the exciton radius. This dependence is shown in FIG. 1.10b and reveals that the exciton energy can be tuned over a few hundred meV up to ~ 3 eV for 4 nm nanocrystals. For larger NCs, the emission energy does not deviate much from the bulk band-edge energy while for NC sizes

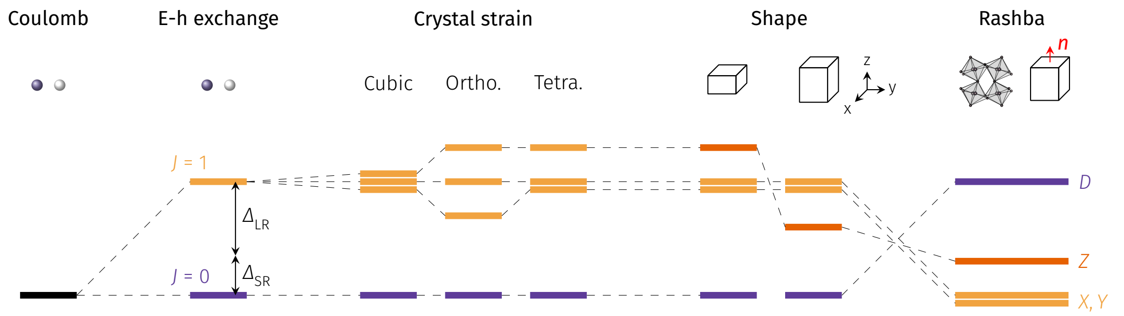

Figure 1.9 | Detailed exciton fine structure in CsPbX$_3$ nanocrystals. Contribution to the exciton fine structure as detailed in the main text.

below 2 a_B, the emission energy starts to deviate significantly from green to deep blue.

Exciton fine structure

Additional effects further dictate the exciton fine structure and the relative ordering of the exciton sublevels.

Exchange interaction

In cubic crystals, electron-hole exchange interaction (EI), related to Coulomb interaction, further splits the four-fold degenerate exciton state into an optically passive singlet ($J = 0$) below a three-fold degenerate optically active triplet state ($J = 0, J_z = \pm 1, 0$) (Fig. 1.9). This singlet-triplet energy splitting depends on the overlap between the electron and the hole, such that both crystal symmetry and shape anisotropy can further lead to degeneracy lifting [106, 111, 112]. These effects are depicted in Fig. 1.9. So either for orthorhombic NCs with cubic shape or cubic NCs with full anisotropy, EI fully splits the bright triplet into three orthogonal states but always with the dark singlet as the lowest energy state. Taking into account both short- and long-range exchange interaction, the expected energy splittings between bright triplet dark singlet in CsPbBr$_3$ are on the order of a few meV [85, 89, 105, 112] decreasing from 5 meV to 1.5 meV with increasing size from 7 nm to 17 nm [113], always showing a singlet ground state.

Rashba effect

In addition to EI, the band-edge states in LHPs have been predicted to exhibit a Rashba effect [85, 114, 115], i.e. a momentum-splitting of the electronic bands depending on spin.

There are several requirements for the Rashba effect to be operant, namely the presence of both spin-orbit coupling and inversion asymmetry. A large spin-orbit coupling exists in perovskites [87, 90] but, for inorganic LHPs, the three crystal structures reported (Pm3m, I4/mcm, Pnma) all possess an inversion centre and therefore should not exhibit a Rashba effect. Due to the highly dynamic character of the perovskite structure with its octahedral and cation instabilities, inversion symmetry could be broken, at least locally as suggested for hybrid LHPs [114, 115]. In addition, in NCs, strain on the lattice due to the finite size of the object could also lead to inversion asymmetry.

While the exact origin of the Rashba effect is still unclear, it was theoretically hypothesized that, in contrast with EI, the Rashba effect in LHPs should lead to a level re-ordering with a bright triplet ground state (FIG. 1.9), thereby tentatively explaining the exceptional optical properties of LHPs [85]. However, these calculations only took into account the short-range exchange interaction. In contrast, other studies tentatively explained the bright triplet energy splittings as a combined result of long-range EI and shape anisotropy of the NCs [89, 106, 111, 112]. Calculations of [85] were then updated to take into account both short-range and long-range exchange interaction together with the Rashba effect, and predict different size regimes for the bright-dark level orderings [104, 105] (FIG. 1.10a). Namely, while for smaller NCs EI is expected to dominate, leading to dark ground state, the Rashba effect would dominate for larger NCs, leading to a bright ground state. A critical prediction of this model is the increase of bright triplet energy splittings with the NCs size [105], whereas without taking into account the Rashba effect, bright triplet energy splittings are expected to decrease with increasing NC size (FIG. 1.10a). With that respect, seemingly contradictory experimental results were reported [106, 116] albeit in a small range of sizes and further experimental work is needed to elucidate this matter.

Other experimental results suggest the influence of the Rashba effect. Magneto-optical measurements on single $CsPbBr_3$ NCs have reported a non-linear energy shift at low magnetic fields consistent with a Rashba effect in contrast with the linear Zeeman shift at higher fields [117]. Similarly to earlier reports on zinc-blende and wurtzite NCs [118–120], single $CsPbI_3$ NCs exhibit a permanent dipole moment interpreted as the result of surface-related strains of the NCs [121]. This cannot be explained with the symmetric orthorhombic Pnma crystal structure and requires a breaking of inversion symmetry due to cation position instability for example, which is the same requirement as for the Rashba effect. The question is thus still open.

The debate today Experimental works on both hybrid [113] and all-inorganic LHPs [116] have revealed the presence of a dark ground state upon application of a magnetic field in contradiction with the predictions of [85]. However, the prediction of a bright ground state was made for $CsPbBr_3$ and not for $FAPbBr_3$ or $CsPbI_3$. Thus, in this work we investigated the case of $CsPbBr_3$ (CH. 4).

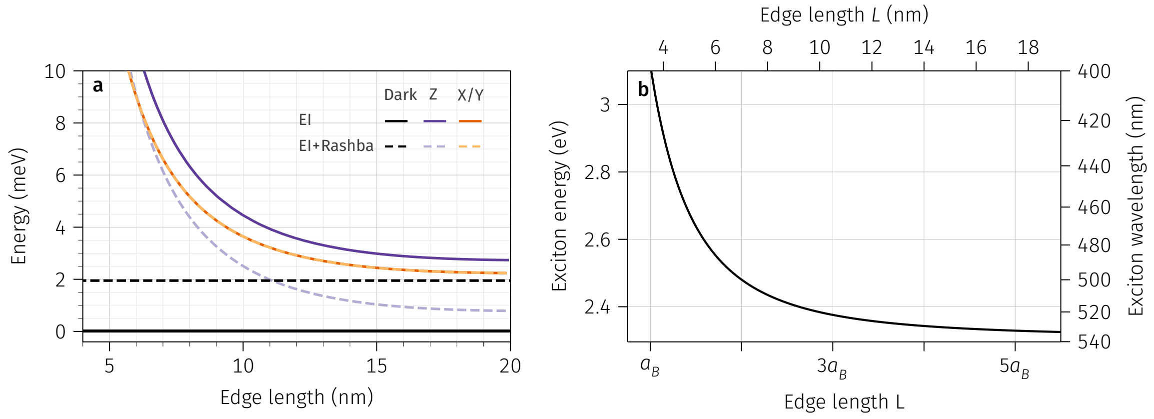

Figure 1.10 | Exciton energy and fine structure: size-dependence. **a**, Exciton sublevels energies as a function of NC size for a tetragonal $CsPbBr_3$ NC taking into account short-range and long-range exchange interaction with and without the Rashba effect. **b**, Exciton energy as a function of the edge length L of a cubic $CsPbBr_3$ NC from expression 1.15 using E_g = 2.342 eV and E_b = 33 meV at 2 K from [122]. Panel **a** is adapted from [105].

Summary

The emission energy of LHP NCs can be tuned by varying their size. The exciton fine structure is dominated by electron-hole exchange interaction, which sets the fine structure ordering depending on the crystal structure and shape of the NCs. The outstanding optical properties of LHP NCs were tentatively explained by the Rashba effect placing the bright triplet as a ground state. Experimental studies of hybrid and all-inorganic LHPs have revealed the presence of a dark ground state, thereby refuting the predictions related to the Rashba effect. Alternatively, the brightness of LHPs was understood as resulting from reduced bright-dark transitions, with vanishing first-order phonon-driven transitions. In this aspect, two questions remain today: one related to the importance of the Rashba effect, as inversion symmetry is likely broken in LHP NCs, and another related to the apparent lack of first-order bright-dark transitions.

1.3 Exciton dephasing

The figure of merit for emitters within the context of quantum optics and quantum information processing is given by the Fourier transform of their spectral profile and its relation to their temporal profile. This figure is directly related to the decoherence of the emitting quantum system and to the indistinguishibility of the emitted photons. Within this context, an emitter is deemed suitable for applications if the Fourier transform of its temporal profile, characterised by its spontaneous lifetime T_1, approaches its spectral profile, characterised by its optical coherence relaxation time T_2. The equality is referred to as the radiative limit where $T_2 = 2T_1$. Recent studies have suggested that LHPs are promising easily-processed and readily integrable emitters at low temperature. In addition to the fast radiative recombination of band-edge exciton [123], photon-correlation spectroscopy revealed optical coherence times $T_2 \sim 10 - 80\,\text{ps}$ [124, 125], i.e. $T_2/2T_1 \lesssim 0.2$ which is already on par with the coherence times obtained with the best engineered II-VI NCs studied up to date [126]. However, charge noise, via spectral diffusion, and coupling to the phonon bath are still efficient decoherence pathways for the system and thus a source for faster coherence relaxation.

1.3.1 Spontaneous relaxation

Dephasing

Let us consider an idealised two-level system with a ground state $|0\rangle$ and an excited state $|1\rangle$. In all generality, the state of the system can be parametrised by two real numbers θ and ϕ as $|\theta, \phi\rangle \equiv \cos\frac{\theta}{2}|1\rangle + \sin\frac{\theta}{2}e^{i\phi}|0\rangle$ and represented on the Bloch sphere as shown in Fig. 1.11a together with pathways for population evolution and coherence evolution. For a fully coherent system, we can show within the Lindblad formalism that interaction with the electromagnetic field triggers the spontaneous relaxation of the system at a rate $1/T_1$ (Fig. 1.11c). The associated spectral power density is given by a lorentzian line with full-width at half-maximum (FWHM) $\Gamma = \hbar/T_1$. In this

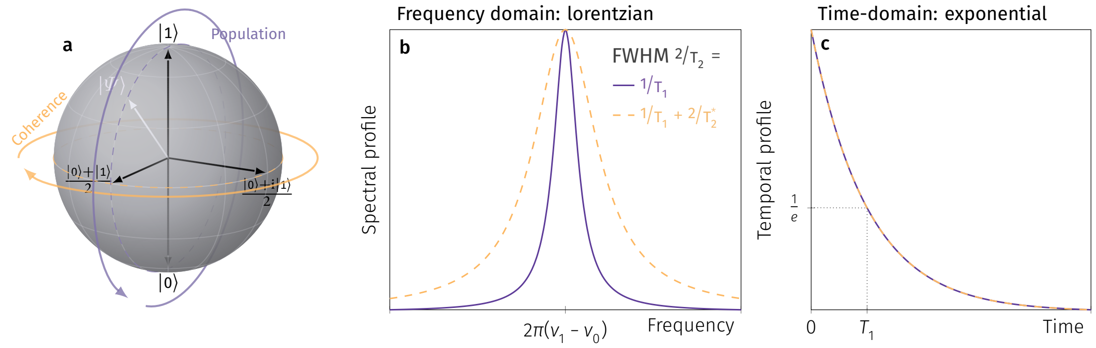

Figure 1.11 | Decoherence of a two-level system. **a**, Bloch sphere representation of a two-level system showing population relaxation along the polar angle and azimuthal dephasing. **b,c**, Frequency and time domain response of the two-level system. **b**, In the frequency domain, the linewidth is given by the sum of the radiative linewidth and additional dephasing. **c**, In the time domain, the emission shows an exponential radiative limit, the population relaxation is accompanied by a minimal amount of dephasing such that $T_2 = 2T_1$.

case (Fig. 1.11b —), the linewidth of the source is given by its lower limit $^{2\hbar}/_{T_2} = {}^{\hbar}/_{T_1}$, where T_1 is the radiative relaxation lifetime of the excited state and T_2 the coherence relaxation lifetime. This is a fundamental limit for the linewidth of a source in which case all emitted photons are indistinguishible. In the solid-state, the coherence relaxation lifetime T_2 of the system is not only limited by its spontaneous relaxation but also by the coupling to lattice vibrations and the local electrostatic environment. These additional dephasing processes (Fig. 1.11b - -) are characterised by T_2^* such that the system linewidth is given by

$$\frac{2\hbar}{T_2} = \frac{\hbar}{T_1} + \frac{2\hbar}{T_2^*} \tag{1.16}$$

and contains direct information about the pure dephasing mechanisms at play. Notably, this means that not all emitted photons have the same energy and emission lines are broadened. Both the population relaxation T_1 and dephasing T_2 are thus imprinted on the degree of coherence of the emitted photons. Let us note here that because of the finite linewidth of an emitter, even in the radiative limit, the Dirac delta in Fermi's golden rule should be replaced by a Lorentzian line with a linewidth given by $2\hbar/T_2$. Before discussing the coherence properties of the emitted radiation, let us consider additional effects due to the environment.

Local environment

In addition to setting the emitter's linewidth via T_2^*, the local electromagnetic environment of the emitter also dictates both the directionality of the source and the relaxation rate. Indeed, spontaneous emission is not a purely intrinsic property of quantum emitters but rather a result of the emitter's coupling to the electromagnetic environment. Purcell first realised that the spontaneous relaxation of a magnetic dipole could be influenced by its environment [127]. The modification of the spontaneous emission of an electric dipole in the vicinity of a planar interface was later investigated [128–132], revealing that the decay of an object can either be inhibited or accelerated depending on its actual position with respect to the field node/anti-nodes. Besides this acceleration of the radiative emission rate, the local electromagnetic environment also impacts the directionality of the emitter. Let us note that the modification of the emission rate, induced by the local electromagnetic environment via the Purcell effect, is only operand on the radiative part of the decay.

Quantum yield

Indeed, not all absorbed photons lead to emission. This loss is quantified by the quantum yield, which is effectively a measure of the conversion efficiency between the input (excitation) and the output (emission) of a quantum system. Several definitions of the quantum yield are used in the literature. The most common one is the quantum yield η of a state (QY_i) defined as the ratio of the radiative recombination rate Γ_{rad} to the overall decay rate Γ such that the overall decay rate is given by $\Gamma = \Gamma_{\mathrm{rad}} + \Gamma_{\mathrm{nr}} = \Gamma_{\mathrm{rad}}/\eta$. We can also talk about the quantum yield of a nanoparticle, $\mathrm{QY}_{\mathrm{NC}}$, which can be defined as the ratio of the number of emitted photons to the number of absorbed photons and can be measured with an integrating sphere [133]. In the case of non-resonant excitation, QY_{NC} is a probe to the recombination of the emitting state, the internal efficiency, and to the relaxation of carriers from the higher-energy excitation (relaxation efficiency). Only in the case of resonant excitation then, can the quantum yield QY_i be directly linked to QY_{NC} ratio between the number of emitted photons and the number of absorbed photons.

Quantum emission: degree of coherence

Coherence and interference are closely related and are both essential in the description of electromagnetic radiation. In particular, coherence is essential to describe the quantum aspect of light [134]. Fundamentally, coherence is a measure of the statistical similarity of a field taken at different space-time coordinates. It gives direct information about the relative phases of the field, hence the term dephasing which here refers to the loss of spatial and temporal coherence of the field. Considering a scalar electric field $E(\boldsymbol{r},t) = E^{(+)}(\boldsymbol{r},t) + E^{(-)}(\boldsymbol{r},t)$ with linear polarisation decomposed into positive and negative frequencies [135], the radiation can be characterised by its n-th order correlation function

$$G^{(n)}(\boldsymbol{r}_1,\dots,\boldsymbol{r}_{2n};t_1,\dots,t_{2n}) = \left\langle E^{(-)}(\boldsymbol{r}_1,t_1)\cdots E^{(-)}(\boldsymbol{r}_{2n},t_{2n})E^{(+)}(\boldsymbol{r}_1,t_1)\cdots E^{(+)}(\boldsymbol{r}_{2n},t_{2n})\right\rangle \tag{1.17}$$

The coherence properties of the emitting state are directly reflected in the n-th order correlation functions of its radiated field, i.e. the photons we detect. Assuming a stationary field, the normalised first and second order correlation functions can be expressed as a function of a single time delay τ as

$$g^{(1)}(\tau) = \frac{G^{(1)}(\tau)}{G^{(1)}(0)} \quad \text{and} \quad g^{(2)}(\tau) = \frac{G^{(2)}(\tau)}{G^{(1)}(0)^2} \tag{1.18}$$

The first order correlation function $g^{(1)}(\tau)$ can be directly related to the spectrum of the emitter using Wiener-Khinchin theorem as $g^{(1)}(\tau) \propto \mathrm{FT}\left[I(\omega)\right]$ [135]. As it describes the field amplitude autocorrelation, it can be measured with an amplitude interferometer such as a Michelson interferometer. However, in the presence of fast spectral dynamics, the necessary acquisition time in regular Fourier spectroscopy hinders the possibility of getting meaningful information about the coherence of the source. In such cases, photon-correlation Fourier spectroscopy can be used to access the optical coherence time of the emitter on short time scales. This technique was used on $CsPbBr_3$ NCs and revealed coherence times between 50 ps and 80 ps [124]. The second-order correlation function $g^{(2)}(\tau)$ describes the intensity autocorrelation of the field and is thus directly related to the time statistics of the photons. It can be measured with an intensity interferometer such as the Hanbury Brown and Twiss interferometer described in Sec. 2.3.4. Notably, the second-order correlation function can be understood as a conditional presence probability taken at two points in time. Particularly of interest in quantum emission applications, are the light states that cannot be understood using classic interpretations. While at long time delays, essentially all fields are uncorrelated, the near zero time delay value $g^{(2)}(0)$, i.e. the probability of having exactly two or more photons at the same time, is a direct signature of the type of radiation and therefore gives information about the emitting state. Considering a single mode of the electromagnetic field, the positive and negative frequency part of the modes

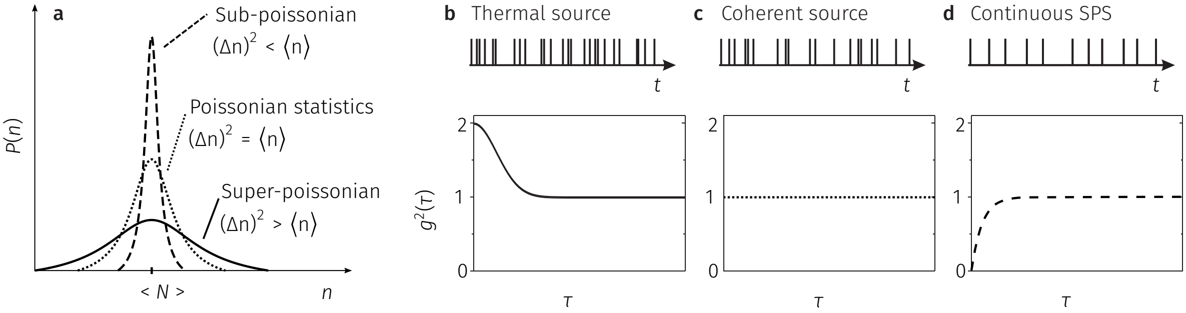

Figure 1.12 | Photon statistics. **a**, Photon number distributions shown for large *n*. **b-d**, Distribution of photon arrival time and second-order correlation function for: **b**, a thermal source, **c**, a coherent source (Glauber state), **d**, a continuous single-photon source (Fock state).

are expressed respectively as a function of a_k the annihilation operator and $a_k^\dagger$ the creation operator of a photon in mode k, such that $g^{(2)}(\tau)$ can be expressed as

$$g^{(2)}(0) = \frac{\langle a^\dagger a^\dagger a a \rangle}{\langle a^\dagger a \rangle^2} = \frac{\langle n(n-1) \rangle}{\langle n \rangle^2} = 1 + \frac{(\Delta n)^2 - \langle n \rangle}{\langle n \rangle^2} \tag{1.19}$$

The variance of the photon number distribution in this mode is therefore directly encoded in the zero-delay value $g^{(2)}(0)$ as depicted in FIG. 1.12. A source of photon number states, purely quantum, will thus exhibit a dip in the second-order correlation function at zero time-difference (FIG. 1.12d). For $n = 1$, we have the hallmark result for single-photon emission $g^{(2)}(0) = 0$ that would exhibit a system such as the one in FIG. 1.11. In contrast, a thermal source would exhibit super-poissonian fluctuations of its intensity, such that the emission of a photon ”increases” the probability of observing another photon at small delays giving rise to the bunching peak in the correlation. A coherent laser source on the other hand, showing poissonian fluctuations, will present a flat $g^2(\tau) = 1$ illustrating the randomness of the time distribution of the emitted photons.

Summary

The spontaneous relaxation of a two-level system with a time T_1 is triggered by its interaction with its electromagnetic environment and gives rise to an emission line characterised by its linewidth $2\hbar/T_2$. These properties of the relaxing system are encoded in the emitted photon stream and can be probed via the n-th order correlation functions of the field. As a competing mechanism to radiative relaxation, the system can also relax non-radiatively to the ground state. The probability that recombination happens radiatively is given by the quantum yield of the state η. As relaxation is triggered by the environment, it can be controlled by modelling the electromagnetic and dielectric environment of the emitter. In the solid state, interaction with the lattice and nearby charges leads to additional dephasing.

1.3.2 Dephasing mechanisms

Exciton-phonon interaction

Electron-phonon (EP) interaction is an effective pathway for non-radiative population relaxation as well as coherence relaxation in semiconductor nanostructures. Notably, emission lines exhibit a thermally induced linewidth broadening related to interaction with both acoustic and optical phonons. Most strikingly compared to atoms, the lineshape of single NCs is found to deviate from the symmetric lorentzian profile with an asymmetric profile due to the appearance of acoustic-phonon sidebands [136] and other phonon replica [65] related to the recombination of an exciton together with the absorption/emission of a phonon. The asymmetric profile is related to the fact that at low temperatures, compared to the phonon mode energy, the emission of a phonon is more probable than its absorption. Further considering the set of closely spaced exciton states in the band-edge of LHPs, EP interaction also plays a role in the thermalisation of the exciton states populations with phonon-assisted transitions between exciton states.

Spectral diffusion

Even when all above dephasing mechanisms are taken into account, the linewidths observed on single NC spectra can still deviate from theoretical expectations solely based on electron-phonon interactions. Indeed, a single NC linewidth is found to depend strongly both on the excitation energy [137] and excitation power [138, 139]. In above band-gap excitation, when the excitation energy approaches the emission energy, i.e. when the energy excess is reduced, one can observe a drastic linewidth narrowing independent of power [137]. This is understood as a reduced effect of the dynamic fluctuating environment of charges created within the QD environment. Conversely, the excitation power dependence of a single QD linewidth was revealed and a peculiar motional narrowing mechanism was evidenced at low temperature and power [138, 139]. From these studies, we can conclude that the spectral broadening of a single NC spectrum is driven by the two mechanisms

- spectral jumps with a strong power-dependence
- the *homogeneous* linewidth, independent of power, which is related to mechanisms much faster than the population decay rate, i.e. pure dephasing

Thus, several regimes of spectral diffusion arise depending on the characteristic spectral diffusion time scale τ_{SD} with respect to: (i) the radiative decay time τ_{rad} and (ii) the integration time T_{acq}. These were later refined by comparing spectrum with population decay rate and relating blinking to underlying microscopic mechanisms. In addition, for these emitters usually embedded in a polymer matrix, photo-induced charges within the NC environment can lead to sub-lifetime spectral diffusion [140].

Blinking

Besides spectral diffusion, though maybe related [141, 142], colloidal NCs usually exhibit the common drawback of emission intermittency, i.e. blinking [143]. Their emission typically presents with consecutive 'off' and 'on' periods and several discrete levels of intensity may be observed. Perovskites NCs on the other hand seem to show a stable emission at low temperature with reduced blinking [123], although some blinking has been observed at higher temperature [144, 145]. This surely stems from a lack of enough work on the matter due to the complexity and disparity in experimental configurations: solvent, polymer, substrate, etc. Indeed, for nanoscale emitters, surface states and nearby charges play a central role in their optelectronic behavior.

Conclusion

In this chapter, we have presented LHPs and their peculiarities with respect to established semiconductors. Starting from the perovskite structure, we have presented the electronic band structure of LHPs and their band-edge fine structure which hosts a majority of dipole-allowed states. In particular, we have highlighted the current debate about their exciton fine structure and detailed the main contributions at play in setting the exciton fine structure and their interplay in light of recent literature. Finally, solid state processes that lead to exciton dephasing has been discussed and the potential of LHP NCs as quantum emitters has been revealed.

In light of this, in this work, we propose a statistical analysis of the spectral properties of a large number of single $CsPbBr_3$ NCs to reveal instrinsic properties related the band-edge exciton fine structure in a wide range of NCs sizes (Ch. 3). In addition, in Ch. 4, we report on a detailed study of the interplay between bright and dark excitons states in single $CsPbBr_3$ via a temperature-dependent time-resolved study on a subset of these NCs.

References for Chapter 1

[1] K. Chondroudis et al., “Electroluminescence from an Organic–Inorganic Perovskite Incorporating a Quaterthiophene Dye within Lead Halide Perovskite Layers”, Chemistry of Materials **11**, 3028–3030 (1999) (p. 25).

[2] A. Kojima et al., “Organometal Halide Perovskites as Visible-Light Sensitizers for Photovoltaic Cells”, Journal of the American Chemical Society **131**, 6050–6051 (2009) (p. 25).

[3] M. M. Lee et al., “Efficient Hybrid Solar Cells Based on Meso-Superstructured Organometal Halide Perovskites”, Science **338**, 643–647 (2012) (p. 25).

[4] J. Jeong et al., “Pseudo-halide anion engineering for α-FAPbI3 perovskite solar cells”, Nature **592**, 381–385 (2021) (p. 25).

[5] A. Al-Ashouri et al., “Monolithic perovskite/silicon tandem solar cell with >29% efficiency by enhanced hole extraction”, Science **370**, 1300–1309 (2020) (p. 25).

[6] L. C. Schmidt et al., “Nontemplate Synthesis of $CH_3NH_3PbBr_3$ Perovskite Nanoparticles”, Journal of the American Chemical Society **136**, 850–853 (2014) (p. 25).

[7] L. Protesescu et al., “Nanocrystals of Cesium Lead Halide Perovskites ($CsPbX_3$, X = Cl, Br, and I): Novel Optoelectronic Materials Showing Bright Emission with Wide Color Gamut”, Nano Letters **15**, 3692–3696 (2015) (p. 25).

[8] M. Auf der Maur et al., “Efficiency Drop in Green InGaN/GaN Light Emitting Diodes: The Role of Random Alloy Fluctuations”, Physical Review Letters **116**, 027401 (2016) (p. 25).

[9] G. Rose, *De novis quibusdam fossilibus quae in montibus Uraliis inveniuntur* (Berolini, 1839) (p. 26).

[10] V. M. Goldschmidt, “Die gesetze der krystallochemie”, Naturwissenschaften **14**, 477–485 (1926) (pp. 26, 27).

[11] E. A. Katz, “Perovskite: Name Puzzle and German-Russian Odyssey of Discovery”, Helvetica Chimica Acta **103**, e2000061 (2020) (p. 26).

[12] C. C. Stoumpos et al., “Crystal Growth of the Perovskite Semiconductor $CsPbBr_3$: A New Material for High-Energy Radiation Detection”, Crystal Growth & Design **13**, 2722–2727 (2013) (p. 26).

[13] H. L. Wells, “Über die Cäsium- und Kalium-Bleihalogenide”, Zeitschrift für anorganische Chemie **3**, 195–210 (1893) (p. 26).

[14] C. K. Møller, “A Phase Transition in Cæsium Plumbochloride”, Nature **180**, 981–982 (1957) (p. 26).

[15] C. K. Møller, “Crystal Structure and Photoconductivity of Caesium Plumbohalides”, Nature **182**, 1436 (1958) (pp. 26, 29).

[16] W. Travis et al., “On the application of the tolerance factor to inorganic and hybrid halide perovskites: a revised system”, Chemical Science **7**, 4548–4556 (2016) (p. 27).

[17] M. R. Filip et al., “The geometric blueprint of perovskites”, Proceedings of the National Academy of Sciences **115**, 5397–5402 (2018) (p. 27).

[18] R. D. Shannon et al., “Effective ionic radii in oxides and fluorides”, Acta Crystallographica Section B Structural Crystallography and Crystal Chemistry **25**, 925–946 (1969) (p. 27).

[19] C. Li et al., “Formability of ABX_3 (X = F, Cl, Br, I) halide perovskites”, Acta Crystallographica Section B Structural Science **64**, 702–707 (2008) (p. 27).

[20] S. Sasaki et al., "Orthorhombic perovskite $CaTiO_3$ and $CdTiO_3$: structure and space group", Acta Crystallographica Section C **43**, 1668–1674 (1987) (p. 28).

[21] A. M. Glazer, "The classification of tilted octahedra in perovskites", Acta Crystallographica Section B Structural Crystallography and Crystal Chemistry **28**, 3384–3392 (1972) (p. 28).

[22] C. J. Howard et al., "Group-Theoretical Analysis of Octahedral Tilting in Perovskites", Acta Crystallographica Section B Structural Science **54**, 782–789 (1998) (p. 28).

[23] R. H. Mitchell et al., "Nomenclature of the perovskite supergroup: A hierarchical system of classification based on crystal structure and composition", Mineralogical Magazine **81**, 411–461 (2017) (p. 28).

[24] J. C. Beimborn et al., "Size-Dependent Pressure-Response of the Photoluminescence of $CsPbBr_3$ Nanocrystals", The Journal of Physical Chemistry Letters, acs.jpclett.0c00174 (2020) (p. 28).

[25] T. J. Whitcher et al., "Dual phases of crystalline and electronic structures in the nanocrystalline perovskite $CsPbBr_3$", NPG Asia Materials **11**, 1–12 (2019) (p. 29).

[26] R. X. Yang et al., "Spontaneous Octahedral Tilting in the Cubic Inorganic Cesium Halide Perovskites $CsSnX_3$ and $CsPbX_3$ (X = F, Cl, Br, I)", The Journal of Physical Chemistry Letters **8**, 4720–4726 (2017) (pp. 29, 30).

[27] T. Lanigan-Atkins et al., "Two-dimensional overdamped fluctuations of the soft perovskite lattice in $CsPbBr_3$", Nature Materials, 1–7 (2021) (pp. 29, 30).

[28] A. Marronnier et al., "Structural Instabilities Related to Highly Anharmonic Phonons in Halide Perovskites", The Journal of Physical Chemistry Letters **8**, 2659–2665 (2017) (p. 29).

[29] C. Gehrmann et al., "Dynamic shortening of disorder potentials in anharmonic halide perovskites", Nature Communications **10**, 3141 (2019) (pp. 29, 32).

[30] P. Cottingham et al., "Depressed Phase Transitions and Thermally Persistent Local Distortions in $CsPbBr_3$ Quantum Dots", Chemistry of Materials **30**, 6711–6716 (2018) (p. 29).

[31] M. V. Kovalenko et al., "Properties and potential optoelectronic applications of lead halide perovskite nanocrystals", Science **358**, 745–750 (2017) (pp. 29, 31).

[32] J. S. Bechtel et al., "Octahedral tilting instabilities in inorganic halide perovskites", Physical Review Materials **2**, 025401 (2018) (pp. 29, 30).

[33] J. S. Bechtel et al., "Finite-temperature simulation of anharmonicity and octahedral tilting transitions in halide perovskites", Physical Review Materials **3**, 113605 (2019) (pp. 29, 30).

[34] J. C. Thomas et al., "Machine learning the density functional theory potential energy surface for the inorganic halide perovskite $CsPbBr_3$", Physical Review B **100**, 134101 (2019) (p. 29).

[35] T. W. Jones et al., "Lattice strain causes non-radiative losses in halide perovskites", Energy & Environmental Science **12**, 596–606 (2019) (p. 30).

[36] Y. Yu et al., "Atomic Resolution Imaging of Halide Perovskites", Nano Letters **16**, 7530–7535 (2016) (p. 30).

[37] F. Bertolotti et al., "Coherent Nanotwins and Dynamic Disorder in Cesium Lead Halide Perovskite Nanocrystals", ACS Nano **11**, 3819–3831 (2017) (p. 30).

[38] M. C. Brennan et al., "Crystal Structure of Individual $CsPbBr_3$ Perovskite Nanocubes", Inorganic Chemistry **58**, 1555–1560 (2019) (p. 30).

[39] Q. A. Akkerman et al., "Genesis, challenges and opportunities for colloidal lead halide perovskite nanocrystals", Nature Materials **17**, 394–405 (2018) (pp. 31, 34).

[40] H. J. Queisser et al., "Defects in Semiconductors: Some Fatal, Some Vital", Science **281**, 945–950 (1998) (p. 30).

[41] K. X. Steirer et al., "Defect Tolerance in Methylammonium Lead Triiodide Perovskite", ACS Energy Letters **1**, 360–366 (2016) (p. 31).

[42] J. Kang et al., "High Defect Tolerance in Lead Halide Perovskite $CsPbBr_3$", The Journal of Physical Chemistry Letters **8**, 489–493 (2017) (p. 31).

[43] H. Huang et al., "Lead Halide Perovskite Nanocrystals in the Research Spotlight: Stability and Defect Tolerance", ACS Energy Letters **2**, 2071–2083 (2017) (p. 31).

[44] R. E. Brandt et al., “Identifying defect-tolerant semiconductors with high minority-carrier lifetimes: beyond hybrid lead halide perovskites”, MRS Communications **5**, 265–275 (2015) (p. 31).

[45] R. E. Brandt et al., “Searching for “Defect-Tolerant” Photovoltaic Materials: Combined Theoretical and Experimental Screening”, Chemistry of Materials **29**, 4667–4674 (2017) (p. 31).

[46] X. Zhang et al., “Iodine interstitials as a cause of nonradiative recombination in hybrid perovskites”, Physical Review B **101**, 140101 (2020) (p. 31).

[47] M. W. Swift et al., “Deep levels in cesium lead bromide from native defects and hydrogen”, Journal of Materials Chemistry A **9**, 7491–7495 (2021) (p. 31).

[48] X. Zhang et al., “Defect tolerance in halide perovskites: A first-principles perspective”, Journal of Applied Physics **131**, 090901 (2022) (p. 31).

[49] K. Miyata et al., “Lead halide perovskites: Crystal-liquid duality, phonon glass electron crystals, and large polaron formation”, Science Advances **3**, e1701469 (2017) (pp. 31, 32).

[50] O. Yaffe et al., “Local Polar Fluctuations in Lead Halide Perovskite Crystals”, Physical Review Letters **118**, 136001 (2017) (pp. 32–34).

[51] Y. Rakita et al., “Mechanical properties of APbX3 (A = Cs or CH3NH3; X = I or Br) perovskite single crystals”, MRS Communications **5**, 623–629 (2015) (p. 32).

[52] K. Miyata et al., “Large polarons in lead halide perovskites”, Science Advances **3**, e1701217 (2017) (pp. 32, 34, 35).

[53] M. Born et al., *Dynamical theory of crystal lattices*, Oxford Classic Texts in the Physical Sciences (Clarendon Press ; Oxford University Press, Oxford : New York, 1988), 420 pp. (p. 32).

[54] J. F. Nye, *Physical properties of crystals: their representation by tensors and matrices* (Clarendon Press ; Oxford University Press, Oxford; New York, 1984) (p. 33).

[55] M. Roknuzzaman et al., “Towards lead-free perovskite photovoltaics and optoelectronics by ab-initio simulations”, Scientific Reports **7**, 14025 (2017) (p. 33).

[56] A. Létoublon et al., “Elastic Constants, Optical Phonons, and Molecular Relaxations in the High Temperature Plastic Phase of the $CH_3NH_3PbBr_3$ Hybrid Perovskite”, The Journal of Physical Chemistry Letters **7**, 3776–3784 (2016) (p. 33).

[57] A. C. Ferreira et al., “Elastic Softness of Hybrid Lead Halide Perovskites”, Physical Review Letters **121**, 085502 (2018) (p. 33).

[58] Y. Fujii et al., “Neutron-scattering study on phase transitions of $CsPbCl_3$”, Physical Review B **9**, 4549–4559 (1974) (p. 33).

[59] M. Songvilay et al., “Common acoustic phonon lifetimes in inorganic and hybrid lead halide perovskites”, Physical Review Materials **3**, 093602 (2019) (p. 33).

[60] C. M. Iaru et al., “Fröhlich interaction dominated by a single phonon mode in $CsPbBr_3$”, Nature Communications **12**, 5844 (2021) (pp. 33, 34).

[61] S. C. Boehme et al., “Phonon-Mediated and Weakly Size-Dependent Electron and Hole Cooling in $CsPbBr_3$ Nanocrystals Revealed by Atomistic Simulations and Ultrafast Spectroscopy”, Nano Letters **20**, 1819–1829 (2020) (p. 34).

[62] F. Brivio et al., “Lattice dynamics and vibrational spectra of the orthorhombic, tetragonal, and cubic phases of methylammonium lead iodide”, Physical Review B **92**, 144308 (2015) (p. 34).

[63] A. C. Ferreira et al., “Direct evidence of weakly dispersed and strongly anharmonic optical phonons in hybrid perovskites”, Communications Physics **3**, 48 (2020) (pp. 34, 35).

[64] S. Poncé et al., “Origin of Low Carrier Mobilities in Halide Perovskites”, ACS Energy Letters **4**, 456–463 (2019) (p. 34).

[65] M. J. Fernée et al., “The optical phonon spectrum of CdSe colloidal quantum dots”, Physical Chemistry Chemical Physics **16**, 16957–16961 (2014) (pp. 34, 54).

[66] C. F. Klingshirn, *Semiconductor Optics*, Graduate Texts in Physics (Springer Berlin Heidelberg, Berlin, Heidelberg, 2012) (p. 34).

[67] N. Yazdani et al., “Measuring the Vibrational Density of States of Nanocrystal-Based Thin Films with Inelastic X-ray Scattering”, The Journal of Physical Chemistry Letters **9**, 1561–1567 (2018) (p. 34).

[68] G. Rainò et al., “Ultra-narrow room-temperature emission from single $CsPbBr_3$ perovskite quantum dots”, Nature Communications **13**, 2587 (2022) (p. 34).

[69] G. Mie, “Zur kinetischen Theorie der einatomigen Körper”, Annalen der Physik **316**, 657–697 (1903) (p. 35).

[70] E. Grüneisen, “Zusammenhang zwischen Kompressibilität, thermischer Ausdehnung, Atomvolumen und Atomwärme der Metalle”, Annalen der Physik **331**, 393–402 (1908) (p. 35).

[71] M. Cardona, “Phonons: The second type of quantum excitations discovered”, Annalen der Physik **512**, 865–870 (2000) (p. 35).

[72] O. Verzelen et al., “Polaron lifetime and energy relaxation in semiconductor quantum dots”, Physical Review B **62**, R4809–R4812 (2000) (p. 35).

[73] O. Verzelen et al., “Excitonic Polarons in Semiconductor Quantum Dots”, Physical Review Letters **88**, 146803 (2002) (p. 35).

[74] O. Verzelen et al., “Energy relaxation in quantum dots”, Physical Review B **66**, 081308 (2002) (p. 35).

[75] A. J. Neukirch et al., “Polaron Stabilization by Cooperative Lattice Distortion and Cation Rotations in Hybrid Perovskite Materials”, Nano Letters **16**, 3809–3816 (2016) (p. 35).

[76] O. Cannelli et al., “Quantifying Photoinduced Polaronic Distortions in Inorganic Lead Halide Perovskites Nanocrystals”, Mar. 3, 2021 (p. 35).

[77] M. Born et al., “Zur Quantentheorie der Molekeln”, Annalen der Physik **389**, 457–484 (1927) (p. 37).

[78] F. Bloch, “Über die quantenmechanik der elektronen in kristallgittern”, Zeitschrift für Physik **52**, 555–600 (1929) (p. 37).

[79] F. Herman et al., “Relativistic Corrections to the Band Structure of Tetrahedrally Bonded Semiconductors”, Physical Review Letters **11**, 541–545 (1963) (p. 37).

[80] L. D. Landau et al., *Relativistic Quantum Theory*, Course of Theoretical Physics 4 (Pergamon Press, New-York, 1971) (p. 37).

[81] M. Combescot et al., “Spin-orbit coupling: Atom versus semiconductor crystal”, Physical Review B **99**, 245202 (2019) (p. 37).

[82] J. Even et al., “Analysis of Multivalley and Multibandgap Absorption and Enhancement of Free Carriers Related to Exciton Screening in Hybrid Perovskites”, The Journal of Physical Chemistry C **118**, 11566–11572 (2014) (pp. 38, 43).

[83] K. Heidrich et al., “Electronic structure, photoemission spectra, and vacuum-ultraviolet optical spectra of $CsPbCl_3$ and $CsPbBr_3$”, Physical Review B **24**, 5642 (1981) (p. 38).

[84] G. L. Bir et al., *Symmetry and strain-induced effects in semiconductors* (Wiley, New York, 1974), 484 pp. (pp. 38, 39).

[85] M. A. Becker et al., “Bright triplet excitons in caesium lead halide perovskites”, Nature **553**, 189–193 (2018) (pp. 38–40, 43, 44, 46–48).

[86] J. Even et al., “Solid-State Physics Perspective on Hybrid Perovskite Semiconductors”, The Journal of Physical Chemistry C **119**, 10161–10177 (2015) (pp. 38, 43).

[87] J. Even et al., “Importance of Spin–Orbit Coupling in Hybrid Organic/Inorganic Perovskites for Photovoltaic Applications”, The Journal of Physical Chemistry Letters **4**, 2999–3005 (2013) (pp. 39, 43, 47).

[88] J. Ramade et al., “Exciton-phonon coupling in a $CsPbBr_3$ single nanocrystal”, Applied Physics Letters **112**, 072104 (2018) (p. 39).

[89] R. Ben Aich et al., “Bright-Exciton Splittings in Inorganic Cesium Lead Halide Perovskite Nanocrystals”, Physical Review Applied **11**, 034042 (2019) (pp. 39, 43, 46, 47).

[90] J. Even et al., “Electronic model for self-assembled hybrid organic/perovskite semiconductors: Reverse band edge electronic states ordering and spin-orbit coupling”, Physical Review B **86**, 205301 (2012) (pp. 39, 43, 47).

[91] G. Bastard, *Wave mechanics applied to semiconductor heterostructures*, Monographies de Physique (Les Editions de Physique, Les Ulis, France, 1988), 357 pp. (p. 40).

[92] P. Y. Yu et al., *Fundamentals of Semiconductors*, Graduate Texts in Physics (Springer Berlin Heidelberg, Berlin, Heidelberg, 2010) (p. 40).

[93] D. A. Egger et al., “What Remains Unexplained about the Properties of Halide Perovskites?”, Advanced Materials **30**, 1800691 (2018) (p. 40).

[94] M. Puppin et al., “Evidence of Large Polarons in Photoemission Band Mapping of the Perovskite Semiconductor $CsPbBr_3$”, Physical Review Letters **124**, 206402 (2020) (p. 40).

[95] M. Sajedi et al., “Is There a Polaron Signature in Angle-Resolved Photoemission of $CsPbBr_3$?”, Physical Review Letters **128**, 176405 (2022) (p. 40).

[96] P. A. M. Dirac, “The Quantum Theory of the Emission and Absorption of Radiation”, Proceedings of the Royal Society A **114**, 243–265 (1927) (p. 41).

[97] E. Fermi, *Nuclear Physics: A Course Given by Enrico Fermi at the University of Chicago*, edited by R. edition (University of Chicago Press, Chicago, 1974), 258 pp. (p. 41).

[98] A. I. Ekimov et al., “Quantum size effect in semiconductor microcrystals”, Solid State Communications **56**, 921–924 (1985) (p. 43).

[99] A. L. Efros, “Luminescence polarization of CdSe microcrystals”, Physical Review B **46**, 7448–7458 (1992) (p. 43).

[100] M. Nirmal et al., “Observation of the ”Dark Exciton” in CdSe Quantum Dots”, Physical Review Letters **75**, 3728–3731 (1995) (p. 43).

[101] A. L. Efros et al., “Band-edge exciton in quantum dots of semiconductors with a degenerate valence band: Dark and bright exciton states”, Physical Review B **54**, 4843–4856 (1996) (pp. 43, 44).

[102] J. Even, “Pedestrian Guide to Symmetry Properties of the Reference Cubic Structure of 3D All-Inorganic and Hybrid Perovskites”, The Journal of Physical Chemistry Letters **6**, 2238–2242 (2015) (pp. 43, 44).

[103] M. Gramlich et al., “Dark and Bright Excitons in Halide Perovskite Nanoplatelets”, Advanced Science **9**, 2103013 (2022) (p. 43).

[104] P. C. Sercel et al., “Quasicubic model for metal halide perovskite nanocrystals”, The Journal of Chemical Physics **151**, 234106 (2019) (pp. 43, 45, 47).

[105] P. C. Sercel et al., “Exciton Fine Structure in Perovskite Nanocrystals”, Nano Letters **19**, 4068–4077 (2019) (pp. 43, 46–48).

[106] J. Ramade et al., “Fine structure of excitons and electron–hole exchange energy in polymorphic $CsPbBr_3$ single nanocrystals”, Nanoscale **10**, 6393–6401 (2018) (pp. 43, 46, 47).

[107] R. Ben Aich et al., “Multiband $\mathbf{k}{\cdot}\mathbf{p}$ Model for Tetragonal Crystals: Application to Hybrid Halide Perovskite Nanocrystals”, The Journal of Physical Chemistry Letters, 808–817 (2020) (p. 43).

[108] C. Cohen-Tannoudji et al., *Quantum Mechanics*, Vol. 2 (June 1, 1986), 626 pp. (p. 43).

[109] E. I. Rashba, “Gigantic oscillator strengths inherent in exciton complexes”, in *Excitons at High Density*, Vol. 73, edited by H. Haken et al., Springer Tracts in Modern Physics (Springer Berlin Heidelberg, Berlin, Heidelberg, 1975), pp. 150–170 (p. 44).

[110] T. Itoh et al., “Size-dependent radiative decay time of confined excitons in CuCl microcrystals”, Solid State Communications **73**, 271–274 (1990) (p. 44).

[111] M. Fu et al., “Neutral and Charged Exciton Fine Structure in Single Lead Halide Perovskite Nanocrystals Revealed by Magneto-optical Spectroscopy”, Nano Letters **17**, 2895–2901 (2017) (pp. 46, 47).

[112] M. O. Nestoklon et al., “Optical orientation and alignment of excitons in ensembles of inorganic perovskite nanocrystals”, Physical Review B **97**, 235304 (2018) (pp. 46, 47).

[113] P. Tamarat et al., “The ground exciton state of formamidinium lead bromide perovskite nanocrystals is a singlet dark state”, Nature Materials **18**, 717–724 (2019) (pp. 46, 48).

[114] F. Zheng et al., “Rashba Spin–Orbit Coupling Enhanced Carrier Lifetime in $CH_3NH_3PbI_3$”, Nano Letters **15**, 7794–7800 (2015) (pp. 46, 47).

[115] T. Etienne et al., “Dynamical Origin of the Rashba Effect in Organohalide Lead Perovskites: A Key to Suppressed Carrier Recombination in Perovskite Solar Cells?”, The Journal of Physical Chemistry Letters 7, 1638–1645 (2016) (pp. 46, 47).

[116] P. Tamarat et al., “The dark exciton ground state promotes photon-pair emission in individual perovskite nanocrystals”, Nature Communications **11**, 6001 (2020) (pp. 47, 48).

[117] M. Isarov et al., “Rashba Effect in a Single Colloidal $CsPbBr_3$ Perovskite Nanocrystal Detected by Magneto-Optical Measurements”, Nano Letters **17**, 5020–5026 (2017) (p. 47).

[118] V. L. Colvin et al., “CdSe nanocrystals with a dipole moment in the first excited state”, The Journal of Chemical Physics **97**, 730–733 (1992) (p. 47).

[119] S. A. Blanton et al., “Dielectric Dispersion Measurements of CdSe Nanocrystal Colloids: Observation of a Permanent Dipole Moment”, Physical Review Letters **79**, 865–868 (1997) (p. 47).

[120] M. Shim et al., “Permanent dipole moment and charges in colloidal semiconductor quantum dots”, The Journal of Chemical Physics **111**, 6955–6964 (1999) (p. 47).

[121] B. Lv et al., “Probing Permanent Dipole Moments and Removing Exciton Fine Structures in Single Perovskite Nanocrystals by an Electric Field”, Physical Review Letters **126**, 197403 (2021) (p. 48).

[122] Z. Yang et al., “Impact of the Halide Cage on the Electronic Properties of Fully Inorganic Cesium Lead Halide Perovskites”, ACS Energy Letters **2**, 1621–1627 (2017) (p. 48).

[123] G. Rainò et al., “Single Cesium Lead Halide Perovskite Nanocrystals at Low Temperature: Fast Single-Photon Emission, Reduced Blinking, and Exciton Fine Structure”, ACS Nano **10**, 2485–2490 (2016) (pp. 49, 55).

[124] H. Utzat et al., “Coherent single-photon emission from colloidal lead halide perovskite quantum dots”, Science **363**, 1068–1072 (2019) (pp. 49, 52).

[125] Y. Lv et al., “Quantum Interference in a Single Perovskite Nanocrystal”, Nano Letters **19**, 4442–4447 (2019) (p. 49).

[126] N. Accanto et al., “Engineering the Spin–Flip Limited Exciton Dephasing in Colloidal CdSe/CdS Quantum Dots”, ACS Nano **6**, 5227–5233 (2012) (p. 49).

[127] E. Purcell, “Spontaneous emission probabilities at radio frequencies”, Physical Review **69**, 681 (1946) (p. 51).

[128] H. Bücher et al., “Controlled Transfer of Excitation Energy Through Thin Layers”, Molecular Crystals **2**, 199–230 (1967) (p. 51).

[129] K. Drexhage, “Influence of a dielectric interface on fluorescence decay time”, Journal of Luminescence **1–2**, 693–701 (1970) (p. 51).

[130] K.-H. Tews et al., “Variation of the Luminescence Lifetime of a Molecule near an Interface between Differently Polarizable Dielectrics”, Nature **228**, 276–278 (1970) (p. 51).

[131] K. Tews, “On the variation of luminescence lifetimes. The approximations of the approximative methods”, Journal of Luminescence **9**, 223–239 (1974) (p. 51).

[132] W. Lukosz et al., “Light emission by magnetic and electric dipoles close to a plane interface I Total radiated power”, Journal of the Optical Society of America **67**, 1607 (1977) (p. 51).

[133] N. C. Greenham et al., “Measurement of absolute photoluminescence quantum efficiencies in conjugated polymers”, Chemical Physics Letters **241**, 89–96 (1995) (p. 51).

[134] R. J. Glauber, “The Quantum Theory of Optical Coherence”, Physical Review **130**, 2529 (1963) (p. 51).

[135] M. O. Scully et al., *Quantum Optics* (Sept. 1997) (p. 52).

[136] L. Besombes et al., “Acoustic phonon broadening mechanism in single quantum dot emission”, Physical Review B **63**, 155307 (2001) (p. 54).

[137] C. Kammerer et al., “Line narrowing in single semiconductor quantum dots: Toward the control of environment effects”, Physical Review B **66**, 1306 (2002) (p. 54).

[138] A. Berthelot et al., “Unconventional motional narrowing in the optical spectrum of a semiconductor quantum dot”, Nature Physics **2**, 759–764 (2006) (p. 54).

[139] A. Berthelot et al., “Voltage-controlled motional narrowing in a semiconductor quantum dot”, New Journal of Physics **11**, 093032 (2009) (p. 54).

[140] M. J. Fernée et al., “The ultimate limit to the emission linewidth of single nanocrystals”, Nanotechnology **24**, 465703 (2013) (p. 55).

[141] R. G. Neuhauser et al., “Correlation between Fluorescence Intermittency and Spectral Diffusion in Single Semiconductor Quantum Dots”, Physical Review Letters **85**, 3301 (2000) (p. 55).

[142] T. Plakhotnik, “Anomalous Power Laws of Spectral Diffusion in Quantum Dots: A Connection to Luminescence Intermittency”, Physical Review Letters **105**, `10.1103/PhysRevLett.105.167402` (2010) (p. 55).

[143] M. Nirmal et al., “Fluorescence intermittency in single cadmium selenide nanocrystals”, Nature **383**, 802–804 (1996) (p. 55).

[144] L. Hou et al., “Memories in the photoluminescence intermittency of single cesium lead bromide nanocrystals”, Nanoscale **12**, 6795–6802 (2020) (p. 55).

[145] I. M. Palstra et al., “Intermittency of $CsPbBr_3$ Perovskite Quantum Dots Analyzed by an Unbiased Statistical Analysis”, The Journal of Physical Chemistry C **125**, 12061–12072 (2021) (p. 55).

2

Experimental aspects

In this work, we study colloidal $CsPbBr_3$ nanocrystals (NCs) stabilised by organic ligands that cover their surface (see cartoon in FIG. 2.2a). Together with the reagents' stoichiometry, these ligands have a critical impact on the size, shape and purity of the obtained colloidal NCs. In SEC. 2.1, we introduce the synthesis of semiconductor NCs and the synthesis protocol used in this work. Isolation of single NCs on dielectric substrates and structural characterisation of the synthesis products is then detailed in SEC. 2.2. In SEC. 2.3 we focus on the scanning confocal microscopes built for this study and enabling the reproducible localisation of single nanoemitters. Single NC spectroscopic experiments are presented with an emphasis on time-resolved single-photon spectroscopy.

2.1 Colloidal synthesis of lead halide perovskite nanocrystals

Colloidal synthesis is an established wet chemistry process where precursors are mixed under controlled conditions to form a precipitate. The obtained precipitate can then be dispersed in an appropriate solvent forming long-term stable colloidal suspensions. In the case of LHPs, particular challenges hinder chemists efforts to obtain phase pure mono-disperse NCs. In addition of the targeted $CsPbX_3$ NCs, a multitude of compounds can form during synthesis such as the insulating Cs_4PbX_6 [1–3], the indirect bandgap $CsPb_2X_5$ [4] as well as CsX and PbX_2 complexes. All these synthesis by-products need to be avoided not only because they can interfere with the desired synthesis product but also for optical characterisation of the solutions because by-products also absorb UV radiation. The synthesis is further complicated by the fast formation kinetics that do not allow for size-selection during the formation of crystals. Synthesis protocols therefore contain a purification step both for size selection and by-product elimination, however these by-products should ideally be reduced to a minimum as they might disturb the growth. To do so, the precursors stoichiometry is varied to optimise the synthesis reaction yield, where in general for LHPs, lead is supplied in excess with respect to bromide which is itself in excess with respect to the limiting cesium reagent [5, 6]. Several solution-based synthesis routes exist for LHP NCs. In the following, we will only consider one route to synthesise metal halide perovskites NCs: the hot-injection method [5, 7, 8].

2.1.1 Literature review

Hot-injection

The LHP NCs synthesis protocols used in this work can be understood by analogy by relying on the same principles as the hot-injection method pioneered on metal chalcogenide NCs in 1993 [9, 10]. The technique itself relied on critical insight on the production of monodisperse colloidal NCs: separating the nucleation and the growth of the NCs (FIG. 2.1) [12]. The nucleation should be a short burst and the nuclei growing rate should exceed the injection rate such that all nucleation centers are formed at the same time. A second slower controlled growth phase, known as Ostwald ripening, follows where seeded particles can continue to grow, dissolving smaller nuclei. By achieving the separation between these two regimes and monitoring the formation of nanoparticles by transmission electron microscopy, a similar mechanism was unveiled for perovskites with a nucleation of metal seeds followed by the growth of NCs by oriented attachment [13]. In contrast with the diffusion-limited growth of zinc-blende and wurtzite NCs synthesis, LHPs NCs are synthesised in a nucleation-limited synthesis which

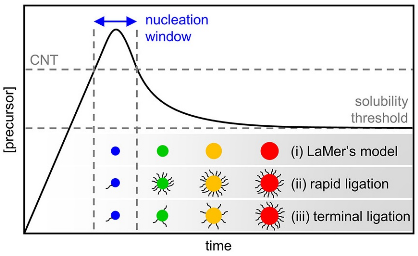

Figure 2.1 | Nanocrystal growth models. Change in precursor concentration with time highlighting the two main steps of the synthesis: nucleation and growth. Several models for NC growth and ligation are shown. The La Mer growth model shown as (i) fails to describe the formation kinetics of perovskite NCs because ligands are not addressed. Reprinted from [11].

happens within seconds.

Fast formation

Because perovskite NCs form within seconds after injection the study of their synthesis is rather challenging. The synthesis of smaller perovskite NCs in particular is thus difficult in comparison to II-VI and III-V NCs where, with a reaction time on the order of minutes, particular sizes can be obtained by stopping the reaction after a fixed duration. The fast formation of perovskite NCs, together with the dynamic binding of ligands [14], both hinder the ability to study the kinetics of nanocrystal capping by surface ligands, during NC formation and colloidal suspension. This explains why perovskite NCs synthesis is still not *mastered* in the weak- to strong-confinement regime with a master recipe for size- and shape-uniform NCs with sizes below 10 nm.

Ligands

While providing critical insight into the formation of NCs, the La Mer model, shown as (i) in Fig. 2.1 does not account for the capping ligands used to complete the coordination of surface atoms and their critical role both during the nucleation and for stabilisation in solution. Surface capping ligands are essential to mitigate the impact of surface defect states that compete with the desired confined exciton state emission, especially in smaller NCs owing to the large surface-to-volume ratio. Indeed, despite the relative defect tolerance of the perovskite structure [15], enabling the synthesis of high photoluminescence quantum yield NCs easily and without shells, proper passivation is still required. Recently, the so-called defect tolerance of perovskites is even being called out as the influence of halide vacancies in particular on non-radiative recombination is being investigated [15, 16]. Defect engineering and ligand selection are therefore still key to improve the optoelectronic properties of LHPs.

Two general types of ligands are used in the synthesis of LHPs: carboxylic acids and amines. Most of LHP NCs to date are synthesised together with a pair of long-chain ligands, an amine (oleylamine) and an organic acid (oleic acid), that passivate the surface of the NCs together. While the ammonium cation (● in Fig. 2.2) replaces the surface A-cation or fills a cation vacancy, the halide or carboxylate (● in Fig. 2.2) maintains the charge neutrality of the structure [14, 17]. Due to their ionic bonding nature and structure, LHPs present a subtle surface/bulk interface that favours substitution of ions to the usual adsorption of ligands in typical NCs [17]. As such, surface ligation is highly dynamic with rapid desorption of the ligand shell upon purification and washing steps [14] and the surface of LHPs is prone to both cation (A) and anion (X) vacancies, depicted respectively as ◌ and ◌ in FIG. 2.2C. Passivation techniques therefore aim at filling in both the cation and anion vacancies, which was originally achieved with a combination of oleic acid (OA, 〰●), a long-chain carboxylate provided with halide ions in excess, and oleylamine (OLA, 〰●) a long-chain ammonium and alkali ion. Although this passivation scheme is the most widely used for the synthesis of LHPs, these ligands bind only weakly to the NCs surface. Partly due to the ionic bonding character of LHPs, but also because the neutral forms COOH and NH_2 also exist in the colloidal solution with constant re-solubilisation, leading to dynamic passivation of NCs and easy loss of ligands during purification and dilution steps. The dual binding of the original oleic acid/oleylamine pair, with both anionic and cationic ligands, has inspired the use of zwitterionic ligands (〰●●), possessing both anion and cation moieties, thus better passivating the surface with a single ligand chain that binds more strongly to the NCs surface than the original labile pair. The main goal in this respect for single nanocrystal spectroscopy is to retain good passivation at low concentrations. Zwitterionic ligands are currently the best bet for these applications as they retain colloidal stability regardless of concentration [19–21]. Conversely, if monodisperse NCs assemblies are to be formed,

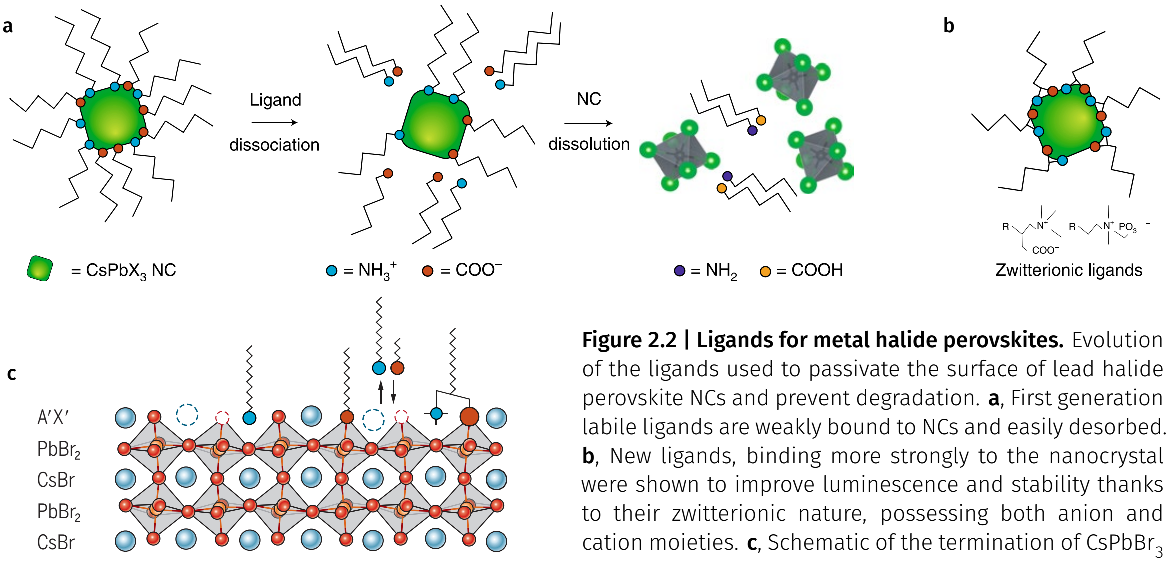

Figure 2.2 | Ligands for metal halide perovskites. Evolution of the ligands used to passivate the surface of lead halide perovskite NCs and prevent degradation. **a**, First generation labile ligands are weakly bound to NCs and easily desorbed. **b**, New ligands, binding more strongly to the nanocrystal were shown to improve luminescence and stability thanks to their zwitterionic nature, possessing both anion and cation moieties. **c**, Schematic of the termination of $CsPbBr_3$ NCs with probable vacancies and passivation routes. Panels are adapted from: **a**-**b** [2], **c** [18].

long-chain sulfobetaine ligands, also zwitterionic ligands, offer the best passivation/transport compromise all the while enabling a precise control of the size of the NCs [22].

Applications and stability

In fact, specific ligands are needed for specific applications, as a one-ligand solution does not (yet) exist for metal halide perovskites. For applications, it is not the stability of the colloidal suspension that matters but rather the actual efficiency of optoelectronic devices based on thin films of that suspension which invariably show a reduction in photoluminescence quantum yield. Because the best ligands for a colloidal suspension (strong interparticle repulsion) are not necessarily the best ligands for dense thin films, researchers are now focusing on finding shorter ligands introduced with a controlled density to improve charge transfer between particles and thus overall efficiency. However, this is still difficult to reconcile with the loss of stability.

Stability

A particular point of interest is the stability of the as-synthesised NCs. The stability of perovskites is hindered by their high reactivity with moisture. To alleviate the degradation, synthesis and experiments are performed under controlled atmosphere. Alternatively, in a view to integrate perovskites in real-world applications, researchers are investigating ways to protect NCs in real-world (moist) atmosphere. As an example, capping of the NCs, as first decribed by Hines et al. [23] in 1996, is still in its infancy for perovskites but is a potential avenue to protect NCs in ambient conditions. Despite this degradation issue, in contrast to metal chalcogenide NCs, perovskites seem to possess a variety of physical properties that alleviate the detrimental effects of the wide variety of defects present in the structure. As such, it seems that sufficient quality perovskite NCs can easily be grown where the concentration of defects can be kept quite low, which has allowed the perovskite boom seen in the recent years without the need (yet?) of core-shell structures for surface states passivation and to alleviate interaction with the environment.

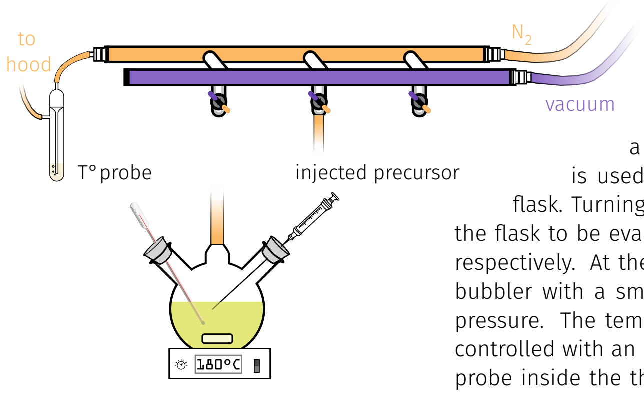

Figure 2.3 | Synthesis platform for $CsPbBr_3$ nanocrystals. The synthesis of metal halide perovskites follows standard atmosphere-controlled chemistry practices. A Schlenk line, shown here with three ports, each with a stopcock, and a dual nitrogen/vacuum manifold, is used to control the atmosphere inside the three-neck flask. Turning the stopcock to the vacuum or nitrogen line allows the flask to be evacuated or filled with an inert nitrogen atmosphere, respectively. At the output of the Schlenk line's nitrogen manifold, a bubbler with a small volume of silicon oil is placed to monitor the pressure. The temperature of the solution in the three-neck flask is controlled with an oil bath heater and monitored using a temperature probe inside the three-neck flask. For the injection, the temperature is increased to the desired temperature and the Cs-oleate is quickly added to the three-neck flask before cooling down the solution in an ice water bath.

2.1.2 Synthesis

The synthesis protocol used in this thesis to synthesise $CsPbBr_3$ NCs are based on the first-generation protocols published by Kovalenko's group [5, 24], and rely on the use of oleic acid and oleylamine as passivating ligands. It consists in two main steps: a Cs-oleate is prepared and then mixed with the Br source. The synthesis of $CsPbBr_3$ NCs used in this work was performed by Caixia Huo [1] and the author for the first part of the thesis (until November 2019) at NTU, while at LPENS synthesis was performed by the author. Let us note that while at NTU the chemistry platform was only slightly adapted to fit our synthesis needs, at LPENS the synthesis platform was put in place from scratch by the author and Zakaria Said [2] in a brand new chemistry room, thus enabling for the first time on-site synthesis of NCs at LPENS. In the following, the chemistry platform built and used to synthesize $CsPbBr_3$ NCs is presented before diving into the synthesis protocol used.

Synthesis platform

As depicted in FIG. 2.3, the platform consists in a set of three-neck flasks that are heated, magnetically stirred and can be alternatively connected to a vacuum pump or an inert gas source. The atmosphere control is achieved using a dual-manifold Schlenk line, a common apparatus for moisture-free and atmosphere-controlled chemistry, that allows us to change the atmosphere inside the flask from nitrogen gas to vacuum and back by simply turning taps (⊗).

---

[1] Visiting chemistry PhD student in Prof. Xiong's group at NTU.
[2] Fellow physics PhD student in the Nano-Optics team at LPENS.

Nitrogen At its output, the nitrogen manifold is vented to the fume hood exhaust through a bubbler for two particular reasons. First, the oil in the bubbler prevents air from coming back in the Schlenk link when the flask is re-filled from vacuum with nitrogen. Secondly, the bubbler serves as an indicator for the nitrogen flow that we tune in order to have approximately 2-3 bubbles per second, roughly corresponding to a pressure slightly larger than 1 atm.

Vacuum For the vacuum manifold, a membrane filter placed between the Schlenk line and the pump prevents contamination in both directions. At its other end, the vacuum manifold is sealed. A pressure indicator, such as a balloon, can be used to visualise the pressure in the line. Alternatively, the pressure can be probed by visualising the silicon oil level in the bubbler when re-filling the vacuumed flask with nitrogen. Indeed, the pressure imbalance causes the oil to rise in the bubbler which, in our case, serves as an indicator that the vacuum is of sufficient quality. Similarly critical, and as discussed in SEC. 2.1.1, we know that the ligands we used up to now are not optimal. However, zwitterionic ligands require large centrifugal forces on the order of 30 kg which cannot be attained with typical tabletop centrifuges at our disposal. We therefore still use the oleic acid/oleylamine pair to passivate our NCs awaiting faster centrifuges.

Synthesis protocol

For nanocubes, we use the synthesis protocol first described by [5] and later updated in [24]. It is briefly outlined here.

Preparation of the Cs-oleate (FIG. 2.4a) Caesium carbonate Cs_2CO_3, octadecene ODE and oleic acid OA are injected into a flask. The content of the flask is dried for 1 h at 120 °C and then heated under nitrogen gas to 150 °C until all the Cs_2CO_3 has reacted.

Synthesis of the nanocubes (FIG. 2.4b) ODE and $PbBr_2$ are injected into a flask and dried under vacuum for 1 h at 120 °C. Dried oleylamine OLA and dried OA are injected at 120 °C under nitrogen gas. After complete solubilisation of the lead-bromide salt, the temperature is increased to the desired synthesis temperature, in our case 180 °C-200 °C, and the Cs-oleate precursor solution is quickly added (FIG. 2.4c). The reaction mixture is then quickly cooled down in an ice water bath. In this synthesis protocol, it is the temperature at which the precursor is added rather than the growth time that determines

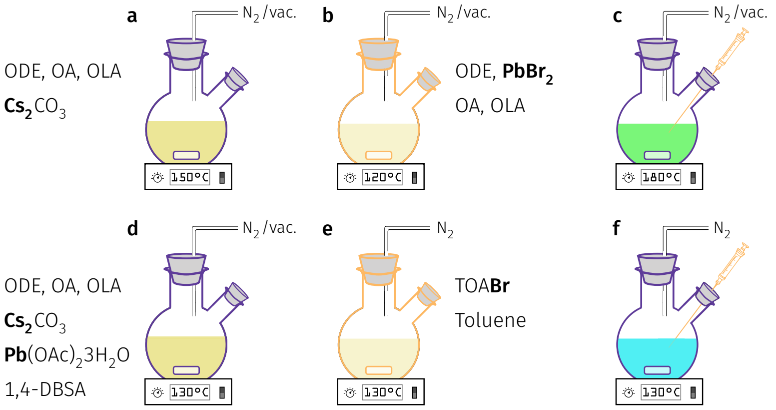

Figure 2.4 | Synthesis of CsPbBr$_3$ nanocrystals. Synthesis of CsPbBr$_3$ nanocubes **a**-**c** and nanoplatelets **d**-**f**. **a**, Reactants are dried for 1 h at 120 °C, and the contents of the flask is heated to 150 °C until all the caesium carbonate has reacted with the oleic acid. **b**, Dried octadecene, lead-bromide, oleylamine and oleic acid are heated to 120 °C until complete solubilisation of the salt. **c**, The temperature is risen to 140 °C-200 °C depending on the targeted particle size, and the Cs-oleate is quickly added. At this point, the NCs are formed and the solution shows a bright green emission under UV illumination. **d**, Reactants are dried for 1 h at 120 °C, and the contents of the flask is heated to 150 °C until all the caesium carbonate has reacted with the oleic acid. **e**, TOABr and toluene are heated to 130 °C. **f**, At this point, the NCs are formed and the solution shows a bright greenish blue emission under UV illumination.

the NCs' size. The higher the temperature is, the bigger the NCs and thus the more redshifted the emission is.

Purification and isolation The cooled down solution is then centrifugated. After two rounds of centrifugation, the supernatant is removed and the NCs are dispersed in toluene forming long-term stable solutions. The NCs can then be stored for weeks to months if kept in a concentrated solution under inert atmosphere.

After centrifugation, we use 20 nm membrane filters to filter the obtained solutions before storage.

2.2 From concentrated solutions to individual nanocrystals on a substrate

2.2.1 Solutions

Conservation techniques

Solutions should be stored away from moisture. We keep concentrated solutions in vials under nitrogen atmosphere that can be stored for a few weeks without noticeable degradation. A few weeks after synthesis however, we can observe noticeable degradation of the colloidal solution. First, the colour of the solution can be seen to shift from green or blue-green towards green-yellow. Second, but related to first, when preparing substrates for single object spectroscopy the proportion of spots corresponding to bunches of NCs increases. The degradation of the colloidal solution is thus seemingly accompanied by agglomeration and coalescence of the NCs. Diluted solutions prepared for single particle spectroscopy, on the other hand, can not be stored for such a long time most probably due to the dissolution of the protecting ligands in the solvent.

Single nanocrystals isolation

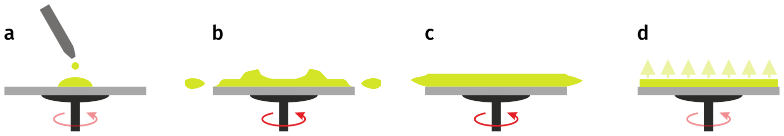

Figure 2.5 | Schematic of the spin-coating process. **a**, The solution is deposited on the substrate. **b**, The substrate accelerates and most of the solution is ejected. **c**, The substrate reaches its maximum velocity, and centrifugal force helps with the dispersion of the NCs. **d**, The solvent evaporates. Figure adapted from Wikimedia Commons, by Stefan Reich [CC0].

The solution can then be used as is for ensemble absorption and photoluminescence measurements, or spin-coated on a quartz or silicon substrate for single particle measurements. To do so, the substrate is maintained on the spinning plate during rotation and the deposited solution is uniformly spread out by the centrifugal force (Fig. 2.5a-c). The solvent used in the solution is chosen to preserve the colloidal dispersion of nanoparticles and is volatile, which enables its evaporation during the spin-coating process. The thickness of the deposited solution on the substrate is controlled by the angular speed, the acceleration, the duration of the process and also by the quantity, density, viscosity, etc. of the deposited solution. In order to get samples of different NC densities, the solution is diluted before the spin-coating. For single NC measurement, the solution is diluted around 1000 times in a mixture of toluene and 3% polystyrene (PS). The mixture is magnetically stirred and again when the dilute solution of NCs is added. The obtained solution can then be spin-coated on a substrate where the solvent will evaporate, leaving a thin film of PS. At this concentration level, the solution is spin-coated at 3000 rpm during 70 s.

2.2.2 Substrates

Substrate preparation

Dielectric substrates were cut to the desired size and sonicated in an ultrasound bath in IPA for 5 min to 10 min. Subtrates are then blow-dried and the procedure can be repeated until the substrates are clean to the eye, i.e. no dust/defects can be observed on their surface. After chemical cleaning, the thin contamination layer (impurities and contaminants) left at this point, is removed

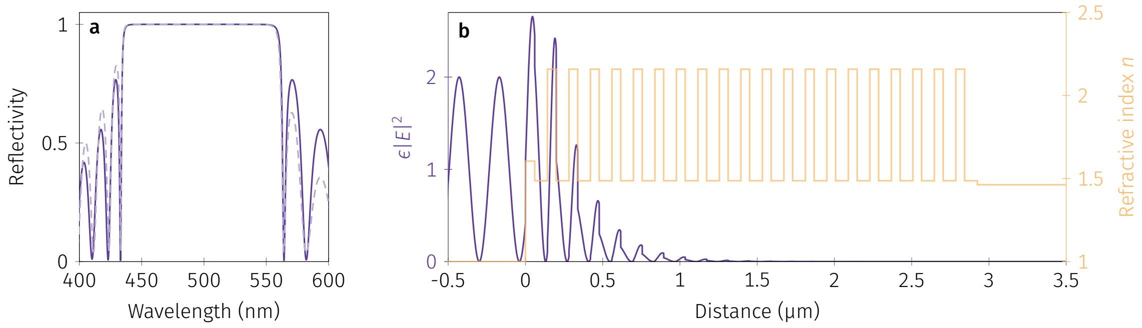

Figure 2.6 | Distributed Bragg reflector. Characteristics of the DBR used in this work. **a**, Reflectivity spectrum of the mirror in the region of interest. **b**, Electric field intensity profile along the structure. The refractive index of the structure is given as a reference.

by the exposure of the surface to the nitrogen and oxygen plasma. The substrates are then to be used as quickly as possible to minimise the surface recontamination.

Dielectric mirrors

Either SiO_2 substrates or Ta_2O_5/TiO_2 (Ta_2O_5/SiO_2) distributed Bragg reflectors with central wavelength at 490 nm (520 nm) and bandwidth of around 100 nm are used as substrates. The former were used at the beginning of the study or for room-temperature ensemble measurements, whereas the latter were used for low-temperature single-particle measurements. FIG. 2.6a shows the reflectivity of the DBR centered at 490 nm while FIG. 2.6b shows the electric field intensity profile along the structure formed by 20.5 pairs of Ta_2O_5/TiO_2 and a thin 100 nm polystyrene layer. The field intensity maximum is found to be located within the polymer layer, as expected.

Effect of the half-cavity configuration We tried to enhance the emission intensity by depositing NCs on top of a DBR. We observed an enhancement of the emission but did not study the matter in detail. Such enhancement of the collected intensity was previously observed, see e.g. [25].

Markers deposition

For single-particle measurements, highly diluted solutions of NCs are used to obtain surface densities on the order of 1 NC per μm^2. For more time-consuming measurements, such as temperature-dependent or second-order correlation measurements, where the sample inevitably drifts over time, following the same emitter over time can be laborious especially if no defects can be seen on the surface of the sample. To overcome these issues and enable reproducible localisation of single emitters, gold markers are deposited on the substrates before spin-coating.

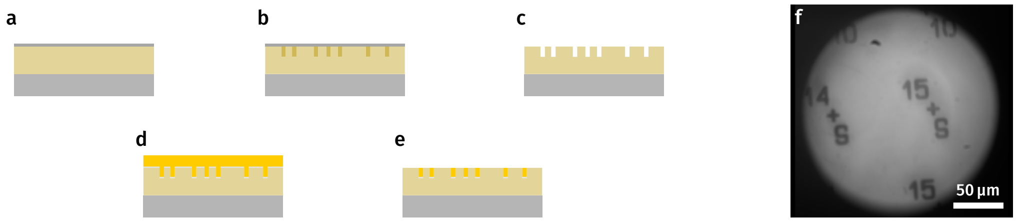

Figure 2.7 | Schematic of Au markers deposition on substrate. **a**, A 200 nm layer of PMMA is spin-coated on the substrate and a layer of transparent conductive oxide (ITO) is deposited on top to increase the conductivity of the surface and yield precise lithography. **b**, The resist is exposed with a 200 kV electron beam to form the desired pattern. The conductive layer is washed with water and the resist is then developed using a 3:1 mixture of isopropyl alcohol (IPA) and methyl isobutyl ketone (MIBK) during 1 min30 s (**c**). **d**, A thin layer (5 nm to 10 nm) of Cr is evaporated onto the structure for adhesion before evaporation of the Au layer (50 nm). **e**, The obtained sample is then washed in acetone to remove the excess metal and the desired structure is obtained. **f**, Confocal microscope image of the substrate after marker deposition.

The procedure is sketched in FIG. 2.7a-e.

2.2.3 Sample structural characterisation

Film thickness determination

As discussed above, reflective substrates are used in this study. This is to increase the luminescence collection efficiency. For a maximum increase, the emissive layer needs to be properly located. Indeed, as distances are on the order of the emission wavelength, interference effects cannot be neglected [26, 27]. Controlling the thickness of the deposited layers is thus paramount to maximise the collection efficiency of the luminescence. Atomic force microscope (AFM) studies were carried out to calibrate the thickness of the spin-coated layers, starting from the results of Walsh et al. [28] summarised in FIG. 2.8a. Samples were prepared as described above, scratched carefully using tweezers and then transferred to an AFM to determine the film thickness, taken as the average over a portion of the height step function. FIG. 2.8b shows the structures investigated in this study with NCs located in a thin layer of PS near $\lambda/4n$. After optimisation of the polymer concentration and spin-coating parameters, we managed to deposit NCs in a polymer matrix with all NCs close to $\sim \lambda/4n$ as depicted in FIG. 2.8b.

Electron microscopy

For transmission electron microscopy, a drop of a diluted solution of NCs in hexane is deposited onto a conductive TEM grid and the solvent is allowed to evaporate. Basic characterisation of NCs morphology was performed by electron microscopy. Both scanning electron microscopy (SEM) and transmission electron microscopy (TEM) were used and images were taken by Chen Bo at

NTU and Aurélie Pierret at LPENS. SEM was primarily used at LPENS to estimate the size and shape of the NCs, but because of the limited resolution precise statistics could not be obtained. For precise statistics, we use TEM and high-resolution TEM. Both methods rely on a beam of electrons but while TEM uses collimated transmitted electrons, SEM relies on a beam focused on the sample. However, for LHPs, information that can be retrieved from electron microscopy studies is limited. Polymorphs are difficult to distinguish as the small amplitudes of octahedral tilting can only be resolved via sophisticated phase-contrast imaging methods [29]. In addition, the structural lability of perovskites renders them prone to alteration by the electron beam.

In our study, we thus used electron microscopy as a basic structural characterisation tool, yielding only the distribution of sizes and aspect ratios of NCs in the sample plane. Results are presented in SEC. 3.1.

Summary

The synthesis of LHP NCs is a new process which has significantly made use of the knowledge acquired over the last thirty years on CdSe and PbS NCs. While their defect tolerance renders them easy to synthesize at a sufficiently good quality, their ionic bonding and labile surface ligation still lead to significant degradation/instability. In this section, the chemistry concepts behind the synthesis of $CsPbBr_3$ NCs were given and the synthesis and characterisation protocols used in this work were detailed.

2.3 Optical spectroscopy platform for single nanocrystals

Single nano-emitter spectroscopy is a unique tool to characterise and understand the optical properties of NCs without the complications induced by ensemble-averaging (especially for less

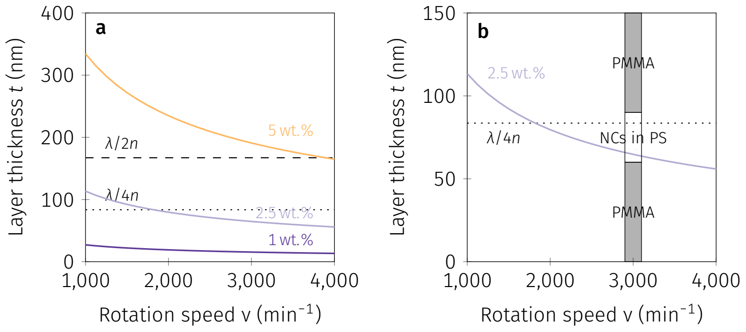

Figure 2.8 | Empirical thickness of spin-coated PMMA films. Thickness of deposited PMMA films in toluene with varying concentrations c as a function of the rotation speed of the spinning plate calculated from the expression in [28]. **a**, Film thickness for PMMA/toluene concentrations up to $c = 10$ wt.%. **b**, Close-up of (**a**) showing $\lambda/2$ and $\lambda/4$ ($\lambda = 500$ nm). (**c**) Schematic of our structure thickness as determined by AFM measurements.

monodisperse objects). The sharp spectral lines at cryogenic temperature and their spectral and temporal evolution with temperature are a direct signature of the underlying exciton fine structure and its interaction with the vibrational landscape of the emitter. They thus provide critical information to understand the physical processes at play in NCs. It also gives unique insight into properties that are not observed in ensemble experiments, such as single photon emission [30, 31], photoluminescence blinking [32–34] and spectral wandering of the spectral lines [35–38]. Depending on the time scale of the process, several investigation methods can be employed. Here, we use both steady-state (time-averaged) and time-resolved photoluminescence to probe the emission dynamics. Time-resolved photoluminescence is essential to the analysis of recombination, blinking and spectral wandering as these processes happen on time scales from ps to s, while steady-state photoluminescence is mainly limited by the detectors response from 100 µs to s. Thus in addition to giving access to the binned stream of photons, time-resolved photoluminescence gives access to the actual time distribution of the detected photons. In the context of this project, we study the optical response of single inorganic perovskite NCs that are randomly dispersed on a substrate. While we often refer to emitters as *bright*, the signal from a single NC remains very low with typical count rates of 10^3–10^6 Hz which is less than a pW. It is therefore of utmost importance to collect most of the photons emitted by the nano-object all the while minimising all other sources of unwanted radiation. This is achieved using a home-built scanning confocal microscope described hereafter. After briefly introducing the experimental platform, the theoretical basis and experimental methods of the various spectroscopy experiments performed during this work are presented and technical information is given on the analysis methods used.

2.3.1 Scanning confocal microscope

The self-built microscopes used in this work are both scanning confocal microscopes based on a steering mirror. In confocal microscopy, the excitation laser is focused close to the diffraction limit on the sample's surface by a microscope objective. If an emitter is at the focal point, its photoluminescence is collected by the same objective. As the studied NCs have a typical size of 10 nm, much smaller than their emission wavelength of 520 nm, they can be considered as point

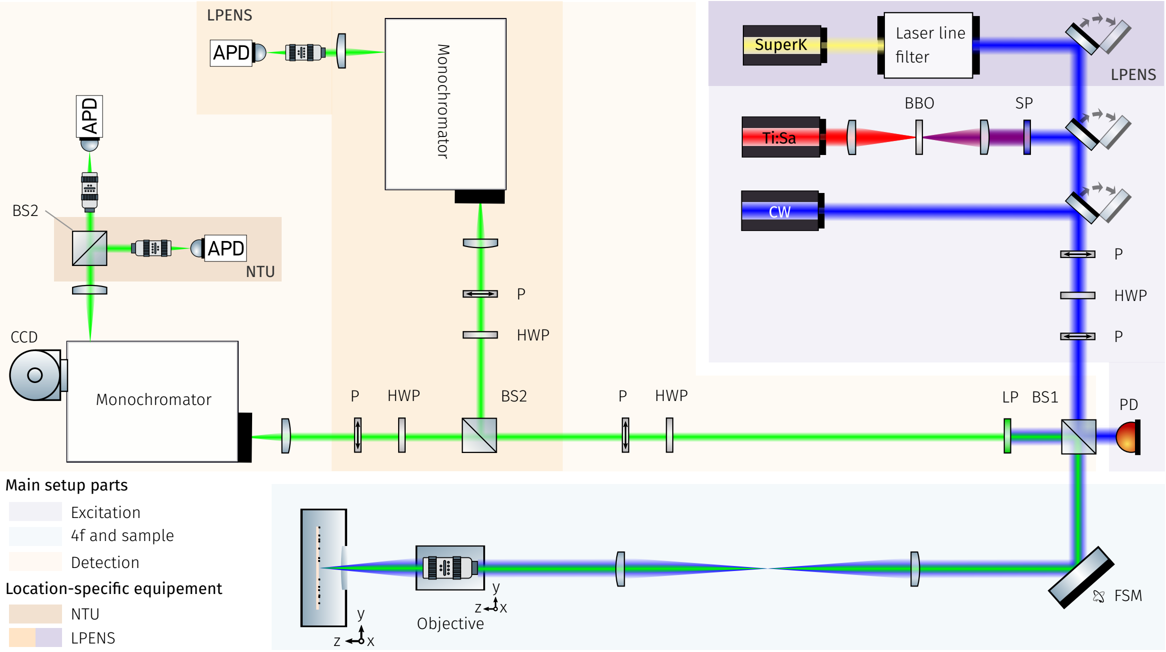

Figure 2.9 | Micro-photoluminescence setup. The top of the figure shows the excitation path. The excitation beam is directed towards the sample via transmission by a beamsplitter while the reflection is directed towards a photodiode to monitor the excitation power. After the beamsplitter, the excitation beam is directed towards the objective by a steering mirror. The sample is kept at low pressure ($5{\times}10^{-6}$mbar) in a liquid helium cryostat. The emission from the sample is collected via the same microscope objective and goes through the $4f$ setup and is directed towards the detection part of the setup. The excitation beam is discarded with a long-pass filter. Once focused at the entrance of the monochromator, the emission can be directed towards a CCD camera or two SPAD in a HBT configuration.

sources. The image of the NCs emission is therefore not a point but rather a circular Airy diffraction image with a central bright disk and concentric dark and bright fringes. Here, with the objectives used, we have excitation spot diameters on the order of 1 µm, close to the diffraction-limit. Beyond the objective, the collected emission is magnified 100× and directed to the detection setup. The beam is then focused using a lens with focal length f at the monochromator entrance. The emission is dispersed and recorded either with a CCD camera or with avalanche photodiodes. Low density samples were fabricated in order to facilitate the

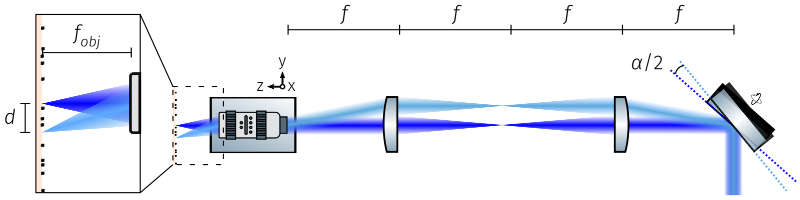

Figure 2.10 | Schematic drawing of the 4f-setup. The dark blue beam shows the reference optical axis. The light blue beam is deviated by an angle α when the mirror is rotated by an angle $\alpha/2$. The two lenses re-center the deviated beam on the objective such that the beam arrives at the optical axis with the same angle α and is focused on the sample at a distance $d = f_{obj} \tan\alpha$ from the focal point of the objective.

localisation of single emitters rather than large aggregates. At first, the localisation could easily be made manually by moving either the sample or the objective, though not in a very precise manner due to coarse actuators. In addition, a small drift could be observed after movement which hindered reproducible localisation of emitters. The implementation of a fast steering mirror (FSM) in a 4f-configuration solves these problems. It allows us to scan the sample over large areas (200 µm × 200 µm) without touching the sample nor the objective, and it frees us from hysteresis effects observed with piezoelectric actuators. If the mirror is rotated by an angle $\alpha/2$, i.e. the beam incidence angle is changed by $\alpha/2$, then the focused beam is shifted on the sample by a distance $d = f_0 \tan\alpha$, where f_0 is the focal length of the focus lens (FIG. 2.10). The steering mirror can be rotated around two axes (vertical and horizontal) by tuning the applied voltage with a response of $2.62\,\mathrm{mrad\,V^{-1}}$, a resolution of 1 µrad and a repeatability of 3 µrad[3]. The setup shown in FIG. 2.10 has the advantage that at whatever angle α the collimated beam comes on the steering mirror, it will arrive centred on the objective with the same angle α. Moreover, the emission path, which is the same as the excitation until the separation beam splitter, BS_1, will not be affected by the change of the mirror angle α after the reflection and can be directed towards the monochromator.

Monochromator All monochromators used in this work are Czerny-Turner type monochromators comprised of diffraction gratings mounted on a rotating turret and two parabolic mirrors. Emission from the source is focused at the entrance of the monochromator by a lens. Once inside the monochromator, the beam is collimated by the first curved mirror, impinges on the diffraction grating, is dispersed and directed towards the second curved mirror which focuses the beam in the output ports. Depending on the output port, there are two ways to measure the spectrum of a source with a grating spectrometer. Either the spectrometer is used with a CCD camera and the full dispersed beam is imaged, or it can be used as a monochromator and the emission is detected by an APD after spectral filtering by the monochromator output slit.

Resolution Our excitation spot size is on the order of 1 µm. It is this size that determines our spatial resolution. The full width at half maximum of a photoluminescence spatial scan is given by the convolution of the excitation spot size and the size of the emitter. Since single nanoemitters, with sizes on the order of 10 nm, can be considered as point sources, the

---

[3] Newport FSM-300-01, User Manual

photoluminescence spatial intensity profile of a single nanoemitter would show a full width at half maximum revealing only the width of the excitation spot size. The single NCs' emission is detected after a monochromator. It is the characteristics of the monochromator together with the detector that determine the spectral resolution of our setup. When using the CCD camera as a detector, the lower bound of the spectral resolution is given by the pixel width. Conversely, when using the SPAD as detectors, it is the monochromator exit slit width that determines our resolution. With our setup, the minimum bin width, i.e. spectral resolution, both with the CCD and the SPAD is, due to the similar size of pixels, of:

- 180 μeV at 2.4 eV (0.039 nm at 515 nm) at NTU
- 60 μeV at 2.4 eV (0.012 nm at 515 nm) at LPENS

Excitation sources Excitation was provided either by a 457 nm or 448 nm continuous wave (CW) diode laser or by a tunable pulsed Ti:Sa laser. Pulsed excitation in the visible range is obtained by second-harmonic generation of the Ti:Sa laser[4] (700 nm to 1000 nm) with a repetition rate of 80 MHz. Second-harmonic generation is achieved using a barium borate (BBO) crystal providing a tunable above band-gap pulsed excitation between 400 nm and 500 nm. Pulsed excitation in the visible range was also obtained by filtering a super-continuum source.

Interfacing Both at NTU and LPENS, custom software was built by the author to interface all setup devices and perform experiments. At minimum, at NTU, 5 devices were interfaced: steering mirror, shutter, polariser, monochromator, detector. At LPENS, a total of 17 individual devices were interfaced: laser, cryostat, 6 piezoelectric positioners, steering mirror, shutter, 3 polarisers, 2 monochromators and 2 detectors. `CARODOT Manip` is the custom software built by the author at LPENS and available online: software and documentation. With this software, experiments can be performed automatically and all available experimental details from devices are automagically saved together with the data. Comments can be added during experiments and later saved with the current experiment data.

---

[4] Mai Tai HP, Spectra-Physics

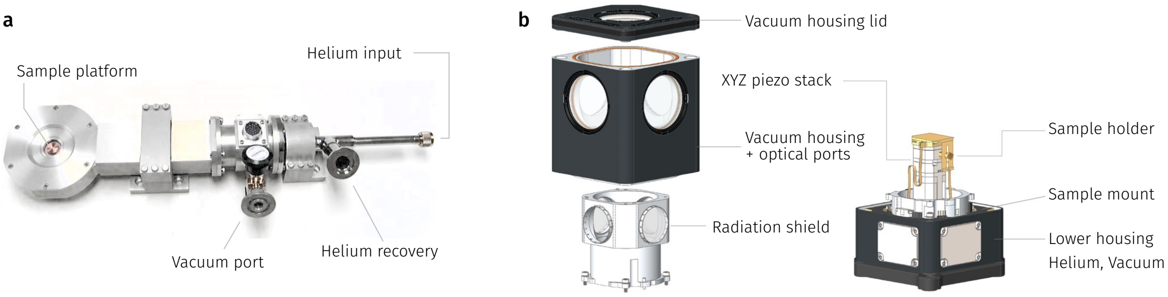

Figure 2.11 | Cryogenic platform. Schematic of the two cryostats used in this work: **a**, an open-cycle and **b**, a closed-cycle cryostat. **a**, The sample holder is mounted on top of the cold finger. **b**, The sample holder stage is mounted on a 3-axis piezo stack with the sample holder put on gallows enabling easy insertion or removal of the sample holder. The sample holder is thus perpendicular to the optical axis and the sample can be optically addressed from one of side windows.

Cryogenic temperatures To study the discrete fine structure emission spectrum of single NCs, linewidth broadening must be reduced to a minimum which requires us to work at cryogenic temperatures. To do so, our samples were first placed in an open-cycle (OC) helium flow cryostat with a nominal temperature of 4.2 K. The OC cryostat is a continuous flow cryostat which does not have a helium tank. It requires liquid helium to be provided from a helium tank via a transfer line and brought in contact with the sample heat exchanger. The vaporised helium is then recovered in the build helium recovery lines to be recompressed later. The helium flow is controlled using a valve on the transfer line. A thermometer, placed next to the sample together with a resistance allow us to vary the sample temperature from 4.2 K up to room temperature with a feedback loop for temperature stabilisation.

Sample position control When using the OC cryostat where nanopositioners could not be fitted, a heavy duty translation stage was used to move the entire cryostat arm in order to move the sample with respect to the microscope objective. In the latest version of the optical setup, the sample is mounted on a 3-axis stack of nanopositioners each with a full range of around 2 mm each. For ease of use, the sample is mounted on a cylindrical sample holder which can be tightened to the cryostat and removed. Using the full stack of piezos, the lowest temperature that can be reached is above 7 K.

Number of excitons At the typical average excitation power used in our experiments, from a few tens of nW to a few tens of μW, continous and pulsed excitations can yield drastically different exciton populations and thus photophysics [39]. From the fluence F, we can now determine the number of absorbed photons as $F\sigma_{\mathrm{abs}}/E_{\mathrm{photon}}$, where σ_{abs} is the absorption cross section and E_{photon} is the energy of the absorbed photon. As each photon absorption event yields the generation of an electron-hole pair, this directly corresponds to the number of excitons created in a NC. Assuming the spatial distribution of the excitation spot size is gaussian, the number of excitons created in the NCs is given by:

$$\langle N \rangle = \ln 2 \frac{P_{\mathrm{av}}\tau_{\mathrm{char}}}{E_{\mathrm{photon}}} \frac{\sigma_{\mathrm{abs}}}{\pi r_0^2} \tag{2.1}$$

where τ_{char} is either the inverse of the repetition rate t_{rep} or the photoluminescence rate τ, under pulsed and continuous excitation respectively. From the expressions of the beam intensity profile, we can determine the corresponding pumping rates. Writing directly the pumping rate as a function of experimental parameters

$$W = \frac{\sigma I}{\hbar\omega_{\mathrm{exc}}} = \frac{\sigma}{\hbar\omega} \frac{10^{-6}\, P(\mu\mathrm{W})}{\pi \left[10^{-4}\, r(\mu\mathrm{m})\right]^2} \tag{2.2}$$

2.3.2 Steady-state photoluminescence

We use the excitation sources described in the previous pages to optically probe the optical response of our NCs. Following excitation of an allowed optical transition, a photon is absorbed, annihilated and converted into an electron-hole pair. The absorption spectrum, i.e. the absorbed intensity as a function of excitation wavelength, thus provides invaluable information about the optically-active transitions in particular higher-lying transitions. We perform absorption measurements on solutions of synthesis products in combination with the structural characterisation described in Sec. 2.2.3. We focus on processes following above band-gap excitation of single NCs, namely the spontaneous emission of photons with energy E_{em} following the relaxation of an excited electron-hole pair. This pair is photoexcited at an energy E_{exc}, thus emission is referred to as photoluminescence. There are two energies at play in the actual emission spectrum, i.e. the emitted intensity as a function of photon energy, the excitation energy E_{exc} and the emission energy E_{em}. In photoluminescence measurements, the E_{exc} is kept fixed while the spectral power density of the source is recorded. In photoluminescence excitation measurements, the spectral power density of the source is recorded while varying E_{exc}, thus probing not only the absorption process but also excited pair relaxation and recombination. Another way to probe excited pair relaxation is to perform excitation power dependent photoluminescence measurements thus effectively varying the number of pairs injected. Information about the high carrier concentration regime can be obtained. The orientation of the optical transition dipole, and thus the orientation of the NCs, can also be probed directly by monitoring the polarisation of the emitted spectral lines [40, 41]. As single NC spectroscopy requires samples with low NC surface density, typically lower than 1 μm^{-2}, mapping techniques are used to find emitters. Photoluminescence mapping is performed using the steering mirror in a 4f configuration allowing for areas as large as 200 µm × 200 µm to be scanned without moving the sample or the microscope objective.

Photoluminescence mapping At the basis of all our experiments is the localisation of single nano-emitters dispersed on a substrate. This is achieved by mapping the photoluminescence intensity of the sample using a weakly dispersive grating set around the median emission energy. Using the steering mirror in a 4f configuration described in 2.3.1, we can move the excitation beam across the sample and collect the corresponding emission if any. Examples are given in SEC.

Polarisation-resolved photoluminescence To measure the polarisation of the emission from the bright triplet exciton, we use a set of half-waveplate and polariser placed in front of the detection channel. The polariser is fixed along the monochromator's preferential polarisation axis and a half-waveplate is rotated before the polariser to analyse the emission. With the following technique, we truly measure the polarisation of the emission rather than its convolution with the detection setup response. This is exactly equivalent to rotating a polariser in front of a polarisation-response balanced detector with the only difference being that polarisation rotates twice as fast with the half waveplate.

2.3.3 Time-resolved photoluminescence

As already discussed, single particle spectroscopy is a powerful tool to study systems in the nanoscale via the information encoded in the emitted photon stream. Furthermore, the optical properties of single NCs also fluctuate in time and can be inferred by the careful study of the emitted photons and the temporal dynamics of the emission at different timescales. The most commonly used technique to this end is to record the emission intensity and its fluctuations with a spectrally resolved detector, usually a CCD. It is a useful tool for timescales greater than a few ms and has the advantage of providing spectral information. However, it is intrinsically a binning process, and as such, it does not provide the exact arrival time of the detected photons with respect to the excitation of the emitter nor can it provide the distribution of arrival times of the detected photons. Here, we briefly present time-correlated single photon counting, and how it can give access to information that would otherwise be unattainable simply using even the fastest detectors available with no correlation.

Time-correlated single photon counting can be used to determine the fluorescence lifetimes of emitters. Ideally, this could be done with a single excitation cycle, however the response time of the detectors would limit such measurement to very long fluorescence decays. Indeed, the dead time of a single SPAD is of 77 ns. To record the fluorescence decay of rapidly decaying emitters, the measurement needs to be repeated over many excitation cycles. As can be seen in FIG. 2.12a, this time-resolved mode consists in measuring the time delays between the excitation of the sample and the arrival times of the emitted photons. It requires a fast photodiode able to record the detection times of a pulsed laser in the MHz-regime and used as a 'start'. The detection of the subsequent single photon event by the SPAD defines the 'stop', and the delay time between these two signals is recorded. This process is repeated over many excitation cycles and the delay times are sorted in a histogram, shown in FIG. 2.12b, representing the occurrences of detected photons over delay times following the excitation pulse. This histogram provides valuable information in that it displays the time decay of the emission and enables the determination of the lifetime of emissive states. The SPAD used in this configuration allows for the measurement of time delays as small as a few ps. The total *real* decay curve is composed of a sum of N exponentials whose analytical expression can be determined using the system's rate equations, and reads

$$I_{\text{th}}(t) = \sum_{i}^{N} A_i e^{-t/\tau_i}$$

Further considering that even a Dirac delta excitation pulse would lead to a response with finite width due to the physics of the optical detection process, we use the re-convolution method to fit the measured data curves with a convolution of the analytical expression given above and the

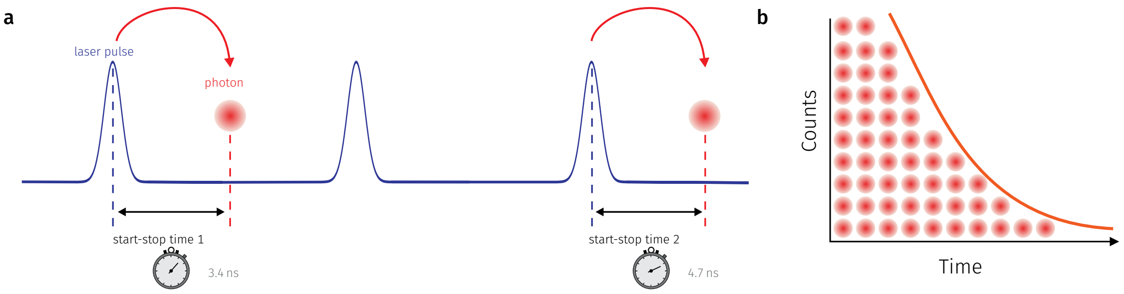

Figure 2.12 | Schematics of time-correlation single photon couting experiments. **a**, Schematic of a time-resolved fluorescence measurement. The start-stop times, time-delay between the laser pulse and detected photon, are recorded over multiple excitation cycles with a pulsed laser and represented as **b** a histogram of arrival times. Panels adapted from ref. [42].

instrument response function (IRF) as

$$I_{\mathrm{exp}}(t) = I_{\mathrm{bkg}} + IRF(t - t_0) \times \sum_{i}^{N} A_i e^{-(t-t_0)/\tau_i}$$

Resolution The finite width of the response is characterised by the IRF which takes into account all possible broadening mechanisms: optical dispersion, detector response, electronics...The full timing uncertainty $\Delta\sigma_{\mathrm{tot}}$ is therefore given by

$$\Delta\sigma_{\mathrm{tot}} = \sqrt{\Delta\sigma_{\mathrm{opt}}^2 + \Delta\sigma_{\mathrm{det}}^2 + \Delta\sigma_{\mathrm{elec}}^2}$$

$\Delta\sigma_{\mathrm{opt}}$ is negligible such that total response is overwhelmingly given by the detectors and electronics. To characterise the full response of the detection setup, we send attenuated fs laser pulses to the detectors and record the obtained decays.

Non-resonant excitation In addition to the IRF, we should take into account the non-resonant excitation used. To better fit the rise of the decays, we allow for a short rise time $\lesssim$ 10 ps. Considering the excitation is done non-resonantly at $\sim$ 250 meV above the emission, this means that we have a typical cooling rate of $\gtrsim$ 25 meV ps^{-1}. To compare to GaAs where the cooling rate for excess energies larger than the LO phonon energy is much faster and $\leq$ 1 eV ps^{-1} [43]. The implications of non-resonant excitation on the decays are discussed in detail in Sec. A.2.1.

2.3.4 Intensity correlations: Hanbury Brown and Twiss experiment

In this section, we present the single-photon interferometry experiments performed during this thesis. In principle, measuring the photon arrival distribution would be as simple as recording the arrival time and building a histogram with the delay times between the detected photons. However, due to practical limitations in the response time of detectors, the minimum measurable time-difference would be limited by the detector dead time ($\sim$ 77 ns), hiding any processes happening at smaller time scales. Moreover, the results obtained in such a manner would be skewed as all the photons impinging on the detector during its "off" period would not contribute to the time-delay calculation. An alternative is to use the setup initially proposed by Hanbury Brown and Twiss to measure the angular diameter of stars [44, 45] applied to quantum light [46, 47]. This experiment is essentially an intensity interferometer, of which we explain the workings hereafter. The stream of photons emerging from the source is directed towards a 50:50 beamsplitter and the two resulting outputs are directed to photon-counting detectors (Fig. 2.13). The electrical pulses generated in the detectors are directed to a system of correlation electronics. The electronics record the time separating the pulses generated in the two detectors all the while recording the number of pulses. The result of such an experiment is typically a histogram of the number of counts as a function of the time interval. Experimentally, to measure the autocorrelation function, a HBT setup, shown schematically in Fig. 2.13 is used.

Figure 2.13 | Hanbury Brown and Twiss interferometer. Schematic of a HBT interferometer. The stream of photons incoming from the right goes through a 50:50 beamsplitter and each arm is focused on a SPAD with a microscope objective. The SPAD are connected to a TCSPC module (PicoHarp 300).

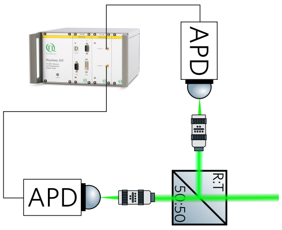

In the following, we discuss the expected disparity between continuous and pulsed excitation second-order correlation measurements. In particular, we highlight their different requirements in terms of single-to-noise ratios.

Let us estimate the integration time T_{acq} needed to obtain a number of coincidences N_{12} within a characteristic time window. This estimation also enables us to normalise the raw coincidences $c(\tau)$ to obtain the second-order correlation $g^2(\tau)$ with a normalisation that does not depend on the chosen time interval of interest.

$$g^2_{\text{norm.}}(\tau) = \frac{c(\tau)}{g^2(\infty)} \tag{2.3}$$

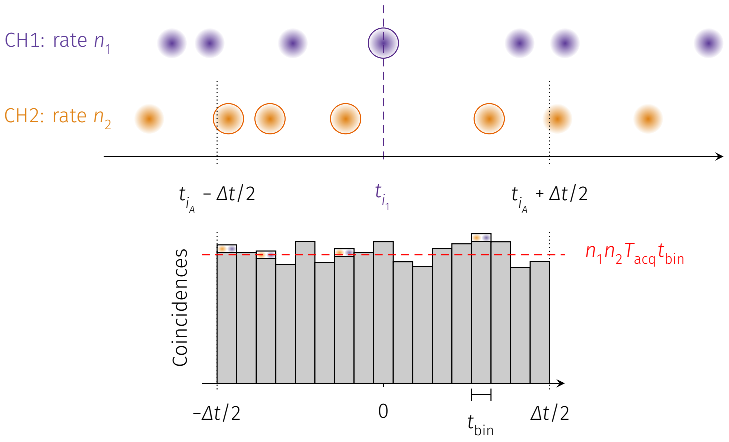

Figure 2.14 | Second-order correlation function measurement from a photon stream. Schematic of time-tagged time-resolved single photon measurement data. Coincident events within a time window Δt are recovered by going through the stream of photon events in CH1 of duration T_{acq} and applying the procedure sketched here. All coincidence events within the time window are then binned with a bin width t_{bin} yielding the correlation histogram $c(\tau)$. The second-order correlation function is directly given by $g^2(\tau) = c(\tau)/(n_1 n_2 T_{acq} t_{bin})$.

Estimations are provided for both continuous and pulsed excitation second-order intensity correlation measurements.

Coincidences estimation

With the help of FIG. 2.14, we can estimate the total number of pairs of photons, one from each channel, that can be created from the two channels. Assuming a total of N_1 (N_2) independent events in channel 1 (resp. 2) for a measurement time T_{acq} and a correlation window of Δt, we have a total number of coincidences N_{12} given by:

$$N_{12}(\Delta t, T_{acq}) = N_1 N_2 \frac{\Delta t}{T_{acq}} = n_1 n_2 T_{acq} T_{acq} \frac{\Delta t}{T_{acq}} = n_1 n_2 T_{acq} \Delta t \tag{2.4}$$

where we have introduced the average rates per channel i as $n_i = N_i / T_{acq}$. This expression refers to the total number of coincidences recovered from a time-tagged time-resolved experiment, searching for coincidences within the characteristic Δt time window best suited for the experiment. This characteristic time window depends on the excitation type. In the following, we investigate the dependence of this optimal Δt on the excitation scheme.

Continuous excitation In the case of CW excitation, electron-hole pairs are created continuously and recombine with a characteristic decay time τ_X which gives an upper limit to the number of generated photons per unit time $1/\tau_X$. For an adequate sampling, enabling the observation and analysis of the potential antibunching signal, the characteristic time bin should be chosen such that $t_{bin}^{CW} \leq \tau_X/10 \sim 10$ ps and therefore

$$N_{12}^{CW} = n_1 n_2 \frac{\tau_X}{10} T_{acq}$$

Pulsed excitation Under excitation by laser pulses, electron-hole pairs are created by pulses with a characteristic frequency $\nu_{\mathrm{rep}} = 1/t_{\mathrm{rep}}$, such that the characteristic time bin is given by $t_{\mathrm{bin}}^{\mathrm{P}} = t_{\mathrm{rep}}$. The laser pulses are typically 130 fs long, which compared to the characteristic decay time τ_X entails that the NC is excited at most once per pulse, i.e. at most one photon can be detected per t_{rep}. We thus have

$$N_{12}^{\mathrm{P}} = n_1 n_2 t_{\mathrm{rep}} T_{\mathrm{acq}}$$

Furthermore, to determine an acquisition time, we set a minimum requirement on the minimum coincidence counts within the obtained histogram. Within a time bin, we demand that $N_{\mathrm{c}} \geq 5\sqrt{N_{\mathrm{c}}}$ for significance. The equality is verified for $N_{\mathrm{c}} = 25$ which we set as a minium target for our experiments. We can thus finally estimate typical acquisition times. For count rates on the order of $n_1 = n_2 = 10^4\,\mathrm{s}^{-1}$ and $\tau_X/10 = 10\,\mathrm{ps}$, we have under continuous excitation

$$T_{\mathrm{acq},CW} = \frac{25}{\left(10^4\,\mathrm{s}^{-1}\right)^2 10\,\mathrm{ps}} = 25\,000\,\mathrm{s} \sim 6.9\,\mathrm{h}$$

while the weaker signals under pulsed excitation $n_1 = n_2 = 2 \times 10^3\,\mathrm{s}^{-1}$ and $t_{\mathrm{rep}} \sim 12.5$ ns give us

$$T_{\mathrm{acq},P} = \frac{25}{\left(2 \times 10^3\,\mathrm{s}^{-1}\right)^2 12.5\,\mathrm{ns}} = 500\,\mathrm{s}$$

So we have a ratio $T_{\mathrm{acq},CW}/T_{\mathrm{acq},P} \sim 50$, directly related to the ratio between the source decay time and excitation repetition rate, as well as the different count rates in typical experimental conditions, i.e. spectrally resolving a single emission line of a single NC spectrum.

Conclusion

In this chapter, we have described the chemistry platforms and scanning confocal microscopes built at NTU and LPENS and that enabled us to study single $CsPbBr_3$ NCs. We have presented the synthesis of LHPs in general, and have focused on the synthesis protocols used in this work to synthesise $CsPbBr_3$ NCs. The scanning confocal microscopes, built from scratch for this project, and designed to perform automated micro-photoluminescence experiments at the single object level have also been presented. In particular, we have presented the spectroscopic experiments performed in this work and time-resolved sngle-photon counting experiments.

References for Chapter 2

[1] Q. A. Akkerman et al., “Nearly Monodisperse Insulator Cs_4PbX_6 (X = Cl, Br, I) Nanocrystals, Their Mixed Halide Compositions, and Their Transformation into $CsPbX_3$ Nanocrystals”, Nano Letters **17**, 1924–1930 (2017) (p. 63).

[2] Q. A. Akkerman et al., “Zero-Dimensional Cesium Lead Halides: History, Properties, and Challenges”, The Journal of Physical Chemistry Letters **9**, 2326–2337 (2018) (pp. 63, 66).

[3] Z. Qin et al., “Revealing the Origin of Luminescence Center in 0D Cs_4PbBr_6 Perovskite”, Chemistry of Materials **31**, 9098–9104 (2019) (p. 63).

[4] G. Li et al., “Shape and phase evolution from $CsPbBr_3$ perovskite nanocubes to tetragonal $CsPb_2Br_5$ nanosheets with an indirect bandgap”, Chemical Communications **52**, 11296–11299 (2016) (p. 63).

[5] L. Protesescu et al., “Nanocrystals of Cesium Lead Halide Perovskites ($CsPbX_3$, X = Cl, Br, and I): Novel Optoelectronic Materials Showing Bright Emission with Wide Color Gamut”, Nano Letters **15**, 3692–3696 (2015) (pp. 64, 68, 69).

[6] I. Lignos et al., “Synthesis of Cesium Lead Halide Perovskite Nanocrystals in a Droplet-Based Microfluidic Platform: Fast Parametric Space Mapping”, Nano Letters **16**, 1869–1877 (2016) (p. 64).

[7] Y. Bekenstein et al., “Highly Luminescent Colloidal Nanoplates of Perovskite Cesium Lead Halide and Their Oriented Assemblies”, Journal of the American Chemical Society **137**, 16008–16011 (2015) (p. 64).

[8] Q. A. Akkerman et al., “Tuning the Optical Properties of Cesium Lead Halide Perovskite Nanocrystals by Anion Exchange Reactions”, Journal of the American Chemical Society **137**, 10276–10281 (2015) (p. 64).

[9] C. B. Murray et al., “Synthesis and characterization of nearly monodisperse CdE (E = sulfur, selenium, tellurium) semiconductor nanocrystallites”, Journal of the American Chemical Society **115**, 8706–8715 (1993) (p. 64).

[10] C. B. Murray et al., “Synthesis and Characterization of Monodisperse Nanocrystals and Close-Packed Nanocrystal Assemblies”, Annual Review of Materials Science **30**, 545–610 (2000) (p. 64).

[11] J. C. Sadighian et al., “Just Scratching the Surface: *In Situ* and Surface-Specific Characterization of Perovskite Nanocrystal Growth”, The Journal of Physical Chemistry C **125**, 20772–20782 (2021) (p. 64).

[12] V. K. LaMer et al., “Theory, Production and Mechanism of Formation of Monodispersed Hydrosols”, Journal of the American Chemical Society **72**, 4847–4854 (1950) (p. 64).

[13] T. Udayabhaskararao et al., “Nucleation, Growth, and Structural Transformations of Perovskite Nanocrystals”, Chemistry of Materials **29**, 1302–1308 (2017) (p. 64).

[14] J. De Roo et al., “Highly Dynamic Ligand Binding and Light Absorption Coefficient of Cesium Lead Bromide Perovskite Nanocrystals”, ACS Nano **10**, 2071–2081 (2016) (pp. 65, 66).

[15] J. Kang et al., “High Defect Tolerance in Lead Halide Perovskite $CsPbBr_3$”, The Journal of Physical Chemistry Letters **8**, 489–493 (2017) (p. 65).

[16] X. Zhang et al., “Defect tolerance in halide perovskites: A first-principles perspective”, Journal of Applied Physics **131**, 090901 (2022) (p. 65).

[17] V. K. Ravi et al., “Origin of the Substitution Mechanism for the Binding of Organic Ligands on the Surface of $CsPbBr_3$ Perovskite Nanocubes”, The Journal of Physical Chemistry Letters **8**, 4988–4994 (2017) (pp. 65, 66).

[18] G. Almeida et al., “Resurfacing halide perovskite nanocrystals”, Science **364**, 833–834 (2019) (p. 66).

[19] F. Krieg et al., “Colloidal $CsPbX_3$ (X = Cl, Br, I) Nanocrystals 2.0: Zwitterionic Capping Ligands for Improved Durability and Stability”, ACS Energy Letters **3**, 641–646 (2018) (p. 66).

[20] F. Krieg et al., “Stable Ultraconcentrated and Ultradilute Colloids of $CsPbX_3$ (X = Cl, Br) Nanocrystals Using Natural Lecithin as a Capping Ligand”, Journal of the American Chemical Society **141**, 19839–19849 (2019) (p. 66).

[21] H. Utzat et al., “Coherent single-photon emission from colloidal lead halide perovskite quantum dots”, Science **363**, 1068–1072 (2019) (p. 66).

[22] F. Krieg et al., “Monodisperse Long-Chain Sulfobetaine-Capped $CsPbBr_3$ Nanocrystals and Their Superfluorescent Assemblies”, ACS Central Science **7**, 135–144 (2021) (p. 67).

[23] M. A. Hines et al., “Synthesis and Characterization of Strongly Luminescing ZnS-Capped CdSe Nanocrystals”, The Journal of Physical Chemistry **100**, 468–471 (1996) (p. 67).

[24] M. A. Becker et al., “Bright triplet excitons in caesium lead halide perovskites”, Nature **553**, 189–193 (2018) (pp. 68, 69).

[25] S. Carayon, “Propriétés de fluorescence de nanocristaux de semiconducteurs ii-vi”, Doctoral Thesis (Université Joseph-Fourier - Grenoble I, 2005) (p. 72).

[26] H. Bücher et al., “Controlled Transfer of Excitation Energy Through Thin Layers”, Molecular Crystals **2**, 199–230 (1967) (p. 73).

[27] K. Drexhage, “Influence of a dielectric interface on fluorescence decay time”, Journal of Luminescence **1–2**, 693–701 (1970) (p. 73).

[28] C. B. Walsh et al., “Ultrathin PMMA films spin-coated from toluene solutions”, Thin Solid Films **429**, 71–76 (2003) (pp. 73, 74).

[29] Y. Yu et al., “Atomic Resolution Imaging of Halide Perovskites”, Nano Letters **16**, 7530–7535 (2016) (p. 74).

[30] P. Michler et al., “Quantum correlation among photons from a single quantum dot at room temperature”, Nature **406**, 968–970 (2000) (p. 75).

[31] B. Lounis et al., “Photon antibunching in single CdSe/ZnS quantum dot fluorescence”, Chemical Physics Letters **329**, 399–404 (2000) (p. 75).

[32] M. Nirmal et al., “Fluorescence intermittency in single cadmium selenide nanocrystals”, Nature **383**, 802–804 (1996) (p. 75).

[33] M. Kuno et al., ““On”/“off” fluorescence intermittency of single semiconductor quantum dots”, The Journal of Chemical Physics **115**, 1028–1040 (2001) (p. 75).

[34] P. Frantsuzov et al., “Universal emission intermittency in quantum dots, nanorods and nanowires”, Nature Physics **4**, 519–522 (2008) (p. 75).

[35] S. A. Blanton et al., “Photoluminescence wandering in single CdSe nanocrystals”, Applied Physics Letters **69**, 3905–3907 (1996) (p. 75).

[36] S. A. Empedocles, “Quantum-Confined Stark Effect in Single CdSe Nanocrystallite Quantum Dots”, Science **278**, 2114–2117 (1997) (p. 75).

[37] S. A. Empedocles et al., “Influence of Spectral Diffusion on the Line Shapes of Single CdSe Nanocrystallite Quantum Dots”, The Journal of Physical Chemistry B **103**, 1826–1830 (1999) (p. 75).

[38] R. G. Neuhauser et al., “Correlation between Fluorescence Intermittency and Spectral Diffusion in Single Semiconductor Quantum Dots”, Physical Review Letters **85**, 3301 (2000) (p. 75).

[39] J. A. Smyder et al., “The influence of continuous vs. pulsed laser excitation on single quantum dot photophysics”, Physical Chemistry Chemical Physics **16**, 25723–25728 (2014) (p. 79).

[40] S. A. Empedocles et al., “Three-dimensional orientation measurements of symmetric single chromophores using polarization microscopy”, Nature **399**, 126–130 (1999) (p. 81).

[41] T. Ha et al., “Polarization Spectroscopy of Single Fluorescent Molecules”, The Journal of Physical Chemistry B **103**, 6839–6850 (1999) (p. 81).

[42] M. Wahl, “Time-Correlated Single Photon Counting”, PicoQuant Technical Notes, 14 (2014) (p. 83).

[43] M. Bernardi et al., “Ab initio study of hot electrons in GaAs”, Proceedings of the National Academy of Sciences **112**, 5291–5296 (2015) (p. 83).

[44] R. Hanbury Brown et al., “A new type of interferometer for use in radio astronomy”, The London, Edinburgh, and Dublin Philosophical Magazine and Journal of Science **45**, 663–682 (1954) (p. 84).

[45] R. Hanbury Brown et al., “A Test of a New Type of Stellar Interferometer on Sirius”, Nature **178**, 1046–1048 (1956) (p. 84).

[46] R. Hanbury Brown et al., “Interferometry of the intensity fluctuations in light - I. Basic theory: the correlation between photons in coherent beams of radiation”, Proc. R. Soc. Lond. A **242**, 300–324 (1957) (p. 84).

[47] R. Hanbury Brown et al., “Interferometry of the intensity fluctuations in light. II. An experimental test of the theory for partially coherent light”, Proc. R. Soc. Lond. A **243**, 291–319 (1958) (p. 84).

3

Spectral fingerprint of single $CsPbBr_3$ nanocrystals

Perovksite NCs are a new class of low-dimensional semiconductors that exhibit a bright and narrow emission at room temperature compared to established semiconductors. In this context, the band-edge electronic structure of LHP NCs has been the subject of intense debate in the past years. In particular, to explain the outstanding properties of LHPs, it was hypothesised that the bright exciton state could lie below the dark state. Much debate ensued over the relevant contributions to the energy of band-edge exciton states.

To understand the photophysical properties of these emitters, access to the sharp atomic-like spectral emission lines is paramount and yields direct information about the band-edge states involved in the recombination process. To do so, both ensemble-averaging effects and homogeneous broadening need to be minimised which is achieved with cryogenic temperature single NC studies. However, at the single object level, due to the dispersion in size and shape, the different local environments and degree of passivation of each NC significant differences may arise between different single NCs. Therefore, to reveal the underlying dependencies that lead to the observed spectra, observation of a high number of NCs is required.

In this work, we provide a comprehensive study of the optical properties of single $CsPbBr_3$ NCs at cryogenic temperatures. We start with the structural characterisation of the synthesised NCs and their ensemble properties in solution. We then describe how individual NCs are identified and provide a detailed study of the fine structure of the emission. Namely, we identify emission of the bright triplet exciton, the trion and biexciton states together with their respective optical phonon replica. Doing so, we reveal the size-dependence of single $CsPbBr_3$ NCs spectra over a

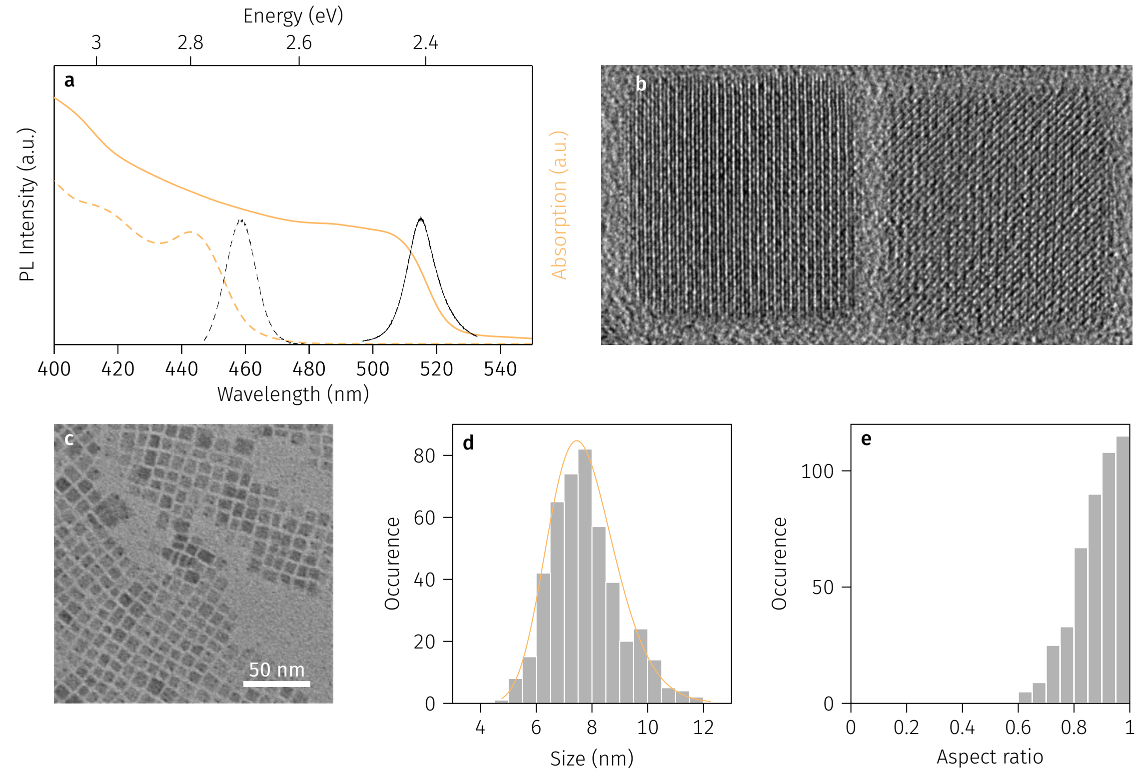

Figure 3.1 | Optical and structural characterisation at NTU. **a**, PL and absorption spectra of: (solid) weakly confined $CsPbBr_3$ NCs and (dashed) strongly confined $CsPbBr_3$ NCs. **b**, Transmission electron micrograph of two large NCs neighbours of the same size close to 17 nm but with different orientations. **c**, Transmission electron micrograph of the solution synthesised at NTU and **d**, size histogram revealing an edge length of 7.7 ± 1.2 nm with 70% of NCs bigger than the exciton Bohr diameter. **e**, Aspect ratio histogram showing a mean of 0.89 ± 0.08. Nanocrystals in **b** are from another synthesis that **c-e** and are shown for illustration purposes.

wide range of sizes.

3.1 Structural characterisation and ensemble characterisation

We can characterise the PL and absorption spectra of the solutions to gain information about the size of the obtained NCs. Using electron microscopy, detailed statistics about the size and shape of the NCs is obtained.

At NTU

The colloidal $CsPbBr_3$ NCs investigated in this work were synthesised as detailed in SEC. 2.1. FIG. 3.1a shows their solution PL and absorption spectra. The PL displays an emission line centered at ~ 2.41 eV revealing only a weak confinement of carriers ($E_g = 2.35$ eV at 2 K and around 2 eV at RT). Absorption measurements reveal an absorption band edge at 2.46 eV, i.e. a Stokes shift of 50 meV. Transmission electron microscopy was performed on NCs deposited on copper grids and the sizes of more than 200 NCs were measured. As shown in FIG. 3.1b-c, the obtained NCs are roughly cubic with mean edge lengths of 7.7±1.2 nm. This size assignment is consistent with the optical data and available literature [1, 2] where a Stokes shift of 50 meV is found to correspond to a NC edge length of ~ 7 nm. From TEM images as FIG. 3.1b, we can determine the characteristic lattice parameter of $CsPbBr_3$ as $a = 0.58$ nm, consistent with prior reports. The lattice constant does not allow us to discriminate between the different crystallographic arrangements of $CsPbBr_3$. Indeed, distortions have small amplitudes that only advanced imaging techniques can resolve [3].

Smaller NCs were also synthesized following [4] and later [5]. The room temperature PL and absorption spectra of the latter are shown as dashed lines in FIG. 3.1a. The emission is centered around 2.7 eV with a Stokes shift of 95 meV, consistent with NC edge lengths $\lesssim 4$ nm [1]. While the synthesized solutions were bright blue-green emitting, isolation of single NCs remained very challenging for these smaller NCs emitting around 460 nm. In addition, our CW laser source was close to the low temperature emission such that significant excitation scattering was detected, degrading the signal-to-noise ratio. Therefore, these small NCs are not used in the subsequent analysis.

Degradation Let us note that while the results presented in the following are performed on days or weeks old solutions, we also have characterised the long term stability of the NCs in solution.

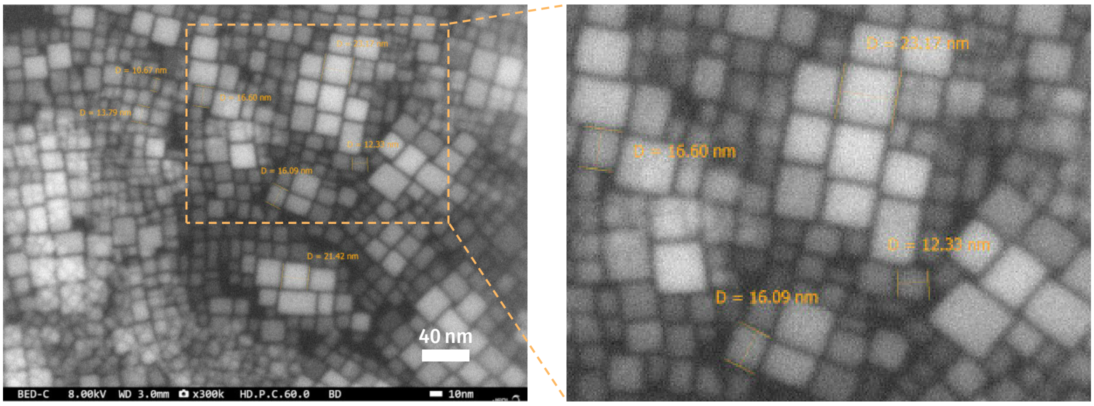

Figure 3.2 | Long-term evolution. Scanning electron micrographs of the solutions synthesised at NTU in late 2019, kept under ambient conditions and measured at LPENS in late 2021.

Solutions used at NTU were shipped to LPENS and stored in ambient conditions for two years. The visual appearance of the solution had changed drastically over time. The original transparent green solution evolved into an opaque yellowish solution. At room temperature and at the ensemble level, the PL showed a slight redshift with an emission at 2.36 eV rather than the original 2.4 eV. Scanning electron microscope (SEM) images of the NCs showed much larger structures than original TEM measurements acquired on fresh solutions and an increase size dispersion. This is consistent with a loss of ligands in solution and subsequent agglomeration and coalescence of NCs. The aged solutions were not used for experiments. They were only used at the initial stage of the study at LPENS for basic alignment purposes.

At LPENS

At LPENS, several batches of NCs were also synthesised, following the same synthesis protocol with only slight modifications of the injection temperature. The morphology and ensemble PL of the NCs synthesized on September 2021, referred to as `BSept`, are shown in FIG. 3.3c-d while measurements on the solutions synthesized in September and November 2021 are shown in FIG. 3.3a-b. The scanning electron micrographs in FIG. 3.3a-c, and others not shown here, give us access to the approximate size and shape of the objects. However, a precise measurement of the size and shape of the objects was not possible as the range of NCs sizes explored is at the limit of SEM resolution.

Nonetheless, we observe similar morphology to that observed at NTU and shown in FIG. 3.1 for `BSept` and `BNov`. Notably, SEM measurements on `BJul` reveal slightly rounded corners in contrast to the cubic NCs observed in all other synthesis batches. Despite this apparent difference in morphology revealed by SEM, optical properties of single NCs were similar and only exhibited lower emission energies due to their larger size. This observation is still not understood as it is not clear if it is due to improper sample handling when preparing SEM samples, misfocused images or indeed a rounded shape. Sizes of NCs synthesised at LPENS, on the other hand, are relatively larger and typically around 10-15 nm depending on the synthesis batch. As we will see, this size dispersion, with the synthesis of smaller NCs at NTU and larger NCs of different sizes at LPENS, will be directly reflected in the observed single NC emission energies at low temperature and provides us with the ability to investigate a wide range of NC sizes.

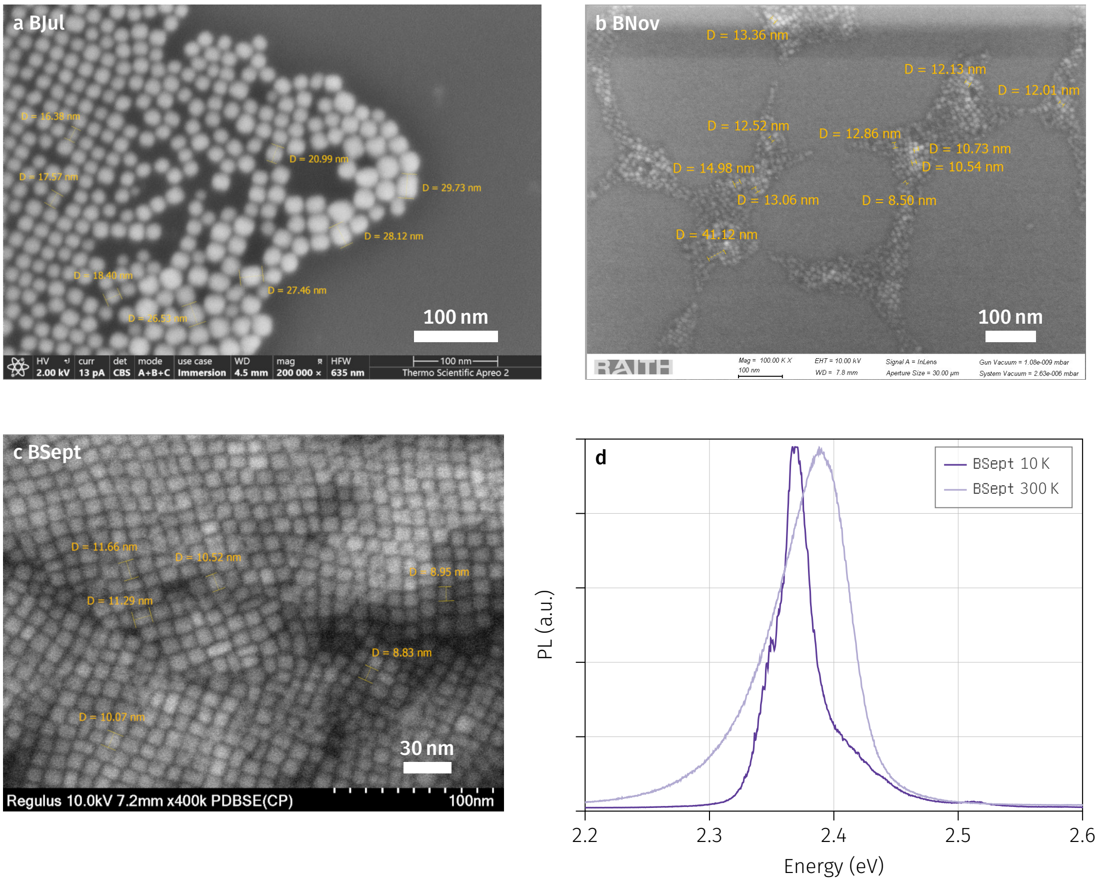

Figure 3.3 | Optical and structural characterisation at LPENS. **a-c**, Scanning electron micrograph of the solutions synthesised at LPENS in: **a**, July, **b**, November and **c**, September 2021. **d**, PL spectrum of an ensemble of $CsPbBr_3$ NCs at 10 K and 300 K.

Full dataset

The full dataset of NCs investigated in this work is thus comprised of four main batches of NCs synthesised at NTU and LPENS as summarised in Tab. 3.1. They were all made following the same synthesis protocol but differed due to both external and experimental factors. Indeed, these synthesis were performed with different brands of reagents and the available purity of reagents differed. In addition, while the synthesis platforms at NTU and LPENS were similar, it seems that the control of the reageants temperature right before injection is a more complicated matter than expected.

3.2 Single $CsPbBr_3$ nanocubes cryogenic spectroscopy

Chronological account

The actual process of finding the right dilutions and spin-coating parameters for single NC spectroscopy was done twice, once at NTU in early 2019 and once at LPENS in mid-2021

Table 3.1 | Synthesis batches. Summary of the different synthesis batches performed in this work and basic properties.

Name	Date	Size (nm)	Emission max. (eV)
`NTUB`	June 2019	7.7±1.2	2.41 (RT)
`BJul`	July 2021	15 - 20	?
`BSep`	September 2021	8 - 10	2.389 (RT), 2.369 (10 K)
`BNov`	November 2021	8 - 12	$\sim$ 2.39 (10 K)

onwards. The following is a somewhat chronological account of the process we followed. First, at NTU, we tried to isolate the single NCs at room temperature directly. This proved challenging, such that we moved on to cryogenic temperature measurements. We managed to isolate single NCs at cryogenic temperature and studied $\sim$ 50 NCs' spectral properties. A more detailed study was also performed on a subset of these NCs, following their spectral and temporal properties as a function of temperature. This study is detailed in CH. 4. Here we present the spectral properties of single NCs at the lowest cryogenic temperatures.

At LPENS, the process was started again from scratch. Thanks to the knowledge acquired from our prior studies at NTU, the experimental setup was optimised to enable fast and easy reproducible localisation of single NCs. With this setup, we took advantage of the size dispersion of the different synthesis batches we performed to study the optical spectra of hundreds of NCs emitting from 2.3 eV to 2.5 eV in an attempt to reveal underlying intrinsic dependencies.

This enabled us to reveal the full spectral fingerprint of single $CsPbBr_3$ NCs with sizes ranging from 7 to 20 nm which we present here after a brief account of how we performed the localisation of single NCs.

3.2.1 Identifying single nanocrystals

Room temperature

We started this study by trying to find single NCs at room temperature. A critical challenge is to be able to discern single NCs from potential aggregates, which is complicated at room temperature due to thermal broadening.

FIG. 3.4a shows a large area low resolution scan displaying some large high intensity spots, likely arising from aggregates, and smaller low intensity spots. High-intensity spots often display a clear spatial modulation of the spectrum depending on the position of the beam, with not only the

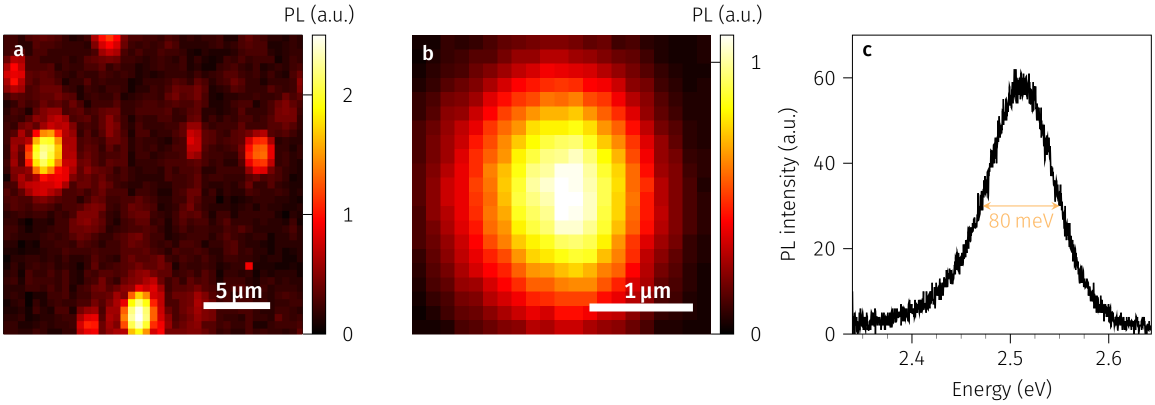

Figure 3.4 | Room-temperature perovskite nanocrystal spectroscopy. **a**, PL map showing multiple emission spots. **b**, PL map of a single emission spot and **c** corresponding spectrum.

intensity but also the shape of spectrum evolving. In contrast, some low-intensity emission spots which do not show such spatial dependence can also be identified. Fig. 3.4b shows a small area high resolution scan of such an emission spot, corresponding to a potential single NC. The emission spot displays the same width and spatial profile as our excitation spot with a width close to 1.3 µm. A spectrum taken at the centre of Fig. 3.4b spot is also shown in Fig. 3.4c and reveals a spectral width of 80 meV, close to both the room-temperature ensemble linewidth of the solution and the reported single NC linewidths in the literature [6, 7].

While the spatial and spectral widths of the emission indeed suggest the assignment of such emission spots to single NCs, such assignment remains speculative. The ultimate confirmation that these objects are indeed single NCs would have been given by intensity correlation measurements displaying clear antibunching dips with $g^2(\tau) < 0.5$. However, such measurements were not possible due to experimental constraints detailed here. In our experimental configuration, single photon avalanche detectors were placed at the output of a monochromator with a maximum bandwidth of 2 nm. At room temperature, a single NC linewidth is $\sim$ 15 nm such that we could only collect a fraction of the emission. Because of this experimental weakening of the detected signal, exposure times needed to perform correlation measurements rendered the task unlikely in our case. Increasing the excitation power partially solves this issue as the NCs are found to be quite stable under excitation powers up to several tens of µW. However, such measurements would inevitably show signature of high-energy exciton complexes that would distord the antibunching measurement, leading to additional bunching contributions blurring the interpretation in terms of number of emitters.

Cryogenic temperature

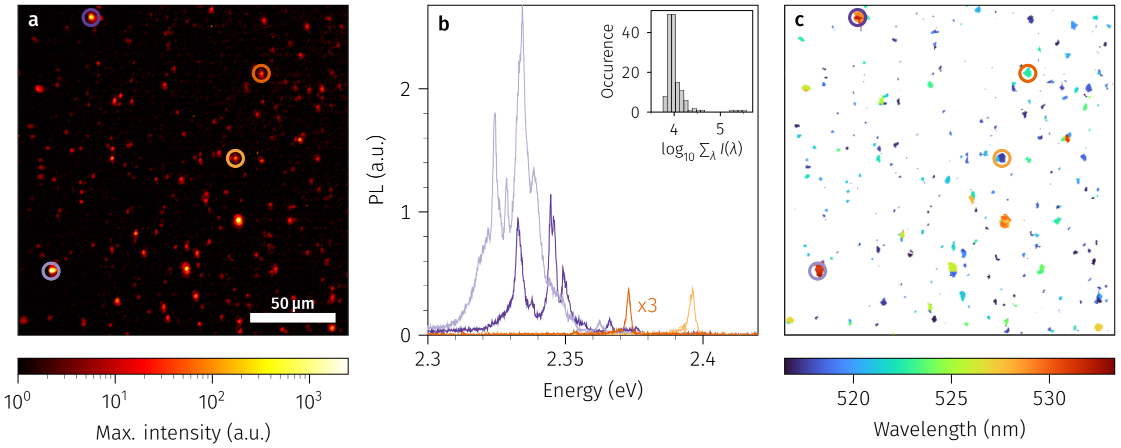

Figure 3.5 | Locating single nanocrystals. **a**, Map of a 200 µm by 200 µm surface area acquired with 250 ms acquisitions and an excitation of 1 µW. Spectra of emission spots identified by circles are shown in **b**. The inset shows the distribution of integrated intensities $\sum_\lambda I(\lambda)$ of the emission spots in **a**. **c**, Same map as **a** with colour-coded emission wavelength.

To minimise the thermally-induced linewidth broadening and investigate the fine structure of single NCs emission, we moved on to liquid helium temperatures. At 4 K, PL maps such as the one shown in FIG. 3.5a confirm the assignment of the two classes of emission spots observed at room temperature. We show in FIG. 3.5b the spectra of four emission spots, two of the brightest and two average intensity spots together with, in the inset, the distribution of intensities recorded in the map in **a**. While the few brightest spots can be identified as aggregates of NCs since they display a clear spatial dependence, other emission spots consist in sharp lines with no spatial dependence. In addition, the two classes exhibit different emission energies, with high intensity emission spots showing up at larger wavelengths, consistent with the potential aggregation and coalescence of NCs. This is depicted in FIG. 3.5c which is the same map as in FIG. 3.5a with the colorbar showing the emission energy of the located emission spots. This distinction and the observed spectra in themselves are a strong indication that we are dealing with single NCs. Nonetheless, we ascertain this identification with intensity correlation measurements.

Single photon emission With thermal broadening minimised, we can now perform correlation measurements of reasonable durations which was not possible with our setup at room temperature. In our study, we performed intensity-correlation measurements with the goal to identify single NCs. In this case, the best choice is pulsed excitation due to the faster acquisition

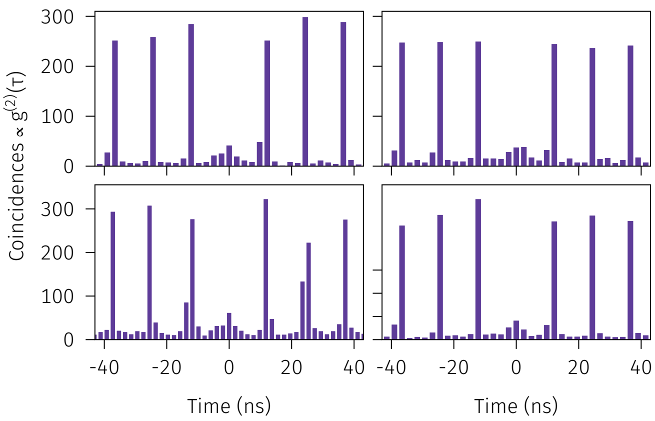

Figure 3.6 | Single photon emission. Results of intensity-correlation measurements yielding the second-order correlation function $g^2(\tau)$. Zero-delay values $g^{(2)}(0)$ show consistent values on the order of 0.1, indicating single photon emission.

times to achieve a similar signal-to-noise ratio as discussed in Sec. 2.3.4. We therefore used a pulsed excitation with $t_{\text{rep}} \sim 12.5$ ns to perform these measurements. Using a Hanbury Brown and Twiss interferometer, we thus measure the second-order correlation function of the emitted photons as shown for four single NCs in Fig. 3.6. Typical measurements yield $g^{(2)}(0) \sim 0.1 < 0.5$, the upper bound for a single emitter; from which we get two pieces of information. First, the emission spots tentatively assigned to single NCs are in fact single NCs. Secondly, single CsPbBr_3 NCs are efficient emitters of single photons at cryogenic temperature. This is similar to previous reports, both at room temperature [6, 8, 9] and cryogenic temperature [10, 11] which reveal zero-delay values $g^{(2)}(0)$ on the order of 0.1. At the start of our study, these results proved invaluable to make sure that the class of emission spots identified are indeed single NCs. In the following of the study, correlation measurements were not performed anymore as single NC spectra could be identified based on prior experience.

Stability of the emission In this work, we used a typical excitation power P_0 of 1 µW corresponding to a mean number of exciton ~ 0.1. At such P_0, the emission of single NCs is stable as evidenced in Fig. 3.7a-c. Over the course of 2 h, the PL intensity of this single NC remains stable displaying only a decrease of 10% over the course of half an hour due to the drift of the sample which is easily picked up around 6200 s by displacing the excitation beam. Fluctuations of the PL intensity over minutes are still present but remain small as the standard deviation of the time traces shown are on the order of 5% of the intensity (▬ in Fig. 3.7c). Furthermore, careful examination of the PL intensity even at the smallest time bin of 10 ms reveals a Poissonian distribution of intensity assessing the stability of the emission. This is in

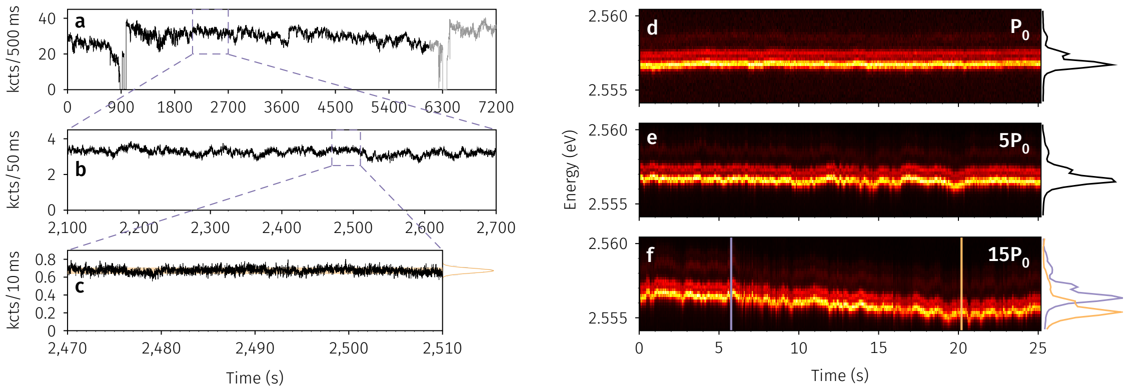

Figure 3.7 | Single nanocrystals' emission stability. **a-c**, Time evolution of the PL intensity of a single NC over the course of 2 h shown with increasing time resolution: **a**, 2 h trace with 500 ms time bin; **b**, 10 min trace with 50 ms time bin; **c**, 40 s trace with 10 ms time bin. Drops in intensity in **a** at 900 and 6300 s are interventions of the author to correct for the spatial drift as observed between 4500 and 6300 s. The distribution of intensities in **c** is shown on its right hand side with the corresponding Poisson distribution. **d-f**, Temporal evolution of the PL spectrum of a single NC displaying three emission peaks for selected excitation powers with P_0 = 2 μW. Intensity traces are built from spectra with an acquisition time of 50 ms. Spectra on the right hand side show the integrated intensity over the full duration of the trace for **d** and **e**, and two individual spectra acquired near 6 and 20 s for **f**.

stark contrast to established colloidal NCs with an intermittent emission and large intensity fluctuations [12]. LHPs do not seem to exhibit such intermittency or fluctuation at low temperature, although some reports at room temperature have been made [13–15]. In our study, we do not evidence such behaviour. However, despite the absence of blinking, the PL of single NCs can exhibit strong spectral fluctuations.

Spectral stability Indeed, while at typical P_0 the emission is also stable spectrally, increasing the excitation power leads to increasing spectral fluctuations on the order of 1 meV. In FIG. 3.7d-f, we show the excitation-power dependence of the time evolution of a single NC spectrum exhibiting three emission peaks. To reveal fast spectral fluctuations, we set single spectra acqusition times to 50 ms and follow the emission for 25 s (500 spectra) at three excitation powers. As the excitation power increases, the three peaks exhibit fully correlated increasing spectral fluctuations. This dependence of spectral diffusion on the pump power reveals its photophysical nature and is generally attributed to a Stark effect induced by nearby charges [16–18] and here manifested by fluctuations at the ms scale.

Linewidths However, even for the smallest powers and acquisition times, linewidths observed are still often larger than our spectral resolution ($\sim$ 100 μeV). Based on the reported radiative decay times on the order of 200 ps, a Fourier-limited emission is expected to exhibit a linewidth of

3.3 μeV, far narrower than the observed emission. At the low temperatures investigated, resonant excitation measurements revealed a linewidth ~ 130 μeV at 10 K [19]. This is consistent with our observations of linewidths close to our resolution. However, a significant proportion of spectra are broadened further with linewidths up to the meV, which suggests that the spectral diffusion phenomenon illustrated in FIG. 3.7d-f in the ms scale may also happen at smaller time scales.

To consider the case of spectral diffusion faster than the acquisition time, let us do it by analogy. We focus on FIG. 3.7d-e and the spectra shown on the right hand side. These spectra are constructed by summing all the individual spectra within the corresponding trace and their comparison highlights the impact of spectral fluctuations on the recovered spectra. At P_0, the integrated spectrum is homomorphic to the instantaneous spectra with a linewidth barely broader. At $5P_0$ however, the integrated spectrum is significantly broadened due to spectral wandering. This is exactly the same behaviour that would be observed on a single instantaneous spectrum in the presence of spectral diffusion faster than the acquisition time, although at a different time scale. And indeed, this behaviour can be directly observed on the respective linewidths of the individual spectra at P_0 and $5P_0$, where the brightest peak shows a linewidth increasing from 600 to 980 μeV. This suggests the presence of spectral diffusion at a variety of time scales and calls for further detailed study.

Selection bias In this study, our initial goal was to study strongly confined $CsPbBr_3$ NCs. Thus, in the first part of the study at NTU, an experimental bias was introduced with the preferential selection of NCs with emission energies ≥ 2.45 eV. This selection was also driven by the fact that aggregates of NCs were observed preferentially at lower energy. On the other side, emission energies larger than 2.6 eV were observed but rarely studied because close to the filter cut-off. In addition to this emission energy bias, there was an obvious bias towards the study of the brightest emitters due to experimental constraints.

At LPENS, thanks to the design and optimisation of the optical platform, much of those biases could be removed. First, having understood that smaller NCs are more fragile and could not so easily be isolated, we moved on towards larger NCs. Next, as for larger NCs the size-dependence of the emission energy is less pronounced (see FIG. 1.10b), emission energies are found to be less spread out and size-selection is inevitably prevented. Finally, thanks to the fast automated mapping of the sample, the selection bias towards the brightest emitters is removed.

Emission energy statistics

All in all, we recorded the emission of hundreds of NCs whose emission energies at cryogenic temperatures between 4 and 10 K are summarised in Fig. 3.8. The synthesis batch–emission energy correspondance is also shown.

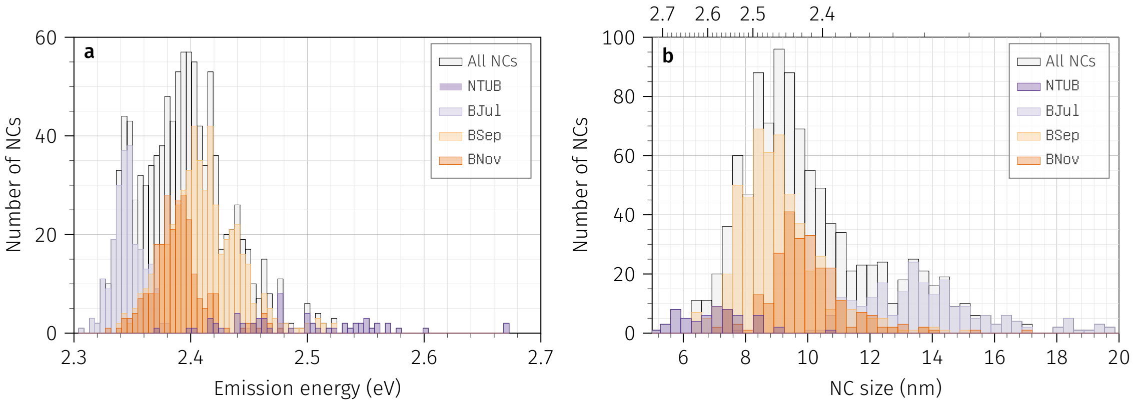

Figure 3.8 | Single nanocrystals' emission energy statistics. **a**, Distribution of NCs emission energies and **b**, corresponding sizes obtained using (1.15).

Based on the approximation (1.15), data can equally be represented as a function of the corresponding NC edge length if it were of cubic shape using parameters $E_g = 2.342$ eV and $E_b = 33$ meV [20]. Doing so yields Fig. 3.8b which shows the approximate size of the observed NCs for each synthesis batch. Comparing the NCs sizes in Fig. 3.8b with the morphological data obtained by TEM and SEM measurements (Tab. 3.1) reveals a good agreement. Notably, the agreement is nearly perfect for three of the four solutions (`NTUB`, `BSep` and `BNov`), while for the fourth synthesis `BJul`, sizes are somewhat underestimated with respect to the SEM data. Of course this is only an approximation as the anisotropic shape of the NCs is not taken into account and this "NC size" must be thought of as an effective size.

Having ascertained that the emission spots successfully isolated are indeed single NCs, we move on to a detailed study of the fine struture of the emission.

3.2.2 Exciton fine structure

At the start of this study, prior works had reported narrow lines grouped in doublets or triplets and attributed to the presence of both tetragonal and orthorhombic NCs [11, 21, 22]. For nanocrystals with cubic shape, these identifications are inconsistent with the reported linear polarisations for *all* emission peaks. However, taking into account the anisotropic shape of the NCs, this requirement is levied such that the triplet can fully split and exhibit polarised emission. The contribution to the energy splittings due to shape anisotropy was found to be similar to that of the crystal field with splittings ∼1 meV [23]. A later work [24] further considered that energy splittings predicted in [23] were overestimated by a factor ∼3 because of an ill-conditioned parameter related to the higher spin-orbit split conduction bands.

As already discussed in SEC. 1.2.3, it seems now clear that NCs exhibit an orthorhombic symmetry and the triplet exciton is thus expected to be fully split. Thus it is the presence of one- and two-peak NCs that remains to be explained. Indeed, for one- and two-peak spectra to be observed for orthorhombic NCs, the contribution of shape anisotropy should exactly compensate the crystal field contribution. This scenario is unlikely to explain the reported proportions of multi-peak spectra with up to 80% of spectra exhibiting two peaks or less [25–27]. This high proportion of few peak spectra was tentatively rationalised in [27] by considering both the orientation of the NCs with respect to the detection axis and thermal occupation of exciton sublevels. Indeed, considering that a dipole does not emit along its axis, two-peak spectra can naturally be explained by considering the third dipole aligned with the detection axis. However, up to 50% of one-peak spectra were observed in [27], seemingly in contrast with the expected triplet in orthorhombic crystals. To reconcile these observations, the authors suggest that in such cases only the lowest exciton sublevel is populated. We will investigate this.

There are thus several factors expected to play a role in the observed fine structure and the number of bright exciton peaks detected. Namely, these are the crystal symmetry, NC shape, exciton states populations, selection rules, dipoles orientation, local environment and collection apparatus. The exact interplay of these contributions thus remains to be understood.

To gain more insight into the fine structure emission of $CsPbBr_3$ NCs, we study the emission of single NCs in detail by considering three quantities we measure: the polarisation of the bright triplet exciton states, their relative intensities and the energy splittings.

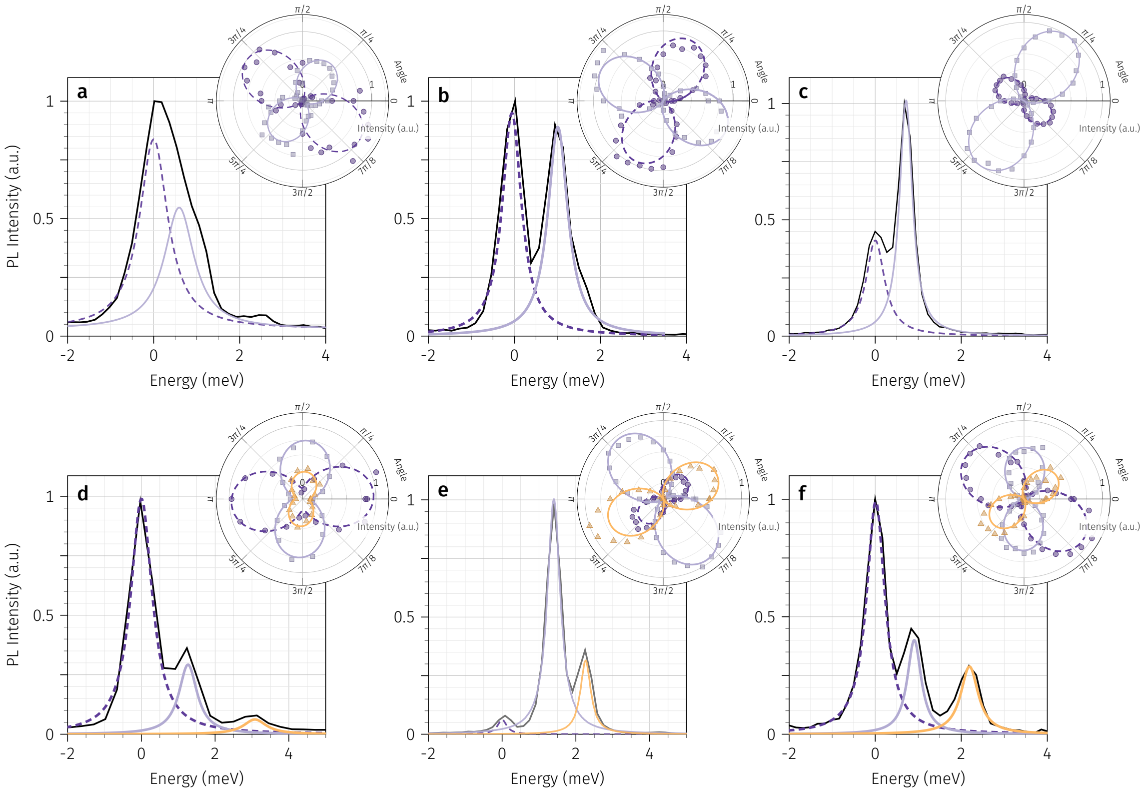

Figure 3.9 | Polarisation of the bright exciton. Spectra and polar diagrams of **a-c** two- and **d-f** three-peak NCs. **a-c**, Three relative intensity configuration are shown from **a** a brightest lowest exciton to **c** a dimmest lowest exciton. **d-f**, Three configurations of three-peak spectra observed.

Polarisation

First, we need to make sure that what we measure is actually what we want to measure, i.e. the polarisation of the emitted photons, not that of the setup, and the relative intensities of the lines, not a convolution of the latter with the setup response.

Methodology To do so, we study the polarisation-dependence of the emission by acquiring the emission spectrum while rotating a half-waveplate in front of a polariser aligned with the detector's preferential polarisation direction. "Unpolarised" spectra are then built by summing the spectra taken at each half-wave plate position. Doing so, the relative intensity ratios between the different emission lines are preserved in contrast to *unpolarised* detection which inevitably favours the detection apparatus preferential polarisation direction. These reconstructed spectra, and the polarisation diagrams they come from, therefore directly display the relative intensities of the emitting state, provided the orientation of the NC is taken into account.

Here, we identify the fine structure of more than 200 NCs with a sufficient signal-to-noise ratio. For these NCs, we observe mainly two- and three-peak spectra. A subset of these NCs was further studied in detail and all reveal peaks with a nearly perfect linear polarisation.

Doublets The majority (∼65%) of NCs investigated exhibit two-peak spectra as those shown in FIG. 3.9a-c with strong degrees of polarisation $\eth > 0.9$. The two peaks always exhibit orthogonal linear polarisations consistent with expectations based on symmetry arguments for a NC with orthorhombic symmetry. The relative intensities of the two peaks are found to vary from a brightest (FIG. 3.9a) to a dimmest (FIG. 3.9c) lowest exciton state, with orthogonal linear polarisation preserved, and no configuration observed preferentially.

Triplets Besides doublets, we also observed three-peak spectra in a ∼35% proportion. The three peaks also exhibit linear polarisations and strong degrees of polarisation $\eth > 0.9$. In FIG. 3.9d-f, we show three different configurations observed. In FIG. 3.9d, the three peaks follow an intensity ordering consistent with that expected from thermal population and the two highest exciton sublevels polarisation are parallel and orthogonal to the lowest exciton state. In contrast, in FIG. 3.9e for example, the lowest exciton peak is the weakest emitting and shows parallel polarisation to the highest exciton state, both perpendicular to the middle peak. At 5 K, with an energy splitting of 1.4 meV, the lowest exciton state is expected to be 26 times more populated than the second lowest state making it unlikely that the lowest exciton is not populated while the other two exciton states are. Considering that the bright exciton states have similar oscillator strengths [24, 27], it becomes clear that the spectrum observed can not solely be explained by thermal occupation of the exciton states.

Populations While we observe mainly two- and three-peak spectra, other works report up to 50% of one-peak spectra [27]. They explained their observation by considering that at the low temperatures investigated ∼5 K, higher exciton states were likely weakly populated.

Indeed, based on Boltzman population statistics, two states i and j separated by $\Delta E = E_j - E_i > 0$ will show relative populations $p_j/p_i = e^{-\Delta E/k_B T}$ where k_B is the Boltzman constant. At typical experiment temperatures of 5 K, assuming an energy splitting of 1 meV, we have $p_j/p_i \sim 0.1$ which should be more than enough to resolve higher lying exciton states. Even more so, when a doublet or triplet is resolved in [27], the effective temperatures deduced from experiments are found to be higher than 5 K, such that higher lying exciton states are expected to be populated enough to be observed spectrally.

Figure 3.10 | Thermal population. Relative population ($I_{\mathrm{rel}} = p_j/p_i$) of a higher lying state j as a function of the energy splitting $\Delta E = E_j - E_i$ and temperature. The same data is shown with a **a** linear and **b** logarithmic color scale.

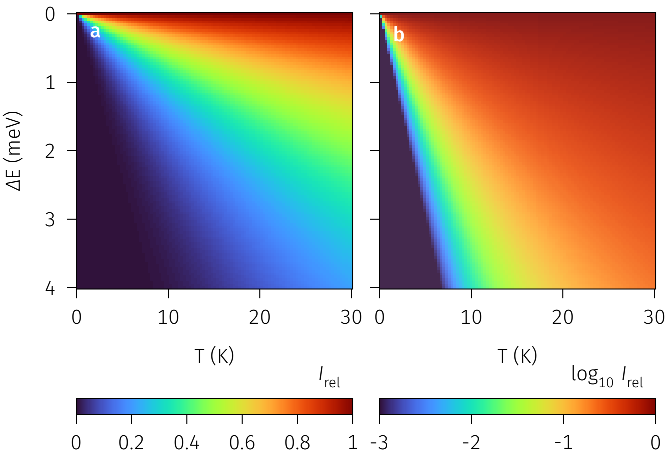

To illustrate this point, we show in FIG. 3.10 p_j/p_i as a function of ΔE and T for typical energy splittings and experiment temperatures. Assuming for example a large energy splitting of 3 meV at 5 K, we find $p_j/p_i \sim 0.001$, such that, at typical signal-to-noise ratios, higher exciton states are likely not to be observed. In contrast, increasing the temperature to 20 K, we get $p_j/p_i \sim 0.1$ and higher exciton states are expected to be observed. From this argument, we can see that the experiment temperature should have a direct impact on the relative proportions of one-, two- and three-peak spectra observed.

Orientation

We have seen that single NC spectra exhibit a variety of fine structures with two or three peaks and linear polarisations.

Before discussing experiment results in detail, let us stop on this point, alone worthy of interest. In principle, the ubiquitous observation of linear polarisation has strong implications on the underlying symmetry of the NCs. Namely, for NCs with cubic shape, the inversion asymmetry axis if present, should be along the Z axis for the band-edge exciton to consist in three orthogonal bright states and a dark state. If the inversion asymmetry is not parallel to the Z axis, the symmetry is further lowered and bright and dark states mix such that linear polarisations are lost [27]. However, this manifestation of the non-orthogonality of the dipoles is expected to be weak [27]. Nonetheless, the observation of all linear polarisations constrains the underlying symmetry of the NCs. Further considering the anisotropic shape of the NCs levies the symmetry requirements discussed above such that linear polarisation could be observed for fully anisotropic NCs with a cubic crystal phase.

That said, we can analyse the polar diagrams in more detail, and in particular the relative phases of the polarisations. The actual level ordering of the X, Y and Z excitons is determined by the crystal field and thus depends on the size and shape of the NCs [23, 26, 28] (see FIG. 1.9). For anisotropic NCs such as a slightly flattened cube along the Z axis, we get the X, Y and Z excitons given with increasing energy. In contrast, for slightly elongated NCs along the Z axis, the levels reorder as Z, X, Y. In both cases, the same arguments we develop in the following apply and only the actual orientations would differ. Thus, let us assume for the sake of this discussion that the level ordering is that originally reported in [27] for cubic shape NCs with orthorhombic crystal phase which matches the level ordering obtained in flattened NCs when taking the Z axis along the elongation axis, i.e. X, Y, Z [26].

Methodology We can describe the emission of the three orthogonal dipoles as a function of their orientation with respect to the detection axis. Based on prior works [27, 29], we simulate the polarisation of the three dipoles as a function of their orientation and take into account thermal population of the exciton states. Doing so, based only on the observed energy splittings, polarisations and intensities we find plausible configurations that reproduce experimental data in FIG. 3.9 and show the results in FIG. 3.11. Note that all coloured lines in FIG. 3.11 are simulated curves and not fits like in FIG. 3.9.

Two-peak analysis We show in FIG. 3.11a an example of a two-peak spectrum that can be tentatively interpreted. The third exciton peak is not observed[1] and we interpret this absence as resulting from the orientation of its emission dipole, parallel to the observation direction. In this case, assuming the higher exciton state dipole parallel to the observation direction which corresponds to the [001] plane, we find that a temperature of 16 K, close to the experiment temperature of 10 K, reproduces the experimental data. In contrast, the same analysis for FIG. 3.11b yields a temperature of 200 K . For this NC, we thus expect the orientation to

---

[1] Note the peak appearing at higher energy results from a spectral jump of the emission during the measurement clearly resolved during the polarisation measurement.

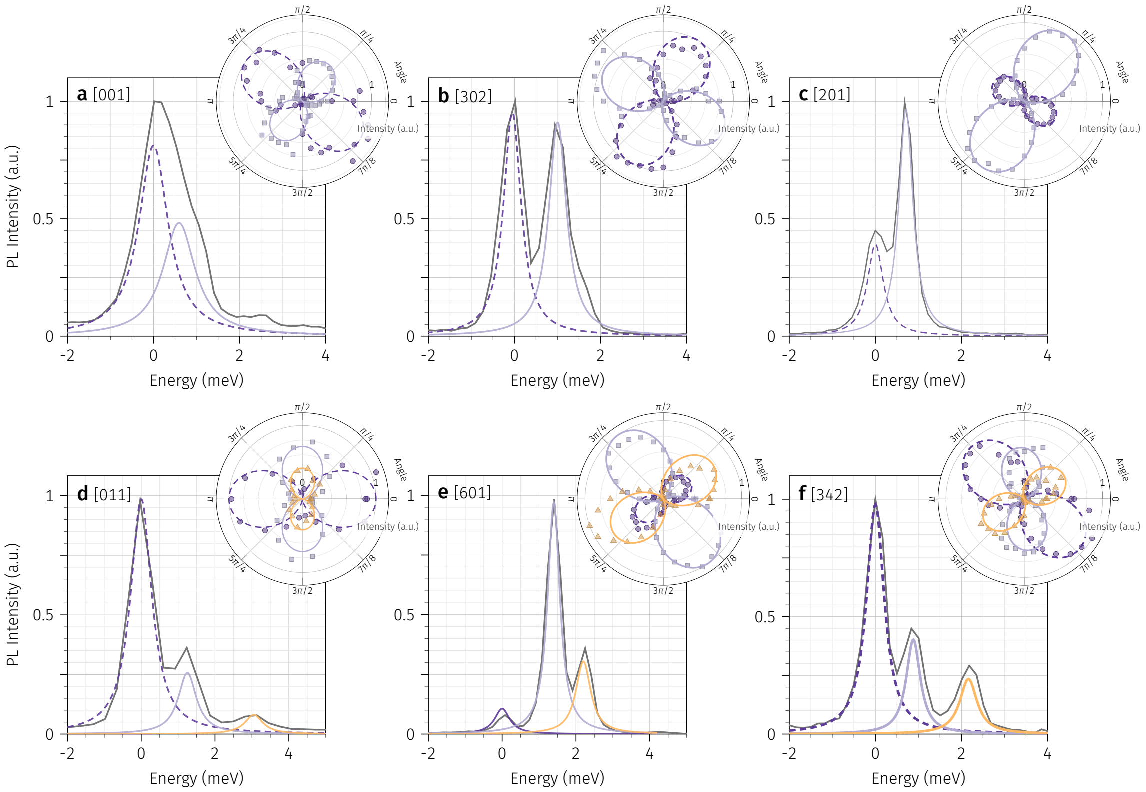

Figure 3.11 | Orientation of the unit cell. Identification of the crystal orientation for the spectra and polarisation diagrams in Fig. 3.9. Coloured lines show the simulated spectra and polarisation based on the energy splittings measured and the orientation deduced, e.g. [001] for **a**. Panels **a-f** correspond to Fig. 3.9**a-f**. Note that polarisation diagrams of three-peak spectra are scaled for clarity, while those of two-peak spectra display true relative intensities.

differ from the assumed [001] direction and the higher energy state to be only weakly populated. Setting the temperature to 10 K, we find a match for an observation along the [302] plane, with the requirement that the highest-lying exciton state lies at more than 2 meV than the middle exciton state. In the case of Fig. 3.11c where the lowest exciton peak is the dimmest a similar reasoning and requirement apply. We find a configuration matching the observed polarisation and relative intensities along the [201] plane if assuming the working temperature of 10 K.

Three-peak analysis The case of three-peak spectra is simpler to interpret since the three exciton peaks are observed. In Fig. 3.11d, we show the case of a three-peak spectrum showing Boltzman-ordered emission peaks. Assuming a temperature slightly higher than experiments at 15 K, we find that this particular NC spectrum and polarisation can be well reproduced if we assume an observation direction along the [011] plane. Similarly, in Fig. 3.11e, we show the case of a three-peak spectrum with the lowest peak being the dimmest. This suggests an observation directly close to parallel to the lowest exciton state dipole. Considering a thermal population at 10 K, we find that this particular NC spectrum and polarisation can be well reproduced if we assume an observation of the [601] plane. Keeping the temperature fixed at 10 K, we can also reproduce the spectrum in FIG. 3.11f with an orientation plane parallel to [342].

Discussion So we have seen that the low-temperature spectrum of single $CsPbBr_3$ NCs is dominated by the emission of the bright triplet exciton manifested by the presence of two- and three-peak spectra. Single NC spectra can be well reproduced by considering both thermal population and the observation direction with respect to emission dipoles. We emphasise that the ”orientations” determined above are dependent on the actual level ordering of the X, Y and Z states. However, a simple permutation of X, Y and Z does not change the core result here, it only leads to a permutation of the orientations. For example, if the actual level ordering is ZYX and not XYZ, then [102] would become [201]. Our results do not depend on this ordering but rather only on the energy splittings and experiment temperature.

A further challenge in view of applications is the determination of the 3D orientation of NCs. This requires the determination of the crystal termination, i.e. the crystallographic planes at the NCs facets. While for $CsPbBr_3$ NCs, the orientation of the crystallographic axes with respect to the NC morphological axes is still not clear, we could base our arguments on the crystal terminations reported for $CsPbBr_3$ nanoplatelets, namely [100] and [010] [30]. Indeed, as considered in [31], the 3D orientation of nanoplatelets can be readily recovered from the analysis of their polarisation diagram as they lie flat on the subtrate. However, in our work NCs are embedded in a thin polymer layer and are thus expected to show random orientations within the matrix which prevents further analysis based on preferred orientations.

Depending on the energy splittings and thermal energy, the model developed here can be refined to take into account the actual rate equations of the exciton where transition rates can be taken into account. This is beyond the scope of this work for bright-bright transitions, however we will see such a refinement for bright-dark transitions in SEC. 4.2.

Nonetheless, to provide information on the bright exciton triplet and the mechanisms at play in the degeneracy lift, we study bright-bright energy splittings in detail.

Bright triplet energy splittings

Ongoing debate In the ongoing debate in the community about the relative importance of the Rashba effect, there are but a few experimental predictions that can be tested. The most striking prediction is the level re-ordering due to the Rashba effect, which would place the bright triplet state below the dark state [27]. This prediction can be directly tested by applying a magnetic field, thereby breaking time-reversal symmetry and leading to a brightening of the dark exciton state. This was done succesfully for $FAPbBr_3$ and $CsPbI_3$ with magnetic field strenghs up to 7 T and revealed a lowest lying dark exciton state [25, 26]. In contrast, prior experiments have failed to unveil the dark state in both $FAPbI_3$ and $CsPbBr_3$ [9, 21]. In this work, we also tried to evidence the emergence of a dark state upon application of magnetic fields up to 5 T. This is the subject of Sec. 4.2.

Further refinements of the model, including both short- and long-range exchange interaction and the Rashba effect, reveals that the level ordering may in fact be size-dependent [24]. This suggests that even though the dark state may be observed above or below the bright triplet for a particular range of sizes, the same ordering may not apply to all NCs sizes. For $FAPbI_3$ and $CsPbI_3$, the successful magnetic brightening of the dark exciton was achieved with intermediately confined NCs and the size-dependence of the bright-dark splittings was evidenced [25, 26]. Bright-dark splittings are found to increase with increasing confinement, consistent with a pure exchange model and fine structure splittings are explained by taking into account the shape anisotropy of the NCs. However, theoretical predictions of a lowest lying bright triplet were made for $CsPbBr_3$ and it is not clear if these findings can transfer.

While we did not manage to evidence magnetic brightening of the dark state in $CsPbBr_3$ (see Sec. 4.2), here we can compare the contradicting predictions of the two models regarding bright-bright exciton splittings. Based on a pure exchange model, bright-bright exciton splittings are expected to increase with increasing confinement [23]. Including the Rashba effect yields the contradicting prediction that bright-bright energy splitings are expected to decrease with increasing confinement [24, 28]. So just as bright-dark splittings, bright-bright splittings and their size-dependence are a direct probe to the underlying mechanism for fine structure splitting.

Statistics In the last three years, the original debate on the relative position of the bright and dark states has now shifted towards quantifying the relative contributions of each term. Here, in order to provide information on the relative contributions of the exchange and Rashba terms, we probe the size-dependence of the bright triplet exciton energy splittings. As shown in Fig. 3.12a-b, we define the energy splitting for doublets as Δ and the lowest, resp. highest energy splitting for triplets as Δ_1, resp. Δ_2. For over more than 250 NCs with energy splittings larger than 200 μeV, we record the energy splittings as a function of the emission energy. The statistics are shown for both two- and three-peak spectra as a function of: (Fig. 3.14c,e,g) the emission energy of the lowest exciton state and (Fig. 3.14d,f,h) the corresponding size.

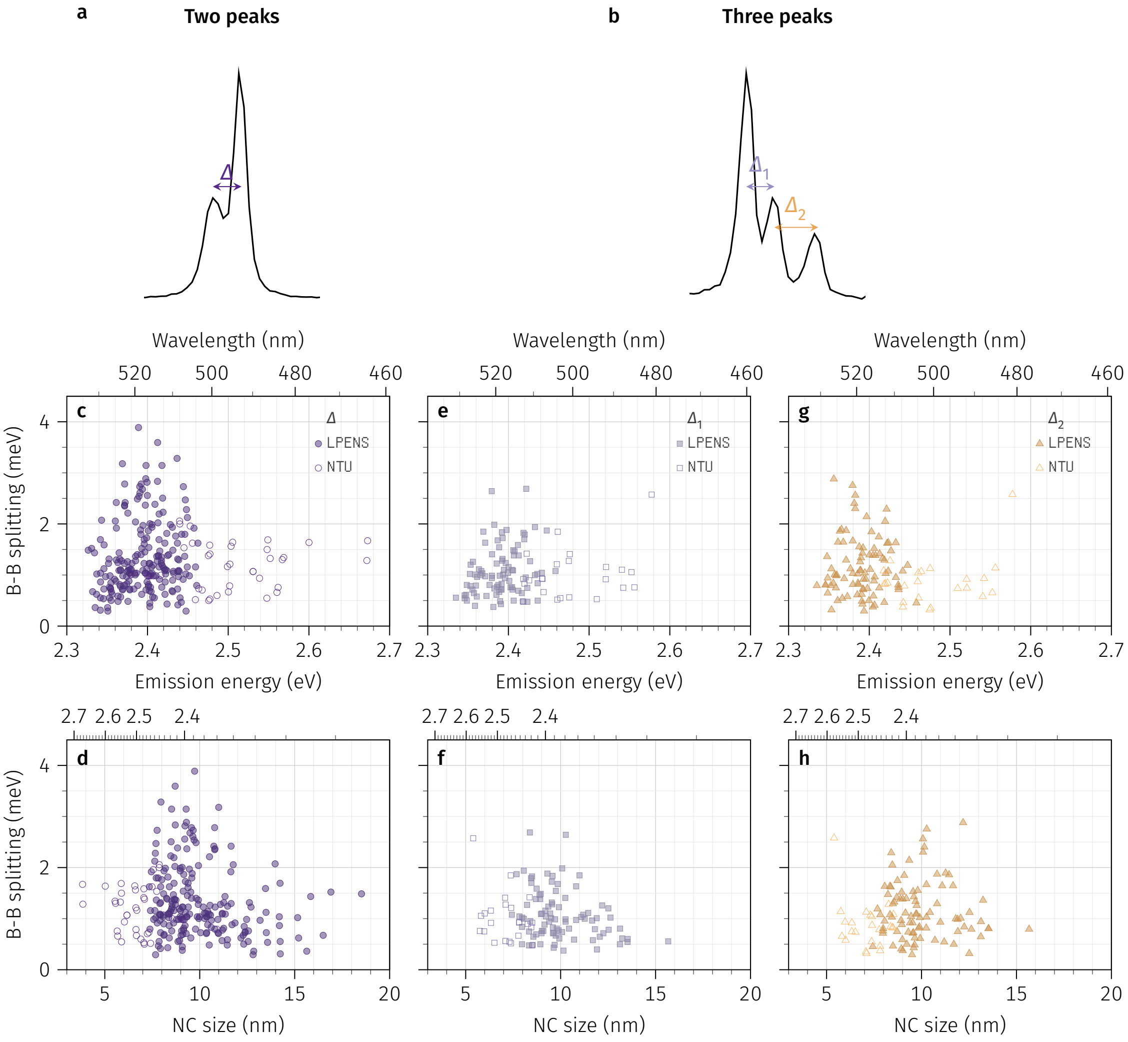

Figure 3.12 | Bright triplet energy splittings. Illustrative spectrum of **a**, a two-peak spectrum and **b**, a three-peak spectrum. For each class, we show the energy splittings as a function of **c,e,g** the emission energy and **d,f,h** the corresponding NC size. Data was acquired at: 4.5 K for NTU data and 10 K for LPENS data.

Two-peak spectra For two-peak spectra (Fig. 3.12a,c,d), we find a mean energy splitting $\Delta = 1.3 \pm 0.7$ meV with a median at 1.1 meV. At a given energy, the spread of energy splittings observed is attributed to the different NCs morphologies observed. While data shows significant variability, we seem to evidence a slight increase of energy splittings with decreasing size in the samples of LPENS (● in Fig. 3.12c,d), in accordance with the prediction of the pure exchange model as reproduced in Fig. 3.13. In contrast, while we investigated NCs with emission energies up to ~2.7 eV at NTU, energy splittings are found to be similar to those recorded at LPENS. We come back to this intriguing point in the following.

Let us note, as discussed previously, that two-peak spectra are interpreted here as a fully split triplet exciton. Prior works have reported two classes of two-peak spectra upon application of a magnetic field [21]. Namely, depending on the orientation of the NC with respect to the magnetic field, two-peak spectra are either observed to split into three peaks if the magnetic field is parallel to the z crystal axis, or only display Zeeman splitting if the magnetic field is orthogonal to the z axis. However, for the latter, we expect the X/Y peak to be unpolarised at zero-field. Since we observe linear polarisations, we interpret two-peak spectra as a fully split triplet exciton with one of the exciton state either weakly populated or parallel to the observation direction. As such, data presented in Fig. 3.12c,d are only separated from the three-peak data because we do not know which of the two splittings we have recorded: either the low energy or the high energy splittings.

Three-peak spectra In the case of three-peak spectra, we can probe the fully split triplet exciton (Fig. 3.12b,e-h) and find mean energy splittings $\Delta_1 = 1.0 \pm 0.5$ meV and $\Delta_2 = 1.16 \pm 0.60$ meV with medians at 1.0 for both. Energy splittings for both two- and three-peak spectra compare well with the literature with $\Delta \sim 1$ meV, $\Delta_1 \sim 0.5$ meV and $\Delta_2 \sim 1$ meV [21, 22]. Similar in [27], mean energy splittings observed are $\Delta = 1.6$ meV and $\Delta_1 \sim \Delta_2 \sim 1.15$ meV. No particular size dependence is observed on either of the two energy splittings.

Comparison between NTU and LPENS datasets Data from LPENS and NTU show comparable energy splittings for three-peak spectra and do not reveal any clear size-dependence. As shown in Fig. 3.12a however, energy splittings measured at LPENS are found to be sensibly larger than those measured at NTU, regardless of any size dependence. A possible explanation stems in the higher temperatures investigated at LPENS. Indeed, while at NTU, the sample was placed directly on the cryostat cold finger, at LPENS a stack of piezoelectric nanopositioners below the sample added significant load on the cryostat such that the lowest temperatures reached were slightly higher than 10 K, in contrast with the 4.5 K at NTU. At higher temperature, the intensity of higher lying exciton states, relatively to the lowest exciton state, are expected to increase. Thus, large energy splittings are more easily observed at higher temperatures as discussed previously and shown in FIG. 3.10. Indeed, with an energy splitting of 3 meV at 5 K we expect a relative intensity of 1×10^{-3}. At the typical signal levels we had at NTU, such emission lines would not have been observed.

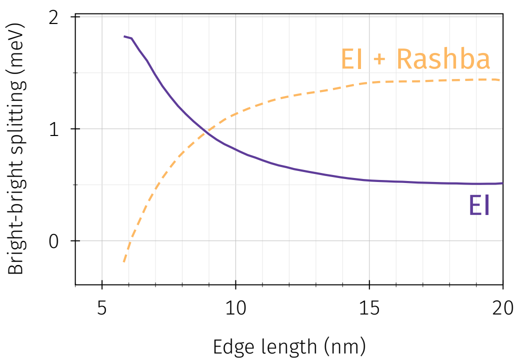

Figure 3.13 | Predicted bright-bright energy splittings. Bright-bright energy splittings for tetragonal $CsPbBr_3$ NCs taking into account both short-range and long-range exchange interaction as well as the Rashba effect. Deduced from the data in Fig. 1.10 reproduced from [24].

Literature Despite the wide range of NCs sizes explored, we do not evidence energy splittings much larger than previous reports [22] on $\sim$ 15 nm size NCs. Based on theoretical predictions, bright-bright energy splittings are expected to exhibit a dependence characteristic of the dominating interaction. As depicted in FIG. 3.13, in the pure exchange model, energy splittings are expected to increase with increasing confinement whereas, taking into account the Rashba effect the dependence is opposite. As such our observation on a large number of NCs with varying sizes provides crucial information for theoreticians to develop a realistic model of the exciton fine structure in single LHP NCs.

Summary

Diluted solutions of $CsPbBr_3$ were deposited on substrates and investigated using a home-made confocal microscope. Single $CsPbBr_3$ NCs were successfully isolated at cryogenic temperatures as evidenced by second order correlation measurements. The emission of single $CsPbBr_3$ is found to be stable in intensity but shows significant power-dependent spectral fluctuations. At low power, we studied the fine structure and polarisation properties of the bright triplet exciton. We evidence two- and three-peak spectra with strong linear polarisations consistent with a fully split triplet exciton. The actual polarisations and relative intensities observed are rationalised by taking into account both thermal occupation and the orientation of the crystallographic axes with respect to the detection axis. To test conflicting predictions of theoretical models taking into account both the exchange interaction and the Rashba effect or just the former, we measure bright triplet exciton splittings for NCs emitting from 2.3 to 2.7 meV, and reveal typical energy splittings $\Delta = 1.3 \pm 0.7$ meV for two-peaks spectra and $\Delta_1 = 1.0 \pm 0.5$ meV, $\Delta_2 = 1.16 \pm 0.60$ meV for three-peak spectra. This suggests intricate contributions of the NC size and shape which taken together may lead to blurring of the underlying dependencies. Doing so, we provide with a critical piece of information at the heart of the actual debate about the fine structure of LHP NCs hoping to motivate further studies.

3.2.3 A variety of Stokes-shifted emission peaks

We have discussed the bright triplet exciton emission and its polarisation. For these measurements, small acquisition times and high spectral resolution are usually required to minimise any linewidth broadening effects. However, because of those experimental choices, such spectra have a limited signal-to-noise ratio and can only be used to probe the most intense emission lines. In our studies, we also evidenced a set of low energy emission peaks with a weaker intensity. We study those here.

Methodology Thanks to the stability of their emission, we can study the emission of some single NCs with acquisition times on the order of seconds and tens of seconds to reveal low-intensity features without leading to significant broadening of the lines which would blur these spectral features. Alternatively, if emission lines are found to wander spectrally, we can study the low-intensity lines by constructing an idealised spectrum. This is done by monitoring the emission of a single NC in time, i.e. acquiring a set of spectra with small acquisition times (usually ≤ 250 ms) in an experiment we will refer to as a time trace. During analysis, spectral diffusion can then be eliminated by realigning the spectra. Doing so, the realigned spectra can be summed to obtain an idealised spectrum in the absence of spectral diffusion on the experiment time scale. We note however that we are still subject to sub-acquisition time spectral diffusion. Nonetheless, with these two complementary techniques, this means that we can study the low-energy low-intensity emission peaks of most NCs even those that show significant spectral fluctuations.

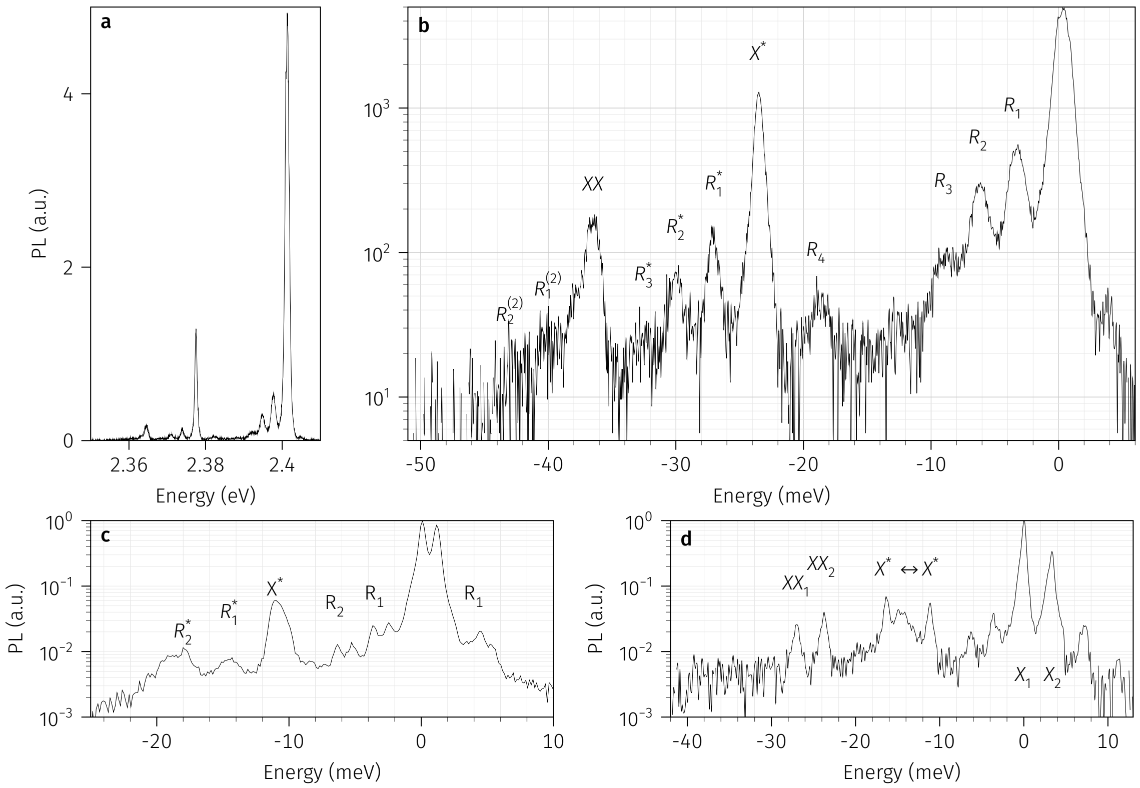

Figure 3.14 | Low-energy side of the exciton zero-phonon line. **a,b** Spectrum of a single NC shown in **a** linear and **b** logarithmic scale displaying a set of peaks below the bright exciton emission energy. Spectra highlighting the: **c** fine structure of optical phonon replica of the exciton line while the trion emission shows no fine structure; **d** fine structure of the biexciton (note that the trion splitting observed is due to a spectral shift during the long acquistion time measurement).

A forest of peaks There are several features of interest in the low energy spectrum of single NCs. An example is shown in Fig. 3.14, where an acquisition time of 10 s reveals a forest of peaks in the low-energy part of a single NC spectrum. Each of the bright exciton (X_B) zero-phonon lines (ZPL) is accompanied by a set of low energy optical phonon replica labelled R_i with $i = 1, \ldots, 4$ (Fig. 3.14b,c). Two sets of other emission lines are also observed and attributed to the trion (X^*) and biexciton (XX) recombination together with their respective lower energy optical phonon spectra labelled R_i^* and $R_j^{(2)}$ up to $i = 3$ and $j = 2$ (Fig. 3.14b-d). While the trion is observed even at low excitation power, it shows an intermittent emission and displays no fine structure (Fig. 3.14c). The biexciton only appears at higher power, is stable in intensity and displays a fine structure mirroring that of the exciton (FIG. 3.14d). The trion and biexciton themselves also exhibit the same set of optical phonon replica as the exciton, which can be resolved when their ZPL is intense enough. In the following, we study each class of peaks in detail and in particular we reveal their size-dependence.

Optical phonon replica

Most NCs exhibit a set of optical phonon replica related to the exciton line. As reported in a prior work [21], two optical phonon replica are observed on the vast majority of NCs at ~ 3.3 and 6.3 meV. Notably, for those two modes, we also observe anti-Stokes replica when not burried in the bright triplet fine structure.

More rarely, and not necessarily for the brightest NCs, we also observe two more peaks at 9 and 19 meV that we attribute to optical phonon replica of the exciton line. These are close to the modes reported in hybrid LHPs [9] and show weaker intensities here. These four replica are shown in FIG. 3.14a-b which display the full set of optical phonon replica observed in this work.

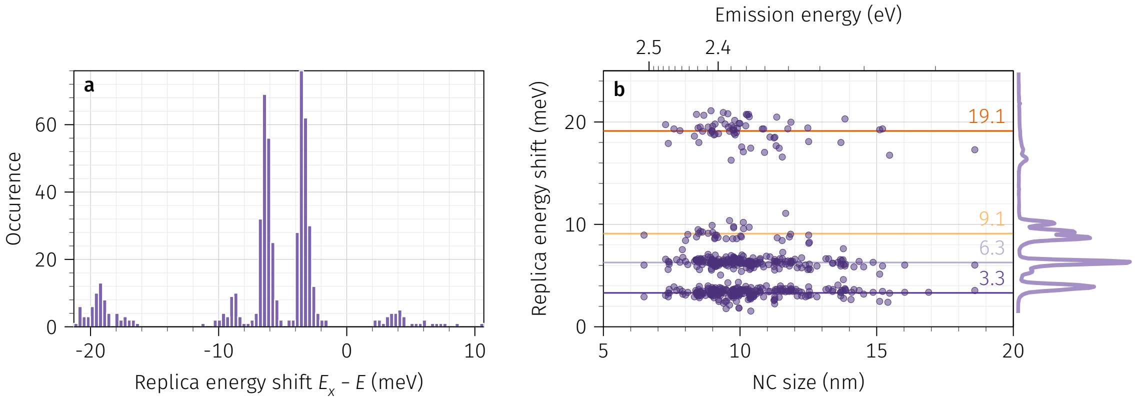

Figure 3.15 | Optical phonon replica. **a**, Statistics of the optical phonon replica observed in the PL of single NCs. **b**, Size-dependence of the optical phonon replica energies shown together with the mean energy of each mode observed. The trace ▬ on the right side of **b** is a 5 K Raman measurement adapted from [32].

The energies of the optical phonon replica observed in this work are summarised in FIG. 3.15 and reveal four distinct modes. To investigate the nature of these modes, we start with Raman measurements and the detailed results provided for $CsPbCl_3$ [33, 34] where three couples of transverse optical (TO) and longitudinal optical (LO) phonons were identified. Using the correspondance based on the ratio of the halogen mass $\sqrt{m_{\mathrm{Cl}}/m_{\mathrm{Br}}} \sim 2/3$ and assuming a linear monoatomic chain, we can estimate the phonon modes energies in $CsPbBr_3$ as

$E_{Br} \sim \sqrt{m_{Cl}/m_{Br}}\, E_{Cl}$. Based on [34], the corresponding energies for $CsPbBr_3$ are given for (TO_i, LO_i) as: $(3.1, 9.5)$meV, $(6.6, 18.5)$meV, $(9.5, 31)$meV. These energies match well with low-temperature Raman measurements where the first two modes close to R_1 and R_2, respectively at 3.3 and 6.3 meV, are attributed to the TO_1 and TO_2 modes. The third mode close to R_3, at 9.1 meV is resonant with both the TO_3 and LO_1 modes. The last mode, close to R_4, at 19.1 meV close to the LO_2 mode. Note that in our experiments, we did not resolve any peak at the expected LO_3 energy ~ 30 meV. As shown on the right side of FIG. 3.15b, the optical phonon replica energies observed here compare well with TO modes identified in low temperature Raman measurements such as in [32]. While modes with energies below ~ 12 meV are related to bending of the $PbBr_6$ cage, higher energy modes are related to stretching of the octahedra [35].

Notably, this assignment is similar to the one done for the hybrid perovskites $FAPbI_3$ and $FAPbBr_3$ where three longitudinal optical phonon modes are resolved at energies below 15 meV [9, 25, 36]. While the organic cation in hybrid perovskites may lead to significant hybridisation of low energy optical modes, a similar phonon landscape is expected in all LHPs. We therefore interpret the four optical phonon replica observed as related to longitudinal optical modes close to the TO modes observed in Raman. Further assignment of the observed energies to particular modes of the perovskite lattice would require detailed theoretical calculations of the vibrational landscape of inorganic LHPs, which require significant computing power due to the unit cell size increase in the orthorhombic phase and is beyond the scope of this work.

These replica are polarised like their respective exciton line which served as an indication for their identification. A single NC spectrum exhibiting two bright exciton peaks is shown in FIG. 3.16a for two orthogonal polarisations, each aligned with one of the bright exciton peaks. Examination of the spectra reveals the same set of optical phonon replica close to 3, 6, 9 and 19 meV for both peaks. Similarly, in FIG. 3.16b, we show a full polarisation measurement on a two-peak spectrum which reveals the polarisation of the brightest bright exciton peak. In this case, the replica related to the second bright exciton peak is not resolved due to its low intensity. Interestingly, in both FIG. 3.16a,b, we also observe an unpolarised emission line that we attribute to the trion as will be discussed later on.

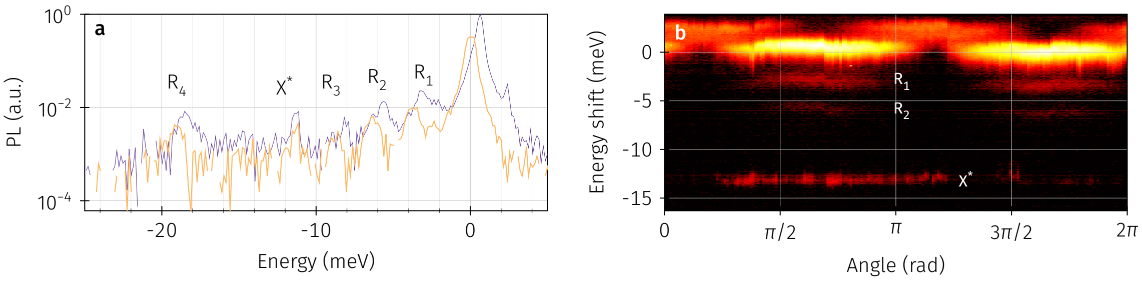

Figure 3.16 | Polarisation of optical phonon replica. **a**, Spectra of a two-peak NC acquired at two orthogonal polarisations. **b**, Spectrum of a NC displaying optical phonon replica as a function of the detection polarisation angle.

Trion and biexciton

At the low power investigated in this work, emission proceeds mainly through the exciton. However, emission of the exciton is usually accompanied by emission of charged excitons, i.e. trions, and/or biexciton (FIG. 3.14) ocurring at lower energy [9, 10]. Trion emission has been assigned to the negative trion, i.e. an exciton with an additional electron [11]. The negative trion and biexciton binding energies are defined as a function of their respective energies as $\Delta_{XX} = 2E_X - E_{XX}$ and $\Delta_{X^*} = E_X + E_{1e} - E_{X^*}$, where E_{1e} is the total energy of a single confined electron and E_X the energy of the single exciton [37]. Selection rule arguments reveal that the biexciton emission happens via the bright exciton state, such that the biexciton is expected to exhibit a fine structure related to that of the exciton [27, 37]. And indeed, this is observed experimentally here (FIG. 3.14d) and elsewhere [26], where the biexciton is found to exhibit a fine structure which mirrors that of the exciton.

In contrast, the trion is not expected to have a fine structure and none is resolved (FIG. 3.14c). However, in contrast to the stable emission of the biexciton, the trion exhibits an intermittent emission accompanied by large spectral shifts with respect to the exciton line on the order of a few meV (FIG. 3.14d). Based on these arguments alone, we can discriminate between the trion and biexciton emission for multi-peak spectra with a sufficient energy splitting. This assignment is supported by similar observations by a prior report [21] where this dispersion in energy was reported but no size-dependence was reported. Notably, we also observe some cases where the trion emission seemingly displays a fine stucture. Depending on the cases, this is attributed either to a resonant trion with the LO replica at 19 meV or a doubly charged exciton state as suggested in [11]. However, limited observations did not allow for detailed study.

Here, we record the energy of the trion and biexciton for NCs emitting from 2.3 to 2.5 eV

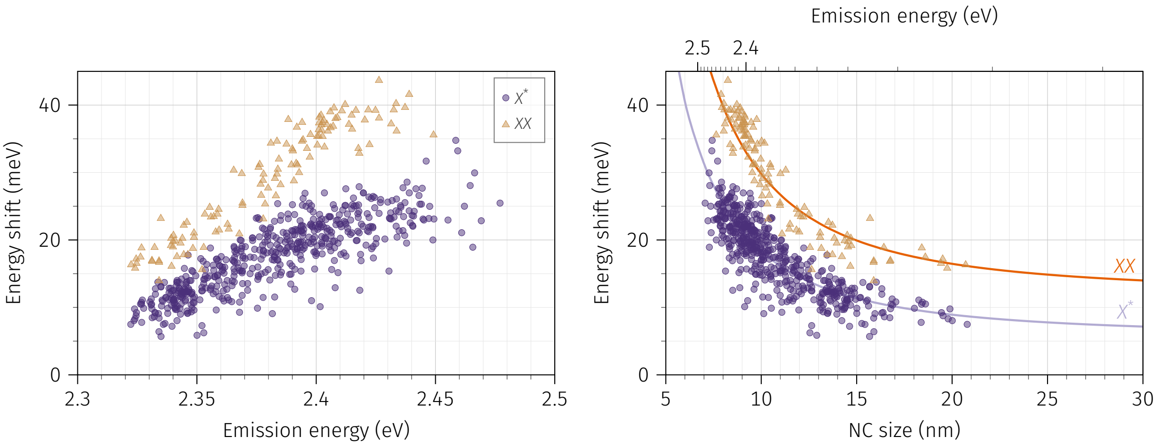

Figure 3.17 | Trion and biexciton. Statistic of trion and biexciton binding energies as a function of **a**, the emission energy and **b**, the NC size.

corresponding to sizes between 7 and 20 nm. Despite the dispersion of energy shifts observed at a given emission energy, Fig. 3.17 reveals a clear trend in the energy shift of the trion and biexciton as a function of emission energy, with energy shifts increasing with increasing confinement. This dependence is in qualitative agreement with the theoretical predictions of [37]. However, we find energy shifts up to 4 times larger than the prediction. It was in fact considered in [37] that predictions may be underestimated because of some approximations and lack of available data to refine the model. In this respect, our results provide critical information to be included in theoretical descriptions to refine our understanding of trions and biexcitons in LHPs.

Let us consider a phenomenological model to reproduce the trion and biexciton binding energies in Fig. 3.17. We write the binding energies as a sum of three terms: a confinement term, a Coulomb term and a bulk binding energy $E(L) = A/L^2 + B/L + C$, where A and B are constants and C is the bulk binding energy [38, 39]. For the trion, we find constants $A_{X^*} = 1240\,\text{meV}\,\text{nm}^2$, $B_{X^*} = 2.36\,\text{meV}\,\text{nm}$ and a bulk trion binding energy $C_{X^*} = 5.7\,\text{meV}$. For the biexciton, a better fit is given by the expression in the weak confinement regime where we can neglect the term in $1/L$ [39] such that we get $E(L) = A/L^2 + C$ with $A_{XX} = 1777\,\text{meV}\,\text{nm}^2$ and a bulk biexciton binding energy $C_{XX} = 12\,\text{meV}$. The recovered bulk binding energies compare well with previous reports on $CsPbBr_3$ and other LHPs [36].

Summary

In this section, we have provided the full spectral fingerprint of single $CsPbBr_3$ NCs as a function of their size. In addition to the bright triplet exciton together with its optical phonon replica, we also evidence emission from both the trion and biexciton together with their respective replica. For hundreds of NCs, we measure the energy shift of the observed spectral features and reveal their size dependence summarised in Fig. 3.18. Optical phonon replica are attributed to exciton coupling to specific modes of the perovskite lattice mainly related to the $PbBr_6$ cage. As expected, they show no dependence on the NC size in this intermediate confinement regime and can thus be attributed to bulk modes not related to the finite nature of the NC.

Figure 3.18 | Spectral fingerprint of single $CsPbBr_3$ nanocrystals. Full spectral fingerprint of single $CsPbBr_3$ NCs as a function of emission energy. For clarity, the trion and biexciton optical replica are omitted.

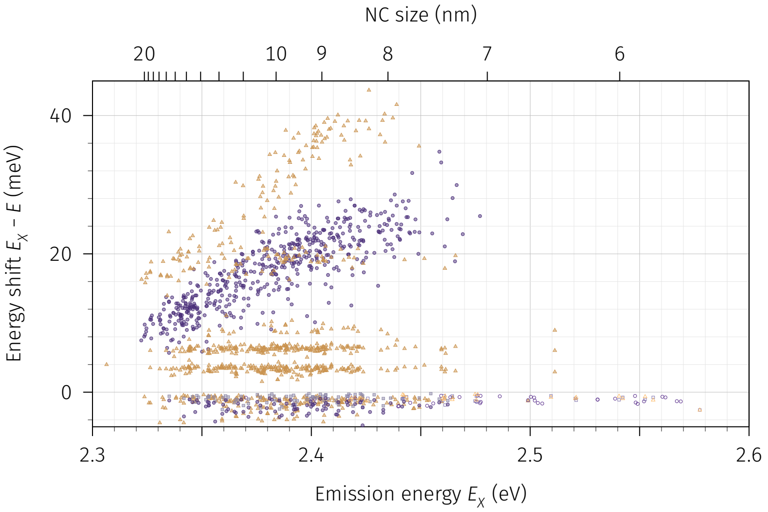

In contrast, both the trion and biexciton exhibit a clear energy shift as a function of the NC size which we reveal here in the PL of single NCs. Notably, thanks to the size-dependence this enables us to determine the bulk binding energies $\Delta_{\mathrm{XX,bulk}} \sim 12$ meV and $\Delta_{\mathrm{X^*,bulk}} \sim 5.7$ meV.

3.3 Temperature-dependent photoluminescence: spectral domain analysis

Up to now, we have discussed the optical properties of single NCs at the lowest cryogenic temperatures where interaction with phonons is minimised. To gain more insight into the coupling of carriers with lattice vibrations, we investigate the steady-state PL of single NCs as a function of temperature.

3.3.1 Bandgap thermal dependence

Established wurtzite and zinc-blende semiconductors usually exhibit decreasing bandgaps with increasing temperature as a result of the thermal expansion of the lattice. However, the band gap in LHPs exhibits a blueshift with increasing temperature as already evidenced in Pb-based materials [40, 41].

Theory

The thermal evolution of the band gap energy is a result of two competing mechanisms and can be written as [40, 42]

$$\left.\frac{\partial E_g}{\partial T}\right|_P = \left[\frac{\partial E_g}{\partial T}\right]_{TE} + \left[\frac{\partial E_g}{\partial T}\right]_{EP} = \left.\frac{\partial E_g}{\partial \ln V}\right|_T \left.\frac{\partial \ln V}{\partial T}\right|_P + \left.\frac{\partial E_g}{\partial T}\right|_V \tag{3.1}$$

The first term of equation (3.1) corresponds to product of the thermal expansion (TE) coefficient and a deformation potential, while the second term arise from electron-phonon interaction. As discussed on p. 34, the first term arises from the anharmonicity of the lattice potentials [43, 44] and leads to a shift in the relative energetic positions of the valence and conduction bands [45, 46]. The second term of (3.1) corresponds to the bandgap renormalisation caused by the temperature-dependent phonon occupation and the corresponding change in electron-phonon interaction (EP).

Empirical law In practice, these dependencies are usually summarised in the empirical Varshni law [47]. However, for LHPs, because of the complex interplay between thermal expansion and the bandgap renormalisation this empirical law is not applicable and we will see here that the emission energy of single $CsPbBr_3$ NCs exhibits a linear blueshift with increasing temperature, in agreement with [22].

Experiment

As exemplified in Fig. 3.19a-b, the emission of a single NC exhibits a blueshift with increasing temperature. Removing the thermally-induced blueshift by aligning spectra to the lowest bright exciton as in Fig. 3.19b reveals, here in logarithmic scale, that all peaks identified in the previous section exhibit the same blueshift with temperature, with only the trion exhibiting

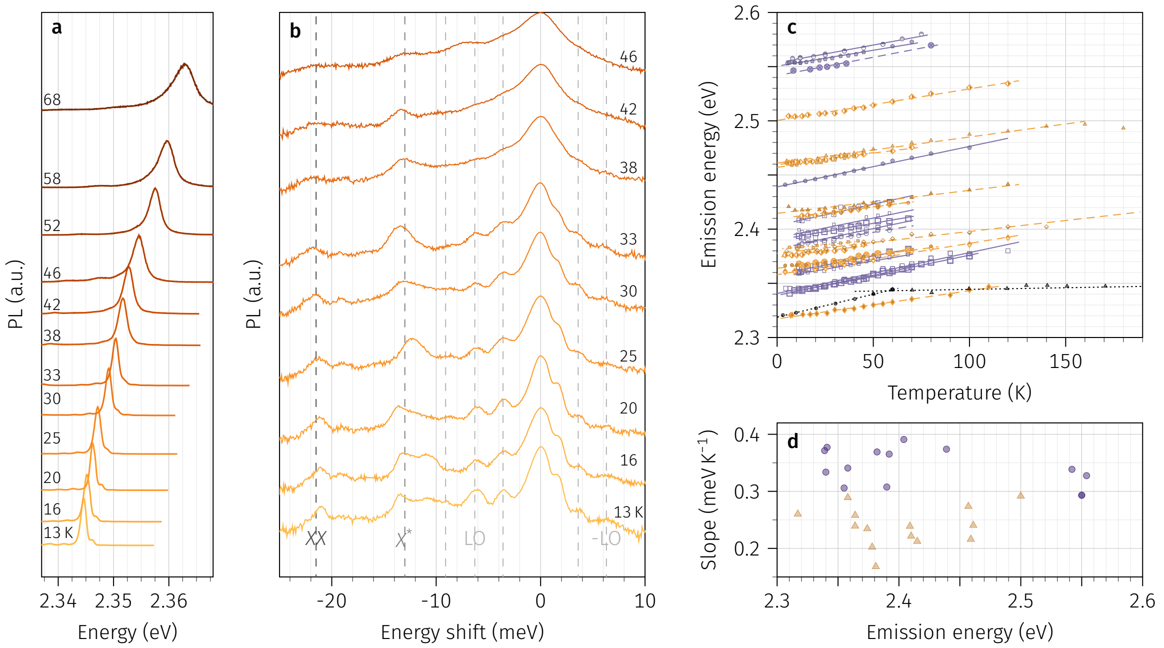

Figure 3.19 | Single nanocrystals' emission energy vs. temperature. Single NC spectrum as a function of temperature in **a** linear and **b** semi-logarithmic scale. **c**, Temperature dependence of the emission energy of 29 single NCs. In black, we show emission energies of a single $CsPbBr_3$ bulk crystal reproduced from [32]. **d**, Emission energy dependence of the slope of $E(T)$ as deduced from **c**. Note that colours in **c** and **d** are for illustration purposes and only indicate slopes larger —, resp. smaller --, than the median of sampled values.

spectral fluctuations at all temperatures. This thermally-induced blueshift is found to be linear up to $\sim$ 100 K with a mean slope of 0.3±9.0 meV K^{-1} and values ranging from $\sim$ 0.2 to 0.4. In Fig. 3.19c, we summarise the emission energy of the lowest bright exciton state as a function of temperature for more than 20 NCs with low-temperature emission energies ranging from 2.3 to 2.55 eV corresponding to NC sizes down to 6 nm. We also show the bandgap energy of bulk $CsPbBr_3$ as a function of temperature (--) showing a slope of 0.4 meV K^{-1}. This corresponds to the upper limit of observed values on single NCs, as shown in Fig. 3.19d where we summarise the slopes observed across all NCs.

In contrast with other reports on hybrid LHPs [9], the temperature dependence of the emission energy is linear up to $\sim$ 100 K and shows no sign of non-monotonous behaviour associated with phase transitions.

3.3.2 Linewidth thermal dependence

The exciton zero-phonon line emission is a lorentzian line which shows a thermally-induced linewidth broadening. This broadening is understood as an interaction of the exciton with phonons, and as such its study provides invaluable information into exciton-phonon coupling in these low-dimensional LHPs.

Experiment

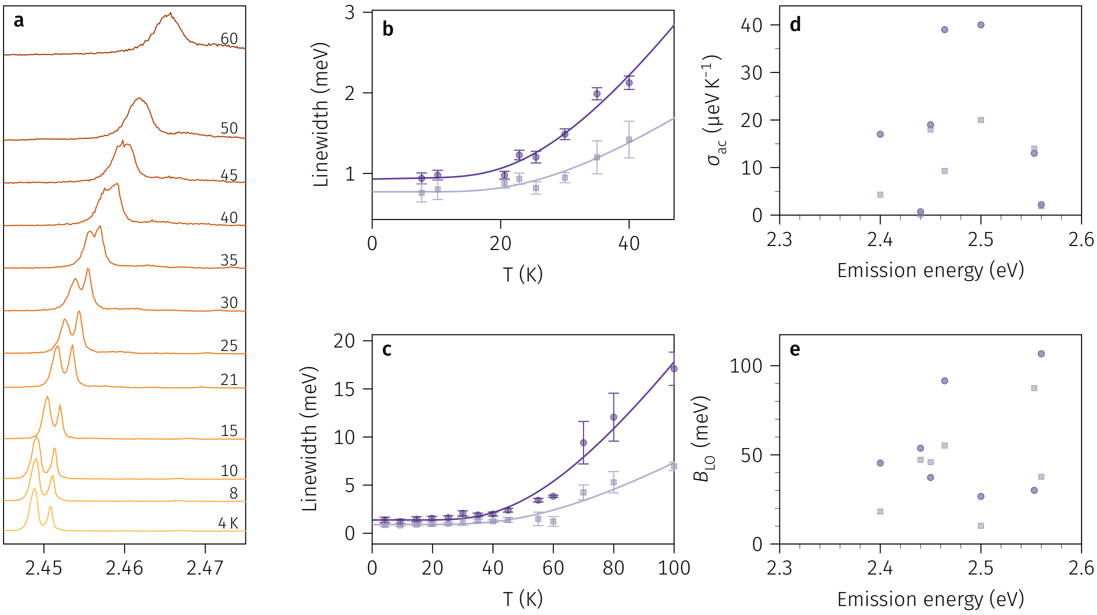

Figure 3.20 | Single nanocrystals' emission linewidth vs. temperature. **a**, Spectrum of a single two-peak NC as a function of temperature and **b**, corresponding linewidths. **c**, Temperature-dependence of the linewidth of another two-peak NC. **d**, Summary of recovered acoustic phonon coupling parameter. **e**, Summary of recovered optical phonon coupling parameter.

We follow the emission of single NCs as a function of temperature. Fig. 3.20a shows the temperature-dependence of the emission of a single two-peak NC. Notably, in this case we can observe a thermally-induced redistribution of the population between the two exciton states not always observed. For such two-peak spectra with a sufficient energy splitting, we can study the emission linewidth of each peak as a function of temperature. Two examples are shown in Fig. 3.20b,c where the linewidths follow a weak linear dependence at low temperature before interaction with optical phonons dominates.

Model

Dephasing origin Based on the equations developped in [48], we can express the temperature-dependence of the emission linewidth as a sum of the exciton-acoustic phonon and exciton-optical phonon interaction terms. In general, the contribution to the linewidth of a particular coupling mechanism is given by $cn_B(T)$, where c is the coupling constant. For acoustic phonons, we can assume a linear coupling in light of the low energies reported . In this case, we can write the linewidth as [48]

$$\varGamma_{\mathrm{PL}}(T) = \varGamma_0 + \varGamma_{\mathrm{ac}} + \varGamma_{\mathrm{opt}} = \varGamma_0 + \sigma_{\mathrm{ac}} T + \gamma_{\mathrm{opt}} n_B(T) \tag{3.2}$$

where $n_B(T) = \left(\exp\left(E_{\mathrm{opt}/k_B T}\right) - 1\right)^{-1}$.

We can further express each coupling coefficient σ_{ac} and γ_{opt} the acoustic and optical coupling strengths respectively dependent on the actual mechanisms.

Acoustic phonons The acoustic phonon coupling coefficient σ_{ac}, due to the deformation potential, can be estimated as [48]

$$\sigma_{\mathrm{ac}} = \frac{M^2 k_B (D_e - D_h)^2}{\pi v \varrho \hbar^3} \sim \mu\mathrm{eV\,K^{-1}} \tag{3.3}$$

The acoustic phonon coefficient in LHPs is found to be smaller than in GaAs or CdS [48]. For hybrid $FAPbI_3$, a value of 0.4 μeV K^{-1} was reported, while for $CsPbBr_3$ this contribution was found to be negligible. Other reports completely neglect this part. In fact, this contribution may not be observable in ensembles due to averaging effects. At the single NC level, emission linewidths are already broadened ~ 1 meV at liquid helium temperature, due to pure dephasing, the limited spectral resolution in experiments and spectral diffusion, such that the initial linear contribution to broadening of acoustic phonons is difficult to resolve. In fact, we can distinguish between the contributions related to pure dephasing and spectral diffusion. While the former leads to linewidth broadening of the lorentzian line, spectral diffusion leads to a gaussian line.

Optical phonons For optical phonons, coupling happens mainly through Fröhlich interaction with typical coupling strengths as shown in Tab. 3.2. For LHPs, it is the most reported term with coupling to a mode near 16 meV related to Pb−Br stretching [49]. Optical phonon coupling constants B_{LO} reported show a wide variability. Focusing on studies at the single object level, Ramade et al. reported an average $B_{\mathrm{LO}} = 42 \pm 15$ meV coupling to a single phonon mode at 16 meV, assuming the bulk phonon energy [50]. For NCs, Fröhlich interaction in $CsPbBr_3$ was reported to proceed predominantly through a single phonon mode at 19 meV [51]. For smaller NCs however, coupling to lower energy surface modes was reported to be responsible for the increased emission linewidths [52].

Table 3.2 | Reported linewidth parameters. Values of the linewidth parameters for the different materials.

Material	Γ_0 (meV)	A_{ac} (μeV K^{-1})	B_{LO} (meV)	E_{LO} (meV)	Γ(300 K) (meV)	Refs.
GaN	2.8	21	525	91.5	21.9	[53]
CdTe QDs	50-55	14-33	14-21	20-22	65-85	[54]
InAs/GaAs QD	0.007	1.55			0.5	[55]
$CsPbBr_3$ NC	0.40 ± 0.08	8 ± 3	42 ± 15	16	10	[50]
$FAPbBr_3$ NC	2.6	0	31.8	13.2	50	[56]
$CsPbI_3$?						
$MoSe_2$	4.3	91	15.6	30	40	[57]
WS_2	9.2	28	6.5	20	25	[57]
(9,4) CNTs	6	32 ± 3	11 ± 4	25	21	[58]

Fitting parameters FIG. 3.20d,e shows the recovered acoustic and optical phonon coupling strenghs for several single NCs. The acoustic phonon coupling coefficient is found to be on the order of tens of μeV K^{-1}, slightly larger than a previous report [50]. Optical phonon coupling coefficients are found to be on the order of tens of meV, on par with previous reports. While we observe an optical phonon replica at $\sim$19 meV, concomittant least squares optimisation of both linewidths dependences with a shared phonon mode energy readily yields comparable values. Notably, in most cases, we find that the lowest exciton state couples more strongly than the higher lying state.

Thus, as per previous reports the linear contribution of acoustic phonons is weak and linewidth broadening is dominated by optical phonons for temperatures as low as $\sim$ 20 K.

Ill-defined lineshapes Due to the high number of peaks observed near the bright exciton ZPL, the peak linewidths are not well-defined as the underlying emisison lines cannot be resolved. Indeed, already at temperatures close to 20 K, due to the typical linewidths $\sim$ 1 meV and neighbouring replica, the ZPL linewidth is ill-defined. To illustrate this point, we show in FIG. 3.20 the evolution of two single NC spectra as a function of temperature.

At low temperature, the ZPL and its phonon replica can be clearly identified. As temperature is increased, the phonon replica are burried in the tail of the ZPL such that ultimately we observe a non-lorentzian lineshape. As such, already at temperatures as low as 30 K, the linewidth of a single NC PL is ill-defined and both the ZPL and optical phonon replica need to be taken into account. In fact, even what we refer to here as the exciton ZPL itself is not lorentzian. Indeed, as

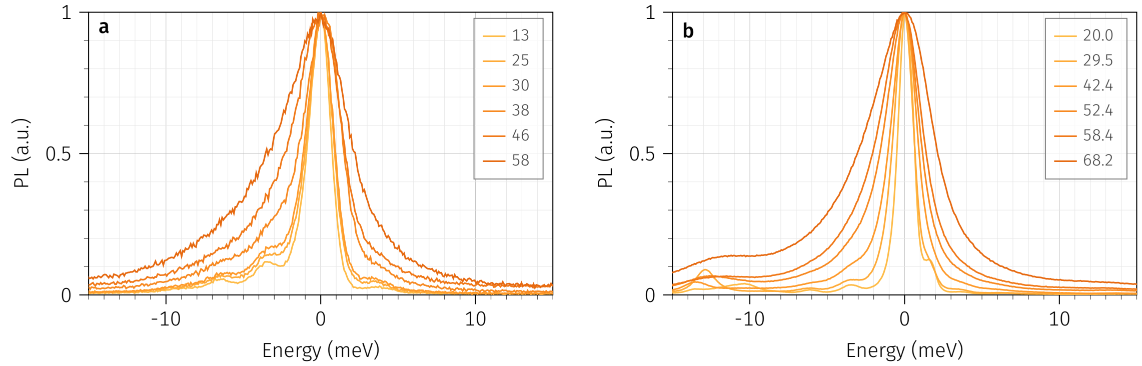

Figure 3.21 | Evolution of ZPL and replica with T. Two single NCs spectra as a function of temperature. The proximity of both Stokes and anti-Stokes optical phonon replica lead to asymmetric lines with ill-defined lineshapes depending on the actual resolution and experiment temperature.

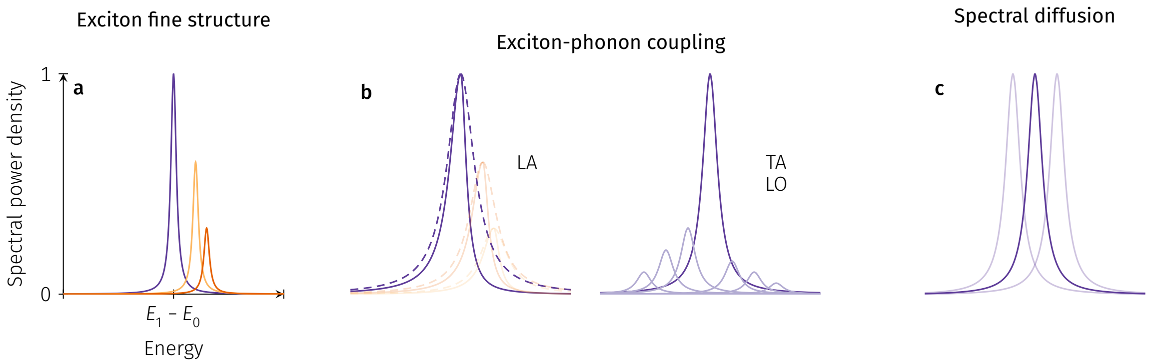

Figure 3.22 | Deconstructing single nanocrystal spectra. Single NC spectra are the result of several combined effects. **a**, The exciton fine structure is revealed in the multiple emission peaks at low temperature. The Fourier-limited spectrum broadens with increasing temperature. **b,c**, Both Stokes and anti-Stokes acoustic and optical phonon replica emerge together with an acoustic phonon pedestal. **d** The full set of emission lines can further exhibit spectral wandering on time scales from ns to s.

demonstrated in the low temperature PL of epitaxial quantum dots [55] and carbon nanotubes [59], the exciton emission consists in a ZPL accompanied by low and high energy acoustic phonon sidebands related to the recombination of the exciton with simultaneous emission/absorption of a phonon. The emission lineshape is therefore to be understood as asymmetric at low temperature where absorption of a phonon is more probable, while as temperature is increased, the high energy acoustic sideband relatively brightens and a symmetric lineshape is recovered. This was recently evidenced on single $CsPbI_3$ NCs under resonant excitation, where coupling to both size-quantised TA and a continuum of LA phonons was reported [19]. Already at 10 K, while under resonant excitation, the exciton emission exhibits a non-lorentzian lineshape characterised by a full-width at half-maximum $\sim 130\,\mu eV$ and additional low-and high energy tails. Thus in fact, the emission of a single perovskite NC is a subtle interplay between several contributions summarised in Fig. 3.22.

Conclusion

In this work, we have synthesised several batches of $CsPbBr_3$ NCs with emission energies ranging from 2.3 meV to 2.7 meV and corresponding sizes between 7 to 20 nm. With a home-made scanning confocal microscope, we isolated single NCs at cryogenic temperature and studied the optical spectra of hundreds of single NCs. Based on the dataset acquired in this work, we have provided with the full spectral fingerpring of single $CsPbBr_3$ across NC sizes ranging from 7 to 20 nm. Notably, in addition to the bright exciton ZPL, we observe both Stokes and anti-Stokes optical phonon replica related to modes of the lead halide cage. Most NCs investigated also exhibit emission from the trion X^* even at low excitation powers, while emission of the biexciton XX appears at higher excitation powers. We evidence the size-dependence of both the exciton and trion energy shifts showing an increase with increasing confinement. Finally, we have also investigated the interaction between carriers and lattice vibrations via the temperature-dependence of the emission single NCs. Doing so, we observe the peculiar blueshift with increasing temperature exhibited by LHPs and other Pb-based coumpounds and study the temperature-dependence of the emission linewidth.

References for Chapter 3

[1] M. C. Brennan et al., “Origin of the Size-Dependent Stokes Shift in $CsPbBr_3$ Perovskite Nanocrystals”, Journal of the American Chemical Society **139**, 12201–12208 (2017) (p. 91).

[2] M. C. Brennan et al., “Universal Size-Dependent Stokes Shifts in Lead Halide Perovskite Nanocrystals”, The Journal of Physical Chemistry Letters **11**, 4937–4944 (2020) (p. 91).

[3] Y. Yu et al., “Atomic Resolution Imaging of Halide Perovskites”, Nano Letters **16**, 7530–7535 (2016) (p. 91).

[4] A. Dutta et al., “Tuning the Size of $CsPbBr_3$ Nanocrystals: All at One Constant Temperature”, ACS Energy Letters **3**, 329–334 (2018) (p. 91).

[5] Y. Dong et al., “Precise Control of Quantum Confinement in Cesium Lead Halide Perovskite Quantum Dots via Thermodynamic Equilibrium”, Nano Letters **18**, 3716–3722 (2018) (p. 91).

[6] Y.-S. Park et al., “Room Temperature Single-Photon Emission from Individual Perovskite Quantum Dots”, ACS Nano **9**, 10386–10393 (2015) (pp. 95, 97).

[7] G. Rainò et al., “Underestimated Effect of a Polymer Matrix on the Light Emission of Single $CsPbBr_3$ Nanocrystals”, Nano Letters **19**, 3648–3653 (2019) (p. 95).

[8] F. Hu et al., “Superior Optical Properties of Perovskite Nanocrystals as Single Photon Emitters”, ACS Nano **9**, 12410–12416 (2015) (p. 97).

[9] M. Fu et al., “Unraveling exciton–phonon coupling in individual $FAPbI_3$ nanocrystals emitting near-infrared single photons”, Nature Communications **9**, 3318 (2018) (pp. 97, 108, 114–116, 120).

[10] G. Rainò et al., “Single Cesium Lead Halide Perovskite Nanocrystals at Low Temperature: Fast Single-Photon Emission, Reduced Blinking, and Exciton Fine Structure”, ACS Nano **10**, 2485–2490 (2016) (pp. 97, 116).

[11] C. Yin et al., “Bright-Exciton Fine-Structure Splittings in Single Perovskite Nanocrystals”, Physical Review Letters **119**, 6401 (2017) (pp. 97, 100, 116).

[12] P. Michler et al., “Quantum correlation among photons from a single quantum dot at room temperature”, Nature **406**, 968–970 (2000) (p. 98).

[13] N. A. Gibson et al., “Excitation Intensity Dependence of Photoluminescence Blinking in $CsPbBr_3$ Perovskite Nanocrystals”, The Journal of Physical Chemistry C **122**, 12106–12113 (2018) (p. 98).

[14] L. Hou et al., “Memories in the photoluminescence intermittency of single cesium lead bromide nanocrystals”, Nanoscale **12**, 6795–6802 (2020) (p. 98).

[15] I. M. Palstra et al., “Intermittency of $CsPbBr_3$ Perovskite Quantum Dots Analyzed by an Unbiased Statistical Analysis”, The Journal of Physical Chemistry C **125**, 12061–12072 (2021) (p. 98).

[16] S. A. Empedocles, “Quantum-Confined Stark Effect in Single CdSe Nanocrystallite Quantum Dots”, Science **278**, 2114–2117 (1997) (p. 98).

[17] S. A. Blanton et al., “Photoluminescence wandering in single CdSe nanocrystals”, Applied Physics Letters **69**, 3905–3907 (1996) (p. 98).

[18] S. A. Empedocles et al., “Influence of Spectral Diffusion on the Line Shapes of Single CdSe Nanocrystallite Quantum Dots”, The Journal of Physical Chemistry B **103**, 1826–1830 (1999) (p. 98).

[19] Y. Lv et al., “Exciton-acoustic phonon coupling revealed by resonant excitation of single perovskite nanocrystals”, Nature Communications **12**, 2192 (2021) (pp. 99, 124).

[20] Z. Yang et al., “Impact of the Halide Cage on the Electronic Properties of Fully Inorganic Cesium Lead Halide Perovskites”, ACS Energy Letters **2**, 1621–1627 (2017) (p. 100).

[21] M. Fu et al., “Neutral and Charged Exciton Fine Structure in Single Lead Halide Perovskite Nanocrystals Revealed by Magneto-optical Spectroscopy”, Nano Letters **17**, 2895–2901 (2017) (pp. 100, 108, 110, 114, 116).

[22] J. Ramade et al., “Fine structure of excitons and electron–hole exchange energy in polymorphic $CsPbBr_3$ single nanocrystals”, Nanoscale **10**, 6393–6401 (2018) (pp. 100, 110, 111, 119).

[23] R. Ben Aich et al., “Bright-Exciton Splittings in Inorganic Cesium Lead Halide Perovskite Nanocrystals”, Physical Review Applied **11**, 034042 (2019) (pp. 101, 105, 108).

[24] P. C. Sercel et al., “Exciton Fine Structure in Perovskite Nanocrystals”, Nano Letters **19**, 4068–4077 (2019) (pp. 101, 103, 108, 111).

[25] P. Tamarat et al., “The ground exciton state of formamidinium lead bromide perovskite nanocrystals is a singlet dark state”, Nature Materials **18**, 717–724 (2019) (pp. 101, 108, 115).

[26] P. Tamarat et al., “The dark exciton ground state promotes photon-pair emission in individual perovskite nanocrystals”, Nature Communications **11**, 6001 (2020) (pp. 101, 105, 108, 116).

[27] M. A. Becker et al., “Bright triplet excitons in caesium lead halide perovskites”, Nature **553**, 189–193 (2018) (pp. 101, 103–105, 108, 110, 116).

[28] P. C. Sercel et al., “Quasicubic model for metal halide perovskite nanocrystals”, The Journal of Chemical Physics **151**, 234106 (2019) (pp. 105, 108).

[29] C. Lethiec et al., “Measurement of Three-Dimensional Dipole Orientation of a Single Fluorescent Nanoemitter by Emission Polarization Analysis”, Physical Review X **4**, 021037 (2014) (p. 105).

[30] F. Bertolotti et al., “Crystal Structure, Morphology, and Surface Termination of Cyan-Emissive, Six-Monolayers-Thick $CsPbBr_3$ Nanoplatelets from X-ray Total Scattering”, ACS Nano **13**, 14294–14307 (2019) (p. 107).

[31] A. Schmitz et al., “Optical Probing of Crystal Lattice Configurations in Single $CsPbBr_3$ Nanoplatelets”, Nano Letters, acs.nanolett.1c02775 (2021) (p. 107).

[32] Y. Guo et al., “Dynamic emission Stokes shift and liquid-like dielectric solvation of band edge carriers in lead-halide perovskites”, Nature Communications **10**, 1175 (2019) (pp. 114, 115, 120).

[33] S. Hirotsu, “Experimental Studies of Structural Phase Transitions in $CsPbCl_3$”, Journal of the Physical Society of Japan **31**, 552–560 (1971) (p. 114).

[34] D. M. Calistru et al., “Identification of the symmetry of phonon modes in $CsPbCl_3$ in phase IV by Raman and resonance-Raman scattering”, Journal of Applied Physics **82**, 5391–5395 (1997) (pp. 114, 115).

[35] K. Miyata et al., “Large polarons in lead halide perovskites”, Science Advances **3**, e1701217 (2017) (p. 115).

[36] K. Cho et al., “Luminescence Fine Structures in Single Lead Halide Perovskite Nanocrystals: Size Dependence of the Exciton–Phonon Coupling”, Nano Letters **21**, 7206–7212 (2021) (pp. 115, 117).

[37] T. P. T. Nguyen et al., “Calculation of the biexciton shift in nanocrystals of inorganic perovskites”, Physical Review B **101**, 125424 (2020) (pp. 116, 117).

[38] T. Takagahara, “Biexciton states in semiconductor quantum dots and their nonlinear optical properties”, Physical Review B **39**, 10206–10231 (1989) (p. 117).

[39] Y. Masumoto et al., “Biexciton binding energy in CuCl quantum dots”, Physical Review B **50**, 18658–18661 (1994) (p. 117).

[40] M. Schlüter et al., “Pressure and temperature dependence of electronic energy levels in PbSe and PbTe”, Physical Review B **12**, 650–658 (1975) (p. 119).

[41] M. S. Gaponenko et al., “Temperature-dependent photoluminescence of PbS quantum dots in glass: Evidence of exciton state splitting and carrier trapping”, Physical Review B **82**, 125320 (2010) (p. 119).

[42] P. B. Allen et al., “Theory of the temperature dependence of the direct gap of germanium”, Physical Review B **23**, 1495–1505 (1981) (p. 119).

[43] G. Mie, “Zur kinetischen Theorie der einatomigen Körper”, Annalen der Physik **316**, 657–697 (1903) (p. 119).

[44] E. Grüneisen, “Zusammenhang zwischen Kompressibilität, thermischer Ausdehnung, Atomvolumen und Atomwärme der Metalle”, Annalen der Physik **331**, 393–402 (1908) (p. 119).

[45] F. Möglich et al., “Über den einfluß der wärmedehnung auf das absorptionsspektrum von isolatoren”, Zeitschrift für Physik **119**, 472–481 (1942) (p. 119).

[46] J. Bardeen et al., “Deformation Potentials and Mobilities in Non-Polar Crystals”, Physical Review **80**, 72–80 (1950) (p. 119).

[47] Y. P. Varshni, “Temperature dependence of the energy gap in semiconductors”, Physica **34**, 149–154 (1967) (p. 119).

[48] S. Rudin et al., “Temperature-dependent exciton linewidths in semiconductors”, Physical Review B **42**, 11218 (1990) (pp. 121, 122).

[49] A. D. Wright et al., “Electron–phonon coupling in hybrid lead halide perovskites”, Nature Communications **7**, 11755 (2016) (p. 122).

[50] J. Ramade et al., “Exciton-phonon coupling in a $CsPbBr_3$ single nanocrystal”, Applied Physics Letters **112**, 072104 (2018) (pp. 122, 123).

[51] C. M. Iaru et al., “Fröhlich interaction dominated by a single phonon mode in $CsPbBr_3$”, Nature Communications **12**, 5844 (2021) (p. 122).

[52] G. Rainò et al., “Ultra-narrow room-temperature emission from single $CsPbBr_3$ perovskite quantum dots”, Nature Communications **13**, 2587 (2022) (p. 122).

[53] X. B. Zhang et al., “Influence of electron-phonon interaction on the optical properties of III nitride semiconductors”, Journal of Physics: Condensed Matter **13**, 7053 (2001) (p. 123).

[54] G. Morello et al., “Temperature and Size Dependence of Nonradiative Relaxation and Exciton–Phonon Coupling in Colloidal CdTe Quantum Dots”, The Journal of Physical Chemistry C **111**, 5846–5849 (2007) (p. 123).

[55] I. Favero et al., “Temperature dependence of the zero-phonon linewidth in quantum dots: An effect of the fluctuating environment”, Physical Review B **75**, `10.1103/PhysRevB.75.073308` (2007) (pp. 123, 124).

[56] O. Pfingsten et al., “Phonon Interaction and Phase Transition in Single Formamidinium Lead Bromide Quantum Dots”, Nano Letters **18**, 4440–4446 (2018) (p. 123).

[57] M. Selig et al., “Excitonic linewidth and coherence lifetime in monolayer transition metal dichalcogenides”, Nature Communications **7**, 13279 (2016) (p. 123).

[58] D. T. Nguyen et al., “Excitonic homogeneous broadening in single-wall carbon nanotubes”, Chemical Physics, Photophysics of Carbon Nanotubes and Nanotube Composites **413**, 102–111 (2013) (p. 123).

[59] F. Vialla et al., “Unifying the Low-Temperature Photoluminescence Spectra of Carbon Nanotubes: The Role of Acoustic Phonon Confinement”, Physical Review Letters **113**, 057402 (2014) (p. 124).

4

Exciton recombination dynamics

Perovskite NCs have gained a lot of attention recently due to their outstanding properties. Indeed, compared to established wurtzite and zinc-blende NCs, perovskite NCs exhibit a bright emission without the need of complex passivation. However, seemingly in contrast with this efficient emission, the low temperature decay of single LHP NCs is found to be faster than at room temperature, nearly two orders of magnitude faster than in conventional NCs. This is striking as usually such fast rates are associated with non-radiative decay channels that deplete the emission. This lead Becker et al. to postulate in 2018 that due to the strong spin-orbit coupling in LHPs the Rashba effect could lead to a level inversion, with a bright exciton as the lowest energy state [1]. The community soon embraced this idea, and the statement can be found as an affirmation in the introduction of many papers as an explanation for the brightness of LHP NCs. However, as first demonstrated on $FAPbBr_3$ in 2019, a fast decay time can coexist with a dark exciton below the bright exciton [2]. Further work by the same team revealed that an inorganic LHP, $CsPbI_3$, also exhibited a dark exciton state below the bright state [3]. In light of these results, we set ourselves to investigate the case of the prototypal $CsPbBr_3$ for which the original prediction of [1] was made.

In the preceding chapter, we have investigated the steady-state photoluminescence (PL) of single NCs. While these experiments provide invaluable information about the spectral properties of a single NC emission, all the information about the actual photon stream is lost and only the total number of detection events with the acquitisiton time (≥ms) is resolved. In contrast, in this chapter, we investigate the PL of single NCs with single photon detectivity down to the ps scale. In SEC. 4.1, we investigate the time-resolved emission of single $CsPbBr_3$ NCs at the lowest cryogenic temperatures (∼4.5 K) with time-resolved PL decay measurements. In SEC. 4.2, we report on studies that aimed at probing the dark exciton state in $CsPbBr_3$. First, in SEC. 4.2.1 we report on our attempt to magnetically brighten the dark exciton state via magneto-optical measurements on single NCs. Our results show no emerge of an additional peak with magnetic field strengths up to 5 T. Alternatively in SEC. 4.2.2 we investigate the temperature-dependence of the PL decay in an attempt to probe the dark exciton state indirectly. Based on these results and a complementary model, we investigate the phase space of possible values for the bright-dark energy splitting and phonon-assisted transition rates between these states for six scenarios varying both the level ordering and the thermal mixing scheme.

4.1 Time-resolved photoluminescence of single NCs

Perovskite NCs, and especially those Br- and Cl-based, exhibit a fast decay at low temperatures on the order of a few 100 ps, much faster than conventional NCs. In this section, we report on measurements of the PL decay of single $CsPbBr_3$ NCs. As these decay times approach the timing-resolution of the fastest single photon couting detectors, special attention is given to the timing resolution and its effect on the recovered timing parameters.

Decay measurements

We measure the PL decay of single NCs at cryogenic temperature using the experimental setup detailed in FIG. 2.9. NCs are excited using a frequency-doubled Ti:Sa laser with ~ 100 fs pulses and an 80 MHz repetition rate. The emission of the bright triplet exciton is selected using a monochromator and detected with an avalanche photodiode at the output. At the lowest temperatures investigated (~ 4.5 K), the emission of the bright exciton triplet is found to be totally depleted within 2 ns after the excitation pulse. Fitting the decays using the reconvolution method described in SEC. 2.3.3, we find mono-exponential decay times with a mean decay time $\tau = 60 \pm 20$ ps, ranging from 40 ps to ~ 100 ps (FIG. 4.1a,b).

Notably, we also measured the PL decay of each of the bright states, as shown in FIG. 4.1c for

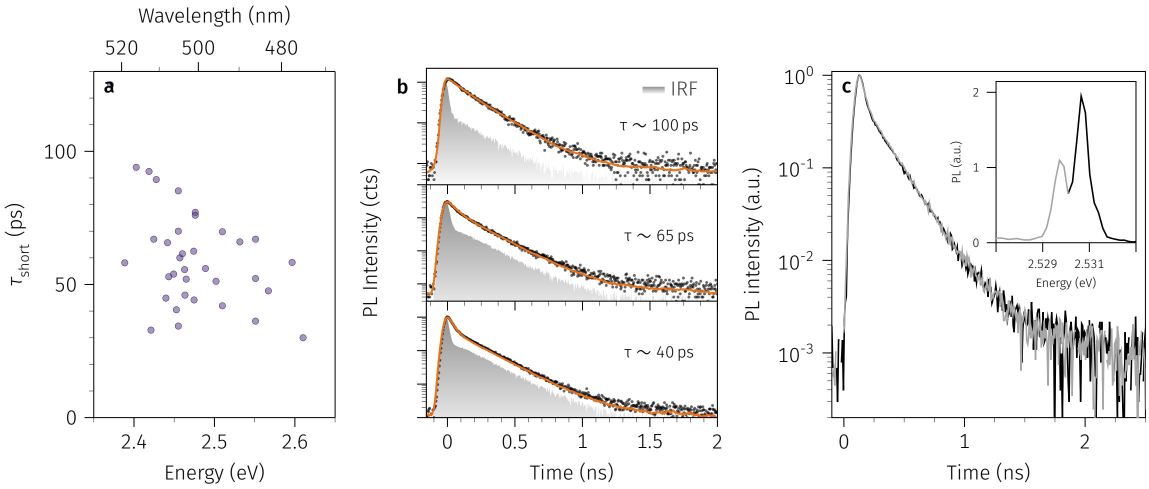

Figure 4.1 | Single nanocrystal decay at 4.5 K. **a**, Statistics of the fast mono-exponential decay time. **b**, Selected single NC decays highlighting the spread of observed values from 40 to 100 ps. **c**, PL decay of each emission line of a two-peak NC.

a two-peak NC by spectrally filtering the emission and find indistinguishible decay curves. While this measurement was only performed on a single NC, we will assume in the rest that this holds generally as other works have reported similar decays for the triplet exciton [4].

Emission energy dependence We observe no clear dependence of the decay times on the emission energy while in the intermediate confinement regime investigated here, decay times are expected to increase with increasing confinement up to $\sim a_B$ [1, 5]. The absence of a clear size-dependence may be explained by the limited sample size in FIG. 4.1 which prevents observation of a dependence because of sample inhomogeneities. Indeed, the actual morphology of the NCs, their passivation degree as well as their dielectric environment have a non-trivial role that may here blur this effect. As the NC size is reduced, the surface-to-volume ratio increases ($\propto L^{-1}$) such that for smaller NCs the incomplete passivation of the surface is expected to play a growing role. This expected dependence is opposite to that expected solely based on confinement effects, and as such may explain the absence of any clear dependence in these NCs with first generation ligands.

Dielectric environment The radiative lifetime of the bright triplet exciton in cube-shaped NCs can be written as $\tau \propto (nI_\parallel^2)^{-1}$ where n is the refractive index of the medium surrounding the NC and $I_\parallel$ is an overlap integral that describes the coupling between the exciton dipole and the electric field of a photon in the NC [1]. In our experiments, NCs are deposited in a polystyrene (PS) matrix with a few tens of nm thickness such that they experience a dielectric environment between two extrema $n_1 = 1$, corresponding to a NC at the PS/air interface, and $n_2 = 1.6$, corresponding to a NC embedded deep inside the layer. We thus expect the ratio between decay times to be given by $\tau_2/\tau_1 \propto n_1/n_2 \sim 0.63$. Experimentally, we have $\tau_2/\tau_1 \sim 0.4$ which compares well with the variable dielectric environment of NCs.

Discussion

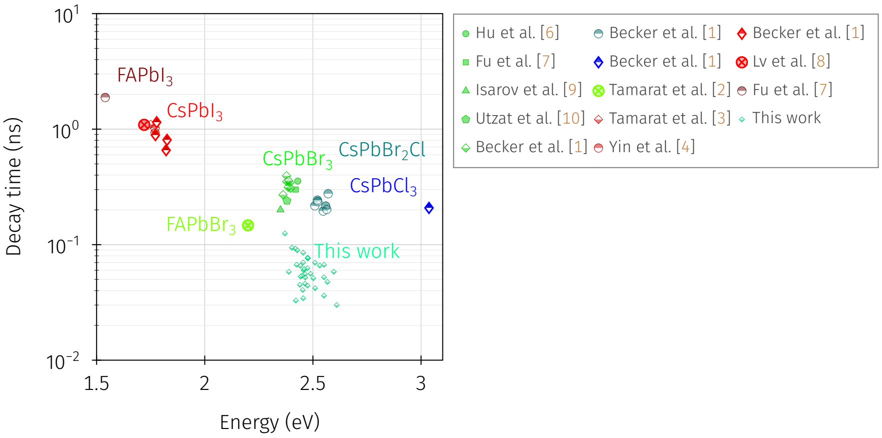

Figure 4.2 | Decay times in single LHP nanocrystals. Summary of reported decay times in single NCs across the LHP family.

Comparion with other LHPs For a given NC size, theory predicts an increase of decay times going from Cl, to Br and to I, as well as from Cs, to FA and MA [1, 5]. As shown in Fig. 4.2, this trend is observed experimentally at the single NC level. In our work, as expected for Br-based LHPs, we find decay times on the 100 ps scale while I-based LHPs have decay times on the order of 1 ns. However, while the decay times recorded here are short as expected, they are $\sim 2-3$ times shorter than previously reported values for single $CsPbBr_3$ NCs.

Table 4.1 | Decay times in $CsPbBr_3$ nanocrystals. Summary of reported values for the decay of $CsPbBr_3$ NCs at liquid helium temperature. In **bold**, we show measurements performed with the same detectors as in this work.

	Size (nm)	Decay (ps)	λ_{exc} (nm)	Resolution (ps)	Pulse width	Γ_{rep} (MHz)	NCs in/on	Ref.
Single	9.4	355	485	250	ps	5.6	fused silica	[6]
Single	8-10	200	488	?	fs	80	1% PMMA on glass	[11]
Ensemble	9.7	200	450	< 50	< 60 ps	5	Si/SiO_2	[9]
Single $CsPb(Br/Cl)_3$	9.5	250	405	< 50	100 fs	80	PS on SiO_2	[12]
Single $CsPbBr_2Cl$	14	380	405	< 50	50 ps	40	3% PS on Si	[1]
Single	13.5	210-275	404 or 488	< 50	fs or <ps	80	3% PMMA on quartz	[10]
Single	16	80	400?	< 2	ps	82	?	[13]

As shown in Tab. 4.1, reported decay times in single $CsPbBr_3$ NCs vary from 80 ps measured with a streak camera [13] to 355 ps measured with a 250 ps resolution [6]. Other measurements performed on $CsPbBr_3$ with the same MPD single-photon detectors as ours with a resolution < 50 ps (**bold** in TAB. 4.1) yield a decay time between 200 and 275 ps for $CsPbBr_3$ [9, 10]. These variations suggest an effect of the measurement resolution, given by the timing resolution of the single photon detection and the temporal width of the excitation pulse, on the recovered decay times. However, there are several potential factors in this discrepancy.

Calibration of the setup response As we are concerned with measuring decay times on the order of 100 ps which is close to the nominal time-resolution of the single-photon detection setup, special attention needs to be given to the measurement of the instrument response function (IRF) which describes the temporal response of the detection setup. The IRF exhibits (FIG. 4.3a) a characteristic shape with a sharp and narrow peak and a lower amplitude tail due to the diffusion of photocarriers generated in neutral regions near the depletion layer [14]. As photons with higher energy tend to be absorbed far from the depletion layer, additional timing delay is observed towards the UV range [14].

In our work, we find that the IRF is strongly wavelength-dependent around 500 nm. To properly account for these variations, we measure the IRF of our setup with a 5 nm step from 460 nm to 525 nm using the scattering of the pulsed laser excitation. The laser pulse is highly attenuated using the same filter used during our experiments and the count rate on the detectors is kept similar to the single nanocrystal emission count rate (well below 1 photon per pulse). Interestingly, we find that the shape of the IRF is highly dependent on the detection wavelength even within this small window. FIG. 4.3a shows the measured IRFs. In FIG. 4.3b, we highlight the difference between the IRF measured at 457 nm and 525 nm together with the features of interest: tail/peak ratio, IRF width and characteristic decay time of the tail. These key features are shown in FIG. 4.3c as a function of the detection wavelength. The tail/peak ratio and IRF width show a similar decreasing trend with increasing wavelength from 0.33 to 0.11 and ~ 75 ps to ~ 40 ps, respectively. The characteristic decay time of the IRF tail is found to be nearly constant across the entire detection range at ~ 210 ps. The characteristic IRF decay time is very similar to the decay times previously reported in the literature for single NCs or ensembles at low temperature, it is thus of utmost importance to properly take into account this response

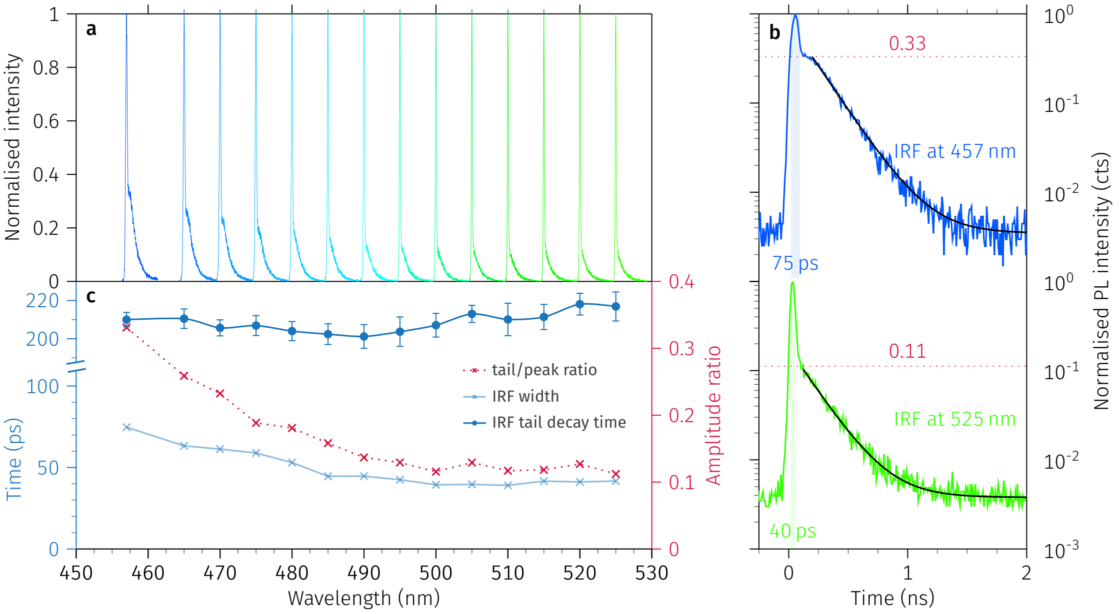

Figure 4.3 | Wavelength dependence of the instrument response. The response of the single-photon counting detectors is highly wavelength-dependent and shows a FWHM ranging from 80 ps at 457 nm to 40 ps at 525 nm. **a**, IRF measured on scattered laser light on the sample at different laser emission wavelengths. **b**, FWHM of the IRF, tail/peak amplitude ratio and exponential decay time of the IRF tail as a function of laser wavelength. **c**, IRF acquired at 457 nm (top) and 525 nm (bottom) showing the quantities plotted in **b**: tail/peak ratio, exponential tail fit and FWHM.

when fitting the time-resolved data.

Influence of the IRF To highlight the importance of the IRF in the physical interpretation of recovered decays, we take the case of a single NC emitting at 523 nm shown in Fig. 4.4.

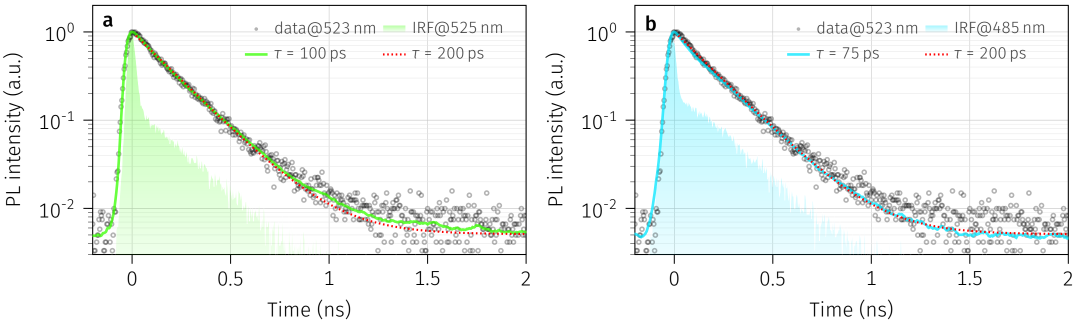

Figure 4.4 | Influence of IRF on recovered decay. Decay of a single NC emitting at 523 nm fitted with: **a**, the IRF acquired at 485 nm and **b**, the IRF acquired at 525 nm. Both yield different decay times of 75 and 100 ps respectively. A tail fit (····) neglecting the IRF yields τ =200 ps.

We show two fit results taking into account IRFs acquired at two different wavelengths: (Fig. 4.4a) within 2 nm of the NC emission and (Fig. 4.4b) 40 nm below. Notably, while both are a good fit to the data, nearly indistinguishible in fact, with similar χ^2, the recovered decay times are strikingly dissimilar. While the physically relevant fit yields a decay time of 100 ps, using the IRF only 40 nm away from the emission yields a shorter decay of 75 ps. We also show the same exponential tail fit to the data, which neglects the IRF, from which we recover $\tau = 200\,\mathrm{ps}$. The variability in the recovered decay parameters in the case presented in FIG. 4.4 thus highlights the importance of taking into account the IRF *at the emission wavelength* when measuring decay times close to the detectors response. In this case only, the decay times recovered can directly be related to the physics of the emission process, rather than the physics of the detection process.

By calibrating the single-photon counting detectors response and using this calibration to fit measured decays, we have uncovered the influence of the IRF on the recovered decay parameters. In particular, in FIG. 4.4, we have shown that the recovered decay parameters are strongly overestimated when fitting only the tail of the decay. Thus, because of the brightness of the NCs we will assume that what we recover is the radiative decay time. However, several factors could also play a role in the fast decay. We discuss them hereafter.

Exciton complexes Notably, for a single NC who after prolonged exposure showed stable emission of the trion for minutes, we managed to record the decay of the trion emission line and compare it to the exciton emission in the absence of the trion peak. FIG. 4.5 shows this experiment result, where the weaker trion emission displays a longer decay time than the exciton, consistent with a previous report [11]. Since radiative recombination rate of the trion is expected to be faster than that of the exciton with $\tau_{\mathrm{X}^*} = 2/3\tau_{\mathrm{X}}$ [1], the fact that we measure $\tau_{\mathrm{X}} < \tau_{\mathrm{X}^*}$ suggests the presence of non-radiative channels for the exciton. In our experiments, we observe that the integrated emission intensity of NCs does not change significantly when trion emission becomes dominant which suggests similar quantum yields for both the exciton and trion in

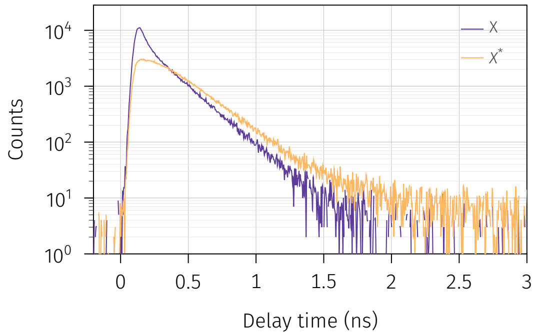

Figure 4.5 | Charged emission decay. Exciton and trion decay on the same single NC.

contradiction with the former prediction. Further work is needed on this part to characterise the trion emission and disentangle the radiative and non-radiative contributions to the PL of the band-edge exciton, e.g. as was previously done on CdSe NCs [15].

Notably, similar observations were made for the biexciton state which is expected to exhibit a decay twice faster than the exciton. In $\mathrm{CsPbBr_3}$, $\tau_{XX}/\tau_X \sim 2$ [16] while in $\mathrm{CsPbI_3}$ $\tau_{XX}/\tau_X \sim 0.38$ closer to the expected value of 0.5 [4]. More work is planned on this part to measure the decay of each emission line in the low-temperature spectrum of single NCs and investigate the full rate equations of the band-edge exciton. Nonetheles, from this discussion, we can conclude that the trion emission nor the biexciton emission can be responsible for the fast decay times observed here.

Non-radiative decay We have seen that the short decay times measured in this work compared to prior reports can be explained by the fact that the IRF was taken into account in this work, such that the ≥200 ps decay reported is overestimated. Alternatively, here we take the opposite approach and assume that the radiative decay time is that previously reported ~ 200 ps and that the short decay times we measure are due to fast non-radiative channels. With these assumptions, we can determine an associated non-radiative rate given that the measured decay rate Γ is given by $\Gamma_{\mathrm{rad}} + \Gamma_{\mathrm{nrad}}$. Assuming then $\Gamma_{\mathrm{rad}} = \left(200\,\mathrm{ps}\right)^{-1}$, we find for $\Gamma = \left(70\,\mathrm{ps}\right)^{-1}$: $\Gamma_{\mathrm{nrad}} \sim \left(110\,\mathrm{ps}\right)^{-1}$. Therefore, if we were to assume that the radiative decay rate is $200\,\mathrm{ps}^{-1}$ the fast decay times observed would be explained with a fast non-radiative decay channel nearly twice as fast as the bright exciton decay. While this is a possibility, in light of the lack of information, we will consider purely radiative recombination from the bright exciton in the following and thus interpret the fast decay times observed here as radiative.

Reflective substrate However, we highlight that in our experiments another factor may play. Indeed, NCs investigated in this chapter, at NTU, were located within a thin polymer layer at a controlled distance of the surface of a distributed Bragg reflector (see SEC. 2.2.2). In contrast, at LPENS, while the same dielectric mirror substrates were used, NCs were deposited directly on top of the mirror in a thicker polymer layer. The few decay measurements made at LPENS in the latest stages of this research have revealed decay times close to 130 ps, between the reported literature values and the values observed in the first part of our study. This fact is still not understood at this stage because both the NCs and the substrates have changed. There are two potential interpretations to these longer decay times. Either we now have better quality NCs with reduced non-radiative decay channels thus yielding a longer decay time. Or, we are in fact probing the effect of the nearby dielectric mirror on the radiative decay rates. Indeed, depending on its distance from the dielectric mirror, the emitter will see a change in its radiative lifetime [17, 18]. Additional measurements will be performed to monitor the decay time of single NCs as a function of their distance to the mirror which would allow to better understand the effect of the mirror and thus, as only the radiative decay rate is affected by the mirror, to unravel the radiative and non-radiative contributions to the PL decay.

Conclusion

In this first section, we have reported on our measurements of PL decay on single $CsPbBr_3$ NCs at the lowest cryogenic temperatures. Fitting the tail of decays, we find decay times on the order of 200 ps. In contrast, taking into account the wavelength-dependent IRF when fitting reveals sub-100 ps decay times, much faster than established colloidal emitters. Our results are discussed critically in light of the literature and compared to other single NC studies across LHPs.

4.2 Probing of the dark exciton state

At the time of the study presented in this section, started in June 2019, there was much debate about the dark exciton state and the bright-dark ordering. A combined theoretical and experimental study tentatively explained the brightness and short emission lifetime of lead halide perovskites, with the case of the prototypal $CsPbBr_3$, by postulating the presence of the Rashba effect which would result in a bright triplet ground state [1]. Soon after, experiments revealed a reduced thermal bright-dark population mixing in a hybrid perovskites [7] and a few weeks before our study, the dark state was magnetically brightenend in another hybrid perovskite [2].

In light of the debate in the community, in Sec. 4.2.1, we report on magneto-optical measurements aimed at investigating the dark exciton state in $CsPbBr_3$, the composition orginally considered in [1].

Alternatively, by relying on the thermally-induced bright-dark exciton population redistribution we can probe the dark exciton state via the bright exciton decay. In SEC. 4.2.2, we report on temperature-dependence PL decay measurements on single $CsPbBr_3$ NCs that evidence decay dynamics characteristic of the thermal mixing of close-lying bright and dark exciton states. With these results and a complementary model, we constrain model parameters based on experiments and discuss the most probable bright-dark mixing mechanisms in LHPs.

4.2.1 Magneto-optical studies

As discussed in SEC. 1.2.3, the singlet state $\Psi_{0,0}$ is dark, i.e. $\langle 0 | \boldsymbol{e} \cdot \boldsymbol{p} | \Psi_{0,0} \rangle = 0$. However, when applying a magnetic field, eigenstates of the system are not the $\Psi_{0,0}$ and $\Psi_{1,\pm1,0}$ states anymore but rather linear combinations of bright and dark states. Depending on the orientation of the magnetic field in the exciton basis, the bright and dark states mix in different ways [19]. In a Faraday configuration, along z, the magnetic field mixes the dark state $\Psi_{0,0}$ with only one of the bright states $\Psi_{1,0}$ thereby transferring the bright transition oscillator strength to the were dark state. In a Voigt configuration, $\Psi_{0,0}$ mixes with $\Psi_{1,1}$ while $\Psi_{1,0}$ mixes with $\Psi_{1,-1}$. This was further confirmed on both hybrid and all-inorganic perovskites at the single object level [2, 3].

Setup

The magneto-optical experiment setup is based on the confocal microscope described in SEC. 2.3.1. Notably, the open-cycle cryostat arm (FIG. 2.11a) is modified with an extension placing the cold finger at $\sim$ 15 cm from the cryostat base. This narrow extension (2 cm in diameter) can then inserted inside an open cycle 5 T cryo-magnet which applies a magnetic field perpendicular to the sample surface. This experimental setup, effectively comprised of two mechanically separated cryostats that are fitted within another, was particularly cumbersome. It required 2 cryostats each with its 100 L liquid helium dewar, 2 inlets/outlets and their tubings for recovery, PID temperature controller. Proper alignment was difficult, and the magnetic field was found to be strong enough to lead to a small $\sim$ few $\mu\mathrm{m}\,\mathrm{T}^{-1}$ shift in the position of the microscope objective, requiring continuous reoptimisation. In addition, pressure from the dewars was controlled manually such that stability was *not the best*. With that said, we managed to study two individual NCs as a function of the applied magnetic field.

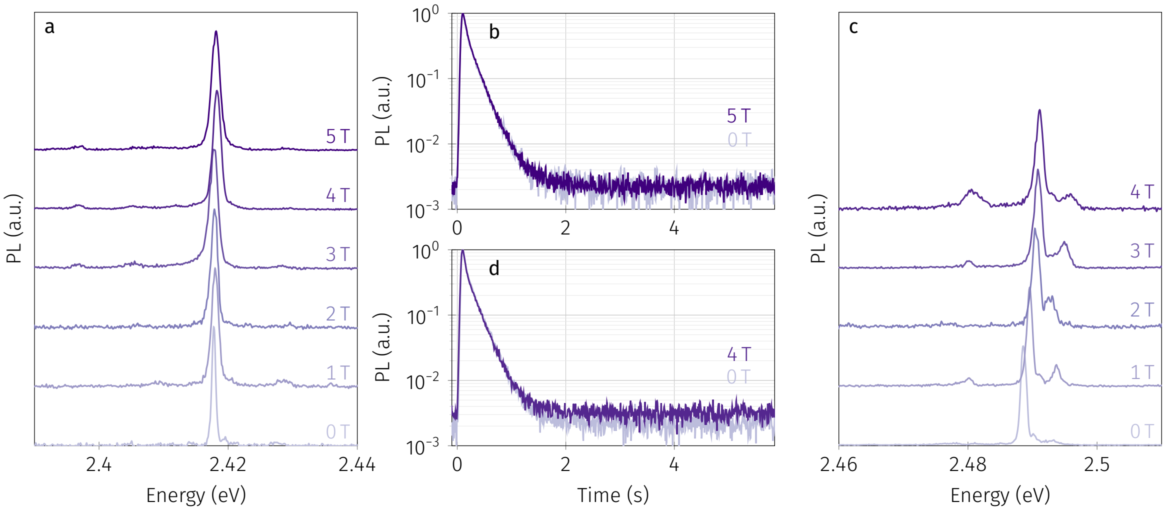

Figure 4.6 | Magnetic field (in-)dependence. Single NC PL (**a-c**) and PL decay (**b-d**) as a function of magnetic field strength.

Experiment

FIG. 4.6 summarises the results obtained on the two NCs studied. For both two-peak NCs, as confirmed by polarisation measurements not shown here, we do not observe any significant Zeeman splitting of the emission lines and no peak emerges with the application of the magnetic field, be it at lower or higher energy. Time-resolved decay measurements as a function of magnetic field further reveal no change in the decay up to 5 T. For the two-peak NC in FIG. 4.6c-d, we observe a peak shifted by $\sim 10\,\text{meV}$ only present at non-zero field, but not at 2 T. This peak is attributed to the intermittent trion emission which was triggered in this NC after prolonged exposure at zero-field.

Due to the cumbersome experimental setup, reduced stability and low signal-to-noise ratio at that time we only managed to study two individual NCs and nothing was revealed. While we investigated the possibility that the magnetic field was not properly applied in light of the absence of any change, this negative result was in fact to be expected. Indeed, for an energy splitting Δ_0, the Zeeman effect is expected to lead to a shift of the emission lines $\Delta = \sqrt{\Delta_0^2 + \Delta_{\text{Zeeman}}^2}$. Considering the typical splittings of 1 meV, the Zeeman splitting for $CsPbBr_3$ is expected to be $\Delta_{\text{Zeeman}} = 1.2\,\text{meV}$ at 5 T with $\varDelta g \sim 2.4$ [11]. This corresponds to two spectral pixels in our setup at that time and was not resolved.

A similar argument could be made for bright-dark energy splittings and the potential magnetic brightening of the dark exciton. Indeed, a previous study [11] had already reported the absence of the dark singlet at magnetic fields up to 7 T. The lack of observation of a magnetic brightening of the dark exciton could potentially be explained by the relatively larger energy splittings in $CsPbBr_3$ and thus by magnetic field strengths too low. Indeed, based on later calculations, bright-dark splittings in $CsPbBr_3$ are expected to be the largest of LHPs at ~ 3 meV without confinement [3] and magnetic brightening is inversely proportional to the square of the energy splitting [20]. However, later studies on $FAPbBr_3$ and $CsPbI_3$ revealed bright-dark energy splittings up to 5 meV at 7 T, such that with similar Landé factors, similar splittings in $CsPbBr_3$ should enable the observation of the dark state [2, 3]. This suggests an even larger energy splitting for $CsPbBr_3$ compared to other LHPs which would lead to a brightening of the dark state at larger field strenghs than used up to now.

This question remains open, and the position of the dark state in $CsPbBr_3$ remains elusive. As we did not manage to evidence any brightening of the dark state, be it via the apparition of an emission line or in the lengthening of the bright decay time, we thus probed the dark exciton state via its effect on the bright exciton state decay. As we will see in the next section, the temperature-dependence of the bright exciton decay already gives constraining information about both the bright-dark energy splittings and the transition rates between them, which as we will show may be in fact more relevant than their actual relative position.

4.2.2 Temperature-dependent time-resolved decay of single nanocrystals

While a magnetic field leads to mixing between exciton states, temperature leads to phonon-assisted transitions between exciton sublevels, i.e. thermally-induced redistribution of population among states. As such, it gives direct information about the exciton fine structure and in particular the interplay between the bright and dark excitons.

Prior studies of the PL decay of LHP NCs have reported an increase of decay times with increasing temperature [6, 21, 22], with nearly an order of magnitude increase from liquid helium to room temperature. Looking more closely at the low temperature dependence of the decay times in ensembles reveals a characteristic bi-exponential decay attributed to thermal population redistribution between bright and dark exciton states [23]. For LHPs, a one-phonon mixing model was used to reproduce the decay times dynamics and usual bright-dark relative orderings were reported with splittings from 5 meV to 14 meV. This is similar to reports of other NCs and CNTs where transitions are interpreted as driven by individual acoustic phonons whose energy matches the bright-dark energy splitting [24–26]. However, the same interpretation does not hold for LHPs as the energy splittings deduced from decay measurements lead to acoustic phonon energies well above that available in these materials. This discrepancy was evidenced first on hybrid LHPs [2, 7] where the bright exciton decay dynamics are interpreted in light of second-order phonon-driven transitions between bright and dark states involving couples of optical phonons.

In this work, we present a quantitative study of the temperature-dependence of the photoluminescence decay of more than 10 single $CsPbBr_3$ NCs.

4.2.2.1 EXPERIMENTS AND MODEL

Experiments

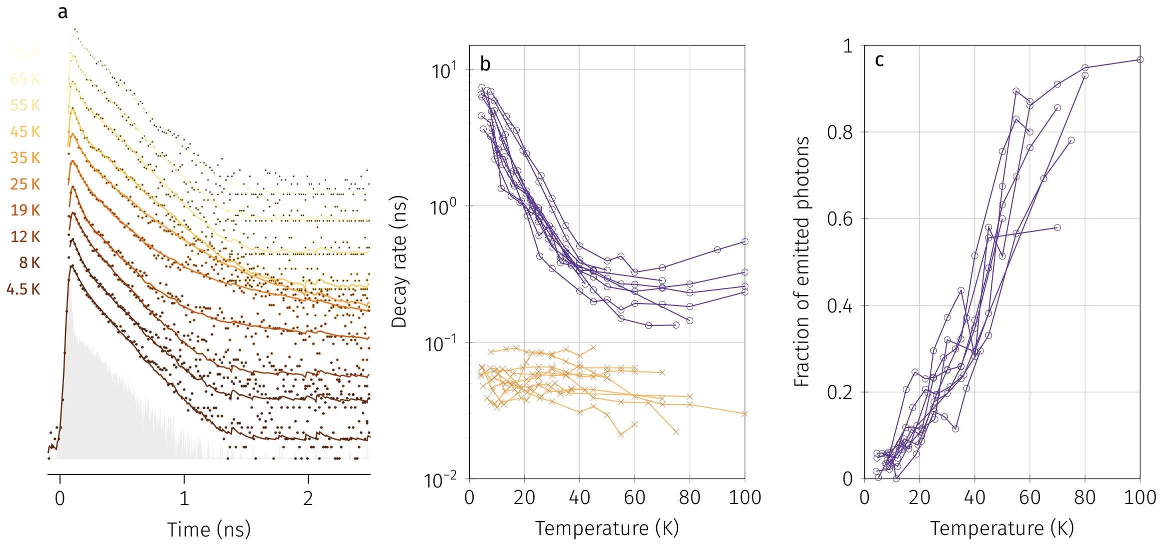

Figure 4.7 | Thermally-driven bright-dark exciton population mixing. **a**, Exemplary thermal dependence of a single NC bright exciton decay. Statistics of the temperature-dependence of: **b**, the short and long decay times and **c**, the long decay channel relative intensity. The short decay channel relative intensity is not shown for clarity.

As discussed in SEC. 4.1, at the lowest temperatures the bright exciton decay is mono-exponential with a fast decay time below 100 ps. As temperature is increased however (FIG. 4.7), a long decay time emerges and gains weight. It becomes the main decay channel around $T_c \sim 45$ K corresponding to a thermal energy of ~3.9 meV (FIG. 4.7c). An example is shown in FIG. 4.7a, while all results are summarised in FIG. 4.7b,c. Let us note that the results summarised in Fig. 4.7b,c are fitting parameters extracted from the measured decays. Each triplet of points (τ_{short}, τ_{long}, I_{long}) shown in Fig. 4.7b,c is the result of a fit of a single decay curve at a single temperature taking into account the closest IRF.

Similar dynamics are observed for all NCs showing the generality of the phenomenon, characteristic of a thermal-driven bright-dark exciton population mixing. To reproduce the low-temperature dynamics observed, we take the usual case of a single bright state coupled to a single dark state which reproduces the main features of the low-temperature decay of many semiconductor nanoemitters [2, 7, 24–26].

Model

We model our experiments by considering the case of a four-level system consisting of a bright exciton state $|B\rangle$, a dark exciton state $|D\rangle$, a higher lying excited state $|E\rangle$ and a ground state $|\mathrm{G}\rangle$ (Fig. 4.8). The possible degeneracy or degeneracy lift of the bright exciton state, due to the crystallographic structure and/or shape of the NC, is neglected at this stage and the bright exciton state is considered as a single level. It is further assumed that the excitation power is kept low enough such that multi-excitonic and charged excitonic populations can be neglected. Indeed, all measurements were performed in these conditions, keeping the excitation power density such that at most 0.1 excitons were created per pulse. Considering an equal population of the bright triplet and dark singlet states after non-resonant excitation, we set an equal branching ratio from the excited state to the bright and dark states, such that $a = 3/4$ of the decay from E populates the bright triplet state. Single exciton states can then decay to the ground state with respective rates Γ_B and Γ_D. Recombination happens either radiatively for the bright exciton state ($\eta_{\mathrm{B}} \sim 1$) or non-radiatively for the dark exciton state ($\eta_{\mathrm{D}} \sim 0$).

Figure 4.8 | Four-level system. Sketch of the four-level system with two excitonic states, B and D representing the bright and dark exciton states with respective recombination rates Γ_B and Γ_D. Optical pumping from the ground state G to an excited state E populates the excited state which decays into the B and D exciton states with a total rate Γ_E and preferential population of bright state ($a = 3/4$).

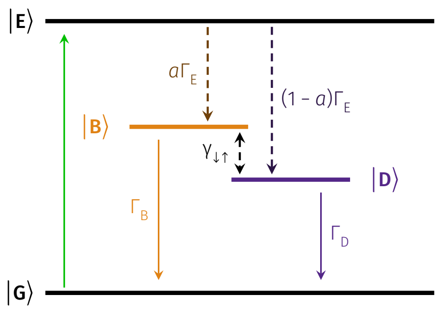

This model is sketched in Fig. 4.8. While here we show a dark state below the bright state, no assumption is made on the relative position of the bright and dark exciton states in the rate equations. It is only when specifying the actual bright-to-dark γ_{BD} and dark-to-bright γ_{DB} transition rates that an implicit level ordering is set.

The rate equations for this system are given in matrix form as $\dot{\boldsymbol{p}} = \boldsymbol{A}\boldsymbol{p}$

$$\begin{pmatrix} \dot{p}_G \\ \dot{p}_D \\ \dot{p}_B \\ \dot{p}_E \end{pmatrix} = \begin{pmatrix} -W & \mathit{\Gamma}_D & \mathit{\Gamma}_B & 0 \\ 0 & -\left(\mathit{\Gamma}_D + \gamma_{DB}\right) & \gamma_{BD} & \mathit{\Gamma}_{ED} \\ 0 & \gamma_{DB} & -\left(\mathit{\Gamma}_B + \gamma_{BD}\right) & \mathit{\Gamma}_{EB} \\ W & 0 & 0 & -\left(\mathit{\Gamma}_{EB} + \mathit{\Gamma}_{ED}\right) \end{pmatrix} \begin{pmatrix} p_G \\ p_D \\ p_B \\ p_E \end{pmatrix} \tag{4.1}$$

where the decay times are given by the eigenvalues Γ_i of $\boldsymbol{A}$ and the amplitudes derive from the corresponding eigenvectors $\boldsymbol{v}_i$. The solution of the matrix equation is given by

$$\boldsymbol{p} = \sum_{i=1}^{N} \alpha_i \boldsymbol{v}_i \, e^{\Gamma_i t}$$

where α_i are constants to be determined with initial conditions, Γ_i are the eigenvalues of $\mathcal{A}$ and $\boldsymbol{v}_i$ the corresponding eigenvectors. Let us note that by definition the eigenvalues Γ_i will be negative, and that $v_i^{(j)}$ is the j-th component of the eigenvector $\boldsymbol{v}_i$. For these time-resolved measurements, we will assume an initial population in the excited state E with a characteristic decay rate Γ_E corresponding to the characteristic non-radiative relaxation from E to the band-edge exciton states. In practice, this rate is larger than the exciton decay rates such that its effect is only a slight $\sim$ps shift of the decay maxima characteristic of the non-instantaneous population of the exciton states. At $t = 0$, we thus have $\boldsymbol{p}(t = 0) = (0, 0, 0, 1)$ and, under pulsed excitation we neglect the pumping rate W at the low powers used. The α_i are thus given by the solution of $\sum_i \alpha_i \boldsymbol{v}_i = \boldsymbol{p}(t = 0)$.

From the solution and initial conditions set above, we can express the total photoluminescence signal as $S(t) = \sum_i \eta_i \Gamma_i p_i$, where the sum runs over all *detected* states. As such, in our experiments where we detect only the bright exciton emission, the total signal is given by $S(t) = \eta_B \Gamma_B p_B$. So, even though actual emission from the dark state is not recorded in our experiments, its presence has a direct impact on the decay rates Γ_i of the bright exciton states. Indeed, note that p_B itself is a sum of three exponential terms: a fast decay, a slow decay and a fast rise related to the relaxation from E.

Up to now, the model is quite general as we have not yet set the transition rates between bright and dark exciton $\gamma_{\uparrow\downarrow}$ which are modelled as thermally-activated processes. These rates depend on the actual mechanism at play as detailed below and summarised in Tab. 4.2.

First-order transitions In other low-dimensional emitters, phonon-driven transitions between bright and dark exciton states are generally attributed to acoustic phonon modes with an energy matching the bright-dark splitting as in the case of II-VI NCs [24] or carbon nanotubes [25, 26]. Namely, transitions are found to be driven by individual acoustic phonons whose energy E matches the bright-dark energy splitting. The temperature-dependence of the upward $\gamma_\uparrow = \gamma_0 \mathrm{N}$ and downward rates $\gamma_\downarrow = \gamma_0 (1 + \mathrm{N})$ are written as a function of $\mathrm{N} = \left(e^{-\mathrm{E}/k_\mathrm{B}\mathrm{T}} - 1\right)^{-1}$ the Bose-Einstein occupation factor. For lead halide perovskites, while the same model has been used [23, 27, 28], the same interpretation leads to acoustic phonon modes energies well above that available in these materials.

Second-order Raman-like process At the time of this study, earlier works had evidenced a reduced bright-dark thermal population mixing in hybrid LHPs [2, 7] but not yet in all-inorganic LHPs. Based on these reports, transitions between the bright and dark state are interpreted as resulting from a Raman-like two-phonon process involving both the emission and absorption of a phonon. Transitions are thus driven by a couple of phonons whose energy difference $\mathrm{E}_2 - \mathrm{E}_1$ matches the bright-dark energy splitting with upward $\gamma_\uparrow = \gamma_0 \mathrm{N}_1 (\mathrm{N}_2 + 1)$ and downward rates $\gamma_\downarrow = \gamma_0 (1 + \mathrm{N}_1) \mathrm{N}_2$, where $E_2 > E_1$.

Second-order sum process There is also another type of second-order process which consists in the emission or absorption of a couple of phonons. Transitions in this case are driven by a couple of phonons whose energy sum matches the bright-dark energy splitting with upward $\gamma_\uparrow = \gamma_0 \mathrm{N}_1 \mathrm{N}_2$ and downward rates $\gamma_\downarrow = \gamma_0 (1 + \mathrm{N}_1) (1 + \mathrm{N}_2)$.This process has not been considered previously in LHPs although recently coupling between the bright exciton states via second-order acoustic phonon coupling was evidenced [29].

Table 4.2 | Six scenarios for phonon-driven transitions. Six scenarios arising from two relative orderings and three phonon-driven mixing schemes *The relative intensity of this component is less than 1% at the lowest temperatures, this limit is therefore not used as a constraint.

	One-phonon processes		Two-phonon processes			
	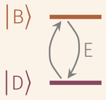	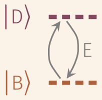	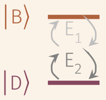	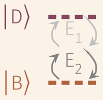	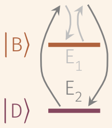	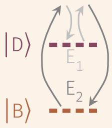
$\gamma_{B\to D}/\gamma_0$	$N + 1$	N	$(N_1 + 1)(N_2 + 1)$	N_1N_2	$N_1(N_2 + 1)$	$N_2(N_1 + 1)$
$\gamma_{D\to B}/\gamma_0$	N	$N + 1$	N_1N_2	$(N_1 + 1)(N_2 + 1)$	$N_2(N_1 + 1)$	$N_1(N_2 + 1)$
$\Gamma_{short}(T \to 0)$	$\Gamma_B + \gamma_0$	Γ_B	$\Gamma_B + \gamma_0$	Γ_B	Γ_B	Γ_B
$\Gamma_{long}(T \to 0)^*$	Γ_D	$\Gamma_D + \gamma_0$	Γ_D	$\Gamma_D + \gamma_0$	Γ_D	Γ_D
$\Gamma_{long}(T >> \Delta)$	$(\Gamma_B + \Gamma_D)/2 \to \Gamma_B/2$					

4.2.2.2 SIMULATIONS

Here, we consider both one-phonon transitions and the two types of two-phonon transitions. The bi-exponential emission evolution is modelled in this framework, and experimentally obtained short- and long-decay times and relative intensities are compared to calculations. The decay dynamics can be modelled using seven parameters (Γ_B, Γ_D, η_B, η_D, a, γ_0, ΔE_{BD}), where γ_0 is the transition rate constant and $\Delta E_{BD} \equiv \Delta$ the bright-dark splitting. To investigate the different cases, we compare the low temperature asymptotic limits to our experimental results enabling us to set or constrain most parameters, such that remain only the two parameters of interest: the transition rate constant γ_0 and the bright-dark splitting Δ.

Simulation parameters Ideally, our experiments would have revealed the dark state energy and therefore the bright-dark energy splittings Δ and from the above analysis we would retrieve the transition rate constant γ_0. However, in the absence of a definite value for Δ, the physical pertinence of the parameters retrieved from such analysis would be questionable. In order to be able to discriminate between the different scenarii explored confidently, we need a more robust method. Here, instead of fitting each curve, which can be adequatly done with several sets of parameters, we find the common characteristics of all observed decays and use them as constraints. Namely, we take advantage of the fact that our experiment results all follow the same trend, exemplified in FIG. 4.7, such that we aim at reproducing this trend instead of the actual measurement results.

To do so, we simulate the decay dynamics for all set of ”reasonable” parameters γ_0 and Δ with $\gamma_0 \in \left[10^{-2};\ 10^{2}\right]$ ns^{-1} and $\Delta \in \left[10^{-2};\ 10^{2}\right]$ meV. Within this phase space, we simulate the decay dynamics and investigate several phonon-assisted mixing scenarii as well bright-dark orderings.

Let us emphasize that in the one-phonon model and two-phonon sum process model, setting γ_0 effectively constrains both Γ_B and Γ_D if we want to be able to reproduce our experiment results, more precisely given the observed low- and high-temperature trends as summarised in TAB. 4.2.

We choose 2D maps as a way to display simulation results, where the coloured intensity displays physical parameters that can be extracted from both simulations and experiments. Each point on the phase space maps therefore corresponds to a couple of parameters $(\gamma_0,\ \Delta)$ such that the decay dynamics correspond to that observed. We first start by presenting the case of the most probable ordering, with a bright exciton above the dark exciton.

One-phonon transitions

We detail the analysis performed in FIG. 4.9 for one-phonon transitions. We calculate the long-decay-time intensity at 0 K and 100 K (FIG. 4.9b), as well as the long decay time at 100 K (FIG. 4.9c). For clarity, we further restrict the range of data displayed to the features observed in experiments (FIG. 4.9e,f). Namely, we only show the region of phase space where the long-decay-time intensity is lower than 0.1 at 0 K and higher than 0.85 at 100 K (FIG. 4.9b), and the region where the long decay time is comprised between 150 ps to 400 ps at 100 K (FIG. 4.9c).

As these criteria define the range within which all experimental decays are observed, we further take the intersection of these requirements (FIG. 4.9d), and find only a small region around $\gamma_0 \sim 6\,\text{ns}^{-1}$ and $\Delta \sim 3$ meV where these requirements can be all met. Interestingly, Δ is close to the expected bright-dark splittings in $CsPbBr_3$, as calculated recently [3]. However, within this small subspace, the obtained characteristic temperature for the thermal mixing, defined as the temperature at which the intensities of the short and long component are equal, is much lower than that observed, i.e. ~15 K vs. ~45 K. This is evidenced in FIG. 4.9e,f, where while both the short and long decay times dynamics can be adequately reproduced within this one-phonon mixing scheme (FIG. 4.9e), the decay components intensity dynamics can not be reproduced

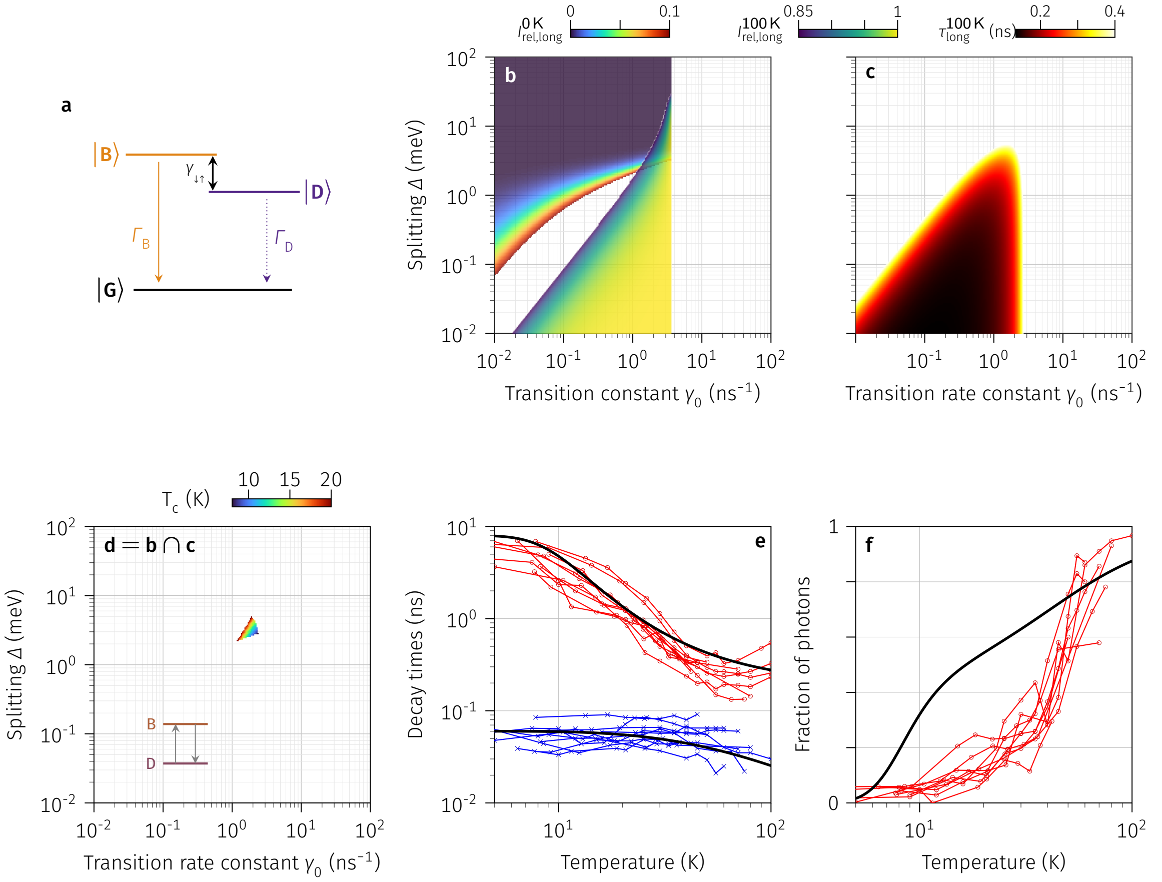

Figure 4.9 | Phase space mapping: one-phonon transitions. Particular features of interest obtained from simulations of the decays obtained varying only γ_0 and Δ while other parameters (a, Γ_B, Γ_D) are set as explained in the text. The intensity of the long-decay component at **b**, 0 K and 100 K and **c**, long-decay time at 100 K are shown, together with **d** the characteristic temperature in the phase subspace defined by the intersection of the **b** and **c** subspaces. **e**, **f**, Experimental decay dynamics retrieved from experiments with **e**, the long and short decay times and **f**, the long decay component fractional intensity. The solid line corresponds to a fit using parameters within the subspace defined in **d**.

(FIG. 4.9f). Thus, fitting both the decay times and decay amplitudes is required to get physically relevant information from the decay dynamics.

Two-phonon transitions

Following the same procedure just described for the first-order bright-dark mixing, we show in FIG. 4.10a,b the characteristic temperatures obtained in the subspace where all criteria are met in the case of a second-order process where $2\hbar\omega = \Delta$ and $\hbar(\omega_2 - \omega_1) = \Delta$ for $\omega_1 = 3.3\,\mathrm{meV}$ matching the lowest energy optical phonon replica observed in the PL. This reveals that in both second-order mixing schemes, we have a large subspace in which the decay dynamics can be adequatly reproduced, examples of which are shown in FIG. 4.10b,c. Notably, by varying γ_0, the decays could be reproduced for a wide range of Δ thus giving no constraining information of the bright-dark energy splittings in our case.

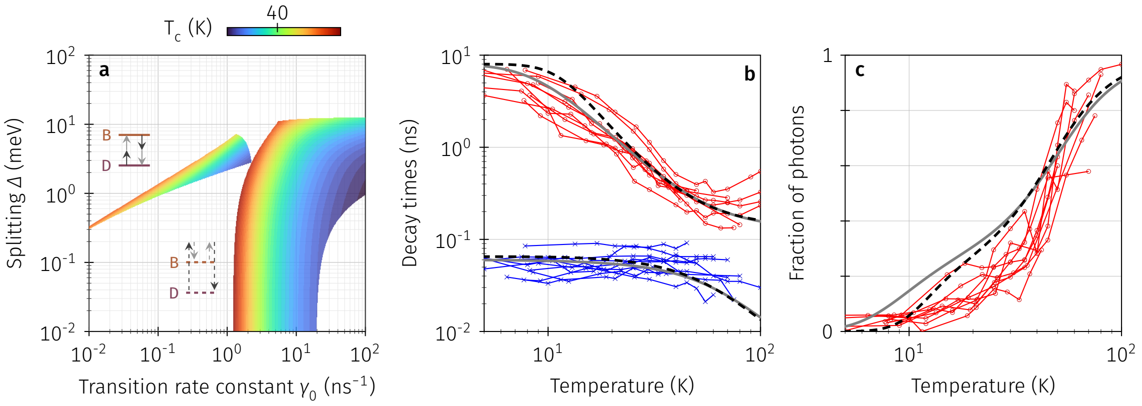

Figure 4.10 | Phase space mapping: two-phonon transitions. Particular features of interest obtained from simulations of the decays obtained varying only γ_0 and Δ while other parameters (a, Γ_B, Γ_D) are set as explained in the text. **a**, Characteristic mixing temperature in the subspaces defined by experimental observations. Simulations are shown for the two-phonon sum process and for the Raman-like model assuming $E_1 = 3.3$ meV. **b**, **c**, Experimental decay dynamics with **b**, the long and short decay times and **c**, the long decay component fractional intensity. The solid, resp. dashed, line is a fit using parameters within the subspace in **a** for the sum process, resp. Raman-like process.

Here, we have in fact shown only a subset of all possible processes. Indeed, for both second-order processes, we have an additional degree of freedom in setting the energy of the involved phonons.

- For the sum process in Fig. 4.10, we have assumed above that the energy of the phonons are equal. However, this is not the only possible case. In fact, for the sum process it is only the sum of the phonons energies that is constrained. We can further vary the relative energies of the two involved phonons and find an intersection for all our requirements. However, due to the limited information about phonon modes with energies below the lowest one observed as a replica ($\sim$ 3.3 eV) interpretation in terms of definite phonon modes is complicated. In fact, given their low energy, such phonon modes are expected to be acoustic modes.
- For the Raman-like process in Fig. 4.10, we have shown the case of a lowest energy phonon matching the lowest energy optical phonon replica observed in the low temperature PL of single NCs. The same analysis can be performed by setting the lowest energy optical phonon to the other observed optical phonon mode energies as shown in Fig. 4.11. For higher energy replica, similarly to the case in Fig. 4.10, there exists a large phase subspace where all requirements are met, however the best match is shown in Fig. 4.9 and obtained for the lowest energy optical phonon mode observed.

This goes to show that the two second-order mechanisms explored both lead to dynamics in

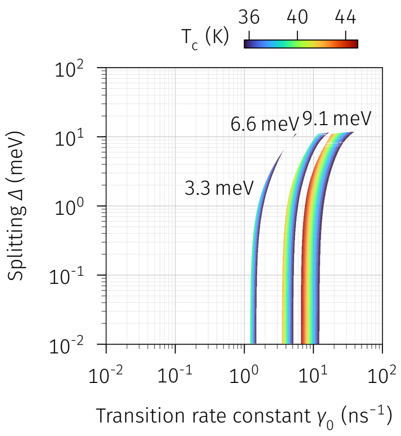

Figure 4.11 | Two-phonon Raman-like transitions. Characteristic mixing temperature in the subspaces defined by experimental observations for the Raman-like process with increasing phonon mode energy matching the optical replica observed in single NC PL.

accordance with experiments and offer a large phase space of possible $(\gamma_0\ \Delta)$.

Discussion

Here, we discuss several aspects related to the simulations performed. Namely, the bright-dark level ordering expected, the dark exction quantum yield and the bright triplet exciton are discussed.

Level ordering In light of the most recent theoretical [30, 31] and experimental results on inorganic perovskites [3], it is most probable that the ~ 8 nm NCs used in this study have a dark ground state. We nevertheless investigated the case of bright ground state for comprehensiveness. In the case of one-phonon transitions, our simulations reveal that the observed dynamics can not be reproduced with a bright ground state, i.e. no intersection is found for all requirements. This is directly related to the fact that downwards transitions do not vanish at zero temperature. In the case of two-phonon transitions, there is a non-zero intersection for all our requirements for the Raman-like process meaning that the observed dynamics can be obtained in this case for a wide range of couples (γ_0, Δ). In contrast, the sum-process, because of its low-temperature limits similar to the one-phonon case, can not reproduce the observed dynamics in the case of a bright ground state.

In summary, while for a dark ground state both the sum and Raman-like processes can reproduce the observed dynamics, in the case of a bright ground state only the Raman-like process leads to dynamics matching experiments.

Dark exciton quantum yield In our simulations, we have assumed a purely non-radiative decay for the dark exciton, i.e. $\eta_D \sim 0$. This is motivated by the dark character of the single exciton and its absence in the low-temperature PL of single LHP NCs. In contrast, in CdSe NCs $\eta_D \sim 1$ [24] and the dark state emission is dominant at low temperature. A puzzling question then arises on the different nature of the dark excitons in LHPs and in CdSe NCs. In particular, if bright-dark transitions are reduced and the dark singlet is the lowest-lying state we expect its emission to be dominant at low temperature. In contrast, the dark exciton in LHPs has been quite elusive. This suggests that there are still some basic ingredients missing to understand the band-edge exciton in LHPs.

Bright triplet exciton The bright exciton is LHPs is a triplet. In our simulations, we take this into account only by setting the population branching ratios from the excited state to the exciton states, i.e. $a = 3/4$. Nonetheless, we also checked with our simulation that the actual bright exciton fine structure (i.e. the presence of three bright exciton sublevels) does not fundamentally change our results. Indeed, assuming similar decay times and oscillator strengths for all bright exciton states, we find that the short decay times obtained by weighted summation of each bright exciton states components are equivalent to the single bright exciton state model.

Lifetime increase with temperature As previously reported [12], the decay time of LHP NCs is found to increase from cryogenic temperature to room temperature. While here we evidence a bright-dark exciton thermal population mixing in the low temperature regime (<100 K), we also observe a slight increase of the dominant long decay component at $T > 80$ K. This behaviour was observed on several NCs and cannot be reproduced within the model used in this section. Indeed, within this model, only monotonous changes can be reproduced. Several potential mechanisms for this increase have been proposed such as an increased exciton coherence volume [32, 33] in these weakly confined NCs but a clear answer remains lacking at the moment.

Discussion

Based on the above discussion, it seems that the bright-dark level ordering is not relevant in light of the slow bright-dark thermal population mixing in LHPs. This is exemplified by the fact that both level orderings can lead to the observed dynamics. As shown here for the case of $CsPbBr_3$ NCs in the intermediate confinement regime, first-order phonon assisted bright-dark thermal population redistribution is strongly reduced. This observation has also been made in other hybrid [2, 7] and inorganic perovskite NCs [3] with determined bright-dark energy splittings, either directly or indirectly, varying over an order of magnitude from ∼300 μeV to ∼3 meV depending on the size and actual composition. Such a widespread observation across both hybrid and inorganic LHP NCs, together with the rich low-energy phonon spectrum, both acoustic and optical, hosted by the perovskite lattice suggests that the underlying reason for the observed absence of first-order transitions is closely linked to some symmetry arguments holding for the entire metal halide perovskite family. However, the underlying reason for such behaviour is still not understood.

In particular, while symmetry arguments predict a vanishing piezoelectric coupling to acoustic phonons in the reference cubic phase [34], non-negligible coupling to both TA and LA phonons was recently reported in single $CsPbI_3$ NCs [29]. This suggests that a more realistic description of LHP NCs should be considered and for that, symmetry arguments, although cumbersome, should provide a solid ground for further investigations.

Speculations While a definite origin for the absence of first-order transitions is lacking, in this section we can speculate about this. Acoustic phonons are found to exhibit very short lifetimes in LHPs [35]. Electron can form polarons with optical phonons which may efficiently shield the carriers from interaction with phonons.

Further arguments can be mobilised based on the quantum mechanical description of the system (see SEC. A.1.3). While the first order electron-phonon coupling term proceeds through the matrix elements for the electron-phonon interaction, the second order electron-phonon coupling term differs in two main ways [36, 37]. First, while in the first order process the sum runs over all phonon modes satisfying momentum conservation, the second-order process contains a sum over all pairs $\boldsymbol{q}, \boldsymbol{q}'$ verifying momentum conservation which represents a broader phase space. In addition, the second-order electron-phonon interaction term is a sum over all intermediate states, and contains an energy shift at the denominator [36, 37]. In LHPs, the band-edge exciton is comprised of a set of finely-spaced states which together with their vibronic sublevels, provide a high density of closely-spaced intermediate states for the interaction to proceed through. This rationalises the fact that the second-order contribution should be significant.

Conclusion

In this chapter, we have studied the PL decay of single NCs. In light of the recent debate on the exciton fine structure of single LHPs, we have tried to probe the dark exciton state both directly an indirectly. Magneto-optical measurements up to 5 T were first performed on single $CsPbBr_3$ NCs and did not reveal any significant change in the PL. Alternatively, we thus probed the dark exciton state via its interaction with the bright exciton states. Doing so, we found that the decay dynamics of single NCs can be reproduced by a simple model with a single bright exciton state and a single dark exciton state. However, as for other LHPs [2, 3, 7], first-order transitions between bright and dark exciton sublevels are found to be vanishing such that second-order transitions are predominant. By investigating two possible second-order bright-dark transition mechanisms, related à priori to the piezoelectric interaction and Fröhlich interaction, we highlight the potential importance of both mechanisms in the low-temperature PL dynamics of single LHP NCs. Since, as we show, decays can be approached by a wide set of parameters (γ_0, Δ), we could not determine the bright-dark exciton splitting with confidence. However, we find that while bright-dark transitions are adequately reproduced by the two second-order mixing schemes for realistic energy splittings, only the Raman-like model yields an interpretation consistent with the phonon mode energies identified in the low energy spectrum of single $CsPbBr_3$ NCs. Further work should therefore aim at disentangling the contributions to exciton-phonon coupling to provide a realistic picture of these nascent systems.

References for Chapter 4

[1] M. A. Becker et al., “Bright triplet excitons in caesium lead halide perovskites”, Nature **553**, 189–193 (2018) (pp. 129, 131, 132, 135, 137).

[2] P. Tamarat et al., “The ground exciton state of formamidinium lead bromide perovskite nanocrystals is a singlet dark state”, Nature Materials **18**, 717–724 (2019) (pp. 129, 132, 137, 138, 140–142, 144, 151, 152).

[3] P. Tamarat et al., “The dark exciton ground state promotes photon-pair emission in individual perovskite nanocrystals”, Nature Communications **11**, 6001 (2020) (pp. 129, 132, 138, 140, 146, 149, 151, 152).

[4] C. Yin et al., “Bright-Exciton Fine-Structure Splittings in Single Perovskite Nanocrystals”, Physical Review Letters **119**, 6401 (2017) (pp. 131, 132, 136).

[5] R. Ben Aich et al., “Multiband **k·p** Model for Tetragonal Crystals: Application to Hybrid Halide Perovskite Nanocrystals”, The Journal of Physical Chemistry Letters, 808–817 (2020) (pp. 131, 132).

[6] F. Hu et al., “Superior Optical Properties of Perovskite Nanocrystals as Single Photon Emitters”, ACS Nano 9, 12410–12416 (2015) (pp. 132, 133, 140).

[7] M. Fu et al., “Unraveling exciton–phonon coupling in individual $FAPbI_3$ nanocrystals emitting near-infrared single photons”, Nature Communications **9**, 3318 (2018) (pp. 132, 137, 141, 142, 144, 151, 152).

[8] Y. Lv et al., “Quantum Interference in a Single Perovskite Nanocrystal”, Nano Letters **19**, 4442–4447 (2019) (p. 132).

[9] M. Isarov et al., “Rashba Effect in a Single Colloidal $CsPbBr_3$ Perovskite Nanocrystal Detected by Magneto-Optical Measurements”, Nano Letters **17**, 5020–5026 (2017) (pp. 132, 133).

[10] H. Utzat et al., “Coherent single-photon emission from colloidal lead halide perovskite quantum dots”, Science **363**, 1068–1072 (2019) (pp. 132, 133).

[11] M. Fu et al., “Neutral and Charged Exciton Fine Structure in Single Lead Halide Perovskite Nanocrystals Revealed by Magneto-optical Spectroscopy”, Nano Letters **17**, 2895–2901 (2017) (pp. 132, 135, 139).

[12] G. Rainò et al., “Single Cesium Lead Halide Perovskite Nanocrystals at Low Temperature: Fast Single-Photon Emission, Reduced Blinking, and Exciton Fine Structure”, ACS Nano **10**, 2485–2490 (2016) (pp. 132, 150).

[13] J. Ramade et al., “Fine structure of excitons and electron–hole exchange energy in polymorphic $CsPbBr_3$ single nanocrystals”, Nanoscale **10**, 6393–6401 (2018) (pp. 132, 133).

[14] P. Kapusta, ed., *Advanced photon counting: applications, methods, instrumentation*, Springer Series on Fluorescence Vol. 15 (Springer, Cham, 2015), 370 pp. (p. 133).

[15] X. Brokmann et al., “Measurement of the Radiative and Nonradiative Decay Rates of Single CdSe Nanocrystals through a Controlled Modification of their Spontaneous Emission”, Physical Review Letters **93**, 107403 (2004) (p. 136).

[16] Z. Wang et al., “Optically Driven Giant Superbunching from a Single Perovskite Quantum Dot”, Advanced Optical Materials, 2100879 (2021) (p. 136).

[17] K. Drexhage, “Influence of a dielectric interface on fluorescence decay time”, Journal of Luminescence **1–2**, 693–701 (1970) (p. 137).

[18] W. L. Vos et al., “Orientation-dependent spontaneous emission rates of a two-level quantum emitter in any nanophotonic environment”, Physical Review A **80**, 053802 (2009) (p. 137).

[19] Z. G. Yu, “Effective-mass model and magneto-optical properties in hybrid perovskites”, Scientific Reports **6**, 28576 (2016) (p. 138).

[20] A. V. Rodina et al., “Radiative recombination from dark excitons in nanocrystals: Activation mechanisms and polarization properties”, Physical Review B **93**, 155427 (2016) (p. 140).

[21] K. Wei et al., “Temperature-dependent excitonic photoluminescence excited by two-photon absorption in perovskite $CsPbBr_3$ quantum dots”, Optics Letters **41**, 3821 (2016) (p. 140).

[22] B. T. Diroll et al., “Low-Temperature Absorption, Photoluminescence, and Lifetime of $CsPbX_3$ ($X = Cl$, Br, I) Nanocrystals”, Advanced Functional Materials **28**, 1800945 (2018) (p. 140).

[23] L. Chen et al., “Composition-Dependent Energy Splitting between Bright and Dark Excitons in Lead Halide Perovskite Nanocrystals”, Nano Letters **18**, 2074–2080 (2018) (pp. 140, 144).

[24] O. Labeau et al., “Temperature Dependence of the Luminescence Lifetime of Single CdSe/ZnS Quantum Dots”, Physical Review Letters **90**, 404 (2003) (pp. 141, 142, 144, 150).

[25] S. Berger et al., “Temperature Dependence of Exciton Recombination in Semiconducting Single-Wall Carbon Nanotubes”, Nano Letters **7**, 398–402 (2007) (pp. 141, 142, 144).

[26] T. Gokus et al., “Mono- and Biexponential Luminescence Decays of Individual Single-Walled Carbon Nanotubes”, The Journal of Physical Chemistry C **114**, 14025–14028 (2010) (pp. 141, 142, 144).

[27] D. Rossi et al., “Intense Dark Exciton Emission from Strongly Quantum Confined $CsPbBr_3$ Nanocrystals”, Nano Letters **20**, 7321–7326 (2020) (p. 144).

[28] D. Rossi et al., “Size-dependent dark exciton properties in cesium lead halide perovskite quantum dots”, The Journal of Chemical Physics **153**, 184703 (2020) (p. 144).

[29] Y. Lv et al., “Exciton-acoustic phonon coupling revealed by resonant excitation of single perovskite nanocrystals”, Nature Communications **12**, 2192 (2021) (pp. 144, 151).

[30] P. C. Sercel et al., “Exciton Fine Structure in Perovskite Nanocrystals”, Nano Letters **19**, 4068–4077 (2019) (p. 149).

[31] P. C. Sercel et al., “Quasicubic model for metal halide perovskite nanocrystals”, The Journal of Chemical Physics **151**, 234106 (2019) (p. 149).

[32] J. Feldmann et al., “Linewidth dependence of radiative exciton lifetimes in quantum wells”, Physical Review Letters **59**, 2337–2340 (1987) (p. 150).

[33] T. Itoh et al., “Size-dependent radiative decay time of confined excitons in CuCl microcrystals”, Solid State Communications **73**, 271–274 (1990) (p. 150).

[34] W. Nie et al., “Light-activated photocurrent degradation and self-healing in perovskite solar cells”, Nature Communications **7**, 1–9 (2016) (p. 151).

[35] M. Songvilay et al., “Common acoustic phonon lifetimes in inorganic and hybrid lead halide perovskites”, Physical Review Materials **3**, 093602 (2019) (p. 151).

[36] E. A. Muljarov et al., “Dephasing in Quantum Dots: Quadratic Coupling to Acoustic Phonons”, Physical Review Letters **93**, 237401 (2004) (p. 151).

[37] A. V. Uskov et al., “Dephasing Times in Quantum Dots due to Elastic LO Phonon-Carrier Collisions”, Physical Review Letters **85**, 1516–1519 (2000) (p. 151).

5

Single perovskite nanoplatelets as single photon emitters

In this chapter, we present a side study on strongly anisotropic $CsPbBr_3$ NCs with one-dimensional intermediate confinement. These will be referred to as nanoplatelets (NPLs), in opposition to the more isotropically confined NCs studied in the preceding chapters. Large isotropic inorganic LHP NCs have been widely investigated since their first synthesis [1]. A number of other shapes have also been synthesized in an attempt to bridge the gap of blue-emitting colloidal NCs and the less stable Cl-based LHPs [2–5].

Here, we synthesise and isolate single $CsPbBr_3$ NPLs. Doing so, we demonstrate their comparable properties with $CsPbBr_3$ NCs. Notably, while the signal-to-noise ratio was quite low, emission was stable over the course of several minutes allowing us to perform second-order correlation measurements. This enabled us to provide the first demonstration of single photon emission in $CsPbBr_3$ NPLs in [6].

5.1 Synthesis and basic characterisation

Nanoplatelets synthesis

The synthesis of NPLs differs from nanocubes in the ligands that are used and the lead and bromide sources. Here, the synthesis is done at lower temperature 130 °C and the nucleation is triggered by adding the lead cesium precursor into the bromide in a polar solvent (FIG. 2.4d-f). We

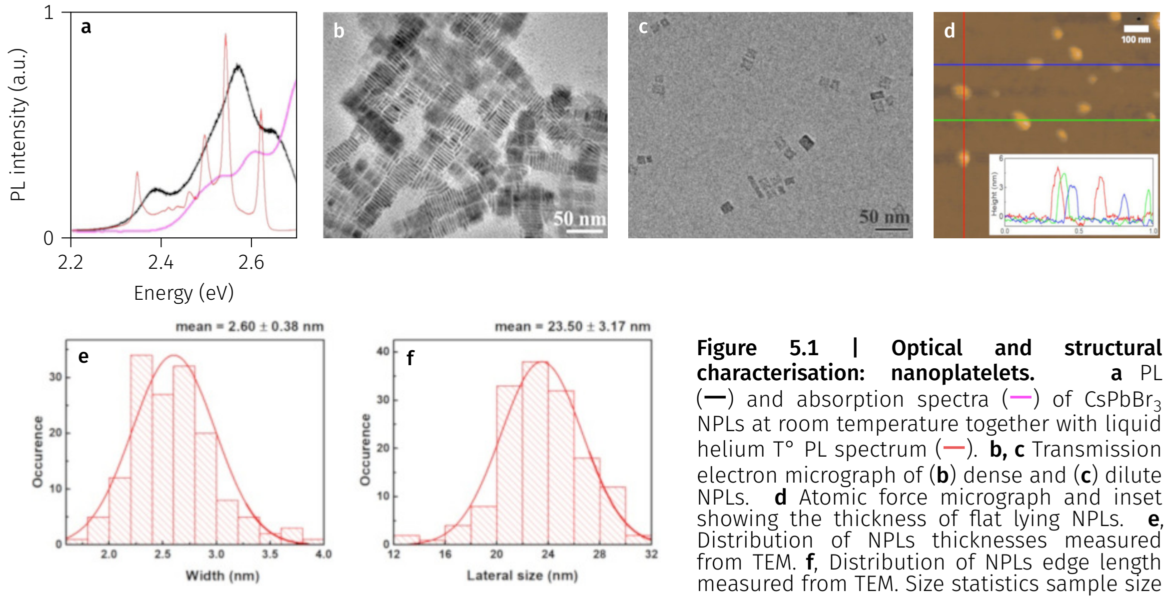

Figure 5.1 | Optical and structural characterisation: nanoplatelets. **a** PL (—) and absorption spectra (—) of $CsPbBr_3$ NPLs at room temperature together with liquid helium T° PL spectrum (—). **b, c** Transmission electron micrograph of (**b**) dense and (**c**) dilute NPLs. **d** Atomic force micrograph and inset showing the thickness of flat lying NPLs. **e**, Distribution of NPLs thicknesses measured from TEM. **f**, Distribution of NPLs edge length measured from TEM. Size statistics sample size is 150. Reprinted from [6].

reproduce here briefly the synthesis protocol while the exact proportions can be found in [6].

Preparation of the Cs-oleate (Fig. 2.4d) Caesium carbonate Cs_2CO_3, octadecene (ODE) and oleic acid (OA), oleylamine (OLA), $Pb(OAc)_{23}H_{20}$ and 1,4-DBSA are added into a three-neck flask and heated under vacuum at 130 °C until complete solubilisation. The mixture is then kept at 130 °C under N_2.

Synthesis of the $CsPbBr_3$ nanoplatelets (Fig. 2.4e) TOABr (tetraoctylammonium bromide) is added to toluene and heated to 130 °C until complete solubilisation of the TOABr. (Fig. 2.4f) The TOABr-toluene solution is then quickly added to the oleate. After 5 s the flask is cooled down in a water bath.

Purification and isolation The crude solution is centrifugated 5 min at 5000 rpm and the supernatant is discarded. The precipitate is redispersed in hexane and centrifuged again. The supernatant is then separated forming a long-term stable solution.

Geometry

Before investigating the optical properties of the synthesis products, we first need to characterise their geometry.

Anisotropic NCs, with aspect ratios ∼ 10, were synthesized with Caixia Huo with the synthesis protocol detailed above and in [6]. As shown in Fig. 5.1, transmission electron microscope (TEM) images of dense areas show long and thin nano-objects with typical lengths $L = 23.5 \pm 3.2$ nm and thicknesses $h = 2.6 \pm 0.4$ nm. On the other hand, dilute areas show mostly large squares with edge lengths similar to L. From this information the 3D morphology of the objects can be determined. Indeed, while at high concentrations, NPLs tend to display order by aligning on their thickness, at lower concentrations NPLs are observed to lie flat on their longest edge. Based on these results and prior reports [2, 3], it was therefore concluded that these objects were approximately square few-monolayer thick NPLs.

Atomic force microscopy measurements were also performed to measure the thickness of the objects in dilute dispersions and thicknesses compatible with those deduced from the TEM images were found (FIG. 5.1c). With this structural information, we can now interpret the PL spectrum of these NPLs.

Ensemble characterisation

PL and absorption measurements at room temperature and 4 K reveal a multi-peak structure that we assign to different thicknesses of NPLs. Based on prior reports [2, 3], the peaks observed at low temperature were assigned to NPLs with thicknesses $h = na$ with $3 < n < 7$ and $a = 0.58$ nm (FIG. 5.2), directly consistent with the thicknesses deduced from structural characterisation.

Based on later low temperature absorption measurements [7], it seems that this peak assignment is off by 2 monolayers. This is further supported by the strongly overestimated (× 3) effective mass deduced as latest results yield results on the order of 0.15 m_e. However, such peak assignment would be inconsistent with the structural data shown in FIG. 5.1. This inconsistency will be discussed here in detail.

Peak identification

For NPLs, we can assume a confinement along a single direction such that we can approximate the emission energy as a function of the number of layers as [1]

$$E(T) = E_g + \frac{\hbar^2 \pi^2}{2m^* a^2} \frac{1}{n^2} \tag{5.1}$$

where m^* is the exciton effective mass, and $h = na$ the thickness along the confined direction with a the lattice parameter and $n \geq 1$. FIG. 5.2b shows the peak energy as a function of $1/n^2$, where

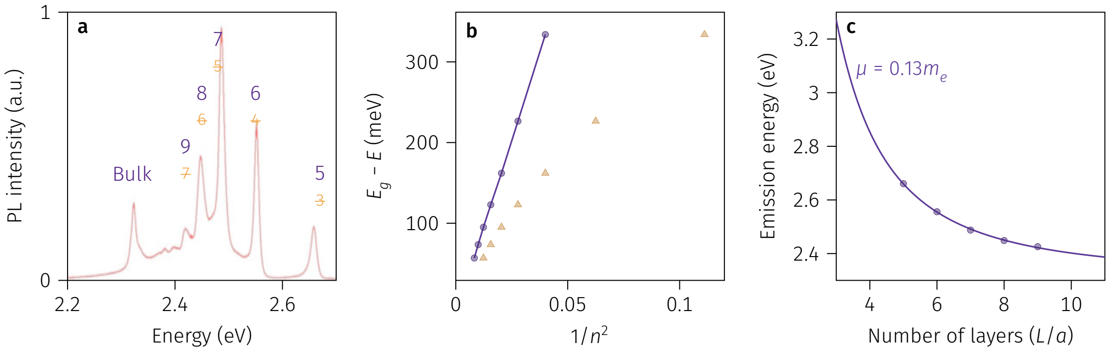

Figure 5.2 | Peak identification. **a** Liquid helium temperature PL spectrum of an ensemble of NPLs showing the original and corrected thicknesses in terms of monolayers (ML). **b** Emission energies as a function of the inverse number of layers squared. The linear trend expected is reproduced with the corrected peak assignments but not with the original assignment. **c** Emission energy as a function of the number of layers and fit yielding $\mu = 0.13\,m_e$. Panel **a** is adapted from [6].

n is the number of monolayers, for both the original (▲) and corrected (—●—) peak assignments. Doing so yields an effective mass of $\mu = 0.13\,m_e$ (Fig. 5.2c), close to the predicted values [1, 8].

Discrepancy with structural information

The new peak assignment, with 5 to 9 layers, is inconsistent with the structural information shown in Fig. 5.1. Indeed, with a lattice parameter taken as $a = 0.58$ nm, the thickness of NPLs ranges rom 2.9 nm to 5.2 nm, while the thicknesses deduced from the structural characterisation range from 1.5 nm to 4 nm. There are several possible factors for this discrepancy, namely the coalescence of the NPLs and a selection dilution which preserves larger particles preferentially.

Therefore, the reported thicknesses were underestimated by about 1 nm. Nonetheless, with the given edge lengths 23.5 nm and corrected thicknesses of 4 nm, we still have an aspect ratio close to 6 with one length close to the Bohr exciton radius.

5.2 Optical spectroscopy of single nanoplatelets

At the single object level, we find single NPLs emission from 2.4 to 2.6 eV lying close to the peaks identified in Fig. 5.2a and thus attributed to thicknesses of 6 to $\sim$ 10 layers.

Spectral domain

A typical single NPL emission displays two sets of closely spaced emission lines as shown in Fig. 5.3a as a function of excitation power. At low temperature, emission originates from the higher energy set of peaks (A) while, as excitation power density is increased, a set of low energy

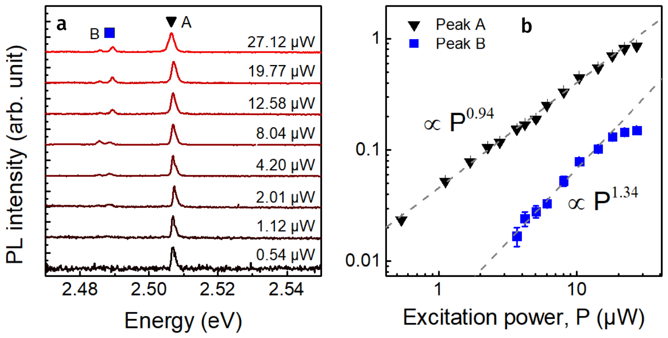

Figure 5.3 | Single nanoplatelets power-dependence. **a** PL spectrum of a single NPL as a function of exciton power. At low power, emission arises from the exciton state while at higher power, an additional low energy line emerges attributed to the trion. **b** Integrated emission intensity for each line defined in **a** as a function of power showing a linear, resp. super-linear, behaviour for the exciton, resp. trion. Reprinted from [6].

peaks (B) emerge. These spectral features are attributed to the exciton (A) line and trion (B) line. This assignment is supported by characteristic excitation power dependence exhibited by each line as shown in Fig. 5.3b, with respective slopes of 0.95 and 1.35 for the exciton and trion.

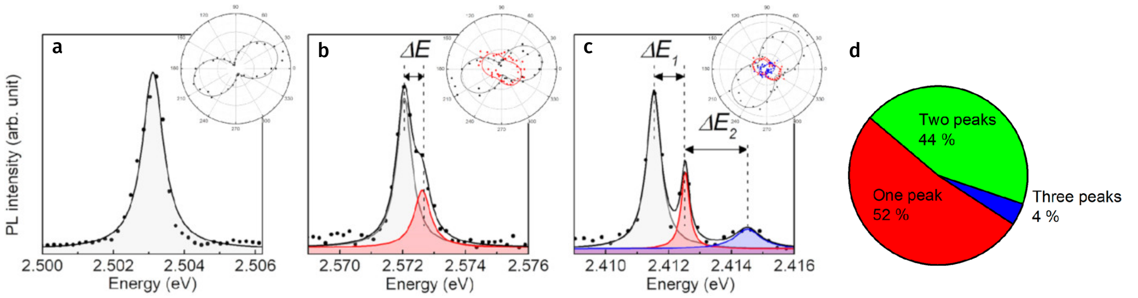

Figure 5.4 | Single nanoplatelets properties: spectral domain. Single emitter PL spectrum at liquid helium temperature. **a** One-peak, **b** two-peak and **c** three-peak spectrum together with their polarisation diagram. **d** Pie chart displaying relative occurences of one-, two- and three-peak spectra with a sample of 8 NPLs. Reprinted from [6].

Bright exciton fine structure Looking in more detail to the high-energy set of peaks, thus attributed to the exciton, reveals an exciton fine structure in half the cases investigated (Fig. 5.4). Notably, all emission peaks are found to be close to linearly polarised. This concurs with prior reports on single $CsPbBr_3$ NCs (nanocubes), and can be attributed to the bright triplet exciton fine structure emission. Interestingly, while single $CsPbBr_3$ NCs are expected to show an orthorhombic crystal structure [4] and thus exhibit a fully-split triplet exciton fine structure, here we observed a majority of single-peak spectra.

These could arise from several phenomena: first, due to thermal occupation, only the lowest exciton state may be populated enough. Secondly, due to the orthogonal nature of the three emitting dipoles, emission from the three dipoles could not be detected depending on the orientation of the NPLs. Finally, the limited signal-to-noise ratio may explain why higher energy states, with lower thermal occupation, are not resolved.

A later study [9], relying on the crystal termination of [4], directly identified two- and three-peak structures to different orientations of the NPLs. The relative proportions of multiple-peak spectra reported are strinkingly different than those reported here. One-peak spectra were also observed in [9] with unpolarised emission, while here, one-peak spectra are found to have a linear polarisation. In their paper, they relied on the assumption that all NPLs lie flat on the subtrate. However, in our case, we dispersed the NCs in a 5% solution of polystyrene in toluene, which yields film thicknesses $\sim 200\,\text{nm}$, such that NPLs are expected to be randomly oriented. The argument is then the same made for more isotropic NCs in Sec. 3.

Energy splittings between the bright exciton states are found to be similiar to nanocubes and $\sim 1\,\text{meV}$. This is surprising considering the high aspect ratio of the NPLs. Nonetheless, this seems to be the typical values reported for single NPLs as in [9].

Time domain

The optical properties of the bright exciton state were further studied in the time domain. The emission of the bright exciton state is found to be stable in time despite the limited signal-to-noise ratio (Fig. 5.5a). Using single avalanche photodiodes, we can record the emission of the bright triplet exciton with short binning time. Fig. 5.5b displays a 15 min intensity trace with a 10 ms binning time exemplifying the stability of the detected emission. Nonetheless, the emission intensity histogram is found to deviate from a random Poisson distribution. Deviations in intensity are attributed to the limited stability of the setup at that time, with an inevitable drift of the sample and possible interaction with the trion state although excitation power was kept low for these measurements and emission did not display significant switching between exciton and trion lines.

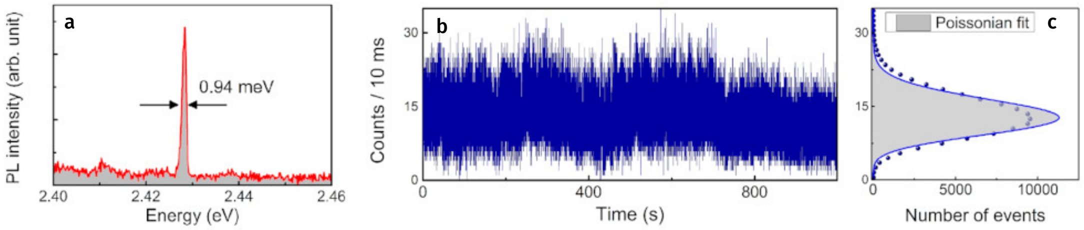

Figure 5.5 | Emission intensity. **a** PL spectrum of a single emitter. **b**, Intensity time trace of about 15 min with 10 ms binning time displaying the relative stability of the emission. **c** Intensity distribution and Poisson fit. Reprinted from [6].

This relative stability allows us to study the time-dependent behaviour of the bright exciton state. The exciton emission displays a fast emission of single photons (FIG. 5.6b-c). The bright exciton decay time is found to be short ∼ 80 ps and typical $g^{(2)}(0)$ describing the single-photon purity are found ∼ 0.1.

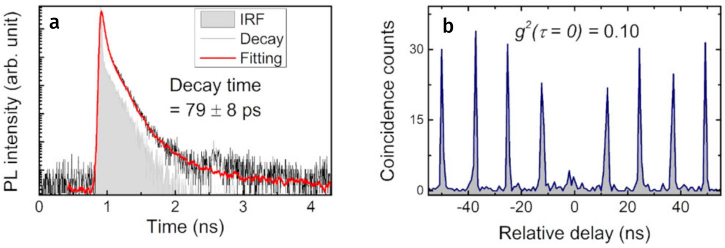

Figure 5.6 | Time-resolved emission. **a** Time-resolved PL decay of a single NPL. **b** Second-order correlation $g^{(2)}(\tau)$ measurement displaying a missing peak at $\tau = 0$ characteristic of single-photon emission. Reprinted from [6].

$CsPbBr_3$ NPLs are thus found to exhibit similar temporal properties to more isotropic NCs.

Conclusion

We have reported on single photon emission from single $CsPbBr_3$ nanoplatelets at liquid helium temperature. The emission consists in a set of peaks attributed to the bright triplet exciton and a low energy peak which emerges at higher power, attributed to the trion emission.

The bright exciton emission, as in more isotropic NCs, consists in a set of one, two and three peaks attributed the three orthogonal exciton dipoles and whose actual spectrum depends on the temperature and the orientation of the NPLs with respect to the detection apparatus. Time-resolved measurements reveal that the emission of single NPLs is fast on the 100 ps scale with a pure single photon emission $g^{(2)}(0) \sim 0.1$. These results highlight the similarities between so called nanocubes and nanoplatelets and calls into question our understanding of confinement in LHPs. Indeed, these results and others [9] report, for nanoplatelets, very similar properties to nanocubes with no clear energy splitting increase or decay accelereration as evidenced. This echoes our results in CH. 3 where no significant clear size-dependence is resolved for bright-bright energy splittings.

References for Chapter 5

[1] L. Protesescu et al., "Nanocrystals of Cesium Lead Halide Perovskites ($CsPbX_3$, X = Cl, Br, and I): Novel Optoelectronic Materials Showing Bright Emission with Wide Color Gamut", Nano Letters **15**, 3692–3696 (2015) (pp. 155, 157, 158).

[2] Q. A. Akkerman et al., “Solution Synthesis Approach to Colloidal Cesium Lead Halide Perovskite Nanoplatelets with Monolayer-Level Thickness Control”, Journal of the American Chemical Society **138**, 1010–1016 (2016) (pp. 155, 157).

[3] Y. Bekenstein et al., “Highly Luminescent Colloidal Nanoplates of Perovskite Cesium Lead Halide and Their Oriented Assemblies”, Journal of the American Chemical Society **137**, 16008–16011 (2015) (pp. 155, 157).

[4] F. Bertolotti et al., “Crystal Structure, Morphology, and Surface Termination of Cyan-Emissive, Six-Monolayers-Thick $CsPbBr_3$ Nanoplatelets from X-ray Total Scattering”, ACS Nano **13**, 14294–14307 (2019) (pp. 155, 159, 160).

[5] Y. Dong et al., “Precise Control of Quantum Confinement in Cesium Lead Halide Perovskite Quantum Dots via Thermodynamic Equilibrium”, Nano Letters **18**, 3716–3722 (2018) (p. 155).

[6] C. Huo et al., “Optical Spectroscopy of Single Colloidal $CsPbBr_3$ Perovskite Nanoplatelets”, Nano Letters **20**, 3673–3680 (2020) (pp. 155, 156, 158–161).

[7] V. Steinmetz et al., “Anisotropic shape of $CsPbBr_3$ colloidal nanocrystals: from 1D to 2D confinement effects”, Nanoscale **12**, 18978–18986 (2020) (p. 157).

[8] J. Ramade et al., “Fine structure of excitons and electron–hole exchange energy in polymorphic $CsPbBr_3$ single nanocrystals”, Nanoscale **10**, 6393–6401 (2018) (p. 158).

[9] A. Schmitz et al., “Optical Probing of Crystal Lattice Configurations in Single $CsPbBr_3$ Nanoplatelets”, Nano Letters, acs.nanolett.1c02775 (2021) (pp. 160, 161).

Conclusion

This thesis was a fundamental study of the optoelectronic properties of single $CsPbBr_3$ nanocrystals (NCs) in both the spectral and time domains. Starting from scratch, platforms enabling the study of single NCs, from the synthesis to the optical characterisation, were built by the author both at NTU and LPENS. Doing so, solutions of $CsPbBr_3$ NCs were successfully synthesised and single NCs were isolated.

The optical properties of single $CsPbBr_3$ NCs were studied at cryogenic temperatures where two classes of single NC spectra are evidenced, exhibiting either two or three bright exciton emission peaks as previously reported [1–4]. Given an orthorhombic crystal structure, the bright triplet exciton is expected to fully split and lead to three-peak spectra [1, 3, 5]. Alternatively, for higher symmetry crystalline phases, the shape anisotropy of NCs can also lead to a splitting of the bright triplet exciton [6–8]. Regardless of the underlying mechanisms, with a simple model taking into account the orientation of the orthogonal emission dipoles and the population of the bright-triplet exciton states, we can explain the observation of two- and three-peak spectra and in fact directly simulate observed spectra.

By a statistical analysis on a large number of NCs, we have found that bright-bright exciton splittings are only weakly size-dependent in the intermediate confinement regime pointing to an overwhelming contribution of the NC morphology anisotropy in setting the fine structure splittings. This provides critical information in light of the ongoing debate about the fine structure of LHPs which should enable further theoretical works to be refined. In addition to the fine structure of the bright exciton state, we also evidenced a set of lower-energy emission peaks attributed to the recombination of the exciton state accompanied by the simultaneous emission or absorption of an optical phonon. These optical phonon replica can readily be related to phonon modes of the lead halide cage with a minimal influence of the inorganic or organic cation. When increasing the excitation power, two additional emission lines can be resolved: an intermittent emission line attributed to the trion and a stable emission line attributed to the biexciton. Notably, we evidence a strong size-dependence for the energy shifts of both the trion and biexciton with respect to the exciton line. This size-dependence is understood as a consequence of the increased electron-hole interactions as the size of the NCs is reduced and the contributions of confinement and Coulomb interaction are disentangled.

In addition to this detailed spectral analysis of single $CsPbBr_3$ NCs emission, we also investigated the time-domain behaviour of the NCs. We verified that the bright emission spots evidenced in PL mapping experiments were in fact single NCs by performing second-order intensity correlation measurements and evidence strong antibunching under pulsed excitation. The time-domain behaviour of NCs was probed via temperature-dependent decay measurements which reveal the influence of the dark state on the bright exciton PL. Doing so, we investigated three different coupling schemes between the bright and dark excitons and discussed their relative pertinence in light of recent literature and available phonon modes in LHPs. Notably, we highlight the importance of low energy optical phonon modes most likely at play in bright-dark population redistribution at cryogenic temperatures.

While the exact origin for the outstanding properties of LHPs is still not clear, let us summarise here some findings that should reveal crucial in understanding this “issue”. As said, LHP NCs are structuraly labile materials with a dynamic structure that is expected to host polarons [9, 10]. Such polarons could efficiently shield carriers from scattering by phonons. This may be related to the reduced bright-dark transitions that vanish in the first order such that the second order term is dominant. Further works should aim at characterising the phonon spectrum of single NCs and its influence on both homogeneous broadening and phonon-assisted population redistribution as this recent study [11]. In addition, while LHP NCs are often referred to as bright, quantification of this brightness remains elusive. Proper understanding of the photophysical properties of single LHP NCs will surely require to disentangle the contributions of radiative and non-radiative transition.

More generally, the development of quantum applications will require a wide diversity of quantum sources, from lasers to single-photon and more generally N-photon sources. In this respect, while the nanocrystals studied here are rather simple structures we note that there is a strong move towards the development of more complex structures based on the assembly of NCs [12, 13] which offers the potential of an unparalleled control of the nm-scale elementary building blocks of mesoscopic systems exhibiting many-body light matter interactions.

References

[1] M. Fu et al., "Neutral and Charged Exciton Fine Structure in Single Lead Halide Perovskite Nanocrystals Revealed by Magneto-optical Spectroscopy", Nano Letters **17**, 2895–2901 (2017) (p. 163).

[2] G. Rainò et al., "Single Cesium Lead Halide Perovskite Nanocrystals at Low Temperature: Fast Single-Photon Emission, Reduced Blinking, and Exciton Fine Structure", ACS Nano **10**, 2485–2490 (2016) (p. 163).

[3] J. Ramade et al., "Fine structure of excitons and electron–hole exchange energy in polymorphic $CsPbBr_3$ single nanocrystals", Nanoscale **10**, 6393–6401 (2018) (p. 163).

[4] C. Yin et al., "Bright-Exciton Fine-Structure Splittings in Single Perovskite Nanocrystals", Physical Review Letters **119**, 6401 (2017) (p. 163).

[5] M. A. Becker et al., "Bright triplet excitons in caesium lead halide perovskites", Nature **553**, 189–193 (2018) (p. 163).

[6] M. O. Nestoklon et al., "Optical orientation and alignment of excitons in ensembles of inorganic perovskite nanocrystals", Physical Review B **97**, 235304 (2018) (p. 163).

[7] P. Tamarat et al., "The dark exciton ground state promotes photon-pair emission in individual perovskite nanocrystals", Nature Communications **11**, 6001 (2020) (p. 163).

[8] R. Ben Aich et al., "Bright-Exciton Splittings in Inorganic Cesium Lead Halide Perovskite Nanocrystals", Physical Review Applied **11**, 034042 (2019) (p. 163).

[9] O. Cannelli et al., "Quantifying Photoinduced Polaronic Distortions in Inorganic Lead Halide Perovskites Nanocrystals", Mar. 3, 2021 (p. 164).

[10] K. Miyata et al., "Large polarons in lead halide perovskites", Science Advances **3**, e1701217 (2017) (p. 164).

[11] G. Rainò et al., "Ultra-narrow room-temperature emission from single $CsPbBr_3$ perovskite quantum dots", Nature Communications **13**, 2587 (2022) (p. 164).

[12] G. Rainò et al., "Superfluorescence from lead halide perovskite quantum dot superlattices", Nature **563**, 671–675 (2018) (p. 165).

[13] I. Cherniukh et al., "Perovskite-type superlattices from lead halide perovskite nanocubes", Nature **593**, 535–542 (2021) (p. 165).

A

Rate equations

Rate equations are essential to describe a wide variety of phenomena. They are at the basis of the description of atomic lines as provided by Einstein who considered that three different processes can occur [1]. FIG. A.1 shows a two-level system with the associated absorption, spontaneous emission and stimulated emission rates. The so-called Einstein coefficients, which give the transition probabilities for each process, are explicitated. Detailed balance of the excited state gives

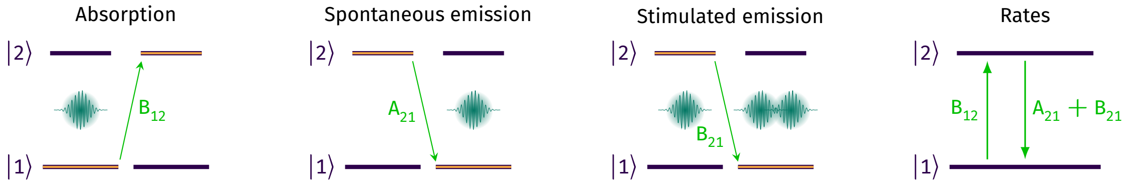

Figure A.1 | Light-matter interaction: Einstein coefficients. Sketch of the three light-matter interaction processes identified by Einstein in [1]. The full rate model is shown on the right hand side.

$$\frac{dp_2}{dt} = B_{12}p_1 - (B_{21} + A_{21})\, p_2 \tag{A.1}$$

This equations therefore provided critical insight for light-matter interactions with equations that basically describe any probabilistic decay process. Mathematically, such equations consist in a system of linear differential equations that can be equally expressed in the form a matrix equation.

In this work, we have investigated several classes of cases varying both the number of states and transition rates. For the rate equations, we have used a general expression in matrix form which could be solved numerically, however some simple cases were also investigated analytically. Here, we detail the different cases explored and their associated equations. This enables us to determine the time-dependence of the populations in each state and thus provides direct information for time-resolved decay and correlation measurements.

A.1 General model

A.1.1 Description

We derive here the general rate equations for N levels. For $N \leq 3$, we get quite convoluted equations which could be solved analytically but are rather tedious to express. For larger N, it is better to directly solve the rate equations using linear algebra.

Let us write the population dynamics of a N level system in matrix form as

$$\dot{\boldsymbol{p}} = \mathcal{A}\boldsymbol{p}$$

The decay times are given by the eigenvalues Γ_i of $\boldsymbol{A}$ and the amplitudes derive from the corresponding eigenvectors. The solution of the matrix equation is given by

$$\boldsymbol{p} = \sum_{i=1}^{N} \alpha_i \boldsymbol{v_i}\, e^{\Gamma_i t}$$

where α_i are constants to be determined with initial conditions, Γ_i are the eigenvalues of $\mathcal{A}$ and $\boldsymbol{v_i}$ the corresponding eigenvectors. Let us note that by definition the eigenvalues Γ_i will be negative, and that $v_i^{(j)}$ is the j-th component of the eigenvector $\boldsymbol{v_i}$. At $t = 0$, we set the initial population in the excited state which decays at a rate Γ_{E}. Thus the α_i are given by the solution of $\sum_i \alpha_i \boldsymbol{v_i} = \boldsymbol{p}(t = 0)$ and the total photoluminescence signal is given by $S(t) = \sum_i \eta_i \Gamma_i p_i$.

Even though actual emission from all states is not recorded in our experiments, their presence is directly observed on the decay rates Γ_i of the detected bright exciton states.

A.1.2 Implementation

We numerically solve the matrix equation using custom scripts in MATLAB. In practice, we input the effective matrix containing information about the transition rates. The matrix equation is then solved by diagonalising the matrix and expressing the populations as a function of eigenvalues and eigenvectors as decribed above.

A.1.3 Electron-phonon interaction in lead halide perovskites

Electron-phonon (EP) interaction is an effective pathway for non-radiative population relaxation as well as coherence relaxation in semiconductor nanostructures. In the following, we start from the theoretical description of the EP system and investigate the different mechanisms at play in light of their manifestations in the low-temperature PL of single nanoemitters.

Constituting equations

EP interactions can usually be treated as a perturbation to the lattice potential leading to a change in bandgap due to the displacement of lattice ions. In this context, EP interactions can be expanded in terms of powers of small displacements. In an extension of the independent boson model, the hamiltonian $\mathbf{H}$ of the system comprised of exciton states i with energies $E_{i\boldsymbol{K}}$ and lattice phonons j with energies $\hbar\omega_{j\boldsymbol{q}}$ can be expressed as [2–5]

$$
\begin{aligned}
\mathbf{H} &= \mathcal{H}_{\text{ex}} + \mathcal{H}_{\text{ph}} + \mathcal{H}^{(1)}_{\text{ex-ph}} + \mathcal{H}^{(2)}_{\text{ex-ph}} \\
&= \sum_{i} E_{i\boldsymbol{K}}\, \hat{c}^{\dagger}_{i\boldsymbol{K}}\, \hat{c}_{i\boldsymbol{K}} + \sum_{j,\boldsymbol{q}} \hbar\omega_{j\boldsymbol{q}}\, \hat{b}^{\dagger}_{j\boldsymbol{q}}\, \hat{b}_{j\boldsymbol{q}} && \text{(A.2a)} \\
&\quad + \sum_{i,i',\boldsymbol{K},j,\boldsymbol{q}} \hbar g^{ii'}_{j\boldsymbol{q}}\, \hat{c}^{\dagger}_{i\boldsymbol{K}+\boldsymbol{q}}\, \hat{c}_{i'\boldsymbol{K}} \left(\hat{b}_{j\boldsymbol{q}} + \hat{b}^{\dagger}_{j\boldsymbol{q}}\right) && \text{(A.2b)} \\
&\quad + \sum_{i,i',\boldsymbol{K},j,\boldsymbol{q},j',\boldsymbol{q}'} \hbar g^{ii'}_{j\boldsymbol{q}j'\boldsymbol{q}'}\, \hat{c}^{\dagger}_{i\boldsymbol{K}\pm\boldsymbol{q}\pm\boldsymbol{q}'}\, \hat{c}_{i'\boldsymbol{K}} \left(\hat{b}_{j\boldsymbol{q}} + \hat{b}^{\dagger}_{j\boldsymbol{q}}\right)\left(\hat{b}_{j'\boldsymbol{q}'} + \hat{b}^{\dagger}_{j'\boldsymbol{q}'}\right) && \text{(A.2c)}
\end{aligned}
$$

where the indices i and j run respectively over all exciton states i with associated operators $(\hat{c}^{\dagger}, \hat{c})$, energies $E_{i\boldsymbol{K}}$ and wavevector $\boldsymbol{K}$, and over all phonon branches j with associated operators $(\hat{b}^{\dagger}, \hat{b})$, energies $\hbar\omega_{j\boldsymbol{q}}$ and wavevector $\boldsymbol{q}$. In detail, (A.2a) is the sum of $\mathcal{H}_{\text{ex}}$ the exciton and $\mathcal{H}_{\text{ph}}$ the phonon hamiltonian, (A.2b) is the first-order EP interaction $\mathcal{H}^{(1)}_{\text{ex-ph}}$, and (A.2c) is the second-order EP interaction $\mathcal{H}^{(2)}_{\text{ex-ph}}$. In the weak interaction regime, we can write the EP interaction hamiltonian for the exciton as the sum of the carrier-phonon interaction hamiltonians independently on the electron and hole. In this case, the coupling matrix element involving exciton states i and i' with a phonon $(j,\ \boldsymbol{q})$ can be separated in two factors: one related to the actual coupling mechanism $\mathcal{G}_{j\boldsymbol{q}}$

and a form factor as [2, 6]

$$\begin{aligned} g^{ii'}_{j\boldsymbol{q}} &= g^{ii'}_{j\boldsymbol{q},\mathrm{e}} - g^{ii'}_{j\boldsymbol{q},\mathrm{h}} = \mathcal{G}^{\mathrm{e}}_{j\boldsymbol{q}} \mathcal{F}^{\mathrm{e}}_{\boldsymbol{q}} - \mathcal{G}^{\mathrm{h}}_{j\boldsymbol{q}} \mathcal{F}^{\mathrm{h}}_{\boldsymbol{q}} \\ &= \int d^3 r \, \Psi^*_i(\boldsymbol{r}) \, \Psi_{i'}(\boldsymbol{r}) \, \left[\mathcal{G}^{\mathrm{e}}_{j\boldsymbol{q}} \, e^{-i\mathfrak{m}_{\mathrm{e}} \boldsymbol{q} \cdot \boldsymbol{r}} - \mathcal{G}^{\mathrm{h}}_{j\boldsymbol{q}} \, e^{i\mathfrak{m}_{\mathrm{h}} \boldsymbol{q} \cdot \boldsymbol{r}} \right] \end{aligned}$$

where $\mathfrak{m}_{\mathrm{e(h)}} = m_{\mathrm{e(h)}}/M$, $\mathcal{G}^{\mathrm{e(h)}}_{j\boldsymbol{q}}$ is the coupling constant to phonon mode $(j, \boldsymbol{q})$ and $\mathcal{F}^{e(h)}_{\boldsymbol{q}}$ is a form factor that depends on degree of localisation of the exciton written as

$$\mathcal{F}^{e(h)}_{\boldsymbol{q}} = \int d^3 r \, \Psi^*_i(\boldsymbol{r}) \, \Psi_{i'}(\boldsymbol{r}) e^{\mp i\mathfrak{m}_{\mathrm{e(h)}} \boldsymbol{q} \cdot \boldsymbol{r}} \tag{A.3}$$

Similarly, for the second order coupling constant $g^{ii'}_{j\boldsymbol{q}j'\boldsymbol{q}'}$ we need to consider the fact that transitions are not direct but go through an intermediate level v to write [4, 7]

$$g^{ii'}_{j\boldsymbol{q}j'\boldsymbol{q}'} = \sum_{\mathrm{c}=\mathrm{e,h}} \sum_{v} \frac{g^{i'v(\mathrm{c})}_{j\boldsymbol{q}} \, g^{vi(\mathrm{c})}_{j'\boldsymbol{q}'}}{E^{(\mathrm{c})}_i - E^{(\mathrm{c})}_v} \tag{A.4}$$

Actual expressions for the coupling parameters g depend on the coupling mechanism at play, as detailed after expressing scattering rates and discussing some useful considerations. Note that while the independent boson model is exactly solvable and can be used to describe multi-phonon transitions, this is beyong the scope of this work. Here, we only give expressions for the coupling mechanisms and write the corresponding transition rates.

Transition rates

The first and second order interaction hamiltonians describe respectively direct and indirect transitions, such that to determine the scattering rates we need Fermi's golden rules.

Fermi golden rules We will need both Fermi's golden rules. The one we think about when talking about Fermi golden rule is Fermi's golden n°2 which describes the transition rate for a direct transition. We will also need Fermi's golden rule n°1 which describes the transition rate for indirect transitions.[1]

Considering states formed by excitons and phonons $|i\rangle_K \times |n\rangle^{(j)}_{\boldsymbol{q}}$, the scattering rate $1/\tau^{(j)\pm}_{ii'}$ between exciton states i and i' associated with the creation $(^+)$ or annihilation $(^-)$ of a single phonon in mode j containing n phonons with wavevector $\boldsymbol{q}$ can readily be obtained from $\mathbf{H}$ by

---

[1] Let us note that both Fermi's golden rules [8] were first derived by Dirac [9].

applying Fermi's golden rule and taking care of energy and momentum conservation

$$\begin{aligned}
\left.\frac{\hbar}{2\pi}\frac{1}{\tau_{ii'}^{(j)\pm}}\right|_{1^{\text{st}}\text{ order}} &= \sum_{\boldsymbol{q}} \left|\left\langle i'_{\boldsymbol{K}\mp\boldsymbol{q}} \otimes (n\pm 1)_{\boldsymbol{q}}^{(j)} \middle| H_{\text{int}}^{(1)} \middle| i_{\boldsymbol{K}} \otimes n_{\boldsymbol{q}}^{(j)}\right\rangle\right|^2 \delta\left(E_i - E_{i'} \mp \hbar\omega_{\boldsymbol{q}}\right) \\
&= \sum_{\boldsymbol{q}} \left|\hbar g_{j\boldsymbol{q}}^{ii'}\right|^2 \left|\left\langle (n\pm 1)_{\boldsymbol{q}}^{(j)} \middle| (b+b^\dagger) \middle| n_{\boldsymbol{q}}^{(j)}\right\rangle\right|^2 \delta\left(E_i - E_{i'} \mp \hbar\omega_{\boldsymbol{q}}\right) \\
\left.\frac{1}{\tau_{ii'}^{(j)\pm}}\right|_{1^{\text{st}}\text{ order}} &= \frac{2\pi}{\hbar} \sum_{\boldsymbol{q}} \left|\hbar g_{j\boldsymbol{q}}^{ii'}\right|^2 \left|\sqrt{n_B + \frac{1}{2} \pm \frac{1}{2}}\right|^2 \delta\left(E_i - E_{i'} \mp \hbar\omega_{\boldsymbol{q}}\right)
\end{aligned}$$

where n_B is the Bose-Einstein occupation factor and the temperature-dependent part depends on the actual process at play as detailed in Table A.1. For the second-order term, we can develop in the same way and get the scattering rate $1/\tau_{ii'}^{(jj')\pm\pm}$ between exciton states i and i' associated with the creation ($^+$) or annihilation ($^-$) of a single phonon in mode j and the creation ($^+$) or annihilation ($^-$) of a single phonon in mode j' as

$$\begin{aligned}
\left.\frac{\hbar}{2\pi}\frac{1}{\tau_{ii'}^{(j)\pm\pm}}\right|_{\text{2nd order}} &= \sum_{\boldsymbol{q},\boldsymbol{q}'} \delta \times \left|\left\langle i'_{\boldsymbol{K}\mp\boldsymbol{q}\mp\boldsymbol{q}'} \otimes (n\pm 1)_{\boldsymbol{q}}^{(j)} \otimes (n'\pm 1)_{\boldsymbol{q}'}^{(j')} \middle| H_{\text{int}}^{(2)} \middle| i_{\boldsymbol{K}} \otimes n_{\boldsymbol{q}}^{(j)} \otimes n'^{(j')}_{\boldsymbol{q}'}\right\rangle\right|^2 \\
\left.\frac{1}{\tau_{ii'}^{(j)\pm\pm}}\right|_{2_{\text{nd}}\text{ order}} &\propto \frac{2\pi}{\hbar} \sum_{\boldsymbol{q},\boldsymbol{q}'} \delta \times \left| \sum_{\text{c}=\text{e},\text{h}} \sum_{v} \frac{g_{j\boldsymbol{q}}^{i'v(\text{c})} g_{j'\boldsymbol{q}'}^{vi(\text{c})}}{E_i^{(\text{c})} - E_v^{(\text{c})}} \right|^2 \left|\sqrt{n_B + \frac{1}{2} \pm \frac{1}{2}}\sqrt{n'_B + \frac{1}{2} \pm \frac{1}{2}}\right|^2
\end{aligned}$$

where we have defined $\delta = \delta\left(E_i - E_{i'} \mp \hbar\omega_{\boldsymbol{q}} \mp \hbar\omega'_{\boldsymbol{q}'}\right)$ for clarity. Before even expressing the mechanism-dependent term g, we have already unveiled the phonon occupation dependence of electron-phonon matrix elements. The actual matrix elements depend on the relative position of the initial and final states and are summarised in Table A.1.

Useful considerations As is evident from the fact that EP coupling does not contain a spin part, there can be no-phonon assisted transitions between orthogonal exciton states. In the presence of spin-orbit coupling however, orthogonal exciton states with different J and J_z can mix such that the matrix elements taken between them are non-zero [10, 11].

Within this system comprised of exciton states and phonon modes, the diagonal and

Table A.1 | Exciton-phonon interaction: thermal dependence. Three different coupling terms can be identified.

	One-phonon process	Two-phonon processes	
	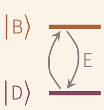	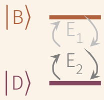	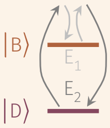
$\gamma_{B\to D}/\gamma_0$	$(N+1)$	$(N_1+1)(N_2+1)$	$N_1(N_2+1)$
$\gamma_{D\to B}/\gamma_0$	N	$N_1 N_2$	$(N_1+1)N_2$

off-diagonal matrix elements of the exciton-phonon interaction with respect to the exciton states are responsible respectively for the pure dephasing part and natural dephasing rate.Explicitely, while g^{ii}_{jq} gives the linewidth broadening g^{ij}_{jq} with $j \neq i$ gives the phonon-assisted transition rate between exciton sublevels i and j [3]. The total exciton dephasing rate is thus given by a sum of two parts as defined in Fig. 1.11c: dephasing related to population relaxation and pure dephasing. The population relaxation processes $j \neq i$ contribute to the dephasing rate by half the population decay rate. Pure dephasing processes ii, that do not involve population relaxation (i.e. no energy change, virtual processes), also contribute to dephasing.

After excitation, electrons relax to the band-edge which can have a sizeable density of available states in semiconductors. Excited electrons are thus rapidly confined to small regions of the Brillouin zone, usually the center, such that, near thermal equilibrium, electron-phonon interactions are mainly driven by long-wavelength phonons. This is the small wavevector approximation which is essential for the following descriptions where we will assume respectively a linear dispersion and no dispersion for acoustic and optical phonon modes. Let us note that this approximation is further motivated by the fact that the form factor defined in (A.3) enforces the validity of the approximation. Indeed, considering a gaussian wavefunction ψ, then the form factor is also a gaussian in reciprocal space with $q_{\max} \propto 1/\sigma$ where σ is the spatial extension of the exciton wavefunction. Exciton-phonon coupling thus happens mainly through small-wavevector phonons.

Coupling mechanisms

That said, three main coupling mechanisms exist for excitons and phonons: the deformation potential interaction, the piezoelectric interaction and the polar Fröhlich interaction.

Deformation potential interaction The deformation potential interaction results from the displacement of atoms in the lattice with respect to their equilibrium position. The net effect of this interaction is a small shift in the energy bands similar to a strain, only when the atomic displacement is along the direction of the wavevector [12]. Thus, for longitudinal acoustic waves only, the short-range interactions between excitons and long-wavelength acoustic phonons are non-zero and can be written as [13]

$$\mathcal{G}^{e(h)}_{\boldsymbol{q},\,\mathrm{DPA}} = \sqrt{\frac{\hbar}{2\varrho\omega_{\boldsymbol{q}}V}}\,|\boldsymbol{q}|\;D_{e(h)} = \sqrt{\frac{\hbar\,|\boldsymbol{q}|}{2\varrho v_s V}}\,D_{e(h)} \qquad \propto |\boldsymbol{q}|^{1/2} \tag{A.5}$$

where as in SEC. 1.1.3 ϱ is the material density and v_s the velocity of sound. $D_{e(h)}$ are the deformation potential constants of the conduction band and valence band respectively which are simply the rate of change of the band energy with pressure [14]. Exciton interaction with both non-polar transverse optical phonons and longitudinal optical phonons can also be described as a deformation potential where lattice displacements effectively lead to small shifts in the energy bands. This interaction term can be written as [15, eq. (5.8)]

$$\mathcal{G}^{e(h)}_{q,\,\mathrm{DPO}} = \sqrt{\frac{\hbar}{2\mu N\omega}}\,\frac{D^{*}_{e(h)}}{a} \tag{A.6}$$

where $\hbar\omega$ is the involved optical phonon mode energy, μ is the reduced mass of atoms in the unit cell, N is the number of unit cells in the crystal and a the lattice constant.

Piezoelectric interaction Many materials are piezoelectric and exhibit the macroscopic effect of the piezoelectric interaction: the generation of an electric field when compressed. Acoustic phonon, being periodic compression dilatation waves like sound can generate periodic electric fields. The crystal should lack an inversion center to exhibit piezoelectricity. Aside from the deformation potential interaction, long-wavelength acoustic phonons thus also induce a strain on the lattice and this piezoelectric coupling term can be written as [13]

$$\mathcal{G}^{e}_{\boldsymbol{q},\,\mathrm{PZA}} = \mathcal{G}^{h}_{\boldsymbol{q},\,\mathrm{PZA}} = i\sqrt{\frac{\hbar}{2\varrho\omega_{\boldsymbol{q}}V}}\,\mathcal{M}_{\lambda}(\hat{\boldsymbol{q}}) = i\sqrt{\frac{\hbar}{2\varrho v_s\,|\boldsymbol{q}|\,V}}\,\mathcal{M}_{\lambda}(\hat{\boldsymbol{q}}) \qquad \propto |\boldsymbol{q}|^{-1/2} \tag{A.7}$$

where $\mathcal{M}_{\lambda}(\hat{\boldsymbol{q}})$ are matrix elements that depend only on the direction $\hat{\boldsymbol{q}}$ of the wavevector $\boldsymbol{q}$. While both LA and TA phonons are concerned by this piezoelectric term, the interaction with TA phonons is usually strongest because of the smaller sound velocity.

Fröhlich interaction In polar materials, the main interaction term is that involving longitudinal optical phonons via the Fröhlich interaction [13, 15]

$$\mathcal{G}^{e}_{q,\text{Frö}} = \mathcal{G}^{h}_{q,\text{Frö}} = i\sqrt{2\pi e^2 \hbar\omega_{\text{LO}} \left(\epsilon_\infty^{-1} - \epsilon_0^{-1}\right)} \frac{1}{\sqrt{V}\,|\boldsymbol{q}|} \qquad \propto |\boldsymbol{q}|^{-1} \tag{A.8}$$

where ϵ_∞ and ϵ_0 are the high- and low-frequency dielectric constants. Assuming a nearly flat dispersion at long wavelengths, $\hbar\omega_{LO}$ becomes $\boldsymbol{q}$-independent and the Fröhlich interaction scales as $|\boldsymbol{q}|^{-1}$. (A.8) can also be expressed as a function of the polaron constant α, which can be related to the effective mass see e.g. [16].

Resulting exciton-phonon interaction

As the resulting interaction is a sum over all phonon modes, detailed theoretical calculations are required to determine the exact strengths of each term. However, based on the wavevector dependence of the interaction terms we can already estimate the dominating contributions.

Acoustic-phonon coupling For acoustic phonons there are therefore two main interaction channels expected: the deformation potential for LA phonons and the piezoelectric potential for TA phonons which scale respectively as $|\boldsymbol{q}|^{1/2}$ and $|\boldsymbol{q}|^{-1/2}$. At small wavevectors, we therefore expect the piezoelectric interaction to dominate.

Optical-phonon coupling For optical phonons, two main interaction channels are expected: the deformation potential for both LO and TO phonons and the Fröhlich potential for LO phonons which are respectively independent of $\boldsymbol{q}$ and scale as $|\boldsymbol{q}|^{-1}$. For small wavevectors, interaction with LO phonons via the Fröhlich interaction is expected to be dominant.

EP interaction thus proceeds mainly through two mechanisms: piezoelectric interaction with TA phonon and Fröhlich interaction with LO phonons. In addition, coupling to TO phonons is expected through deformation potential interaction.

A.1.4 Population redistribution mechanisms

Several mechanisms can be used to redistribute the population between states. They can be classified in two categories:

- non-radiative transitions, i.e. moving population without involving light; these are phonon-assisted in SCs
- radiative transitions (absorption, emission)

In the following, we investigate several types of population redistribution mechanisms based on one- and two-phonon processes.

One-phonon mixing model

In the one-phonon mixing model, at zero temperature, the higher exciton state population spontaneously decays to the lower exciton state at a rate γ_0. At finite temperature, transitions between $|U\rangle$ and $|L\rangle$ happen via the emission (absorption) of a phonon matching the splitting between the two state Δ. Therefore, the probability for these transitions to happen are directly related to the available phonon population. The average number of phonons at a temperature T is given by the so-called Bose-Einstein phonon number as $N_B^{-1} = \exp\left(\Delta/k_BT\right) - 1$. The downward ($|U\rangle \rightarrow |L\rangle$) transition rate, driven by the emission of a phonon, is then given by $\gamma_\downarrow = \gamma_0\left(1 + N_B\right)$ while the upward ($|L\rangle \rightarrow |U\rangle$) transition rate, driven by the absorption of a phonon, is given by $\gamma_\uparrow = \gamma_0 N_B$. Given these expressions for the thermally-activated transition rates, one can express the decay rates in a simple analytical form. To do so, let us note that the difference, the sum and the product of $\gamma_\downarrow$ and $\gamma_\uparrow$ can be written using hyperbolic functions as

$$\begin{aligned}
\gamma_\downarrow - \gamma_\uparrow &= \gamma_0 \\
\gamma_\uparrow + \gamma_\downarrow &= \gamma_0\left(1 + 2N_B\right) = \gamma_0 \coth\frac{\Delta}{2k_BT} \\
\gamma_\uparrow\gamma_\downarrow &= \gamma_0^2 N_B\left(1 + N_B\right) = \frac{\gamma_0^2}{4}\sinh^{-2}\frac{\Delta}{2k_BT}
\end{aligned}$$

Thus, the decay rates $\Gamma_\pm$ can be neatly expressed as

$$\Gamma_\pm = \frac{1}{2}\left(\Gamma_U + \Gamma_L + \gamma_0 \operatorname{cotanh}\frac{\Delta}{2k_BT} \pm \sqrt{\left(\Gamma_U - \Gamma_L + \gamma_0\right)^2 + \gamma_0^2 \sinh^{-2}\frac{\Delta}{2k_BT}}\right)$$

and are represented in Figure A.2 together with the corresponding relative amplitudes for the two scenarios: a lower dark state (DG in plain lines) and a lower bright state (BG in dashed lines). The parameters used are $\Gamma_B = 14.29\,\mathrm{ns}^{-1}$, $\Gamma_D = 0.05\,\mathrm{ns}^{-1}$, $\eta_B = 1$, $\eta_D = 0$, $a = 0.5$, a zero-temperature relaxation rate $\gamma_0 = 0.5\,\mathrm{ns}^{-1}$ and a small bright-dark splitting $\Delta = \pm 300\,\mu\mathrm{eV}$. It is noteworthy that in this simple model the fractional amplitude crossover temperature T_c is directly proportional to the energy splitting as $T_c = \Delta\left[k_B \log f\right]^{-1}$ where f is a function of γ_0, Γ_L, Γ_U and a. See `CrossoverTempSimu.m` for numerical estimations.

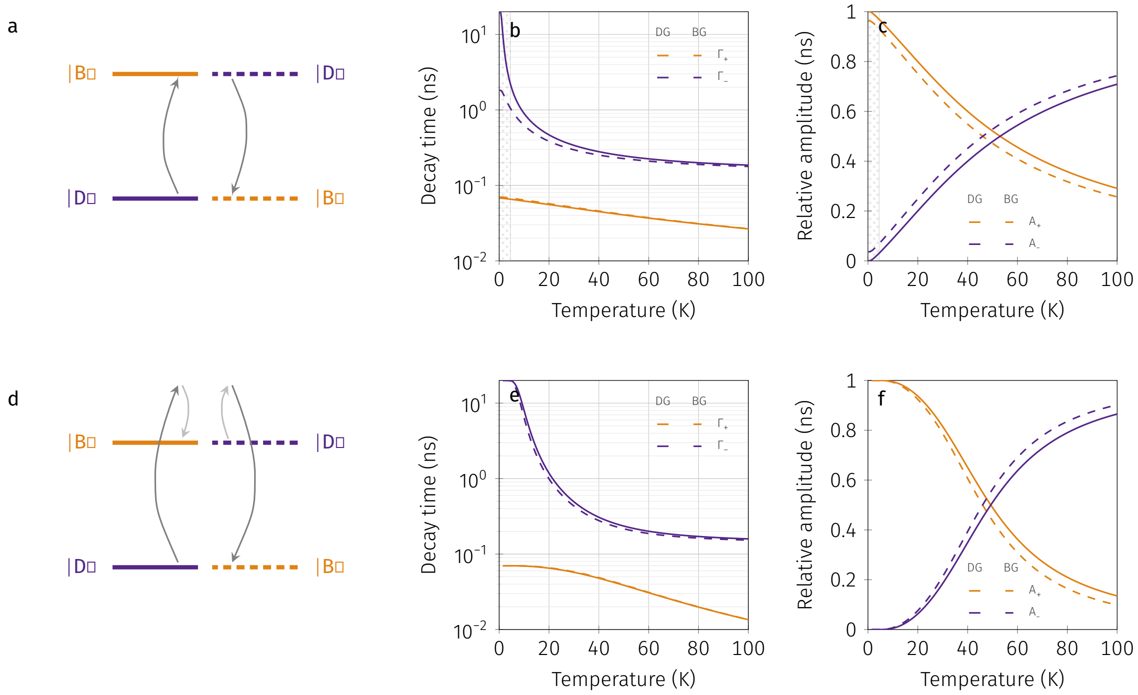

Figure A.2 | Reproducing the decay dynamics: dark vs. bright ground state. Comparison between the scenarios with a lower dark state and a lower bright state with short and long lifetimes comparable to those observed in our experiments. **a**-**c** Photophysics assuming a one-phonon mixing model. **a**, Decay times deduced from the one-phonon mixing model in the case of a dark ground state (—) and a bright ground state (–). **b**, Corresponding relative amplitudes. **c**, Photoluminescence dynamics in the two scenarios at 4 K and 50 K deduced from **a**-**b**. **d**-**f** Photophysics assuming a two-phonon mixing model. **d**, Decay times deduced from the two-phonon mixing model in the case of a dark ground state (DG in plain lines) and a bright ground state (BG in dashed lines). **e**, Corresponding relative amplitudes. **f**, Photoluminescence dynamics in the two scenarios at 4 K and 50 K deduced from **d**-**e**. The parameters used in the simulations are Γ_B =14.29 ns^{-1}, Γ_D = 0.05 ns^{-1}, η_B = 1, η_D = 0 and a = 0.5 assuming a small bright-dark splitting Δ = ± 300 µeV in all cases. The zero-temperature mixing rate is set to 0.5 ns^{-1} for the one-phonon case and to 6 ns^{-1} in the two-phonon case to reproduce similar trends in the two cases.

Raman-like process two-phonon mixing

As reported by the Photons and Nanosystems team of the Institut d'Optique [17–19], the thermal and magnetic coupling between the upper and lower exciton states LHPs ($FaPbI_3$, $FaPbBr_3$, $CsPbI_3$) cannot be reproduced by the single-phonon mixing model presented above. To describe the excitonic dynamics in this material, the bright-dark mixing needs to be driven by the absorption and emission of two optical phonons (E_{LO_1} and E_{LO_2}), rather than one acoustic phonon, with an energy difference matching the fine-structure splitting $|\Delta E_{LO}| = \Delta$. As such, this model is referred to as a two-phonon thermal mixing model.

As they describe the same system, the rate equations remain unchanged. The only difference is that the transition rates between the sublevels $|U\rangle$ and $|L\rangle$ now involve two optical phonons and are given by:

$$\gamma_\uparrow = \gamma_0 \, N_{LO_2} \left(N_{LO_1} + 1\right)$$
$$\gamma_\downarrow = \gamma_0 \, N_{LO_1} \left(N_{LO_2} + 1\right)$$

where N_{LO_i} are the Bose-Einstein phonon numbers. Given these expressions for the thermally-activated transition rates, one can express the decay rates analytically. To do so, let us note that the difference, the sum and the product of $\gamma_\downarrow$ and $\gamma_\uparrow$ can be written using hyperbolic functions as

$$\begin{aligned}
\gamma_\downarrow - \gamma_\uparrow &= \frac{\gamma_0}{2}\left(\coth\frac{E_{LO_1}}{2k_BT} - \coth\frac{E_{LO_2}}{2k_BT}\right)\\
\gamma_\uparrow + \gamma_\downarrow &= -\frac{\gamma_0}{2}\left(1 - \coth\frac{E_{LO_1}}{2k_BT}\coth\frac{E_{LO_2}}{2k_BT}\right)\\
\gamma_\uparrow\gamma_\downarrow &= \left(\frac{\gamma_0}{4}\sinh^{-1}\frac{E_{LO_1}}{2k_BT}\sinh^{-1}\frac{E_{LO_2}}{2k_BT}\right)^2
\end{aligned}$$

Thus, the decay rates $\Gamma_\pm$ can be expressed as

$$\Gamma_\pm = \frac{1}{2}\left(\Gamma_U + \Gamma_L + -\frac{\gamma_0}{2}\left(1 - \coth\frac{E_{LO_1}}{2k_BT}\coth\frac{E_{LO_2}}{2k_BT}\right) \pm \sqrt{\left[\Gamma_U - \Gamma_L + \frac{\gamma_0}{2}\left(\coth\frac{E_{LO_1}}{2k_BT} - \coth\frac{E_{O_2}}{2k_BT}\right)\right]^2 + \left(\frac{\gamma_0}{2\sinh\frac{E_{LO_1}}{2k_BT}\sinh\frac{E_{LO_2}}{2k_BT}}\right)^2}\right)$$

Two-phonon sum-process mixing

In this work, we also investigate the possibility of a another type of two-phonon transitions: the absorption or emission of pairs of phonons. In this case, the low temperature asymmetry between the upward and downward process is restored. Indeed, in the one-phonon case, at low temperature there is always the possibility to emit a phonon while absorption is impossible. In contrast, in the Raman-like two-phonon case, absorption and emission are forbidden at low temperature. The alternate scenario we investigate here restores this low temperature asymmetry as evidenced in the transition rates:

$$\gamma_{\uparrow} = \gamma_0 N_{LO_2} N_{LO_1}$$
$$\gamma_{\uparrow} = \gamma_0 \left(N_{LO_2} + 1\right)\left(N_{LO_1} + 1\right)$$

Similar relations based on hyperbolic equations can be obtained.

A.2 Three-level models

While all dependencies can be included in a single model with three bright states and a dark state it is useful to separate the contributions of the several components of the model. In the following, we take each part of the model separately and give the analytical expressions for the decay rates.

A.2.1 Non-resonant excitation

In our experiments, we excite non-resonantly, approximately $\sim 250\,\text{meV}$ above the optical band gap. Therefore, we do not populate the band-edge exciton states diretly but rather after relaxation from higher lying excited states. This relaxation can take some time, especially in perovskites, where hot carrier cooling was found to happen with a characteristic rate $\sim 25\,\text{meV}\,\text{ps}^{-1}$ much slower than in GaAs for examples $\lesssim 1\,\text{eV}\,\text{ps}^{-1}$ [20]. We account for this contribution, leading to a characteristic rise time in the PL decay, by assuming that non-resonant excitation instantaneously populates a single higher lying excited state with a characteristic decay rate to $\Gamma_\text{R} = 1/\tau_\text{R}$ (FIG. A.3). This state can then populate the band-edge exciton states.

The matrix rate equations for the sub-system comprised of the higher excited state and the emitting state can be written as

$$\begin{pmatrix} \dot{p}_E \\ \dot{p}_1 \end{pmatrix} = \begin{pmatrix} -\Gamma_\text{R} & 0 \\ \Gamma_\text{R} & -\Gamma \end{pmatrix} \begin{pmatrix} p_E \\ p_1 \end{pmatrix} \tag{A.9}$$

Within this system, the population of state 1 at time t is given by

$$p_1(t) = p_1(0)e^{-\Gamma t} + \frac{p_E(0)\Gamma_\text{R}}{\Gamma - \Gamma_\text{R}}\left(e^{-\Gamma_\text{R} t} - e^{-\Gamma t}\right) \tag{A.10}$$

Assuming, as is the case for non-resonant excitation that $p_E(0) = 1$ and $p_1(0) = 0$, yields the result that the population of the emitting state is given by the difference between the decay of each component and reads

$$p_1(t) = \frac{\Gamma_\mathrm{R}}{\Gamma - \Gamma_\mathrm{R}} \left(e^{-\Gamma_\mathrm{R} t} - e^{-\Gamma t}\right) \tag{A.11}$$

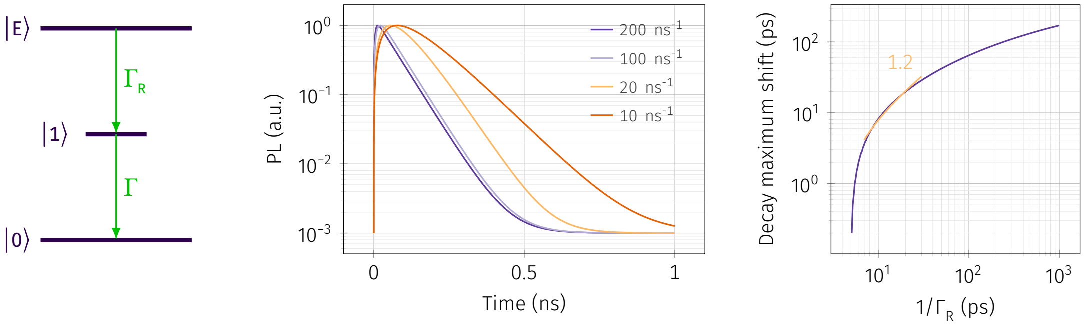

Figure A.3 | Non-resonant excitation. Non-resonant excitation

This is depicted in FIG. A.3b where the decay of the emitting state is shown as a function of the characteristic relaxation time $1/\Gamma_\mathrm{R}$ for $1/\Gamma = 65$ ps. The relaxation time therefore gives rise to two effects. First, the decay maximum is smoothed and the decay deviates from $e^{-\Gamma t}$. Concomittanly, the decay maximum shifts towards longer times, evidencing the role of the higher lying excited state in populating the emitting state. This is shown in FIG. A.3c where the decay maximum shift increases with increasing relaxation time. Notably, for characteristic relaxation times ~ 10 ps, we can approximate this dependence by a linear dependence. In this range, the characteristic relaxation time contributes linearly to the decay maximum shift with conversion of 1.2 ps shift per ps relaxation time.

A.2.2 Bright-dark dynamics

The band-edge exciton states are usually comprised of a set of bright and dark exciton states. At least, we can take into account a single bright state coupled to a dark state.

Model

The matrix rate equations for this sub-system comprised of a single bright state and a single dark state can be written as

$$\begin{pmatrix} \dot{p}_B \\ \dot{p}_D \end{pmatrix} = \begin{pmatrix} -\Gamma_\mathrm{B} & \gamma_\mathrm{DB} \\ \gamma_\mathrm{BD} & -\Gamma_\mathrm{D} \end{pmatrix} \begin{pmatrix} p_B \\ p_D \end{pmatrix} \tag{A.12}$$

where the rates $\gamma_{\mathrm{BD}}, \gamma_{\mathrm{DB}}$ depending on the actual coupling mechanism.

The two exciton states can relax to the ground state with transition rates $\Gamma_{\mathrm{U,L}}$ that are assumed to be temperature-independent. At zero temperature, transitions from the upper to the lower exciton state happen at a rate γ_0 and, at finite temperature, thermally-activated transitions between $|\mathrm{U}\rangle$ and $|\mathrm{L}\rangle$ are driven by the emission or/and absorption of phonons with an energy matching the energy difference Δ between the two states, and happen at a rate $\gamma_{\downarrow\uparrow}$.

Within this model, the rate equations for the populations of the upper $|\mathrm{U}\rangle$ and lower $|\mathrm{L}\rangle$ exciton states, p_{U} and p_{D} are given by a system of first order coupled linear differential equations written in all generality as

$$\dot{p}_U = a_1 p_{\mathrm{U}} + a_2 p_{\mathrm{L}} \tag{A.13}$$

$$\dot{p}_L = a_3 p_{\mathrm{U}} + a_4 p_{\mathrm{L}} \tag{A.14}$$

where the coefficients a_i are supposed time- and temperature-independent. Let us express p_L as a function of p_U:

$$p_L = \frac{\dot{p}_U - a_1 p_U}{a_2} \tag{A.15}$$

and inject (A.15) in (A.14), which yields the second order differential equation

$$\ddot{p}_{\mathrm{U}} - (a_1 + a_4)\,\dot{p}_U + \left(a_1 a_4 - a_2 a_3\right) p_U = 0$$

We can choose an exponential form $p_U \propto e^{-\Gamma t}$ as a test function which gives us the characteristic quadratic equation

$$\Gamma^2 + (a_1 + a_4)\,\Gamma + a_1 a_4 - a_2 a_3 = 0$$

with solutions

$$\Gamma_\pm = -\frac{a_1 + a_4}{2} \pm \sqrt{\left(\frac{a_1 + a_4}{2}\right)^2 + a_2 a_3 - a_1 a_4}$$

The time-dependent populations in the upper and lower excitonic levels can thus be written as

$$p_U = A_1\, e^{-\Gamma_+ t} + A_2\, e^{-\Gamma_- t} \tag{A.16}$$

$$p_L = \frac{1}{a_2}\left[-A_1\left(\Gamma_+ + a_1\right) e^{-\Gamma_+ t} - A_2\left(\Gamma_- + a_1\right) e^{-\Gamma_- t}\right] \tag{A.17}$$

Assuming that after the laser excitation, the upper level population is $p_{\mathrm{U}}(t = 0) = a$, the lower level population then is $p_{\mathrm{D}}(t = 0) = 1 - a$, and the coefficients $A_{1,2}$ are given by:

$$
\begin{aligned}
A_1 &= \frac{a_2\,(a-1) - a\,(\Gamma_- + a_1)}{\Gamma_+ - \Gamma_-} \\
A_2 &= \frac{a_2\,(1-a) + a\left(\Gamma_+ + a_1\right)}{\Gamma_+ - \Gamma_-}
\end{aligned}
$$

The photoluminescence signal given by $S(t) = \eta_{\mathrm{U}}\Gamma_{\mathrm{U}}p_U + \eta_{\mathrm{L}}\Gamma_{\mathrm{L}}p_L$ thus reads

$$S(t) = A_+\,e^{-\Gamma_+ t} + A_-\,e^{-\Gamma_- t}$$

with $A_+ = \eta_{\mathrm{U}}\Gamma_{\mathrm{U}}A_1 - \eta_{\mathrm{L}}\Gamma_{\mathrm{L}}A_1\left(\Gamma_+ + a_1\right)/a_2$ and $A_- = \eta_{\mathrm{U}}\Gamma_{\mathrm{U}}A_2 - \eta_{\mathrm{L}}\Gamma_{\mathrm{L}}A_2\,(\Gamma_- + a_1)\,/a_2$. Here, we have introduced the quantum yield of each state as the fraction of radiative recombinations $\eta_i = \Gamma_{i,R}/\left(\Gamma_{i,R} + \Gamma_{i,NR}\right)$. Finally, we can put back the original expressions of A_i and express $A_\pm$ solely as a function of physical parameters. It is noteworthy that the actual amplitudes depend on a lot of experimental factors making them inaccessible. We will rather be interested in the relative or fractional intensities $I_{\pm,\mathrm{rel}} = A_{\pm,\mathrm{rel}}\tau_\pm$ as deduced from the amplitudes $A_{\pm\,\mathrm{rel}}$

$$
\begin{aligned}
A_{+\,\mathrm{rel}} &= A_+/\left(A_+ + A_-\right) \\
A_{-\,\mathrm{rel}} &= A_-/\left(A_+ + A_-\right)
\end{aligned}
$$

For the sake of simplicity, we have not yet expressed the coefficients a_i. Let us now express the actual coefficients a_i

$$
\begin{aligned}
a_1 &= -\left(\Gamma_{\mathrm{U}} + \gamma_\downarrow\right) \\
a_2 &= \gamma_\uparrow \\
a_3 &= \gamma_\downarrow \\
a_4 &= -\left(\Gamma_{\mathrm{L}} + \gamma_\uparrow\right)
\end{aligned}
\tag{A.18}
$$

such that the measured decay times can be expressed as

$$\Gamma_\pm = \frac{1}{2}\left(\Gamma_{\mathrm{U}} + \Gamma_{\mathrm{L}} + \gamma_\uparrow + \gamma_\downarrow \pm \sqrt{\left(\Gamma_{\mathrm{U}} - \Gamma_{\mathrm{L}} + \gamma_\downarrow - \gamma_\uparrow\right)^2 + 4\gamma_\uparrow\gamma_\downarrow}\right) \tag{A.19}$$

Integrated intensity

From these expressions, we can also determine the relative emission intensities of the bright and dark states, see e.g. [21]. Within this model, we can determine the total emitted intensity I_i of a state i by integrating its population as $I_i = \eta_i \int_0^\infty \Gamma_i p_i \, dt$.

At this point, we can directly get the intensity ratio between the two potential emission lines $|U\rangle$ and $|L\rangle$. To do so, we integrate the system of equations ?? and solve for the integrated intensity.

$$\int_0^\infty \dot{p}_U \mathrm{d}t = a_1 \int_0^\infty p_U \mathrm{d}t + a_2 \int_0^\infty p_L \mathrm{d}t \qquad \int_0^\infty \dot{p}_L \mathrm{d}t = a_3 \int_0^\infty p_U \mathrm{d}t + a_4 \int_0^\infty p_L \mathrm{d}t$$

using the definition of the integrated intensity $I = \eta\Gamma \int_0^\infty p \mathrm{d}t$ we identify

$$p_U \Big]_0^\infty = -p_{\mathrm{U}}(0) = a_1 \frac{I_{\mathrm{U}}}{\eta_{\mathrm{U}}\Gamma_{\mathrm{U}}} + a_2 \frac{I_{\mathrm{L}}}{\eta_{\mathrm{L}}\Gamma_{\mathrm{L}}} \qquad p_L \Big]_0^\infty = -p_{\mathrm{L}}(0) = a_3 \frac{I_{\mathrm{U}}}{\eta_{\mathrm{U}}\Gamma_{\mathrm{U}}} + a_4 \frac{I_{\mathrm{L}}}{\eta_{\mathrm{L}}\Gamma_{\mathrm{L}}}$$

Setting $x = p_{\mathrm{U}}/\eta_{\mathrm{U}}\Gamma_{\mathrm{U}}$ and $y = p_{\mathrm{L}}/\eta_{\mathrm{L}}\Gamma_{\mathrm{L}}$, we solve the system:

$$\begin{cases} -p_{\mathrm{U}}(0) = a_1 x + a_2 y \\ -p_{\mathrm{L}}(0) = a_3 x + a_4 y \end{cases} \quad \text{and find} \quad \begin{cases} x = \frac{p_{\mathrm{U}}(0) a_4 - a_2 p_{\mathrm{U}}(0)}{a_2 a_3 - a_1 a_4} \\ y = \frac{a_1 p_{\mathrm{L}}(0) - p_{\mathrm{U}}(0) a_3}{a_2 a_3 - a_1 a_4} \end{cases} \tag{A.20}$$

We finally find the analytical expressions for the integrated intensity of the upper and lower exciton states as

$$I_{\mathrm{U}} = \eta_{\mathrm{U}}\Gamma_{\mathrm{U}} \frac{p_{\mathrm{U}}(0)\left(\Gamma_{\mathrm{L}} + \gamma_\uparrow\right) + p_{\mathrm{L}}(0)\,\gamma_\uparrow}{\left(\Gamma_{\mathrm{U}} + \gamma_\downarrow\right)\left(\Gamma_{\mathrm{L}} + \gamma_\uparrow\right) - \gamma_\uparrow\gamma_\downarrow} \qquad I_{\mathrm{L}} = \eta_{\mathrm{L}}\Gamma_{\mathrm{L}} \frac{p_{\mathrm{L}}(0)\left(\Gamma_{\mathrm{U}} + \gamma_\downarrow\right) + p_{\mathrm{U}}(0)\,\gamma_\downarrow}{\left(\Gamma_{\mathrm{U}} + \gamma_\downarrow\right)\left(\Gamma_{\mathrm{L}} + \gamma_\uparrow\right) - \gamma_\uparrow\gamma_\downarrow}$$

We can further express the ratio between integrated intensities of the upper and lower exciton states as

$$\frac{I_{\mathrm{L}}}{I_{\mathrm{U}}} = \frac{\eta_{\mathrm{L}}\Gamma_{\mathrm{L}}}{\eta_{\mathrm{U}}\Gamma_{\mathrm{U}}} \frac{p_{\mathrm{L}}(0)\left(\Gamma_{\mathrm{U}} + \gamma_\downarrow\right) + p_{\mathrm{U}}(0)\,\gamma_\downarrow}{p_{\mathrm{U}}(0)\left(\Gamma_{\mathrm{L}} + \gamma_\uparrow\right) + p_{\mathrm{L}}(0)\,\gamma_\uparrow} \tag{A.21}$$

To compare with the expression found in [21], we assume equal initial populations $p_{\mathrm{U}}(0) = p_{\mathrm{L}}(0) = 1/2$ and a one-phonon mixing model to find

$$\frac{I_{\mathrm{L}}}{I_{\mathrm{U}}} = \frac{\eta_{\mathrm{L}}\Gamma_{\mathrm{L}}}{\eta_{\mathrm{U}}\Gamma_{\mathrm{U}}} \frac{\Gamma_{\mathrm{U}} + 2\gamma_\downarrow}{\Gamma_{\mathrm{L}} + 2\gamma_\uparrow} = \frac{\eta_{\mathrm{L}}\Gamma_{\mathrm{L}}}{\eta_{\mathrm{U}}\Gamma_{\mathrm{U}}} \frac{\Gamma_{\mathrm{U}} + 2\gamma_0\left(N_B + 1\right)}{\Gamma_{\mathrm{L}} + 2\gamma_0 N_B}$$

Conclusion

In this chapter, we have given a detailed description of the rate equations commonly used to model semiconductor nanoemitters. In particular, we have described from first principles the expressions for the thermally-driven population redistribution amongst the exciton fine structure states. Finally, we have detailed the analytical expressions deduced from the rate equations in two simple cases related respectively to the non-resonant excitation used and bright-dark exciton interaction. For the latter, we have provided expression for both the time-resolved and time-integrated populations.

References for Chapter A

[1] A. Einstein, “Zur Quantentheorie der Strahlung”, Physikalische Zeitschrift **18**, 121–128 (1917) (p. 167).

[2] S. Rudin et al., “Temperature-dependent exciton linewidths in semiconductors”, Physical Review B **42**, 11218 (1990) (pp. 169, 170).

[3] T. Takagahara, “Electron-phonon interactions and excitonic dephasing in semiconductor nanocrystals”, Physical Review Letters **71**, 3577–3580 (1993) (pp. 169, 172).

[4] E. A. Muljarov et al., “Dephasing in Quantum Dots: Quadratic Coupling to Acoustic Phonons”, Physical Review Letters **93**, 237401 (2004) (pp. 169, 170).

[5] P. Tighineanu et al., “Phonon Decoherence of Quantum Dots in Photonic Structures: Broadening of the Zero-Phonon Line and the Role of Dimensionality”, Physical Review Letters **120**, 7401 (2018) (p. 169).

[6] B. Krummheuer et al., “Theory of pure dephasing and the resulting absorption line shape in semiconductor quantum dots”, Physical Review B **65**, 195313 (2002) (p. 170).

[7] A. V. Uskov et al., “Dephasing Times in Quantum Dots due to Elastic LO Phonon-Carrier Collisions”, Physical Review Letters **85**, 1516–1519 (2000) (p. 170).

[8] E. Fermi, *Nuclear Physics: A Course Given by Enrico Fermi at the University of Chicago*, edited by R. edition (University of Chicago Press, Chicago, 1974), 258 pp. (p. 170).

[9] P. A. M. Dirac, “The Quantum Theory of the Emission and Absorption of Radiation”, Proceedings of the Royal Society A **114**, 243–265 (1927) (p. 170).

[10] E. Tsitsishvili et al., “Exciton-spin relaxation in weakly confining quantum dots due to spin–orbit interaction”, physica status solidi (b) **243**, 2274–2277 (2006) (p. 171).

[11] E. Tsitsishvili et al., “Exciton-spin relaxation in quantum dots due to spin-orbit interaction”, Physical Review B **72**, 155333 (2005) (p. 171).

[12] G. D. Mahan, *Condensed matter in a nutshell*, In a Nutshell (Princeton University Press, Princeton, N.J, 2011), 574 pp. (p. 173).

[13] G. D. Mahan, *Many-Particle Physics*, 3rd ed., Physics of Solids and Liquids (Springer US, 2000) (pp. 173, 174).

[14] D. G. Thomas, “Excitons and Band Splitting Produced by Uniaxial Stress in CdTe”, Journal of Applied Physics **32**, 2298–2304 (1961) (p. 173).

[15] K. Cho, ed., *Excitons*, Vol. 14, Topics in Current Physics (Springer Berlin Heidelberg, Berlin, Heidelberg, 1979) (pp. 173, 174).

[16] M. Puppin et al., “Evidence of Large Polarons in Photoemission Band Mapping of the Perovskite Semiconductor $CsPbBr_3$”, Physical Review Letters **124**, 206402 (2020) (p. 174).

[17] M. Fu et al., “Unraveling exciton–phonon coupling in individual $FAPbI_3$ nanocrystals emitting near-infrared single photons”, Nature Communications **9**, 3318 (2018) (p. 176).

[18] P. Tamarat et al., “The ground exciton state of formamidinium lead bromide perovskite nanocrystals is a singlet dark state”, Nature Materials **18**, 717–724 (2019) (p. 176).

[19] P. Tamarat et al., “The dark exciton ground state promotes photon-pair emission in individual perovskite nanocrystals”, Nature Communications **11**, 6001 (2020) (p. 176).

[20] M. Bernardi et al., "Ab initio study of hot electrons in GaAs", Proceedings of the National Academy of Sciences **112**, 5291–5296 (2015) (p. 178).

[21] E. V. Shornikova et al., "Addressing the exciton fine structure in colloidal nanocrystals: the case of CdSe nanoplatelets", Nanoscale **10**, 646–656 (2018) (p. 182).